Diss. ETH No. 16611

Neutron Diffraction Study
of
Cobaltite Systems

A dissertation submitted to the
SWISS FEDERAL INSTITUTE OF TECHNOLOGY
ZÜRICH

for the degree of
Doctor of Natural Sciences

presented by

SABINE STREULE
Dipl. Phys. ETH Zürich
born July 13, 1975
citizen of Ennetbaden (AG)

accepted on the recommendation of
Prof. Dr. H.R. Ott, examiner
Dr. J. Mesot, co-examiner
Prof. Dr. R. Nesper, co-examiner

2006

Contents

Abstract

The cobaltites $SrCoO_{3-\delta}$ were discovered in 1957 and in 1970 magnetic order was first reported in a cobaltite. These materials attracted attention because of their possible applications as oxidation catalysts, gas sensors and oxygen separation membranes due to their stability in a wide range of oxygen content, high oxygen diffusivity and electron conduction. In 1997, magnetoresistance was found in newly synthesized Co-compounds ($RBaCo_2O_{5.4}$; Ln = Eu, Gd), which lead to enhanced interest because of their potential in improving magnetic data storage. When superconductivity was found in hydrated $Na_{0.35}CoO_2$ in 2003, cobaltites received even more attention.

The crystal structure of all these materials derives from the perovskite structure, but various superstructures are also observed. The structure of $LnCoO_{3-\delta}$ (Ln = Lanthanid) type cobaltites is three dimensional (3D), while a layered (2D) structure is adopted by the $LnBaCo_2O_{5+\delta}$ compounds. Whereas the crystallographic structures for Co-compounds with an integer number of oxygen ions per unit formula are well known, no consensus has been reached for non-integer compounds. Knowledge of the crystallographic structure of a compound is of particular importance for determining magnetic structures, since these two properties are closely related.

The magnetic structures, especially of the layered cobaltite compounds with oxygen content of 5.5 per unit formula, are still debated. The determination of the magnetic structure is a complex task, because, contrary to other materials, the Co ion in these materials can be in different spin states. This is due to the fact that in cobaltites the crystal field splitting of the Co ion's $3d$ energy level and the Hund's rule intra-atomic exchange energy are of the same order of magnitude. Therefore, the electrons in the Co ion $3d$ shell can be distributed among the $3d$ orbitals not necessarily according to Hund's rule, but in two additional ways. This leads to three so-called spin states that a Co ion can adopt.

Regarding electronic transport properties, the cobaltites, depending on oxygen content, either belong to the class of bad metals or semiconductors (with the exception of the metallic $SrCoO_3$ compound). The cobaltites are mixed valent materials, which means that the Co ions can carry different charges. The ratio between different Co ionic configurations is determined by the oxygen content, following the charge neutrality condition.

Changes in the crystallographic and magnetic structures as well as in the spin states and the electronic transport properties can be evoked by varying several parameters, of either intrinsic (oxygen content, lanthanide doping) or extrinsic nature (temperature, pressure, magnetic field). Since only small changes of a parameter can cause a structural, magnetic or electronic transition, it does not come as a surprise that a variety of contradictory models exist, e.g. on crystallographic structures. Detailed studies are therefore urgently needed to clarify the influence of each parameter on the properties of the Co-compounds. In the present work, special emphasis has been put on the **oxygen content and oxygen ordering influence** onto the crystallographic, magnetic and electronic properties of various cobaltites:

1) A series of 3D samples $Ho_{0.1}Sr_{0.9}CoO_{3-\delta}$ with varying oxygen content was studied in detail. An important result is the finding of very clear charge ordering of the Co^{3+} and Co^{4+} ions due to a particularly simple 1-dimensional deformation pattern of alternating elongated and compressed CoO_6 octahedra (Chapter 3.4).

2) As a consequence of charge ordering in 3D cobaltites, all measured magnetic structures can naturally be explained within a simple superexchange scheme (Chapter 3.5).

3) 2D samples $PrBaCo_2O_{5+\delta}$ have been synthesized under two different conditions (quenched and slowly cooled). Large differences in both crystallographic and magnetic properties were found. In contrast to reports in the literature, we show that lattice parameter anomalies alone are not sufficient to infer the existence of long range oxygen/vacancy ordering (Chapter 4.3.1).

4) A purely structural transition in $PrBaCo_2O_{5.48}$ has been discovered at $T_{OD} = 776$ K, which is characterized by the loss of oxygen ordering. Studies of the transport properties in $PrBaCo_2O_{5+\delta}$ ($0.16 \le \delta \le 0.50$) lead to the conclusion that the conduction in all these material is best described by thermally activated hole mobility (Chapter 4.3.3).

The measurements were mostly performed with neutron scattering instruments. Neutrons are the ideal probe to be used in the present work, because they are sensitive to oxygen positions and occupancies and allow to reliably determine magnetic structures. Complementary measurements include x-ray diffraction (crystallographic structure determination), macroscopic magnetization measurements (sample characterization) and transport measurements. A short introduction to the experimental techniques is given in Chapter 2.

Zusammenfassung

Die Kobaltite $SrCoO_{3-\delta}$ wurden 1957 entdeckt, und 1970 wurde das erste Mal über magnetische Ordnung in einem solchen Material berichtet. Kobaltite sind interessant, weil sie in verschiedenen Gebieten eine Anwendung finden könnten. Aufgrund ihrer hohen Sauerstoffdiffusivität, Elektronenleitung und ihres Sauerstoffgehaltes, der über einen weiten Bereich stabil ist, haben sie Potential als Oxidationskatalysatoren, Gassensoren oder Sauerstofftrennmembrane eingesetzt zu werden. Im Jahre 1997 wurde ausserdem an einer neu hergestellten Co-Verbindung ($RBaCo_2O_{5.4}$; R = Eu, Gd) ein Magnetwiderstand gemessen. Damit wuchs das Interesse an Kobaltiten, da diese Eigenschaft sie zu Kandidaten für die magnetische Datenspeicherung machte. In hydratisiertem $Na_{0.35}CoO_2$ wurde 2003 Supraleitung festgestellt, worauf die Forschungstätigkeit auf dem Gebiet der Kobaltite weiter intensiviert wurde.

Die Kristallstruktur der Co-Verbindungen lässt sich von der Perovskitstruktur ableiten, wobei auch verschiedene Superstrukturen auftreten. Man unterscheidet zwischen den drei-dimensionalen (3D) $LnCoO_{3-\delta}$ (Ln = Lanthanid) und den zwei-dimensionalen (2D) $LnBaCo_2O_{5+\delta}$ Kobaltiten. Die Kristallstrukturen der Materialien mit ganzzahligem Sauerstoffgehalt pro Einheitszelle sind eindeutig bestimmt. Für Verbindungen mit nicht-ganzzahligem Sauerstoffgehalt sind die Meinungen jedoch verschieden. Vor allem für die Bestimmung der magnetischen Strukturen ist es wichtig den Aufbau der Einheitszelle zu kennen, denn diese zwei Strukturen sind eng verknüpft.

Die magnetischen Strukturen, vorallem die der zwei dimensionalen Kobaltite mit Sauerstoffgehalt 5.5, sind noch stark kontrovers. Es ist schwierig, die magnetische Struktur zu bestimmen, da das Co Ion verschiedene Spin Zustände annehmen kann. Diese Eigenschaft ist speziell für Co Ionen in Kobaltiten und rührt daher, dass in Kobaltiten die Kristallfeldaufspaltung der $3d$ Energieniveaus des Co Ions und die intra-atomare Hund'sche-Regel-Austauschwechselwirkung von der gleichen Grössenordnung sind. Diese gleiche Grössenordnung hat zur Folge, dass die sechs Elektronen in der Co $3d$ Schale, nicht unbedingt die Hund'sche Regel befolgen müssen, um die Energieniveaus zu besetzen. Insgesamt gibt es drei verschiedene Möglichkeiten, die Niveaus zu besetzen, was zu drei verschiedenen Spinzuständen führt.

Abhängig vom Sauerstoffgehalt sind die Kobaltite bei Raumtemperatur sogenannt schlechte Metalle oder Halbleiter, eine Ausnahme ist die metallische $SrCoO_3$ Verbindung. Kobaltite gehören zu den Materialien mit gemischter Wertigkeit, d.h. eine Verbindung kann aus Co Ionen verschiedener Ladungen bestehen. Ausgehend vom Sauerstoffgehalt einer Verbindung wird das Verhältnis zwischen Co Ionen verschiedener Ladungen durch die Bedingung der Ladungsneutralität bestimmt.

Man kann eine Änderung der Kristall- und Magnetstruktur, der elekronischen Eigenschaften, sowie der Spinzustände hervorrufen, indem man verschiedene Parameter ändert. Diese sind entweder materialspezifisch (Sauerstoffgehalt, Lanthanid-dotierung) oder von aussen einwirkend (Temperatur, Druck, magnetisches Feld). Da nur kleine Änderungen eines Parameters genügen, um die strukturelle, magnetische oder elektronische Eigenschaft des Materials zu verändern, ist

es nicht erstaunlich, dass widersprüchliche Modelle existieren, z.B. was die Kristallstruktur an-
belangt. Es braucht daher ausführliche Untersuchungen des Einflusses jedes Parameters auf
die Eigenschaften der Co-Verbindungen. Diese Arbeit konzentriert sich auf den **Einfluss des
Sauerstoffgehalts und der Sauerstoffordnung** auf die magnetischen und elektronischen
Eigenschaften verschiedener Kobaltite:

1) Eine Reihe von 3D Proben $Ho_{0.1}Sr_{0.9}CoO_{3-\delta}$ ($0.15 \leq \delta \leq 0.49$) wurde untersucht. Ein
wesentliches Resultat ist die Entdeckung von Ladungsordnung der Co^{3+} und Co^{4+} Ionen im
Bereich $0.19 \leq \delta \leq 0.31$. Die Ordnung basiert auf ausgedehnter und komprimierter CoO_6 Ok-
taedern, die sich entlang einer Kristallrichtung abwechseln (Kapitel 3.4).

2) Aufgrund der Ladungsordnung in diesen 3D Kobaltiten lässt sich deren magnetische Struktur
erklären durch die Super-Austauschwechselwirkung alleine erklären (Kapitel 3.5).

3) Eine Reihe $PrBaCo_2O_{5+\delta}$ Proben ($0.17 \leq \delta \leq 0.79$) wurde unter zwei Bedingungen hergestellt
(schnell und langsam abgekühlt). In Abhängigkeit vom Sauerstoffgehalt und der Herstellungsart
wurden grosse Unterschiede in den strukturellen und magnetischen Eigenschaften festgestellt.
Unsere Untersuchungen zeigen, dass man aus Anomalien der Gitterparameter nicht automatisch
auf Sauerstoffordnung schliessen kann, wie dies bisher angenommen wurde (Kapitel 4.3.1).

4) In 2D $PrBaCoO_{5.48}$ wurde ein rein struktureller Übergang bei $T_{OD} = 776$ K gefunden. Bei
dieser Temperatur geht die Sauerstoffordnung verloren. Untersuchungen der Transporteigen-
schaften von $PrBaCo_2O_{5+\delta}$ ($0.16 \leq \delta \leq 0.50$) zeigen, dass die Leitfähigkeit in diesen Materialien
am besten durch thermisch aktivierte Lochbeweglichkeit beschrieben wird (Kapitel 4.3.3).

Die Messungen basierten vor allem auf der Neutronenstreuung. Neutronen sind die ideale Mess-
methode für diese Arbeit, da sich einerseits Sauerstoffpositionen und -besetzungen und anderer-
seits auch magnetische Strukturen zuverlässig bestimmen lassen. Zusätzliche Experimente um-
fassen Röntgenstreuung (Kristallstrukturbestimmung), makroskopische Magnetisierungsmes-
sungen (Probencharakterisierung) and Transportmessungen. Eine kurze Einführung in die ex-
perimentellen Techniken wird in Kapitel 2 gegeben.

Abbreviations

AFM   Antiferromagnetic
B   Debye-Waller factor
BVS   Bond valence sum
CO   Charge order
DE   Double Exchange
DSC   Differential scanning calorimetry
FC   Field cooled
FM   Ferromagnetic
HS   High spin
IS   Intermediate spin
LS   Low spin
NPD   Neutron powder diffraction
OD   Order-Disorder
PM   Paramagnetic
RQ   Rapidly quenched
RT   Room temperature
SC   Slowly cooled
SE   Superexchange
SS   Spin state
SSO   Spin-state ordered
TM   Transition metal
XPD   X-ray powder diffraction
ZFC   Zero field cooled

a_p lattice parameter of cubic perovskite unit cell
d Bond distance
δ Oxygen deficiency
Δ_{cf} Crystal field splitting
E_a Activation energy
J_H Hund's rule intra-atomic exchange energy
λ Wavelength
Ln Lanthanide
μ Mobility
μ_{Co} Co magnetic moment
μ_{eff} Effective magnetic moment in μ_B per formula unit
p Hole concentration
ρ Resistivity
S Thermopower (Seebeck coefficient)
σ Conductivity
2Θ Scattering angle
T_C Curie temperature
T_{CO} Charge order transition temperature
T_N Néel temperature
T_{MI} Metal-insulator transition temperature
T_{OD} Order-disorder transition temperature

Chapter 1

Perovskite Co-Compounds

Cobalt: the name derives from the german silver miners' believe that goblins would steal their silver and replace it by another similar colored material to conceal the theft. The german word for goblin evolved from the middle high german kobolt to the current form of kobold. Cobalt then became the term silver miners used for this worthless element, which was additionally contaminated with arsenic and sulphur.

Before giving a short introduction on the perovskite system and the peculiarties of transition metals (among which are Mn, Fe, Co, Ni and Cu), a few words should be said on the reason for the interest in cobaltites.
On the application side three properties which motivate the investigation of the cobaltites will be mentioned:

1. Magnetoresistance: magnetoresistance displayed by some of the compounds in the family of cobaltites ($LnBaCo_2O_{5.4}$, $Ln = Er$, Gd [1]) is interesting in view of improving magnetic data storage.

2. High ionic conductivity: three dimensional cobaltites exhibit high ionic conduction (first discovered in $Ln_{1-x}M_xCoO_3$, Ln = lanthanide, M = La, Ca, Sr [2, 3, 4, 5], which makes them good candidates for oxidation catalysts, gas sensors and electrode materials for fuel cells.

3. Superconductivity: superconductivity was recently found in $Na_{0.35}CoO_2 \cdot 1.3\ H_2O$ [6] and similarities of superconducting properties between this material and high temperature cuprates were postulated.

These three properties have their origin in the strong interplay between crystallographic, magnetic and transport properties, which leads to very rich phase diagrams as a function of temperature, magnetic field, pressure, oxygen content and size of lanthanide ions.
A property which distinguishes the cobaltites from other $3d$ metal oxides is the following: the crystal field splitting Δ_{cf} of the $3d$ energy level of the Co ion in cobaltites is of the same order of magnitude as the Hund's rule intra-atomic exchange energy J_H. Spin state transitions can therefore easily be provoked by either varying temperature, applying a magnetic field or pressure, and/or by tuning the structural parameters (oxygen content, type of lanthanide) of the material. The number of electrons in the $3d$ shell in Co (or also in Fe) allows for three spin states instead of two.
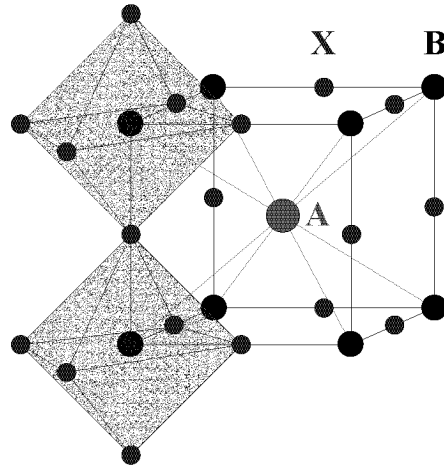
Figure 1.1: Schematic view of the ideal cubic perovskite structure of ABX_3 with corner sharing BX_6 octahedra.

Like other doped transition metal oxides, cobaltites can accomodate oxygen vacancies, allowing the ratio of Co^{2+}, Co^{3+} and Co^{4+} to vary. This has a strong influence on the magnetic and transport properties and is the origin of ionic conduction, which ocurrs primarily in materials with oxygen vacancies.

In the following the perovskite structure will be introduced, as it is the basis for the structural investigations in this work. In order to provide an understanding of the aforementioned spin states of the Co ions, the basic terms for the crystal field splitting of the atomic electron states in a crystal environment will be lined out. An overview of magnetic interactions relevant in these systems follows. Possible transport mechanisms are discussed, and the introductory section is concluded by an outline of this work.

1.1 Structural Properties

The name perovskite was originally assigned to the mineral $CaTiO_3$, but is now used for a large family of compounds having the same crystal structure as this mineral. In the ideal form, the crystal structure of a cubic perovskite ABX_3 [7] can be described as eight B cations sitting at the corners of a cube, each surrounded by six X anions, and an A cation occupying the site in the middle of this cube. The six X anions form a BX_6 octahedra around the B ion and the octahedra are arranged in such a way that they are connected at the corners (Figure 1.1). The interest in compounds belonging to the perovskite family originates from their large variety of physical properties and the flexibility to accomodate most of the elements in the periodic system [7, 8, 9].

The idealized cubic structure is for instance realized in $SrTiO_3$ or $SrCoO_3$. The latter can be described as Sr^{2+} and O^{2-} ions forming a cubic close packed lattice with Co^{4+} ions occupying the octahedral holes created by the oxygens (Figure 1.1). In the general cubic ABX_3 perovskite structure ($a_p = 3.905$ Å, space group Pm3m), the A atoms are in the Wyckoff position 1b (1/2,1/2,1/2); the B atoms in 1a (0,0,0); and the X atoms in 3d (1/2,0,0),(0,1/2,0),(0,0,1/2). However, the perovskite structure is known to be very flexible and most perovskites are distorted instead of adopting the ideal cubic structure. Two of the factors which can be responsible for such distortions will be discussed here: size effects and deviations from the ideal composition.
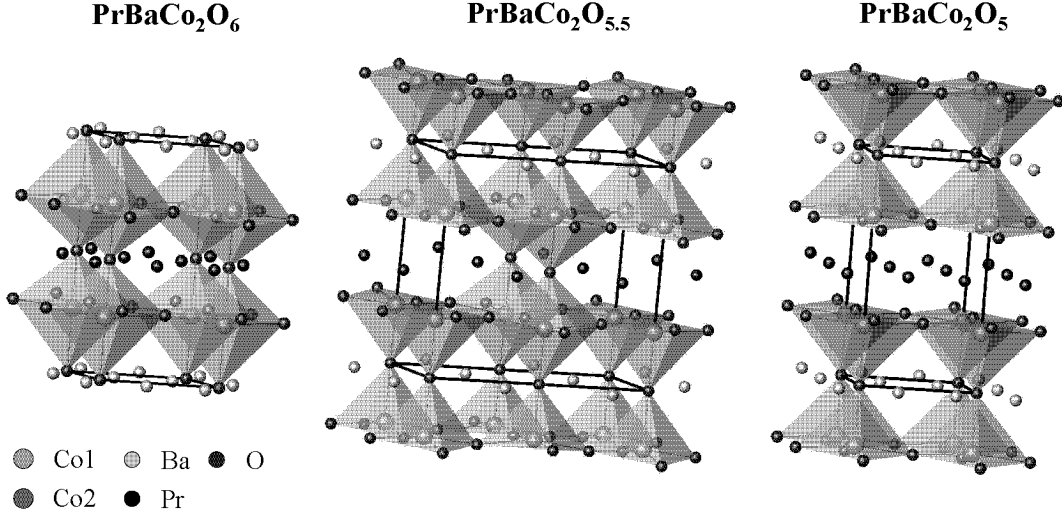
Figure 1.2: Schematic crystal structure of LnBaCo$_2$O$_{5+\delta}$ with a) $a_p \times a_p \times 2a_p$ ($\delta = 0$); b) $a_p \times 2a_p \times 2a_p$ ($\delta = 0.5$) and c) $a_p \times a_p \times 2a_p$ ($\delta = 1$) type unit cells.

1. Size: in the ideal cubic perovskite the cell parameter a_p is related to the ionic radii r_i (i = A, B, X) by

$$a_p = \sqrt{2}(r_A + r_X) = 2(r_B + r_X). \tag{1.1}$$

The Goldschmidt tolerance factor

$$t = \frac{r_A + r_X}{\sqrt{2}(r_B + r_X)}. \tag{1.2}$$

provides an estimate of the degree of distortion [7]. In the ideal cubic case $t = 1$, while the cubic structure is adopted for $0.89 < t \leq 1$ [10, 11]. For smaller values of t, the symmetry of the crystal structure will be lowered. For SrCoO$_3$ it is found that $t = 0.999$ (r$_{Sr}$=1.44 Å, r$_{Co^{3+}}$(HS)=0.61 Å, r$_O$=1.40Å). The reason for $t < 1$ comes from the deviating cation- and anion-ionic radii from the ideal values (SrTiO$_3$: r$_{Sr}$=1.44 Å, r$_{Ti}$=0.605 Å, r$_O$=1.40Å), resulting in a tilting of the [BO$_6$] octahedra to fill out the space. If, due to large A or small B ions $t > 1$, then hexagonal variants of the perovskite structure are stable, leading to a face sharing of [BO$_6$] ocathedra (e.g. BaNiO$_3$ with t=1.13).

2. Composition: one possibility to vary the composition is to reduce the oxygen content (e.g. PrBaCo$_2$O$_{5+\delta}$, $0 \leq \delta \leq 1$), which will change the valence of the Co ions from Co$^{3.5+}$ (1:1 Co^{4+}:Co^{3+}) for $\delta = 1$ to Co^{3+} ($\delta = 0.5$) to Co$^{2.5+}$ (1:1 Co^{3+}:Co^{2+}) for $\delta = 0$ (Figure 1.2). Oxygen vacancies lead to the formation of [CoO$_5$] pyramids and for the composition δ = 0.5, the number of pyramids and octahedra is equal (Figure 1.2). Interestingly, the octahedra and pyramids are ordered along a certain crystallographic direction (Figure 1.2). This leads to an oxygen deficient perovskite related structure with lower symmetry. In Chapter 4.2.1 details on superstructures and structural variations appearing in cobaltites are elaborated. Another oxygen deficient superstructure of the cubic perovskite with order among oxygen vacancies is the so called Brownmillerite structure, which is described in Chapter 3.4.4.

Perovskites with transition metal (TM) ions on the B site show an enormous variety of intriguing electronic and magnetic properties. This is not only related to their chemical flexibility, but rather to the complex interplay of the TM with the oxygen ions [12]. The influence of oxygen ions on the energy levels of the Co ions is described in the next section. Magnetism and electronic properties are related to the unfilled $3d$ electron shells and primarily given by a hierarchy of competing interactions. The hierarchy is determined by the number of $3d$ electrons, the Hund's rule coupling J_H, the crystal electric field Δ_{cf}, the Jahn-Teller splitting of the $3d$ electron orbitals and finally the exchange energies. Superexchange and hopping of electrons occur via oxygen sites due to the overlap of the respective wave functions. Therefore the properties and phase diagrams of a perovskite also depend on the oxygen non-stoichiometry and tilting/distortion of the BO_6 octahedra.

The energy hierarchy is well defined in cuprates where the Cu^{2+} is in a $3d^9$ configuration. One observes an elongation of the octahedra, which results in a splitting of the e_g orbital into two levels ($x^2 - y^2$ and z^2). The hole state in the d shell has e_g $x^2 - y^2$ symmetry (highest lying orbital) and provokes an $S = 1/2$ spin moment. The superexchange and magnetic interactions between the $S = 1/2$ spin moments are restricted to the xy-plane. Extreme limits are pyramidal $[CuO_5]$ or even planar $[CuO_4]$ configurations. This constraint is one of the key ingredients to high temperature superconductivity.

In the cobaltites the above mentioned hierarchy of energies is not well defined, since additional effects such as spin state transitions (e.g. $LaCoO_3$, see Chapter 3.2), charge disproportionation (e.g. in $PrBaCo_2O_{5.5}$, see Chapter 4.3.3) or oxygen ordering (layered cobaltites, Chapter 4) can occur.

1.2 Crystal Field Theory and Spin States

In this section the following question will be treated: to what extent is the energy scheme of a free atom (here Co) influenced by it being incorporated into a lattice of given symmetry (here oxygens surrounding the Co in octahedral or pyramidal geometry)? Knowledge of the energy scheme is important, because the energy scheme directly influences the spin states of the Co ion and thereby affects the possible magnetic interactions in the system.

Crystal field theory is concerned with examining the effect of the electric field of symmetrically arranged neighbouring atoms (O) on a particular lattice atom (Co). To calculate this effect all electrons of the incomplete shell of the Co have to be considered. The relevant Hamiltonian is [13]

$$H = H_0 + H_{el-el} + H_{SO} + H_{CF}, \tag{1.3}$$

where H_0 comprises the kinetic energy of the electrons of the Co atom and their interactions with the nucleus, H_{el-el} is the electron-electron interaction in the Co atom, H_{SO} is the spin-orbit interaction and H_{CF} is the influence of the crystal field (repulsion between electrons of the Co atom and the surrounding O atoms). H_{el-el}, H_{SO} and H_{CF} can be considered as perturbations of H_0. Here two cases will be examined: 1) Weak crystal fields $H_{el-el} > H_{CF}$ (electrons obey the Pauli principle) and 2) Strong crystal fields $H_{CF} > H_{el-el}$. In the following the interaction between the electrons in the Co $3d$ orbital and those in the O $2p$ orbitals will be studied.

It is well known that the atomic orbitals, with the exception of the s orbital, are not spherical symmetric. The angular dependences of the electron density of d orbitals are shown in Figure 1.3 (right) and the oxygen octahedron surrounding the Co ion is shown in the same Figure on the left. The crystal field energy in the case of a Co ion sitting in an octahedral oxygen environment
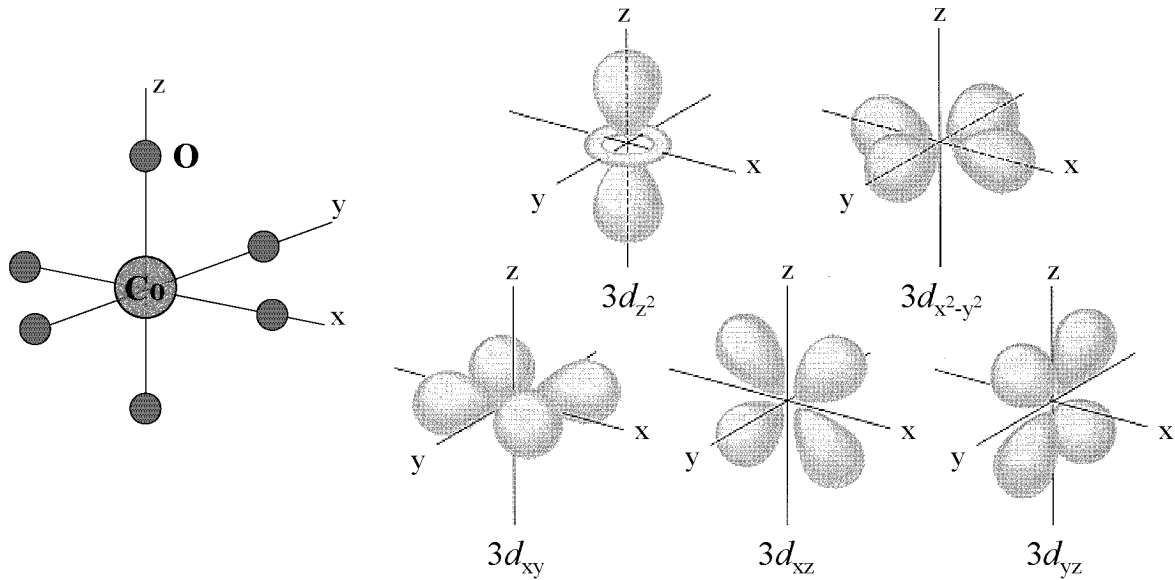
**Figure 1.3:** Left: Arrangement of the oxygen ions around the Co ion in a cartesian coordinate system. Right: Angular dependence of the electron distribution in the six $3d$ orbitals (after [14]).

arises from the electrostatic interaction between the electrons sitting in the $3d$ orbital of the Co ion and the electrons in the oxygen $2p$ orbitals.

Depending on the symmetry of the filled $3d$ orbitals, the orbital overlap of the Co electrons with the O electrons electrons can significantly differ. The d orbitals are divided into two classes: the t_{2g} orbitals whose orientations lie between the x, y, and z axes (d_{xy}, d_{xz} and d_{yz}) and the e_g orbitals which point along these axes (d_{z^2} and $d_{x^2-y^2}$). The cubic environment provided by the oxygen octahedron surrounding the Co ion can lift the degeneracy of these two orbitals: the crystal field is largely produced by the p orbitals on the oxygen ions (which point along x, y or z). The overlap of the p orbitals with the t_{2g} orbitals is smaller than with the e_g orbitals, causing the t_{2g} orbitals to have lower energy compared to the e_g orbitals. In the octahedral environment, the t_{2g} orbital energy is lower than the free ion energy and the e_g orbital energy lies higher (Figure 1.4 middle). The energy difference between these two levels is called the crystal field energy Δ_{cf}. Further splitting of the orbitals can occur if the octahedra are elongated along a certain direction, for example by the Jahn-Teller effect (Figure 1.4 right). The cubic environment is then transformed into a tetragonal one and the d_{z^2} orbital lowered in energy. Usually the elongation along the z direction will lead to a simultaneous shrinking in the xy-plane, also changing the energy of the t_{2g} orbitals. The magnitude of the crystal field splitting Δ_{cf} depends on the transition metal element, its charge and the number of ligands.

$3d$ transition metal ions are special because their d orbitals are only partially filled. In the case of Co^{3+}, only 6 electrons occupy orbital states instead of the maximum possible 10. For a weak crystal field the levels are filled according to Hund's rule (obeying the Pauli principle), which requires that the total spin is maximized. This means that the intra-atomic exchange energy J_H (resulting from the electron-electron interaction) separating the spin up and spin down energy levels is large compared to the crystal field splitting Δ_{cf} (Figure 1.5 middle). If the crystal field splitting Δ_{cf} becomes larger than the intra-atomic exchange energy (as can be the case for Co), it may energetically be more favorable to fill the t_{2g} orbitals first, even though
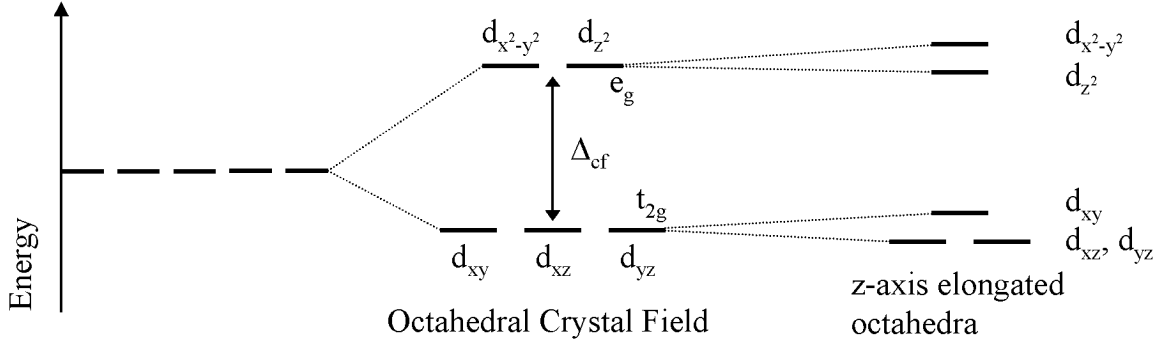
Figure 1.4: Splitting of the free ion $3d$ energy levels in a cubic environment as provided by the oxygen octahedron. The elongation of the octahedra along some direction (here z direction), splits the levels further.

the electron spins are antiparallel (Figure 1.5 right). For Co^{3+} and $\Delta_{cf} < J_H$ this will result in a spin configuration which is called a high spin configuration (HS, $t_{2g}^4 e_g^2$, S = 2), whereas for Co^{3+} and $\Delta_{cf} > J_H$ a low spin state (LS, $t_{2g}^6 e_g^0$, S = 0) will be adopted. For Co^{3+} with 6 electrons in the $3d$ shell, a third possibility exists, namely the intermediate spin state (IS, $t_{2g}^5 e_g^1$, S = 1).
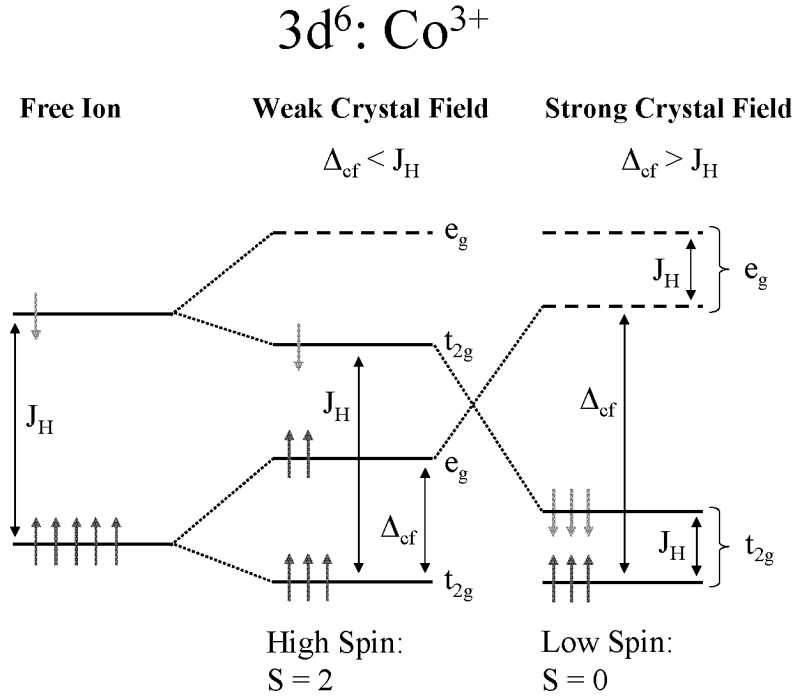
A more simple way to illustrate the different spin states is shown in Figure 1.6. Here the splitting between the energy levels for different spin orientations (J_H) is omitted. The possible spin states and their total spin S are shown for Co^{4+}, Co^{3+} and Co^{2+} (for which the IS state does not exist).

1.3   Magnetic Interactions

Long range magnetic order may set in, if the interactions between the magnetic moments is strong enough. In $3d$ metal oxides, long range order is mainly due to exchange interactions, which are basically of electrostatic origin[1]. Electrostatic interactions are due to the repulsion between charges of the same sign, resulting in an energy cost for such charges to be close together and in a gain of energy when they are far apart. Because they are relevant in the cobaltites, two exchanges will be discussed here, namely double exchange (DE) and superexchange (SE). The double exchange [15, 16, 17, 18, 19] interaction correlates magnetic and electronic properties, more specifically ferromagnetism and metallicity. In cobaltites, double exchange can be introduced by decreasing oxygen content, introducing Co^{4+} at the place of Co^{3+} ions due to charge neutrality. This leads to two degenerate electronic states, which can symbolically be represented by the two wave functions $\Psi_1 = Co^{3+} - O^{2-} - Co^{4+}$ and $\Psi_2 = Co^{4+} - O^{2-} - Co^{3+}$. Zener showed [15, 16] that a magnetic interaction leads to lifting of the degeneracy of these two states by creating two resonant wave functions $\Psi_+ = \Psi_1 + \Psi_2$ and $\Psi_- = \Psi_1 - \Psi_2$ (Figure 1.7). Double exchange associates the appearance of ferromagnetic coupling of the localized magnetic moments (in the t_{2g} energy level) to the delocalisation of an e_g electron. A strong Hund's rule coupling J_H is necessary, which makes an electron transfer from one Co ion to

---

[1]The energy of the magnetic dipolar interaction $E = \frac{\mu_0}{4\pi r^3}\left(\vec{\mu}_1 \cdot \vec{\mu}_2 - \frac{3}{2}(\vec{\mu}_1 \cdot \vec{r})(\vec{\mu}_2 \cdot \vec{r})\right)$ is very small $\sim 10^{-23}$ J (depending on μ), which is equivalent to about 1 K in temperature and cannot account for an ordering at high temperatures.

$3d^6$: Co^{3+}

Free Ion **Weak Crystal Field** **Strong Crystal Field**

$\Delta_{cf} < J_H$ $\Delta_{cf} > J_H$

High Spin: **Low Spin:**
S = 2 S = 0

Figure 1.5: The energy levels and the distribution of the 6 e^- of the Co^{3+} ion are shown for a free ion, weak crystal field splitting ($\Delta_{cf} < J_H$, Hund's rule is obeyed) and strong crystal field splitting ($\Delta_{cf} > J_H$).

$3d^5$: Co^{4+}   **$3d^6$: Co^{3+}**   **$3d^7$: Co^{2+}**

HS	IS	LS		HS	IS	LS		HS	LS
S = 5/2	S = 3/2	S = 1/2		S = 2	S = 1	S = 0		S = 3/2	S = 1/2
$\mu = 5\mu_B$	$\mu = 3\mu_B$	$\mu = 1\mu_B$		$\mu = 4\mu_B$	$\mu = 2\mu_B$	$\mu = 0$		$\mu = 3\mu_B$	$\mu = 1\mu B$
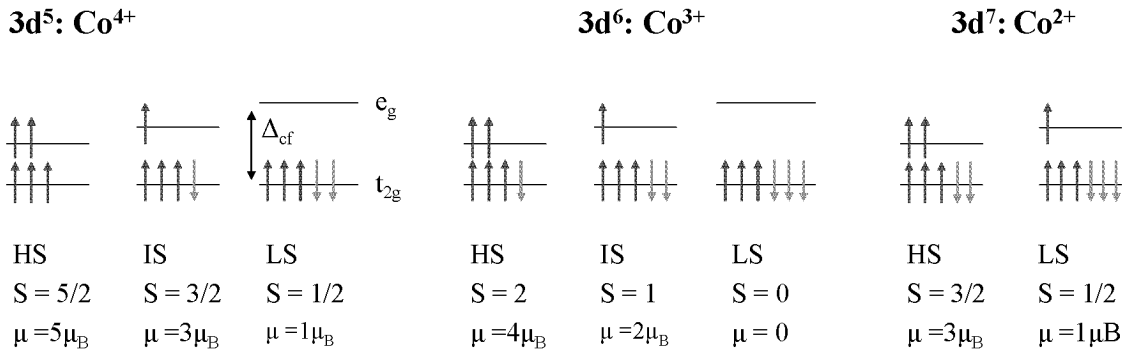
Figure 1.6: Schematic representation of the electron distribution to the orbitals e_g and t_{2g} for LS, IS and HS for Co^{4+} (left), Co^{3+} (middle) and Co^{2+} (right). Note that the Co^{2+} can only adopt LS or HS state.

another energetically favorable if the magnetic moments on the t_{2g} energy levels of the two Co ions coupled via an intermittent O^{2-} ion are parallel to the spin of the delocalized electron (Figure 1.7). In a charge ordered material DE is forbidden, because the wave functions Ψ_1 and Ψ_2 are distinguishable. This has been observed in $La_{0.5}Ca_{0.5}MnO_3$ where 50% Mn^{3+} and 50% Mn^{4+} are ordered below the charge ordering temperature T_{CO}. The material undergoes a magnetic transition from ferromagnetic to antiferromagnetic at $T_N = T_{CO}$, since DE is no longer allowed and is replaced by superexchange [20, 21, 22, 23, 24].
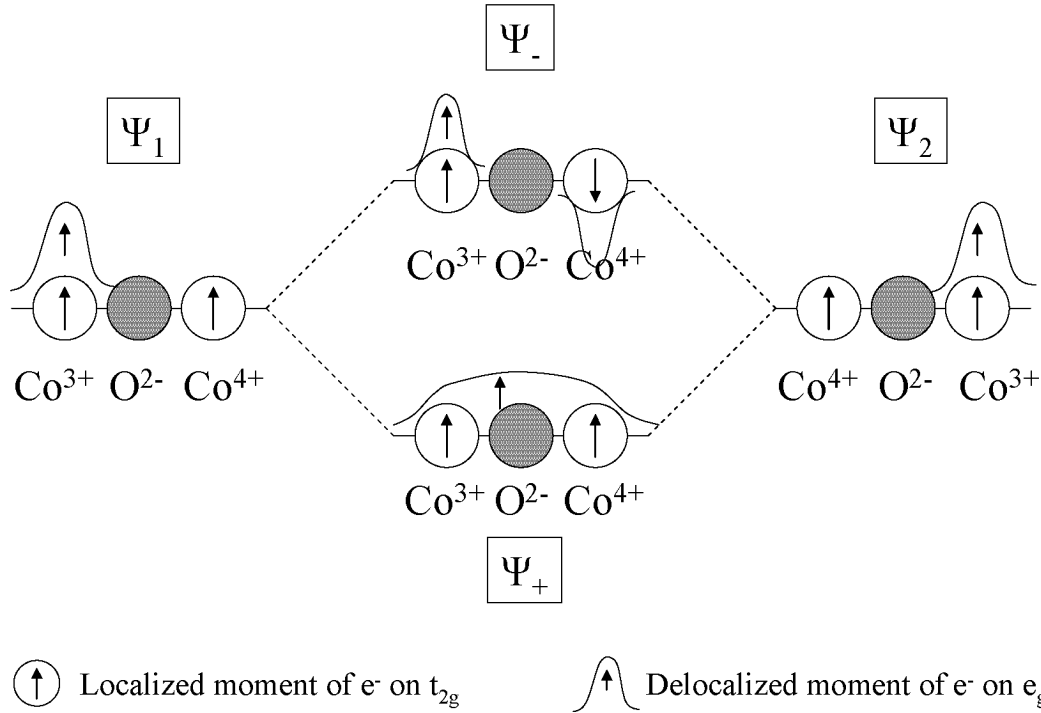
Figure 1.7: Double Exchange according to Zener [15, 16]. For the Ψ_+ wavefunction the exchange is ferromagnetic and the delocalized electron leads to metallicity.

The magnetic coupling in many magnetic oxides cannot be described by the mechanism of the direct exchange[2], because the magnetic ions are too far apart. Additionally, the ions carrying the magnetic moments are often separated by non-magnetic anions, such as, e.g., oxygen. Kramers and later Anderson [25, 26, 27] proposed a mechanism called superexchange, for which the magnetic moments of magnetic cations are coupled indirectly through intermediate anions. The superexchange interaction is based on the minimisation of energy cost for the transfer of a virtual electron from the full p shell of the oxygen ion to the excited states of the neighbouring magnetic Co ions. This process can be treated as a perturbation in the Heisenberg Hamiltonian $H = \sum_{i,j} J_{ij} \vec{S}_i \vec{S}_j$, with S_i and S_j the localized moments on the Co ions. The value of the exchange interaction J_{ij} is difficult to calculate and its sign depends on the geometry of the involved Co/O orbitals. J_{ij} can be approximated by t^2/U, where t is the hopping integral for a transfer of an electron from the oxygen to a neighbouring Co ion and U is the Coulomb energy which has to be paid in order to add an electron to a singly occupied Co orbital. The coupling between the two magnetic ions can either be antiferromagnetic (AFM, $J_{ij} < 0$) or ferromagnetic (FM, $J_{ij} > 0$).

Hopping of the $3d$ Co electrons occurs via the the $2p$ oxygen orbitals. If $\Delta = \epsilon_d - \epsilon_p$ is the energy difference between the $3d$ and $2p$ orbitals (charge transfer energy), then one can distinguish two cases (Figure 1.8): In the first case ($\Delta \gg U$), the $2p$ orbital lies below the $3d$ orbitals. The excited states are those corresponding to the transfer of a $3d$ electron from one Co site to another: $d^n + d^n \rightarrow d^{n-1} + d^{n+1}$. In the second case ($\Delta < U$), the excited state will correspond to the transfer of an oxygen electron to a transition metal: $d^n p^6 \rightarrow d^{n+1} p^5$. The two cases are shown in Figure 1.8 for the simple case of one spin on each Co $3d$ orbital and for AFM (left) and

---

[2]Two neighbouring spins on magnetic ions directly interact with each other.
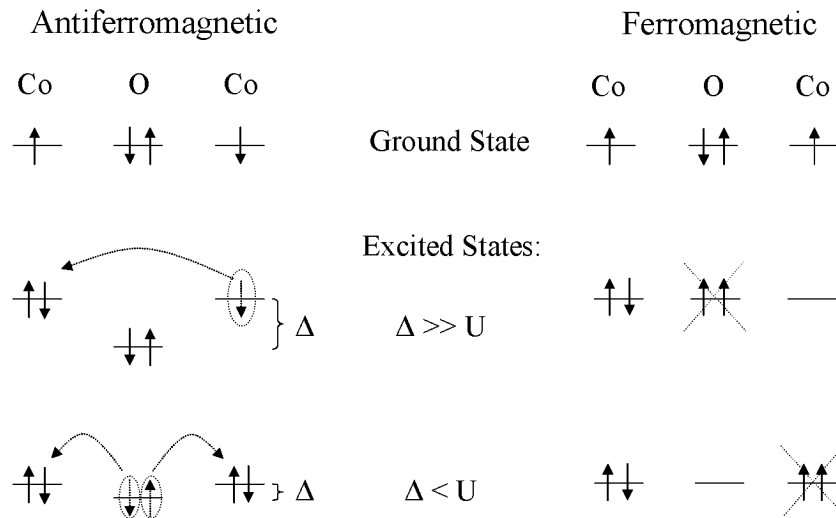
Figure 1.8: Superexchange in magnetic oxides, simplified to one electron per magnetic ion: the arrows represent the spins of the four electrons responsible for mediation of the exchange. Two excited states are shown ($\Delta \gg U$ and $\Delta < U$). For AFM coupling the excited states can mix with the ground state, whereas for FM coupling the excited states are prohibited by the Pauli exclusion principles.

FM (right) coupling of the Co ions. Obviously, the excited states in the FM case are prohibited by the Pauli exclusion principle. The AFM coupling is therefore energetically favored, because it results in a delocalization of the electrons (mixing of ground state with excited states), which lowers the kinetic energy of the system.

However, two Co^{3+} $3d$-orbitals can be coupled via the oxygen $2p$-orbital in three different ways (when the angle of the Co-O-Co bond is 180°), described by the so-called Goodenough-Kanamori rules (Figure 1.9) [28, 29]:

1. Coupling between cations with half filled e_g orbitals: AFM

2. Coupling between cations with half filled t_{2g} orbitals: weak AFM

3. Coupling between a cation with a half filled t_{2g} to one with a half filled e_g orbital: FM

The first two cases result in the above described AFM coupling of the two cations. The difference lies in the direction of the half filled e_g and t_{2g} orbitals with respect to the oxygen $2p$ orbital. Since the exchange integral is larger for larger orbital overlap, the AFM coupling for the second case will be weaker (Figure 1.9). In the third case two different orbitals (e_g and t_{2g}) are occupied at the Co ion sites. Due to the symmetry of the corresponding wave functions, these orbitals are orthogonal and no hopping can occur between them. However, the electron of the t_{2g} orbital (IS Co^{3+} in Figure 1.9) can hop into an empty t_{2g} orbital on the second ion (LS Co^{4+}) which has the same symmetry. Following Hund's rule (minimizing the intra-atomic exchange energy), it is energetically more favorable, if the spin of the electron transferred to the empty orbital is parallel to the electron spin in this ion. This leads to FM coupling between the two magnetic Co ions. The FM coupling is weaker than the AFM one, since for FM coupling the electrons cannot become delocalized (Figure 1.8).

Goodenough-Kanamori Rules
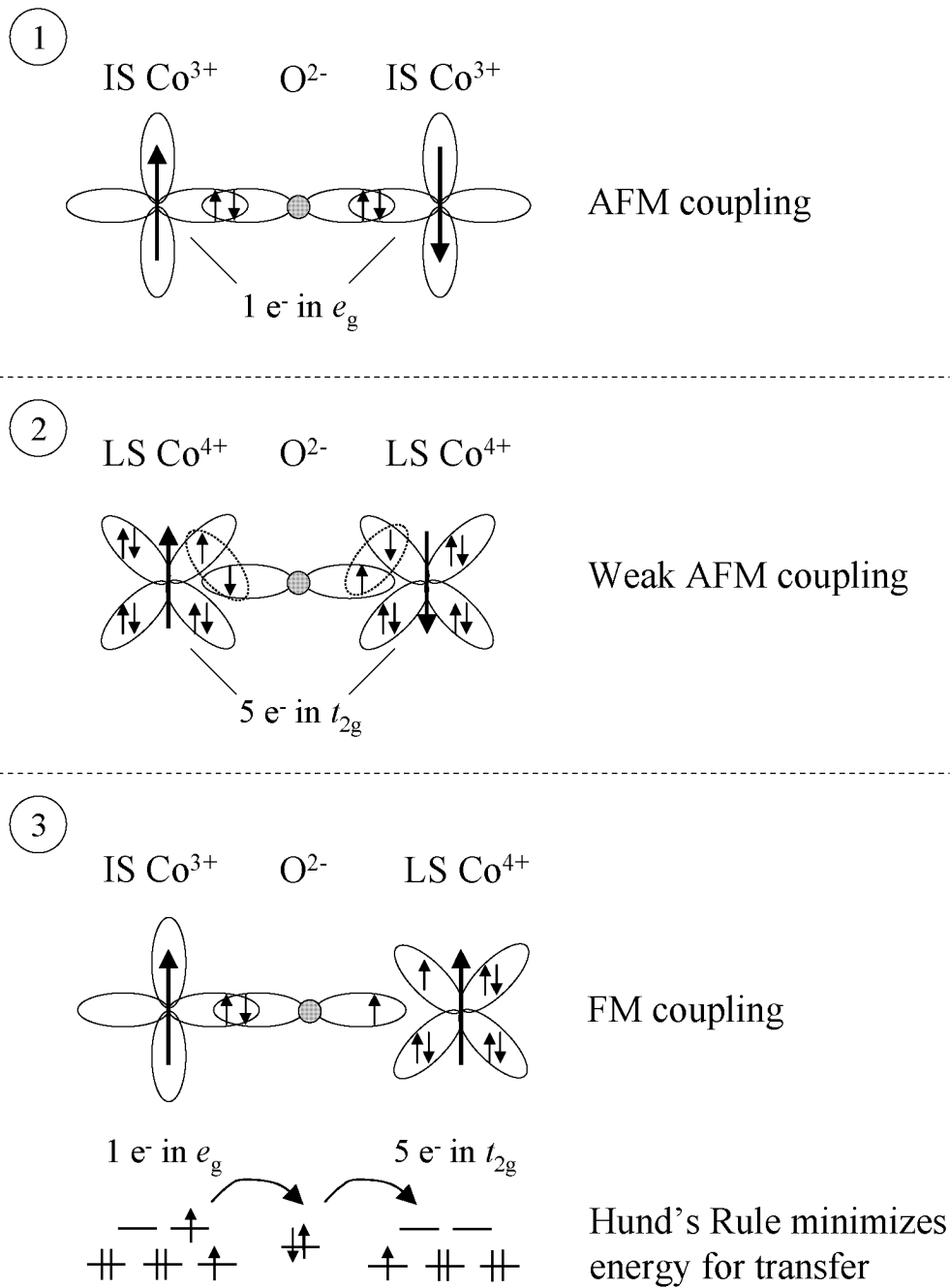
Figure 1.9: Goodenough-Kanamori rules [28, 29]. 1) Two half filled e_g (e.g. $3d_{x^2-y^2}$) orbitals are coupled by an O^{2-}, as is the case for two IS Co^{3+} ions. 2) Two half filled t_{2g} (e.g. $3d_{x^2}$) orbitals are coupled by an O^{2-}, as for two LS Co^{4+} ions. 3) A half filled t_{2g} and a half filled e_g orbital are coupled by an O^{2-}, as for IS Co^{3+} and LS Co^{4+}. The FM coupling can be understood with Hund's rule, where parallel spins minimize energy.
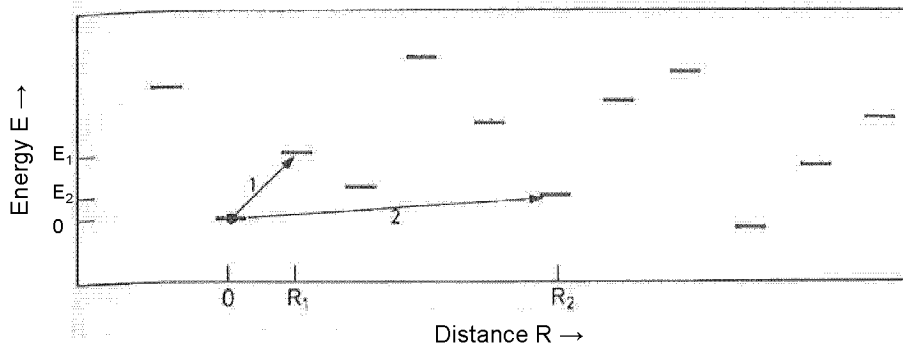
Figure 1.10: Hopping processes between localized states with statistically distributed position R and energy E. The hopping probability is determined by the spatial distance and the energy difference between the two states (after [13]).

1.4 Transport Properties

In transition metal (TM) oxides the $3d$ orbitals of the metal overlap with the $2p$ orbitals of the oxygen and form energy bands which should, in principle, lead to metallic conductivity. However, the transition metal ions are relatively small (especially the $3d$ variety) and the angle of the TM-O-TM is usually tilted, which leads to narrow energy bands with bandwidth W [30]. Additionally the Coulomb repulsion U between the electrons tends to keep the electrons localized, resulting in insulating properties. An approximation which is used to describe the transition metals is the Mott-Hubbard model, in which the repulsion between electrons is only considered when they are on the same atom [31]. This model describes the splitting of the conduction band into a lower and upper so called Hubbard sub-band. The ratio U/W determines the electronic properties of the system. For U/W $\gg$ 1, the splitting between the two bands is relatively large compared to the bandwidth, leading to an energy gap and insulating properties. For U/W $\ll$ 1, the two sub-bands overlap and the system is metallic. The cases with U/W $\sim$ 1 (as in the cobaltites) lie at the transition between the insulating and the metallic state and are of special interest. Small perturbations, such as slight changes of the crystal structure, doping (e.g. oxygen), temperature, magnetic field and pressure can destabilize the balance and lead to a metal-insulator or insulator-metal transition.

For disordered systems with localized states (narrow bandwidth) the electron motion can be explained on the basis of Mott variable range hopping (VRH) [13]. The energies of these localized states can spread over a wide range and adjacent states can have very different energies. In the hopping process the energy difference E is always provided by a phonon. The hopping probability can become so small that transitions to states further away in distance, costing less energy, can become more likely. This is called variable-range hopping and supplements the nearest-neighbour hopping (Figure 1.10).

How can the hopping probability be expressed? The electron states are localized around the Fermi energy E_F with a certain localization length ξ. The electron crosses the distance $R = |\mathbf{R_j} - \mathbf{R_i}|$ between two states by tunneling and the factor which determines the tunneling probability is the overlap of the wavefunctions of the two states. A simple way to write a wavefunction of a localized state is an exponential decay $\psi \propto \exp(-|\mathbf{r} - \mathbf{R_i}|/\xi)$. If ξ is the same for the two states, then the tunneling probability is proportional to $\exp(-2R/\xi)$. Since the energy difference E between two states is provided by a phonon, E cannot be larger than the maximum

phonon energy in the spectrum. The number of phonons of energy E in thermal equilibrium goes into the transition probability. For sufficient low temperatures ($k_B T \ll E$) it is given by the Boltzmann factor $\exp(-E/k_B T)$. The total probability for a hopping process is then [13]

$$p \propto e^{-\frac{2R}{\xi} - \frac{E}{k_B T}}. \tag{1.4}$$

What is the most probable jump distance for a certain energy? Two cases can be distinguished: at high temperature there are enough phonons of energy E_a (mean energy difference between two adjacent states) available to allow hopping between nearest neighbours. At low temperatures no phonons of energy E_a are present, the electron has to tunnel to reach more distant states. For both cases the most likely jump distance can be evaluated and it is found that the resistivity in the two temperature regimes can be written as [13]

$$\text{low temperature} \quad : \quad \rho \propto e^{(T_0/T)^{1/4}}, \qquad T_0 = \frac{5/2}{9\pi \xi^3 k_B g}, \tag{1.5}$$

$$\text{high temperature} \quad : \quad \rho \propto e^{(E_a/k_B T)}. \tag{1.6}$$

Both the high and low temperature behavior of resistivity are observed in cobalt oxides, as will be shown in Chapter 4.2.3 and 4.3.3.

For many transition metal oxides polaronic transport has been reported. A polaron can be described as an electron or hole which displaces the atoms from their equilibrium position and becomes thereby bound inside the potential well produced by the atomic displacement. The quasiparticle composed of such a self-trapped carrier together with the patterns of displacement is known as polaron. Electron-phonon coupling is necessary for the formation of polarons. A carrier with a long-ranged strong electron-phonon coupling is called a large polaron (involves more than one lattice site), while a small polaron is located at a single site. With the absorption of energy, the self-trapped carriers can be excited to move from their localized state to an adjacent localized state. In the small polaron conduction mechanism a self-trapped carrier is excited from its localized state to an adjacent localized state. This transfer is called hopping motion. The small polaronic resistivity can be written as [32]

$$\rho \propto T \cdot e^{E_a/k_B T}. \tag{1.7}$$

Both types of conduction, variable range hopping and polaronic conduction, are more likely when ions with different valences are available. In compounds where only one valence prevails, e.g. $Ln\mathrm{BaCo_2O_{5.5}}$, with only $\mathrm{Co^{3+}}$, a mechanism called charge disproportionation is considered to be the origin of the intrinsic charge carrier formation. Charge disproportionation can take place for HS $\mathrm{Co^{3+}}$ and is of the form $2\mathrm{Co^{3+}} \rightarrow \mathrm{Co^{2+}} + \mathrm{Co^{4+}}$. Attempts were made to find experimental evidence for the charge disproportionation (e.g. in $\mathrm{LaCoO_3}$ [33]), but have not been found up to date. It is assumed that the charge carrier hopping frequencies are too high to be resolved, which would mean that in spectroscopic investigations only averaged valence states are measured.

Ionic conductivity, which is found at high temperatures in 3D cobaltites is strongly connected to the degree of oxygen vacancy disorder in the system. Generally, oxygen diffusion is regarded as a rapid transport of vacancies which migrate by a conventional hopping mechanism. It has been shown by various authors that oxygen vacancy ordering reduces the number of free ionic charge carriers. On the basis of geometrical considerations, it is found that the jump distance in the ordered state is larger than in the disordered state: in the randomly disordered state the shortest distance is along the edge of an octahedron, while in the ordered state (with the

oxygen vacancy at the apical position of an octahedra) the distance is equivalent to the lattice parameter a_p. Additionally, it costs energy to occupy an oxygen vacancy site, which makes the hopping to such a site less favorable [3, 4, 5, 34, 35]. Increased oxygen ionic conductivity has been observed with increasing oxygen vacancies, which would suggest that the layered cobaltites of type $LnBaCo_2O_{5.5}$ are good candidates for ionic conductivity.

1.5   Structure of this Work

Prior to the presentation of our results, the principle measurement techniques will be explained (Chapter 2). Emphasis is put on neutron scattering, as it is the predominant technique utilized for our experiments. Different sample characterization techniques will also be described, as well as the Rietveld method used to evaluate our neutron and x-ray diffraction data.

In Chapter 3 the three dimensional Co-compounds of type $Ln_{1-x}Sr_xCoO_{3-\delta}$ (Ln = rare earth) is introduced and a short summary of the present state of research is given. In the course of the present work the polycrystalline compound $Ho_{0.1}Sr_{0.9}CoO_{3-\delta}$ ($0.15 \leq \delta \leq 0.49$) has been synthesized and investigated by neutron and x-ray diffraction, as well as by bulk magnetic measurements. The sample preparation is described first, and then follows a detailed study on the oxygen content dependent crystallographic and magnetic structures.

In Chapter 4 we concentrate on the more complex two dimensional cobaltites of type $LnBaCo_2O_{5+\delta}$ (Ln = rare earth) for which an introduction on the structural, magnetic and electronic properties is given. Concerning our research, one section deals with the polycrystalline $PrBaCo_2O_{5+\delta}$ compounds, for which the influence of oxygen content and oxygen vacancy ordering on the crystallographic and magnetic properties are discussed. The discussion is based on x-ray diffraction data and bulk magnetization measurements. Temperature dependent neutron powder diffraction is used to investigate the high temperature crystallographic structure of $PrBaCo_2O_{5.48}$. Electronic transport measurements are presented for the same compound. Further, bulk magnetization measurements are discussed for three single crystals $LnBaCo_2O_{5+\delta}$ with Ln = Gd, Dy and $Dy_{0.1}Tb_{0.9}$.

The focus of this work lies in the determination of the oxygen content and oxygen vacancy ordering influence on the crystallographic and magnetic properties of Co-compounds.

Chapter 2

Experimental Techniques

Neutron Scattering is the main experimental technique used in this study. Many other methods contribute in making progress in research and only the combination of all of them will lead to unambiguous results. In order to characterize our samples x-ray diffraction and macroscopic measurements have also been performed. A short introduction to these techniques is given in this chapter, starting with neutron scattering, discussed in more detail, followed by different sample characterization methods and x-ray diffraction. Since Rietveld refinements were used to evaluate the diffraction data, this method will also be explained.

2.1 Neutron Scattering

2.1.1 General Aspects

After the postulation of the existence of a neutral particle in 1920 by Lord Ernest Rutherford, the neutron was discovered in 1932 by James Chadwick [36, 37, 38], a discovery which brought him the Nobel Prize in Physics[1] in 1935. Four years later W. Elsasser, P. Preiswerk and H. von Halban found that neutrons could be Bragg diffracted by solids [39, 40]. It is now accepted that neutron scattering is an important and versatile techniques for probing condensed matter. The physic's Nobel Prize 1994 has been awarded to Clifford G. Shull and Betram B. Brockhouse[2] with the following declaration: "Clifford G. Shull has helped answer the question of where atoms 'are' and Bertram N. Brockhouse, the question of what atoms 'do'" (Nobel citation).
The neutron is a massive particle of 938 MeV ($1.675 \cdot 10^{-27}$ kg) formed of two down quarks (charge -1/3) and one up quark (charge +2/3). Their electrical charges add up to a total of zero charge for the neutron, while the half integer spins of the three quarks add up to a total spin of 1/2, so the neutron is a fermion. The following properties make the neutron an ideal probe to study solid matter:

1. Wavelength: the de Broglie wavelength of thermal neutrons (E = 5 - 100 meV, λ = 1 - 4 Å, T = 60 - 1000 K) is of the order of magnitude of interatomic distances. Interference effects occurr and make structure determination possible.

2. Zero net charge: allows penetration of the neutron deep into the sample and therefore the neutron can interact directly with the nuclei of atoms, making elements which are not or insufficiently accessible to X-rays visible to neutrons.

---

[1] 'for the dicovery of the neutron'; http://nobelprize.org/physics/laureates/1935/press.html
[2] http://nobelprize.org/physics/laureates/1994/presentation-speech.html

3. Energy: the energy of thermal neutrons is comparable to excitations in solids, which permits to measure dispersion relations. The low energy also has the advantage of not destroying delicate biological compounds.

4. Magnetic moment: the neutron spin can interact with the unpaired electron spins in magnetic atoms, with a strength comparable to the nuclear interaction. Information can be gained about electron spin orientations and magnitude of magnetic excitations in the investigated systems.

The interaction of the neutron with the sample is complex and the derivation of a scattering law needs approximations, which are shortly adressed here. The strong force is the main interaction neutrons experience when they encounter matter. For thermal neutrons, the nuclei with dimensions 10^{-4} Å appear pointlike and the interaction can be explained by using an attractive spherical box potential. Scattering from such objects is isotropic (pure s-wave) and is characterized by a single parameter b called the scattering length, which can be determined experimentally. The scattering process can be described using a plane wave for the incoming neutrons and a spherical wave for the outgoing neutrons. In Born approximation the outgoing wave is also described by a plane wave, assuming that the scattering potential is weak. Since the above mentioned box potential is not weak (strong interaction), the Born approximation is not valid. Enrico Fermi found a way to correctly describe the scattering process by distorting the potential in such a way that it becomes less deep (weaker interaction) but longer ranged. This potential is called the Fermi pseudopotential [41, 42]. The distortion of the potential (Equ. 2.4) preserves the expressions for the scattering length, the condition for low energy scattering and also fullfills the condition for the validity of the Born approximation.

### 2.1.2   Elastic Neutron Scattering

Nuclear Scattering

There are a number of good textbooks, describing in detail the experimental neutron scattering technique [43, 44, 45]. In the following a short introduction into this field is given.
The total energy and momentum of the neutron and the scattering system are conserved during the scattering process

$$\hbar\omega \;=\; E_i - E_f \;=\; \frac{\hbar^2}{2m_n}\left(k_i^2 - k_f^2\right), \tag{2.1}$$

$$\hbar\vec{Q} \;=\; \hbar\vec{k}_i - \hbar\vec{k}_f \;=\; \hbar\vec{q} + \hbar\vec{\tau}, \tag{2.2}$$

where $\hbar\omega$ denotes the energy transfer to the sample, m_n is the neutron mass and E_i, E_f the energy of the incident and scattered neutrons. Because of the wave-particle dualism the energy of a neutron can be written as $E = \frac{\hbar^2 k^2}{2m_n}$ with the wave vector $k = \frac{2\pi}{\lambda}$ (λ is the wavelength of the neutron). Equation 2.2 presents the momentum $\vec{Q}$ transferred to the crystal: for elastic scattering, where $|\vec{k}_i| = |\vec{k}_f|$, Bragg's law is fulfilled when $\vec{Q}$ is equal to a reciprocal lattice vector $\vec{\tau}$. For inelastic scattering ($|\vec{k}_i| \neq |\vec{k}_f|$) there is an extra momentum component transmitted to the sample, which can be expressed by a relative value $\hbar\vec{q}$ defined within a Brillouin zone. The Ewald circle (2 dimensions) illustrates this situation (Figure 2.1). When Bragg's law is met a so called Bragg peak is registered at the detector: In a neutron scattering experiment one measures the rate at which the neutrons are scattered into a small solid angle $d\Omega$, in the direction of the wave vector $\vec{k}_f$ with an energy transfer to or from the system
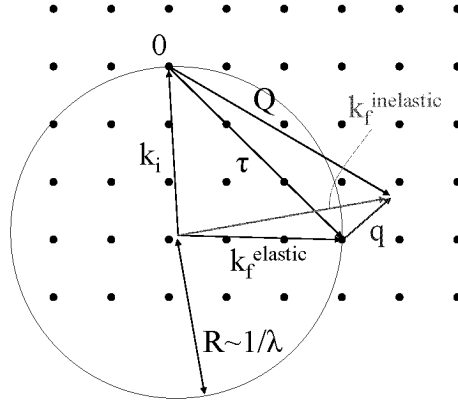
Figure 2.1: View of the reciprocal space in two dimensions showing the Ewald circle for an incoming wave vector k_i. The wave vectors for elastic $(k_f^{elastic})$ and inelastic $(k_f^{inelastic})$ scattering are shown. $\vec{\tau}$ is a reciprocal lattice vector and $\vec{q}$ the momentum transfer within the first Brillouin zone.

between $\mid \hbar\omega \mid$ and $\mid \hbar(\omega + d\omega) \mid$ (Figure 2.2). This quantity, divided by the incoming flux, can be expressed by the double differential cross section $\frac{d^2\sigma}{d\Omega d\omega} = \frac{N'(\omega)}{Nd\Omega}$ ($N'(\omega)$ is the amount of scattered neutrons, N the amount of incoming neutrons). Since the neutron can only cause a transition of the sample from one quantum state to another, it is possible to derive an expression for the differential scattering cross section from Fermi's Golden Rule:

$$\frac{d^2\sigma}{d\Omega d\omega}\left(\vec{Q}, \omega\right) = \frac{k_f}{k_i}\left(\frac{m_n}{2\pi\hbar^2}\right)^2 \sum_{\lambda_i} p_{\lambda_i} \sum_{\lambda_f} |\langle \vec{k}_f \lambda_f | \widehat{U} | \vec{k}_i \lambda_i\rangle|^2 \delta(\hbar\omega + E_{\lambda_i} - E_{\lambda_f}), \qquad (2.3)$$

where $\widehat{U}$ is the operator for the neutron interacting with the sample and p_{λ_i} the probability for the system to be in the state $|\lambda_i\rangle$. $\frac{k_f}{k_i}$ comes from normalization of the cross section to the incident neutron flux.

The interaction potential $\widehat{U}$ in 2.3 for nuclear scattering is, as explained above, described by the Fermi pseudopotential

$$\widehat{U}(\vec{r}) = \frac{2\pi\hbar^2}{m_n}\sum_j b_j \delta(\vec{r} - \vec{R}_j). \qquad (2.4)$$

Summing over all atoms j at positions R_j with inherent scattering lengths b_j (see Appendix B), using the Born approximation (see above), which describes both the incoming and outgoing neutrons as plane waves $|\vec{k}_{i,f}\rangle = e^{\pm i \vec{k}\vec{r}}$, integrating over the energy $\hbar\omega$ and substituting $\vec{R} = \vec{r} - \vec{R}_j$ and $\vec{Q} = \vec{k}_i - \vec{k}_f$ one obtains the coherent elastic nuclear differential cross section for a non-Bravais lattice as

$$\frac{d\sigma}{d\Omega} = N_0 \frac{(2\pi)^3}{v_0}\sum_{\vec{\tau}}|F(\vec{Q})|^2 \delta(\vec{Q} - \vec{\tau}), \qquad \text{with} \qquad (2.5)$$

$$F(\vec{Q}) = \sum_{\vec{d}} b_{\vec{d}} e^{i\vec{Q}\vec{d}} e^{-W_{\vec{d}}}, \qquad (2.6)$$

where N_0 is the number of unit cells in the sample, v_0 their volume and $\vec{d}$ the relative position of the atoms to the origin. $F(\vec{Q})$ is called the nuclear structure factor and contains the thermal
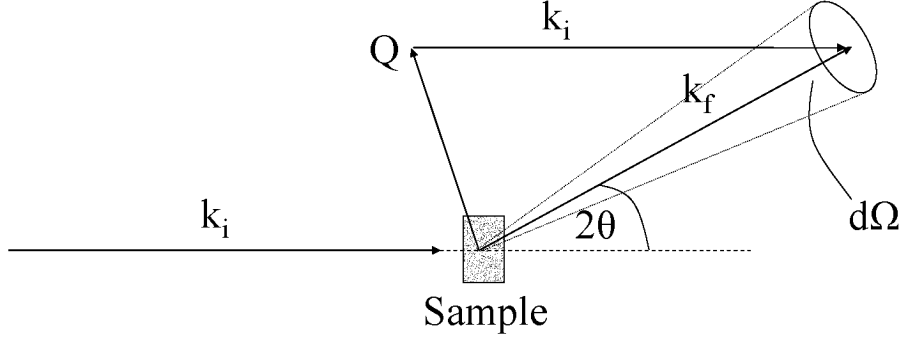
Figure 2.2: Scattering experiment where the neutrons with incident k_i are scattered by an angle 2Θ into the solid angle $d\Omega$ and have a final wave vector k_f.

Debye-Waller factor $e^{-W_{\vec{d}}}$. From the δ-function one sees that elastic scattering occurs only when the moment transfer wave vector equals a reciprocal lattice vector ($\vec{Q} = \vec{\tau}$). In this case a Bragg peak is generated, because Bragg's law $\lambda = 2d\sin\Theta$ is fulfilled (Θ is half of the scattering angle) (Figure 2.2).

Magnetic Scattering

So far only the nuclear interaction has been considered. As mentioned above, magnetic scattering is also possible. This interaction can be expressed in terms of the dipolar interaction of the neutron spin with the spin and orbital moments of the unpaired electrons in the sample:

$$\widehat{U}_M = -\gamma\mu_K\hat{\vec{\sigma}}\vec{B},\tag{2.7}$$

where $\gamma = -1.913$ is the gyromagnetic ratio of the neutron, $\mu_K = \frac{e\hbar}{2mc}$ is the nuclear magneton, $\hat{\vec{\sigma}}$ the Pauli spin operator and $\vec{B}$ is the magnetic field created by the unpaired electrons of the magnetic atoms.

The general cross section for magnetic scattering is defined as follows

$$\frac{d^2\sigma}{d\Omega d\omega}(\vec{Q},\omega) = (\gamma r_0)^2\frac{k_f}{k_i}|f(\vec{Q})|^2 e^{-2W}\sum_{\alpha,\beta}\left(\delta^{\alpha\beta} - \frac{Q^\alpha Q^\beta}{Q^2}\right)S^{\alpha\beta}(\vec{Q},\omega),\tag{2.8}$$

$$S^{\alpha\beta}(\vec{Q},\omega) = \sum_{i,j}e^{i\vec{Q}\cdot(\vec{r}-\vec{r}_i)}\sum_{\lambda_i,\lambda_f}p_{\lambda_i}\langle\lambda_i|\widehat{S}_i^\alpha|\lambda_f\rangle\langle\lambda_f|\widehat{S}_j^\beta|\lambda_i\rangle\delta(\hbar\omega + E_{\lambda_i} - E_{\lambda_f}),\tag{2.9}$$

where $S^{\alpha\beta}(\vec{Q},\omega)$ is the magnetic scattering function and $F(\vec{Q})$ the static magnetic form factor, which can be determined from the Fourier transformation of the spin density. $r_0 = 0.282\cdot10^{-12}$ cm the classical electron radius and $\widehat{S}_i^\alpha$ ($\alpha = x,y,z$) the spin operator of ion i at the position $\vec{r}_i$.

From Equation 2.8 and 2.9 one can see three important characteristics of magnetic scattering: First, magnetic scattering is proportional to the magnetic moment $\langle\widehat{S}\rangle^2$ and therefore temperature dependent. Second, since the magnetic form factor $F(\vec{Q})$ is the Fourier transform of the spin density, it decreases rapidly with $\vec{Q}$. Thirdly, the polarization factor $\left(\delta^{\alpha\beta} - \frac{Q^\alpha Q^\beta}{Q^2}\right)S^{\alpha\beta}$ allows only the observation of components of the magnetic moment perpendicular to $\vec{Q}$.

For a ferromagnet with the spins aligned in z-direction ($\langle\widehat{S}^x\rangle = \langle\widehat{S}^y\rangle = 0$) one finds for the

differentiel cross section

$$\frac{d\sigma}{d\Omega} = N\frac{(2\pi)^3}{v_0}\left(\frac{\gamma e^2}{m_e c^2}\right)^2 e^{-2W}|F(\vec{Q})|^2\langle\widehat{S^z}\rangle^2\sum_{\vec{\tau}}\left(1 - \left(\frac{\vec{\tau}\cdot\vec{z}}{\tau}\right)^2\right)\delta(\vec{Q} - \vec{\tau}), \qquad (2.10)$$

where m_e is the electron mass

The calculation of an antiferromagnetic spin alignement is more complex, since two antiparallel sublattices A and B have to be considered (with staggered spins $\langle S^z\rangle$). The unit cell of the sublattice A (or B) is called the magnetic unit cell (index m) and can be larger than the nuclear unit cell. One obtains the cross section

$$\frac{d\sigma}{d\Omega} = N_m\frac{(2\pi)^2}{m_e c^2}\left(\frac{\gamma e^2}{m_e c^2}\right)^2 e^{-2W}\sum_{\vec{\tau}}|F_m(\vec{\tau}_m)|^2\left(1 - \left(\frac{\vec{\tau}_m\cdot\vec{z}}{\tau_m}\right)^2\right)\delta(\vec{Q} - \vec{\tau}_m),$$

$$(2.11)$$

$$F_m(\vec{\tau}_m) = \langle\widehat{S^z}\rangle F(\vec{\tau}_m)\sum_{\vec{d}_m}\sigma_{\vec{d}}e^{i\vec{\tau}_m\cdot\vec{d}}, \qquad (2.12)$$

with a magnetic structure factor F_m. It is characterized by the valueof $\sigma_{\vec{d}}$, which is ± 1, depending on whether the magnetic ion is in sublattice A or B.

Comparing ferromagnetic and antiferromagnetic scattering one notices that the ferromagnetic alignement of the spins enhances the intensity at the positions of nuclear Bragg peaks (due to $\delta(\vec{Q} - \vec{\tau}_m)$), while antiferromagnetic order can produce magnetic Bragg peaks at positions different from the nuclear Bragg peaks.

2.1.3   Inelastic Neutron Scattering

In the preceding section the double differential cross section $\frac{d^2\sigma}{d\Omega d\omega}$ was simplified to $\frac{d\sigma}{d\Omega}$ by integrating over energy. This results in a loss of information about the neutron's energy after the scattering process. However, one is often interested in the energy a neutron gains or loses (probing magnetic or lattice excitations). There is a coherent and an incoherent double cross section for phonon scattering: The coherent one is used to determine dispersion relations, the incoherent one to determine for example phonon density of states or diffuse motions. Their formulas will not be given here, but can be found in literature [43, 44, 45].

The cross section for neutron scattering by magnetic excitations is derived from the most general formula for magnetic scattering (2.8) and can be written as
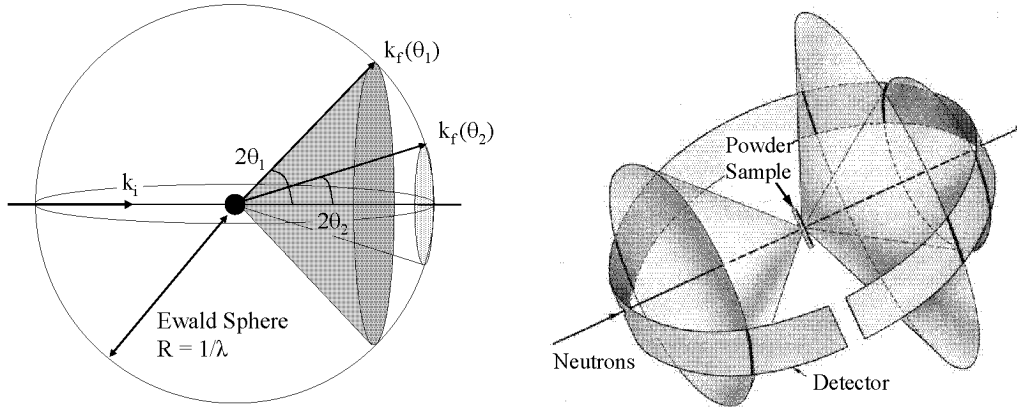
$$\frac{d^2\sigma}{d\Omega d\omega} \propto \left(1 + \frac{Q_z^2}{Q^2}\right)\frac{k_f}{k_i}F^2(\vec{Q})\sum_{\vec{\tau}_m,\vec{q}}[\langle n_{\vec{q}} + 1\rangle\delta(\vec{Q} - \vec{q} - \vec{\tau}_m)\delta(\hbar\omega_{\vec{q}} - \hbar\omega) +$$

$$+ \langle n_{\vec{q}}\rangle\delta(\vec{Q} + \vec{q} - \vec{\tau}_m)\delta(\hbar\omega_{\vec{q}} + \hbar\omega)], \qquad (2.13)$$

where $n_s(\vec{q})$ stands for the occupation number and $\omega_{\vec{q}}$ is the change in energy.

The cross section corresponds to the creation (first term) and the annihilation of one magnon. For the creation of a magnetic excitation the relations:

$$\frac{\hbar^2}{2m_n}(k_i^2 - k_f^2) = \hbar\omega_{\vec{q}}, \qquad (2.14)$$

$$\vec{k}_i - \vec{k}_f = \vec{\tau} + \vec{q}. \qquad (2.15)$$

Figure 2.3: Left: View of two diffraction cones coming from two different Bragg planes of a polycrstalline sample. k_i and k_f denote the initial and final neutron wave vector, respectively. Right: Schematic view of a Debye Scherrer camera which registers all Bragg reflexes simultaneously [46].

are valid. The spin wave gains energy $\hbar\omega_{\vec{q}}$ and the kinetic energy of the neutron decreases by the same amount. The initial and the final wavevectors of the neutron have to satisfy condition 2.15. In the magnon annihilation process the neutron absorbs the energy which is released due to the annihilation of a magnon.

In order to measure dispersions it is necessary stay at the reciprocal lattice position $\vec{q}$ and measure the neutrons at the detector for varying energy transfer values. If performed at various q-values, one obtains a the magnon dispersion, namely the energy necessary to excite a magnon as function of reciprocal space.

2.1.4   Two Neutron Scattering Instruments

Powder Diffraction

In angular dispersive powder diffraction measurements either monochromatic neutrons, x-rays or electrons are scattered by a polycristalline sample. A powder always contains some cristallites which have the right orientation with respect to the scattering vector $\vec{Q}$ on the Ewald Sphere in Fig. 2.1. The reciprocal lattice shells satisfying the Bragg law (characterized by k_i and a certain Θ_n depending on the scattering plane), intersect the Ewald sphere and therefore the neutrons diffracted by a powder sample lie on the surface of cones with half angle $2\Theta_n$ as illustrated in Figure 2.3 on the left. Since simultaneous scattering from different crystal planes is possible, many cones exist for one setup. A radial detector with the center at the sample position will therefore register the reflexes coming from all Bragg planes (Figure 2.3 right).

The neutron powder diffraction (NPD) method gives a first quick insight into crystal and magnetic structure [47] and allows very precise measurement of lattice constants. On the other hand it can be very hard to determine structures of samples with, e.g., low crystal symmetry (low multiplicity) and/or very similar lattice constants, since this causes the Bragg peaks to overlap. The information contained in powder diffraction patterns are mainly the peak positions, intensities and shapes/widths. From the position one can derive the unit cell dimension, the
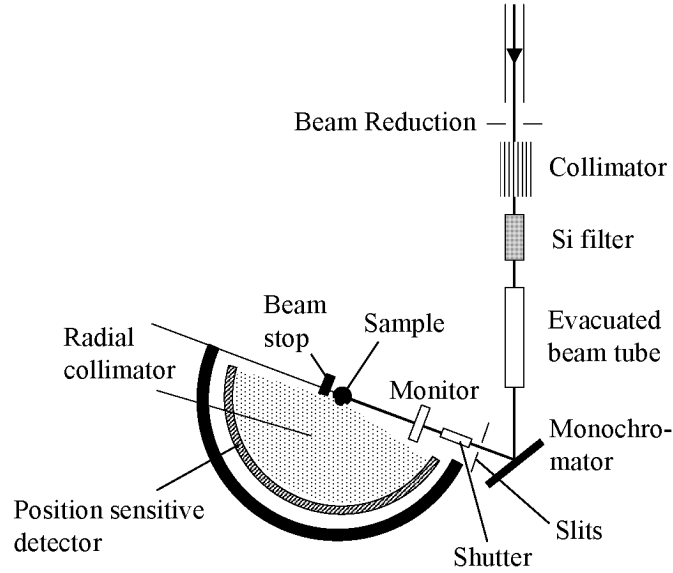
Figure 2.4: Schematic picture of the powder diffractometer HRPT [48] at SINQ.

crystal system (space group) and the Laue class, while the intensity leads to knowledge of the unit cell contents and point symmetry. Finally, the peak shapes and widths determine crystallite sizes, microstrain effects and defects. Another property which has an effect on the pattern is the atomic motion, which causes an exponential decay of peak intensities with increasing 2Θ. In Fig. 2.4 the setup of the High-Resolution Powder diffractometer for Thermal neutrons (HRPT [48]) located at SINQ (PSI, Switzerland) is shown schematically.
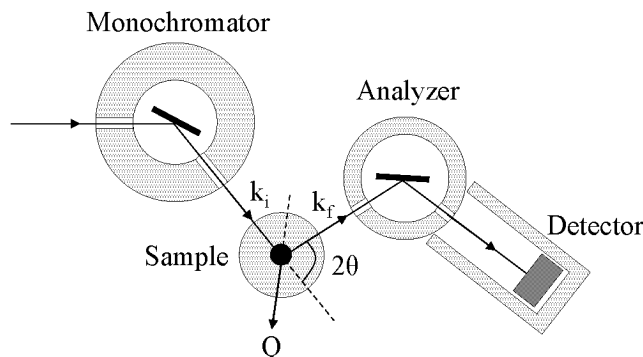
Triple Axis Spectrometer

In some neutron scattering experiments, controlled access to the variables $\vec{Q}$ and ω is required. The triple axis spectrometer (TAS) is a powerful instrument to measure inelastic scattering, because it allows to measure the scattered intensity as a function of momentum transfer $\hbar\vec{Q}$ and energy transfer $\hbar\omega$ in a controlled manner. A schematic picture of a TAS is shown in Figure 2.5. The monochromator (axis 1) defines the wave vector $\vec{k}_i$ of the incident neutron beam. The neutrons are scattered from the sample (axis 2) in a second direction $\vec{k}_f$ onto an analyzer crystal (axis 3), from where the neutrons with the desired energy are Bragg reflected to the detector. When the analyzer is removed (two axis instrument) the possibility of adressing one specific place in reciprocal space remains, but the energy selection is eliminated. This is equivalent to integrating over all neutron energies.

2.2 Sample Characterization

2.2.1 Macroscopic Properties

Macroscopic measurements (e.g. direct current (DC) magnetization, alternating current (AC) susceptibility, resistivity, specific heat,...) are the primary experiments to characterize various properties of materials. Temperature or field dependent DC and AC measurements give information on the sample's magnetic response to a small external magnetic field. Depending on

Figure 2.5: Schematic view of a triple axis spectrometer.

the response it can be decided what kind of magnetic correlations govern the magnetism in the sample (ferromagnetic, antiferromagnetic, diamagnetic, cluster glass, etc...). It is also possible to detect magnetic phase transitions. External magnetic fields applied along different crystallographic directions of a single crystal sample can reveal magnetic anisotropies. From temperature dependent resistivity measurements it is possible to determine the conduction mechanism in the sample (metallic, superconductive, semicondcutive, polaronic, etc...). Metal-insulator transition can be seen. Applying an external magnetic field can reveal a possible magnetoresistive effect. Heat capacity measurements show structural transitions.

The macroscopic magnetic measurements shown in this work were all performed on a Quantum Design Physical Properties Measurement System (PPMS)[3]. We concentrated on DC magnetization measurements, which we performed in both zero field cooled mode (ZFC, cooling the sample in zero field, then applying a small external field and measuring the magnetic response on warming) and field cooled mode (FC, cooling with a small external magnetic field applied and measuring on warming). We varied the temperature between 2 and 350 K and applied external magnetic fields of up tp 9 T. Resistivity was measured using a standard four probe arrangement and an AC resistivity bridge. Gold wires were attached to the samples with silver epoxy.
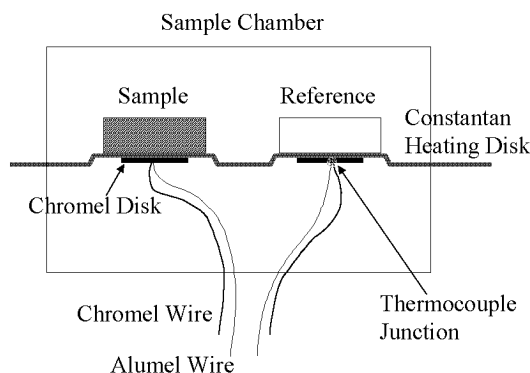
2.2.2   Differential Scanning Calorimetry

Differential scanning calorimetry (DSC) is an ideal tool to investigate the occurence of structural phase transitions as a function of temperature. With DSC one measures the energy necessary to establish a nearly zero temperature difference between a substance and an inert reference material, when the two specimens are subjected to identical temperature regimes in an environment heated or cooled in a controlled manner. There are two main types of DSC systems in common use, power-compensated and heat flux DSC. Both work with the concept of two identical pans, one containing the sample and the other one empty (reference). In power-compensation DSC, the temperatures of the sample and reference are controlled independently using separate, identical heaters. The temperatures of the sample and reference are kept identical by varying the power going to the respective heaters; the energy required to do this is a measure of the heat capacity changes in the sample relative to the reference.
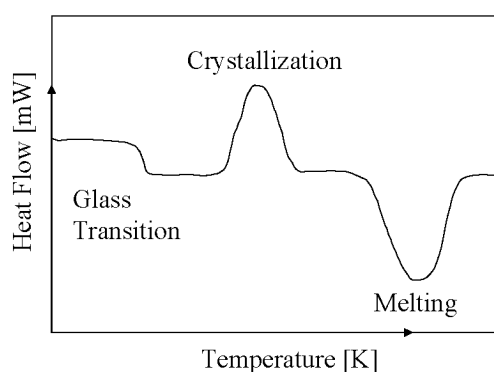
In Figure 2.6 the setup for a heat flux DSC measurement is shown: Heat is transferred to the sample and reference through a disk made of Copper and Nickel. The heat transported to both

---

Figure 2.6: Schematic view of a heat flux differential scanning calorimeter.

Figure 2.7: Schematic view of the heat flow curve across different transitions.

the sample and reference is strictly controlled and at the same time the instrument monitors the temperature difference between the two pans, which arises from heat capacity changes in the sample. Through the constantan-chromel thermocouple the differential heat flow is measured, while the temperature is monitored by chromel-alumel thermocouples attached beneath the chromel wafers. From the ratio of the heat flow and the resulting heating rate (temperature difference with time) the heat capacity of the sample can be calculated.

DSC can be used to measure a number of characteristic properties of a sample, such as melting, crystallization, as well as glass transition temperatures. DSC can also be used to study oxidation processes. In Figure 2.7 a schematic view of the manifestations of different transitions on the heat flow curve is shown. For a detailed description see [49, 50, 51].

DSC measurements are a good starting point to obtain an overview of possible structural phase transitions of a given material. What kind of transitions one deals with has to be investigated with alternative techniques (e.g. macroscopic measurements (magnetism), x-ray or neutron powder diffraction (structural changes), etc.).
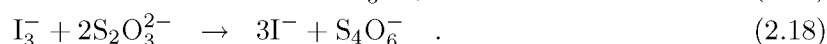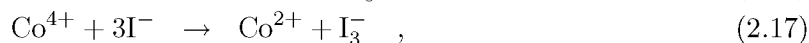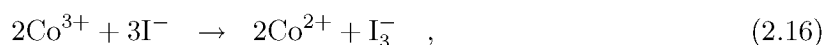
2.2.3 Oxygen Content Determination

Iodometry, Gas Volumetry and Thermogravimetry

For all our measurements it was necessary to know the exact oxygen content of the given sample. Several techniques are available: Iodometry, gas volumetric determination and thermogravimetric reduction. The three methods are described in detail by Conder *et al.* [52]. A short summary
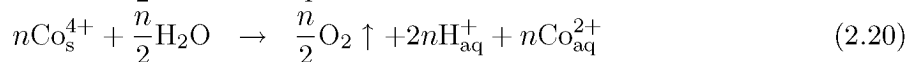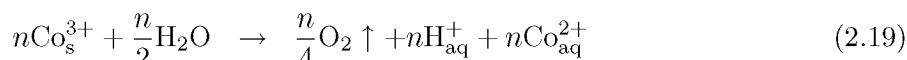
will be given here, focussing on a layered cobaltite of type $LnBaCo_2O_{5+\delta}$. In these materials, due to variation of the oxygen content, the ratio of Co^{3+}/Co^{4+} ($\delta \geq 0.5$) is not constant.

Iodometry is an analytical technique involving titration, where the appearance of elementary iodine indicates the end point of the reaction. The sample is dissolved in two steps (with KI and then HCl), liberating iodine I_3^- (2.16, 2.17). To this solution a reagent is added (usually sodium thiosulfate ($Na_2S_2O_3$ as tritrant) (2.18). Starch is used as an indicator to detect the end-point of the titration (it forms a blue complex with the iodine molecules). The following reactions take place:

$$2Co^{3+} + 3I^- \quad \rightarrow \quad 2Co^{2+} + I_3^- \quad , \tag{2.16}$$

$$Co^{4+} + 3I^- \quad \rightarrow \quad Co^{2+} + I_3^- \quad , \tag{2.17}$$

$$I_3^- + 2S_2O_3^{2-} \quad \rightarrow \quad 3I^- + S_4O_6^- \quad . \tag{2.18}$$

From the amount of thiosulfate needed to remove the blue color of the solution (turn iodine I_3^- into elementary iodine I^-) one can calculate the amount of liberated iodine. From that it is possible to calculate the volume ratio of Co^{3+}/Co^{4+} ions and conclude on the initial oxygen content.

In **gas volumetric determination** $LnBaCo_2O_{5+\delta}$ is dissolved in acid (HNO_3), which leads to the formation of gaseous oxygen (2.19, 2.20). This oxygen can be measured and again the ratio Co^{3+}/Co^{4+} and therefore oxygen content can be calculated:

$$nCo_s^{3+} + \frac{n}{2}H_2O \quad \rightarrow \quad \frac{n}{4}O_2 \uparrow +nH_{aq}^+ + nCo_{aq}^{2+} \tag{2.19}$$

$$nCo_s^{4+} + \frac{n}{2}H_2O \quad \rightarrow \quad \frac{n}{2}O_2 \uparrow +2nH_{aq}^+ + nCo_{aq}^{2+} \tag{2.20}$$

In the **thermogravimetric reduction** the sample is heated in a reducing atmosphere (usually H_2) and from the weight loss (assuming that the products of the reduction are known) the oxygen content in the starting sample can be calculated:

$$LnBaCo_2O_{5+\delta} + (2.5 + \delta)H_2 \rightarrow 0.5Ln_2O_3 + BaO + 2Co + (2.5 + \delta)H_2O \tag{2.21}$$
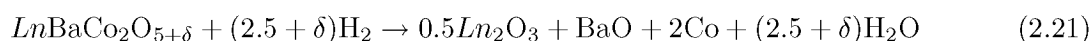
The three techniques have very different accuracies: For iodometry and the gas volumetric method the average reproducibility error of oxygen content determination is $\pm$ 0.005. For the thermogravimetric reduction, this value is much higher, namely ± 0.02 [52]. This is an important result, since in literature oxygen contents are often determined by thermogravimetric reduction, which is least accurate.

2.2.4   X-Ray Powder Diffraction

X-ray powder diffraction was used for both the determination of symmetry and lattice constants of a sample as well as for the detection of impurity phases. In the course of preparing a sample, x-ray diffraction is also useful to check if the reaction process has been successful, or if further sintering of the material at higher temperatures is necessary. Silicon can be added to the powder sample in order to have an external reference of which the exact lattice constants are known. Our X-ray powder diffraction experiments were all perfomed on a Siemens D500 instrument with Cu Kα radiation λ_1= 1.5406 Å, λ_2=1.5444 Å ($I_2/I_1 = 0.5$) at room temperature.

2.2.5 Coulometric Titration

Coulometric titration is used to determine the equilibrium oxygen pressure in materials with varying oxygen content (e.g. $Ln\mathrm{BaCo_2O_{5+\delta}}$) for different tempeartures. The oxygen content of the material can be calculated from the coulometric titration data. A four probe arrangement can be used to simultaneoulsy measure high temperature conductivity and thermopower. This has the advantage that one has an arrangement for which different measurements can be performed simultaneously.

The sample (with known initial oxygen content) is located inside a so called coulometeric cell, which is made out of the oxygen ionic conductor zirconia. Two pairs of platinum electrodes are located on the inner and outer sides of the cell and serve as the electrochemical oxygen sensors and pump. The oxygen pressure (of which the initial value is known) inside the measuring cell can be calculated from the voltage at the oxygen sensor of the measuring cell. Raising sample temperature will lead to a loss of oxygen in the sample, and increase oxygen pressure inside the cell. This in terms will increase the voltage across the electrochemical oxygen sensor. Oxygen content in the sample can be increased by increasing the oxygen pressure inside the cell with the electrochemical pump. From the oxygen pressure inside the cell and knowing how much oxygen was pumped inside the cell, the oxygen content of the sample can be calculated.

This method is very useful, when one is interested in measuring one property for samples with different oxygen content: the measuring set-up stays the same, only the oxygen content is varied.

2.3 Rietveld Refinement

Before H. M. Rietveld introduced the profile refinement method (today called Rietveld refinement) [53, 54] in 1969, structure refinements were performed using integrated neutron powder intensities. This had a severe drawback: due to the overlap of independent diffraction peaks important information was lost. Rietveld had the idea to analyze the profile intensities instead of integrated quantities in the refinement procedure. In Rietveld refinement least-square refinements are carried out until the best fit is obtained between the entire observed powder diffraction pattern taken as a whole and the entire calculated pattern based on the simultaneously refined models for the crystal structure(s), instrumental properties and diffraction optics effects. A completely new feature of this procedure is the feedback, which improves the model from one refinement cycle to the next.

It is possible to simultaneously refine more than one nuclear (or magnetic) phase, which results in a large number of parameters to be refined. They are divided into global (the same for all phases) and phase specific ones. Among the global parameters are the 2Θ-Zero, instrument profile, background, profile asymmetry, wavelength and absorption. The local parameters include first the lattice parameters, atomic positions, site-occupancies, thermal parameters, scale factor and components of the magnetic vector. In a second step, anisotropic temperature factors, preferred orientation, crystallite size (size effect), microstrain and extinction can also be modelled. A detailed discussion about microstrain and size effect is presented in Chapter 3.4.2.

A Rietveld type refinement procedure requires some analytical expression to describe the form of the intensity profile contribution from an individual reflection. The intensity y_i at a given point $2\Theta_i$ in a profile can be expressed by:

$$y_i(calc) = \sum_k I_k \Omega(2\Theta_i, 2\Theta_k) + y_{bi} \propto \sum_k |F_k|^2 L_k \Phi(2\theta_i - 2\theta k) P_k A + y_{bi} \quad , \quad (2.22)$$

$$I_k \propto F_k^2 \quad . \tag{2.23}$$

The summation is made over all possible contributing reflexions at $2\Theta = 2\Theta_i$; I_k is the calculated integrated intensity for a reflexion k; $\Omega(2\Theta_i, 2\Theta_k)$ is the function assumed to describe the peak shape ($\int_{-\infty}^{+\infty} \Omega \, d(2\Theta_i) = 1$); $2\Theta_k$ is the calculated 2Θ for the reflexion k and y_{bi} is the background intensity. In the second equation the profile function term is broken down. $|F_k|^2$ is the structure factor of the k th Bragg reflection, L_k contains the Lorentz, polarization, and multiplicity factors, ϕ is the reflection profile function, P_k the preferred orientation function, and A is an absorption factor. Irrespective of the form of the function Ω used to describe the profile, the refinement procedure involves the minimization of the function χ^2:

$$\chi^2 = \sum_i w_i \left(y_i(\text{obs}) - y_i(\text{calc}) \right)^2 ; \qquad y_i \propto F_k^2 \quad , \tag{2.24}$$

where $w_i = 1/y_i(\text{obs})$ is the weight assigned to an individual observed net intensity $y_i(\text{obs})$, $y_i(\text{calc})$ is the calculated intensity. In order to describe the contents of the complete unit cell, it is sufficient to to give the set of symmetry operations, which generate the remaining positions and magnetic vectors in the cell from the initial information. Because the problem is not linear in the parameters, approximate values for all parameters are needed for the first refinement cycle. In order to be able to make some quantitative judgement on the agreement between observed and calculated profiles reliability indices are defined

$$R_{profile} \quad = \quad \frac{\sum_i |y_i(\text{obs}) - y_i(\text{calc})|}{\sum_i y_i(\text{obs})} \quad , \tag{2.25}$$

$$R_{weighted} \quad = \quad \left(\frac{\sum_i w_i |y_i(\text{obs}) - y_i(\text{calc})|^2}{\sum_i w_i (y_i(\text{obs}))^2} \right)^{1/2} \quad , \tag{2.26}$$

$$R_{Bragg} \quad = \quad \frac{\sum_i |I_{obs,i} - I_{calc,i}|}{\sum_i |I_{obs,i}|} \quad . \tag{2.27}$$

Since R_{Bragg} is not based on the observed intensities, but on those deduced with the model, it is therefore always in favor of the model being used. $R_{weighted}$ is the most meaningful of the R's, because the numerator is the residual (χ^2) being minimized. One can also use the goodness of the fit S

$$S \quad = \quad \left[\frac{\chi^2}{N - P} \right]^{1/2} = \frac{R_{weighted}}{R_{expected}} \quad , \tag{2.28}$$

$$R_{expected} \quad = \quad \left[(N - P) / \sum w_i y_i(\text{obs})^2 \right] \quad . \tag{2.29}$$

However, all these numbers are nice, but as written in the book by Young [55]: "numerical criteria are very important, but numbers are blind". It is therefore necessary to use graphical criteria of the fit, such as difference plots, as well as simultaneouse plotting of observed and calculated profiles, where it is possible to zoom in and see how well the small reflections are modelled. Additionally, it is important to analyze the solution with respect to its physical feasibility.

For the current investigation the programm FullProf [56] has been used, in combination with the graphical tool WinPLOTR. The program can be downloaded from the following website:

http://www-llb.cea.fr/fullweb/powder.htm

Chapter 3

The 3D Cobaltites: $Ln_{1-x}Sr_xCoO_{3-\delta}$ (Ln = Lanthanide)

In this chapter we present new structural and magnetic information of the three dimensional (3D) cobaltite $Ho_{0.1}Sr_{0.9}CoO_{3-\delta}$ ($0.15 \leq \delta \leq 0.49$). This material (with nominal Co charge $+3.5$ at $\delta = 0.20$) is known to have a tetragonal crystal structure in a wide region around oxygen deficiency $\delta = 0.25$. From neutron powder diffraction measurements (NPD) we find that 1) the oxygen vacancies lie in the planes of the oxygen octahedra surrounding the Co ions; and 2) the tetragonal structure does not arise from the mentioned oxygen vacancy order, as is widely accepted, but from a systematic displacement of the oxygen ions from their symmetric positions. The displacement leads to two different Co ion environments together with an almost complete charge order ($+3.07$ and $+3.95$ for $\delta = 0.19$). The charge order is short ranged, with cluster size of ~ 200 Å. 3) The magnetic structure evolves from ferromagnetic (FM) in $\delta = 0.15$ to antiferromagnetic (AFM) in $\delta = 0.49$. Our models for the magnetic structures can be explained using the superexchange interaction.

3.1 Motivation

One of the reason to study the three-dimensional (3D) compounds of type $La_{1-x}Sr_xCoO_{3-\delta}$ is because they are good mixed (ionic and electronic) conductors. Such materials are of potential use in solid oxide fuel cells (SOFC) [5, 57, 58] as cathode materials. The SOFC is of great industrial interest, because it is energetically efficient and stresses the environment less than other energy production systems. Improvement of the SOFC would be possible if a reduced operating temperature were achieved (today $\sim 1000°C$). Reduction of operating temperature would decrease material degradation and therefore ease the use of cheaper components. The cathode material, where oxygen is reduced, has to meet some requirements, among which are high electrical and ionic conductivity, high catalytic activity for oxygen reduction, and compatibility with the electrolyte. Cobalt containing perovskite oxides, such as $La_{1-x}Sr_xCoO_{3-\delta}$, tend to exhibit higher ionic conductivity than other perovskite materials due to a greater concentration of oxygen vacancies [59] and are also good catalytic oxygen reductors. However, $La_{1-x}Sr_xCoO_{3-\delta}$ reacts with the electrolyte and the oxygen reduction process is hampered. Other Co-compounds are therefore investigated, which would react less with the electrolyte [57]. Further, in order to reduce the operating temperature, it is necessary to understand why these materials are such good ionic conductors. A good starting point is the precise determination of the crystallographic structure, which will give information about the location of the

oxygen vacancies within the unit cell.

Recent discovery of superconductivity in the cobaltite $Na_xCoO_2 \cdot y\, H_2O$ ($x \sim 0.35$, $y \sim 1.3$) [6] has lead to a strong increase of interest in the Na containing Co-compounds. Before being able to understand the complicated mechanisms which lead to superconductivity in these hydrated systems, it is necessary to understand the more basic properties. Among these are the crystallographic/magnetic structures, electronic properties, Co spin states, and nature of magnetic interactions. Additionally it is necessary to understand, how these properties are influenced by changing doping or oxygen content, as well as external parameters such as temperature, magnetic fields and pressure.

In the case of the series $Ho_{0.1}Sr_{0.9}CoO_{3-\delta}$ the decreasing oxygen content leads to an increasing amount of oxygen vacancies (influencing the crystallographic structure) and also to a varying Co^{4+}/Co^{3+} ion ratio (affecting the type of magnetic interactions). The goal is to find whether the crystallographic structure and the magnetic interactions evolve smoothly on reducing oxygen content and whether well-defined explanations for an eventual evolution can be found.

In order to have a complete picture, it is necessary to also investigate the dependence of the above mentioned properties on tunable parameters other than oxygen content (e.g. type of lanthanide). Understanding the dependence of the system on different parameters can make it easier to synthesize more application oriented systems. Therefore, this work is part of a large effort to understand the underlying mechanisms which control the physical properties displayed by three-dimensional cobaltites.

3.2   From $LaCoO_3$ to $SrCoO_3$

The 3D cobaltites $LaCoO_3$ and $SrCoO_3$ were first mentioned in the literature in 1953 by G. H. Jonker and J. H. van Santen [60] and H. Watanabe [61]. Since then a large number of groups have worked on these compounds. Especially $LaCoO_3$ keeps on attracting a lot of interest, due to its rich, but also confusing properties, which have lead to very controversial discussions.

$LaCoO_3$ crystallizes in the rhombohedrally distorted cubic perovskite structure with space group $R\bar{3}c$ [62, 63]. The temperature dependent reciprocal magnetic susceptibility $1/\chi$ can be divided into four regions (Figure 3.1) [64, 65]: i) $0 < T < 100\,K$: non-magnetic, insulating ground state with the Co^{3+} ions in a low-spin (LS) state (t_{2g}^6, $S = 0$); ii) $100\,K < T < 400\,K$: a magnetic, semiconducting state with a low effective magnetic moment; iii) $400\,K < T < 600\,K$: bad metallic, magnetic state; iv) $T > 600\,K$: metallic state with increased effective magnetic moment. The low temperature crossover from state i) $\rightarrow$ ii) has many interpretations: The most plausible was given by Raccah and Goodenough [66] in 1967. They explain the transition in terms of a thermally induced population of the low-lying Co^{3+} high-spin (HS) state ($t_{2g}^4 e_g^2$, $S = 2$).

Since no model could be found which could explain both the nature of the spin state transition and the evolution of the electronic properties for the $LaCoO_3$ compound, research started to concentrate on the mixed compound $La_{1-x}Sr_xCoO_{3-\delta}$[1] in the 1970's. The substitution of Sr^{2+} for La^{3+} in $LaCoO_3$ brings about remarkable changes in the system [60, 68, 69, 70] due to the introduction of Co^{4+} ions: while $LaCoO_3$ shows high resistivity and antiferromagnetic (AFM) exchange interactions, the $La_{1-x}Sr_xCoO_{3-\delta}$ ($x > 0.3$, δ small) material becomes a ferromagnetic (FM) metal [71].

Detailed studies [67, 72, 73, 74, 75] performed in the 1980's and 90's have lead to a complex phase

---

[1]As prepared samples with $x \leq 0.25$ δ are stoichiometric, while $x \geq 0.25$ results in oxygen loss of $\delta \leq 0.06$, according to Señarís-Rodriguez and Goodenough [67].
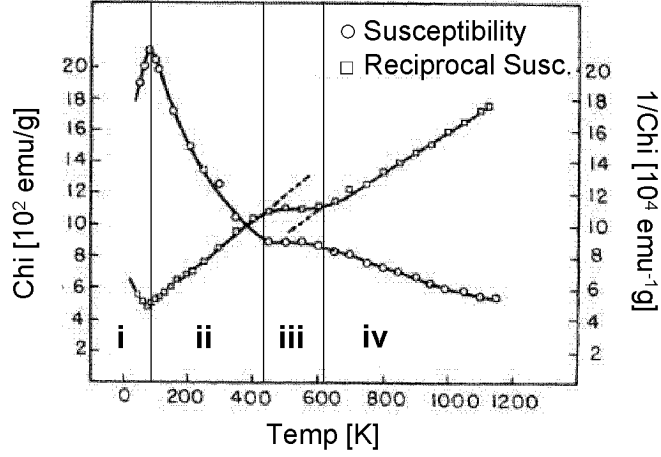
Figure 3.1: Temperature dependences of the magnetic susceptibility and its reciprocal value for LaCoO$_3$ (after Bhide *et al.* [65])

diagram (Figure 3.2 right) for La$_{1-x}$Sr$_x$CoO$_3$ in the doping region $0 \leq x \leq 0.5$. Main interest still lies in the determination of the Co^{3+} spin state in LaCoO$_3$, but the evolution of electronic and magnetic properties with increasing Sr^{2+} content has also been studied extensively.

The temperature dependent spin state as reported by Señarís-Rodríguez and Goodenough [64] is shown in Figure 3.2 on the left: with increasing temperature the Co^{3+} spin slowly evolves from LS $\rightarrow$ LS/HS $\rightarrow$ IS/HS. The metallicity at high temperatures is attributed to a gradual change from localized to itinerant behavior ($t_{2g}^4 e_g^2 \rightarrow t_{2g}^4 \sigma^{*2}$ and $t_{2g}^5 e_g^1 \rightarrow t_{2g}^5 \sigma^{*1}$) of the HS and IS Co^{3+} spins in the temperature region from 350 K to 650 K.

In view of this work the magnetic and crystallographic properties of La$_{1-x}$Sr$_x$CoO$_{3-\delta}$ will be described shortly. They can be divided into two compositional ranges separated by the percolation threshold $x_m = 0.2$ [67]:

1. $0 < x < x_m$: phase segragation into hole rich superparamagnetic[2] regions and a hole poor matrix (similar to LaCoO$_3$ [64]). Substitution of Sr^{2+} for La^{3+} oxidizes the CoO$_3$ array and LS Co^{4+} ions are introduced within the CoO$_3$ complex. With increasing x, clusters containing more than one LS Co^{4+} ion are formed. Inside the hole rich regions, FM coupling through HS Co^{3+}-O- LS Co^{4+} superexchange interactions give rise to the superparamagnetic behavior observed below T_c. The coupling between these superparamagnetic regions is AFM via superexchange interactions. The crystallographic structure at $T \leq 600$ K is rhombohedral as in the parent compound LaCoO$_3$.

2. $x_m < x < 0.5$: At $x_m \sim 0.20$, the ferromagnetic clusters reach a magnetic percolation threshold and a FM state is established below T_c. Some superparamagnetic clusters remain isolated, which leads to cluster glass behavior [74], due to the frustration between AFM superexchange (between Co^{3+}-Co^{3+} and Co^{4+}-Co^{4+}) and FM double exchange (Co^{3+}-Co^{4+}). For $0.20 \leq x \leq 0.30$ metallic conduction is observed for $100 < T < T_c$. For $x > 0.3$ the material becomes metallic in the whole investigated temperature region. The

---

[2]Superparamagnetism occurs when the material is composed of very small crystallites. In this case even though the temperature is below the Curie or Neel temperature, the thermal energy is sufficient to change the direction of magnetization of the entire crystallite. The resulting fluctuations in the direction of magnetization cause the magnetic field to average to zero. The material behaves in a manner similar to a paramagnet.
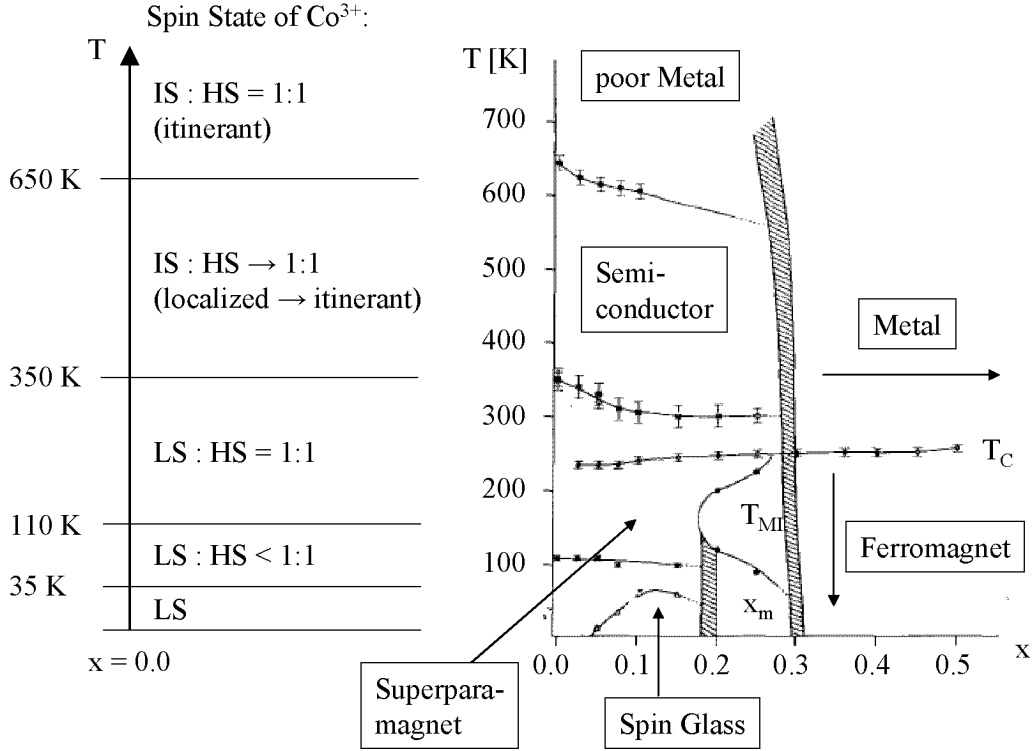
Figure 3.2: Left: evolution of the spin states of the Co ions in LaCoO$_3$ (after Señarís -Rodríguez and Goodenough [67]). Right: phase diagram of La$_{1-x}$Sr$_x$CoO$_{1-\delta}$.

crystallographic structure at temperatures $T < 400$ K is rhombohedral, while for x close to 0.5 a high temperature transition to a cubic perovskite structure occurs.

The other end member of the family La$_{1-x}$Sr$_x$CoO$_{3-\delta}$, namely SrCoO$_{3-\delta}$, was first synthesized and characterized by Watanabe 1957 [61]. Two samples were investigated by this group, one heat-treated in oxygen ($\delta \sim 0.15$), the other heat-treated in vacuum. The crystallographic structure of the first one was found to be cubic, while the crystal symmetry of the second sample could not be determined. The sample heat-treated in oxygen shows a spontaneous magnetization below $T_C = 223$ K (Figure 3.4a) with a magnetic moment of 3.32 μ_B per magnetic ion. From reciprocal susceptibility data (Figure 3.4b) a positive paramagnetic Curie temperature can be extracted. On the contrary, the sample heat-treated in vacuum has a negative paramagnetic Curie temperature (Figure 3.4b). From conductivity measurements (Figure 3.4b) it is found that the sample heat-treated in oxygen has very low resistivity values at 20°C (3.9×10^{-4} Ωcm), while the values for the vacuum heat-treated sample is higher by a factor 10^{10}.

Ferromagnetic order was later confirmed for SrCoO$_3$, with a Curie temperature of $T_c = 220$ K (280 K) and a magnetic moment of $\mu_{eff} = 3\mu_B$ ($2\mu_B$) [76] ([77]). According to early groups the Co^{4+} ion is in the LS state [78, 79, 80, 81]. More recent calculations suggest an IS ground state [82].

SrCoO$_{2.5}$ was investigated by both Takeda *et al.* [78] and Grenier *et al.* [83] and was found to crystallize in the complicated brownmillerite type structure *Imma* with the orthorhombic unit cell $\sqrt{2}a_p \times 4a_p \times \sqrt{2}a_p$. It is a G-type AFM with ordering temperature T_N either 570 K [78] (Figure 3.5a) or 545 K [83]. The spin state of the Co^{3+} ions according to Takeda *et al.* [78] is HS
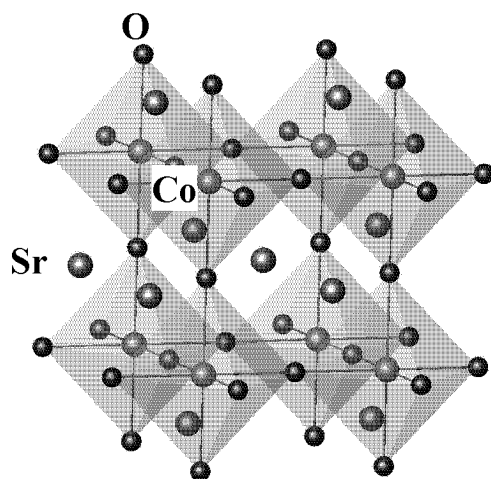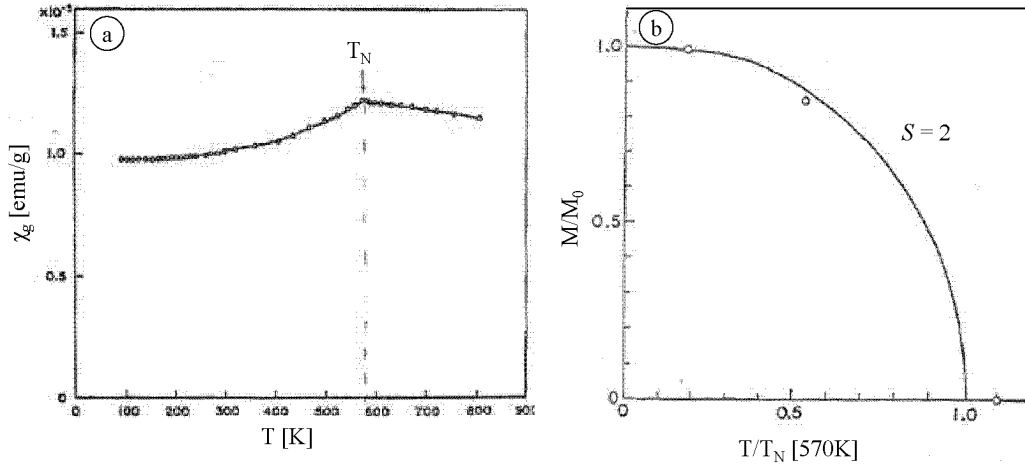
Figure 3.3: Cubic perovskite structure as displayed by SrCoO$_3$.
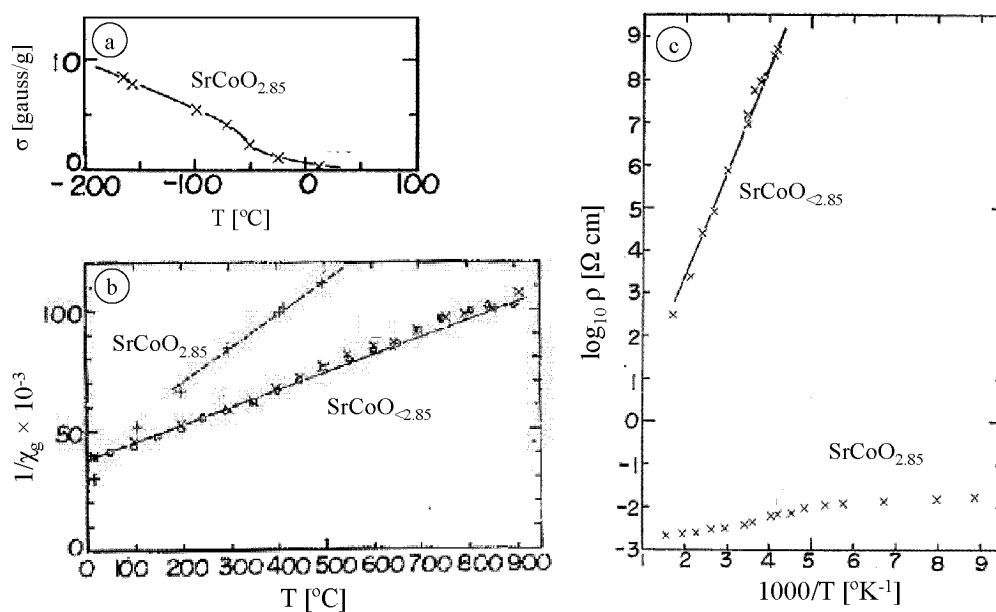
Figure 3.4: Temperature dependent a) Magnetization per gram at H = 15000 Oe for SrCoO$_{2.85}$; b) Reciprocal susceptibility per gram for SrCoO$_{2.85}$ and SrCoO$_{2.85}$ and c) logarithm of electrical resistivity for SrCoO$_{2.85}$ and SrCoO$_{<2.85}$. Taken from H. Watanabe [61].

Figure 3.5: Temperature dependent a) susceptibility per gram and b) reduced sublattice magnetization ($\circ$ are experimental points and the line is a Brillouin curve with S = 2) for $SrCoO_{2.5}$. Taken from H. Takeda [76].

with a magnetic moment of $3.3 \pm 0.5 \mu_B$ at liquid nitrogen temperature, where the temperature dependent magnetic moment can be fit by a Brillouin curve with S = 2 (Figure 3.5b).

The $Ln_{1-x}Sr_xCoO_{3-\delta}$ compounds with $0.5 \leq x \leq 1$ have started to attract attention only recently. However, in these studies, to stabilize the the pure perovskite phase, a small amount of Sr^{2+} has been substituted by a lanthanide Ln, as shown by James $et~al.$ [84]. Most of the $Ln_{1-x}Sr_xCoO_{3-\delta}$ compounds investigated have an oxygen deficiency of $\delta \sim 0.20$ [5, 85, 84, 86, 87, 88, 89], which is the equilibrium oxygen deficiency. It is generally accepted that at room temperature (RT) the compounds show a tetragonal superstructure. But there are two possibilities to describe the unit cell: in one case (mostly for lanthanides with a small ionic radius, among them Gd, Ho and Dy), it is $I4/mmm$ (Figure 3.6 left) with unit cell $2a_p \times 2a_p \times 4a_p$ with a_p the lattice parameter of the cubic perovskite [85, 87, 88]. In the other case, mostly for larger lanthanides (La, Pr and Nd) or for $x = 0.95$, a unit cell $a_p \times a_p \times 2a_p$ with space group $P4/mmm$ (Figure 3.6 right) is suggested [5, 84, 86].

All authors agree that at RT the oxygen vacancies in the $Ln_{1-x}Sr_xCoO_{3-\delta}$ compounds are ordered, but discrepancies exist on their location. Two possibilities are described: at an apical octahedral position (Figure 3.6 right) [5, 84, 86] or in the basal plane of the octahedra (Figure 3.6 left) [85, 87, 88]. Interestingly, the choice of oxygen vacancy site is directly correlated to the space group of the system: for $P4/mmm$ spacegroup the oxygen vacancies are at the apical octahdral position, while for $I4/mmm$ the basal plane position of the octahedra is occupied.

The nature of the magnetic interactions in $Ln_{1-x}Sr_xCoO_{3-\delta}$ has also been investigated. Whereas superexchange [26, 29] is appropriate for insulating and semiconducting cobaltites, the proper choice of the relevant coupling mechanism in metallic cobalt oxides strongly depends on the actual spin state(s) of the Co ions.

A system which illustrates this problematic is $SrCoO_3$: in this compound, which is a ferromagnetic metal below $T_C = 280$ K [77], the origin of the FM order of Co^{4+} is presently controversial. According to early groups [79], Co^{4+} is in the LS state, in spite of the slightly higher experimental value of the Co magnetic moment ($1.6\mu_B$) compared to the expected value ($1\mu_B$). However, within this hypothesis, the Zenner-deGennes double exchange [16] (DE) appears to be clearly inappropriated due to the absence of carriers in the Co e_g - O 2p $\sigma*$ band. If, as
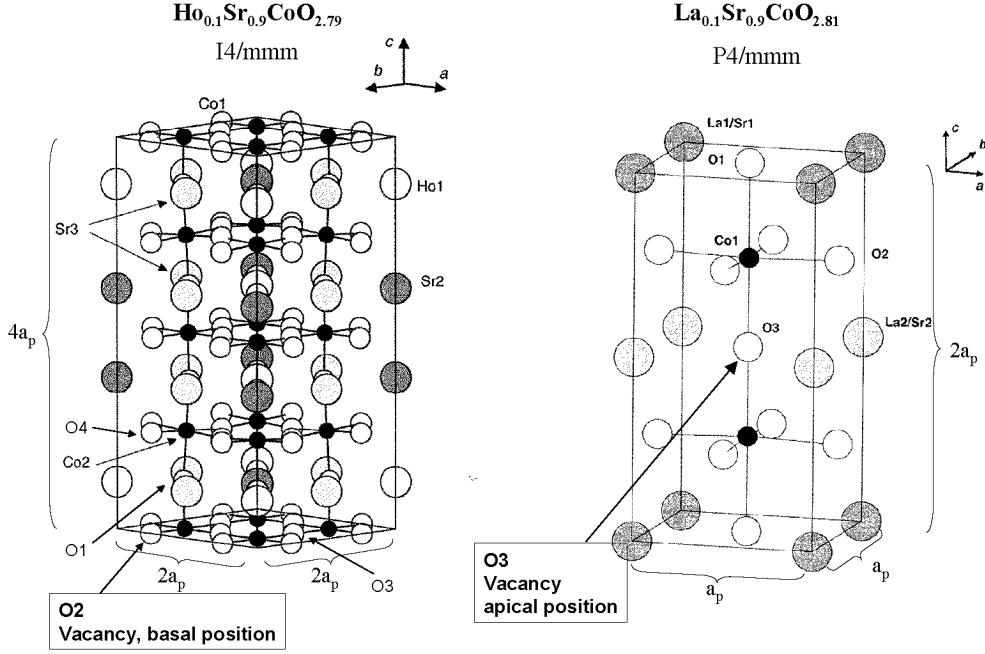
Figure 3.6: Left: refined structure for Ho$_{0.1}$Sr$_{0.9}$CoO$_{2.79}$. Oxygen vacancies lie in the layers at $z = 0$ and $1/2$ and are in the basal plane of the octahedra. Right: refined structure for La$_{0.1}$Sr$_{0.9}$CoO$_{2.81}$. Oxygen vancies lie in the layer at $z = 1/2$ and are at the apical position of the octahedra. After James *et al.* [85, 86].

suggested by Potze and Sawatzky [82], Co^{4+} is in the IS state, a mechanism similar to DE, involving real charge transfers of the form Co $t_{2g}^4 e_g^1$ - O 2p^6 $\leftrightarrow$ Co $t_{2g}^4 e_g^2$ - O 2p^5 could account for ferromagnetism and conductivity due to the coupling between the IS ($S = 2$) cobalt ion moments induced by the mobile oxygen holes. Nevertheless, a major criticism to this model comes from the fact that, as in the case of mixed-valence magnetoresistive manganese oxides [29], a close relationship between conductivity and ferromagnetism would be expected. The absence of sharp anomalies in the transport properties at T$_C$ put this model in question.

For intermediate oxygen compounds little studies exist which focus on magnetism. James *et al.* [84] find that for all Ln and $\delta \sim 0.20$, the materials undergo a transition to a spin glass state in the temperature region $99\,\mathrm{K} \le T_C \le 148\,\mathrm{K}$. From the magnetic moment extrapolated from the magnetization curves of the $Ln = \mathrm{Y}$ compound, these authors calculated that the Co^{3+} ions are in LS state and the Co^{4+} ions in IS. On applying a magnetic field, a transition to a FM state was found. For increasing Ho content $((1 - x) > 0.05)$ ferromagnetic clusters embedded in a long-range antiferromagnetic matrix are reported by Goossens *et al.* [87].

The electronic properties of Ln_{1-x}Sr$_x$CoO$_{3-\delta}$ have not been investigated in detail. It has been shown by Luo *et al.* [89], that in contrast to La$_{1-x}$Sr$_x$CoO$_3$, the compounds Gd$_{1-x}$Sr$_x$CoO$_3$ ($x \ge 0.60$) are insulating. No resistivity measurements performed on other Ln_{1-x}Sr$_x$CoO$_{3-\delta}$ compounds have been published to our knowledge.

3.3   Synthesis of $Ho_{0.1}Sr_{0.9}CoO_{3-\delta}$

The polycrystalline $Ho_{0.1}Sr_{0.9}CoO_{3-\delta}$ sample is the only one synthesized as part of this work and therefore the process will be described in detail.

Since it is known from literature that it is hard to stabilize a pure perovskite structure of $SrCoO_3$ without applying very large pressures ($\sim$ 1500 bar [76, 79, 81]) or using electrochemical oxidation [76, 77], 10% of Holmium at the place of Strontium was included. Inclusion of a lanthanide eases the stabilization of the phase pure perovskite structures [84]. Recently it has been shown that including Thorium (actinide) also stabilizes the perovskite phase [90]. The samples were synthesized by the solid state reaction method with the starting powders Ho_2O_3, $SrCO_3$ and Co_3O_4 which had a minimum purity of 99.99%. The initial weight of the oxides was calculated through their molar weight (18.89, 132.87 and 80.27 g/mole for Ho_2O_3, $SrCO_3$ and Co_3O_4 respectively). The amount of carbonoxide CO_2 released during the reaction process can be estimated (in this case $\sim$ 17%).

The powders were well mixed, pressed by hand into a crucible, then heated[3] to 900°C and left at this temperature for 24 h. In a next step the sintered material was crushed to fine powder using an automatic mortar. Again the powder was pressed into the crucible by hand, and subsequently heated to the higher temperature 1000°C, at which it was left for 50 h. The material was ground even finer and then pressed into pellets of diameter $\varnothing = 1$ cm using hydraulic pressure of $\sim$ 5000 kg/m^2. The sample was heated up to 1150°C (500°C/h), left there for 50 h and was then cooled down slowly (100°C/h).

After this step phase purity was checked by x-ray diffraction on a Siemens D500 diffractometer. The $5° < 2\Theta < 110°$ range was scanned with a stepsize of 0.05°, measuring 18 sec per point. Impurity peaks were detected (Figure 3.7, pattern 1), therefore the material was crushed and pressed into pellets again. The sintering temperature was increased by 25°C to 1175°C, and the sample was left at this temperature for 50 h. X-ray diffraction was performed at the same condition as mentioned before and this time no impurity phase was detected (Figure 3.7 pattern 2). The reflections could be indexed using a tetragonal unit cell ($a_p \times a_p \times 2a_p$, where a_p is the cubic perovskite cell parameter) with $P4/mmm$ symmetry and lattice parameters $a = 3.8371$ Å, $b = 3.8434$ Å and $c = 7.6991$ Å.

The as-synthesized compound had an equilibrium oxygen deficiency of $\delta \sim 0.27$ as determined by thermogravimetric hydrogen reduction. To obtain higher oxygen content it was necessary to expose the sample to high oxygen pressure at an intermediate temperature. With the help of the group of J. Karpinski at ETH Zürich[4], who have the equipment to produce 800 bar oxygen pressure[5], the sample in form of sintered pellets was annealed at 800°C and 800 bar of oxygen pressure for 24 h and then slowly cooled down (1°C/h). The oxygen deficiency was determined to be $\delta = 0.18$, but unfortunately a strong impurity phase was present (Figure 3.7, pattern 3). With the hope to recover the state before the high-pressure synthesis, the sample was heated to 1000°C. X-ray diffraction showed that indeed, the sample was again single phased with tetragonal $P4/mmm$ symmetry. Suspecting that the temperature had been too high during the high pressure experiment, in the next run the sample was annealed at only 500°C, again for 1 h, with the same cooling rate. This temperature turned out to be the right choice, see Figure 3.7 pattern 4. Oxygen content determination showed that the oxygen content corresponded to 2.85. Refinement of the diffraction pattern suggested that the crystal structure is cubic with $Pm3m$ symmetry. Detailed structure analysis will be presented in Section 3.4.

---

[3]The maximum sintering temperature was taken from various articles dealing with similar compounds.

[4]http://www.highpress.ethz.ch/

[5]http://www.highpress.ethz.ch/infrastructure/index
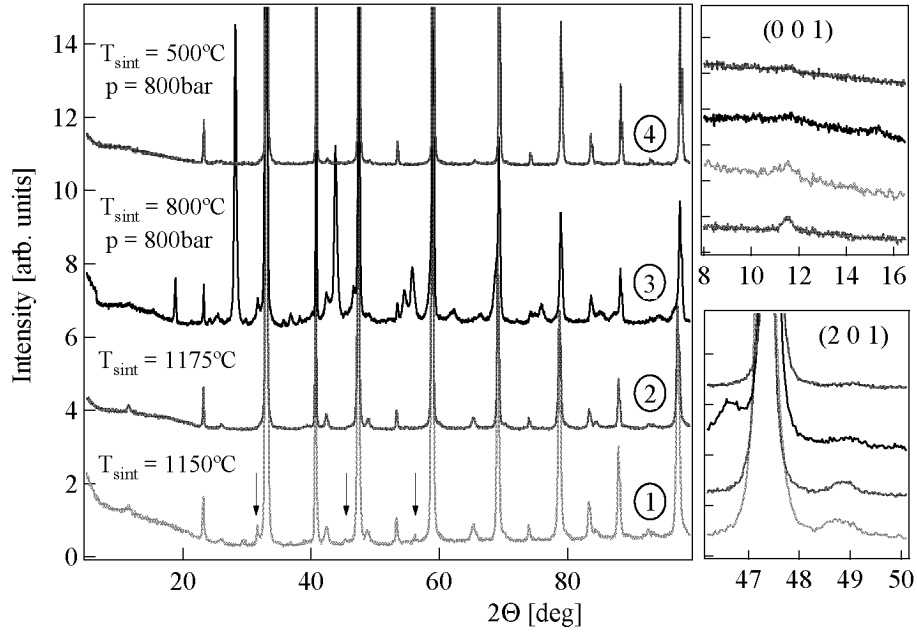
Figure 3.7: Left: x-ray diffraction patterns of $Ho_{0.1}Sr_{0.9}CoO_{3-\delta}$ after different sintering and high oxygen pressure processes (see text). The sintering temperatures and oxygen pressures are indicated. Impurity reflections are seen in patterns 1 (arrows) and 3, while patterns 2 and 4 are typical for a pure tetragonal and cubic structure, respectively. Right: close up of the (0 0 1) (top) and (2 0 1) (bottom) reflections. These are absent for pattern 4, which shows that the high pressure oxidation induces a change in crystal structure from tetragonal to cubic.

This sample was then separated into batches of 1g, which were treated in two different ways in order to reduce oxygen content: the first samples were individually annealed in evacuated quartz ampoules together with an appropriate amount of metallic copper getter (samples with $\delta = 0.15, 0.27, 0.31, 0.42, 0.49$). The samples of the second batch were separately reduced by annealing at $500°C$ in $20 - 50$ bar of oxygen pressure (samples with $\delta = 0.18, 0.19, 0.22, 0.24, 0.37$). The experimental uncertainty in the oxygen deficiency, as determined by reduction in the flow of $5\% \, H_2 + 95\% \, He$ at $T = 1000°C$, was 1%.

In view of a possible single crystal synthesis, where the sample has to be kept at the melting point, the melting temperature of the initial material $Ho_{0.1}Sr_{0.9}CoO_{3-\delta}$ ($\delta = 0.27$) was additionally determined. For these measurements the differential thermal analysis method in combination with mass spectrometry were used. In a first run the sample was heated to $T = 1400°C$ in $He + O_2$ flow, while in the second run only He was used. The flow constants during the measurements were for O_2 15 cm^3/s and for He 30 cm^3/s. The heating rate was fast to $1000°$ ($20°C/min$) and slower to $1400°C$ ($10°C/min$). The cooling rate was $10°C/min$ down to $1000°C$ and then $20°C/min$ to roomtemperature. The onset temperature of melting, which is determined by the beginning of energy emission, corresponding to stronger mass loss (Figure 3.8) was different for the two different gas flows: $1288°C$ ($He + O_2$) and $1244°C$ (only O_2).

For future high temperature measurements we investigated at which temperature the most oxidized sample $Ho_{0.1}Sr_{0.9}CoO_{2.85}$ loses oxygen. DTA and mass spectrometry were performed in flowing He and H_2 gas up to $1050°C$. The result is shown in Figure 3.9. Oxygen is lost in two steps: the first starts at $\sim 200°C$ and becomes maximal at $\sim 510°C$, while a second, smaller

$Ho_{0.1}Sr_{0.9}CoO_{2.73}$: He + O_2 flow

$Ho_{0.1}Sr_{0.9}CoO_{2.73}$: He flow
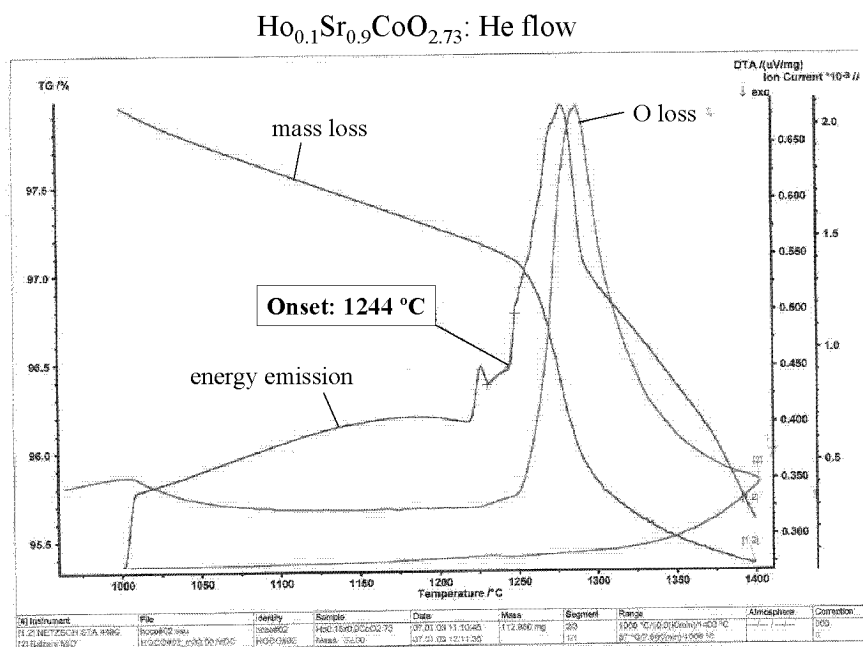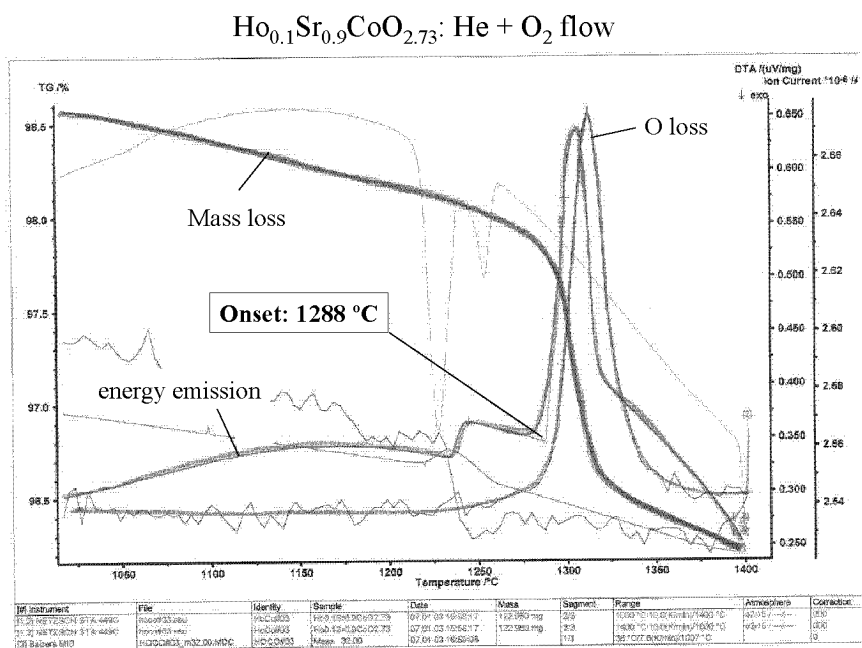
Figure 3.8: DTA and mass spectrometry measurements for $Ho_{0.1}Sr_{0.9}CoO_{2.73}$ in different gas flows. Top: He + O_2, Bottom: He only. The temperature where energy emission begins marks the onset of melting of the sample.
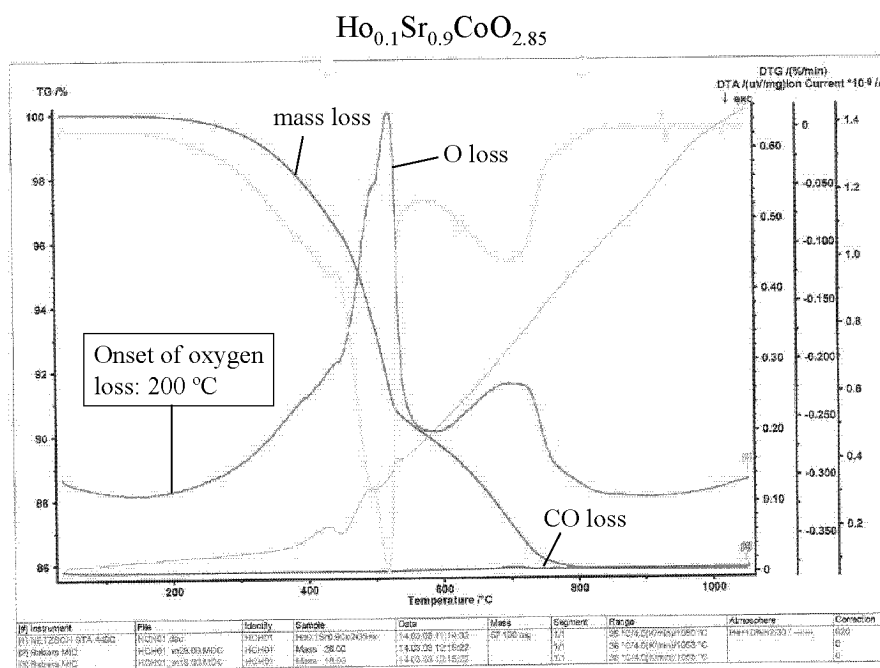
$$Ho_{0.1}Sr_{0.9}CoO_{2.85}$$

Figure 3.9: DTA and mass spectrometry measurements for $Ho_{0.1}Sr_{0.9}CoO_{2.85}$ in He + H_2 flow. Mass loss as well as emission of O and CO (very small) are plotted. At 200°C the sample starts losing oxygen.

emission, starts at 700°C. Loss of CO was also recorded by the mass spectrometer, but compared to oxygen emission this is hardly visible. In subsequent experiments the temperature of 200°C (= 470 K) should not be exceeded in order to be sure to still be dealing with the initial sample.

3.4 $Ho_{0.1}Sr_{0.9}CoO_{3-\delta}$: Crystallographic Structure

In this Section the structure of the material $Ho_{0.1}Sr_{0.9}CoO_{3-\delta}$ ($0.15 \leq \delta \leq 0.5$) which is strongly dependent on oxygen content [91] will be discussed. The samples with low oxygen deficiency ($0.15 \leq \delta \leq 0.31$) adopt a tetragonal crystal structure due to periodic oygen displacement. This 1-dimensional deformation pattern leads to almost complete charge order in the samples with oxygen deficiency $0.19 \leq \delta \leq 0.31$ (charges of +3.07 and +3.95 at the two different Co sites, for $\delta = 0.19$). Oxygen vacancies are found to be located in the basal planes of the oxygen octahedra surrounding the Co ions. Further reduction of oxygen ($\delta \leq 0.37$) does not affect the ordering of oxygen vacancies and these samples have the brownmillerite-type structure.

In order to precisely compare the lattice parameters of the different samples, room temperature x-ray diffraction (XPD) patterns of powders mixed with Si as an internal standard were collected on a Siemens D500 diffractometer using Cu-$K\alpha$ radiation. The patterns were measured in the angular range $4° < 2\Theta < 120°$ using a step size of $0.02°$.

For some representative compositions $\delta = 0.15, 0.27, 0.31, 0.42, 0.49$ (synthesized as described in Section 3.3), neutron powder diffraction data were collected on the high-resolution powder diffractometer HRPT [48] at SINQ (PSI, Switzerland) at room temperature. The data were collected in the angular range $5° < 2\Theta < 165°$ changing the angle stepwise by $0.05°$ and

$\lambda = 1.494$ Å. Additional RT NPD measurements (for $\delta = 0.19$) were performed at D2B at the ILL, France, within $5° < 2\Theta < 160°$ and with $\lambda = 1.60$ Å. The Rietveld program FullProf [56] was used to refine both the crystallographic and micro structures.

3.4.1 $0 \le \delta \le 0.31$: Pseudo Cubic Structure

Figure 3.10 (top) shows the RT x-ray diffraction patterns of $Ho_{0.1}Sr_{0.9}CoO_{2.85}$. The reflections could be properly indexed using the same cubic, perovskite-like structure ($a = b = c = a_p$, space group $Pm3m$) as for the fully oxidized compound $SrCoO_3$ [61, 77]. The site notations and the locations of the atoms with respect to the unit cell for the space group $Pm3m$ and $P4/mmm$ (see later in this text) are shown in Figure 3.11. However, close inspection of the background shows the presence of several extremely small reflections, about 150 times smaller than the most intense peak. These extra features, which are also observed in the neutron diffraction patterns, are much broader than the resolution-limited, $Pm3m$-allowed reflections (see enlargements in Figure 3.10), and could only be indexed by doubling the cubic unit cell along c. Interestingly, the half value of c exactly coincides with that of a_p ($c = 2a_p$), indicating that, in spite of its tetragonal symmetry, the unit cell of the $Ho_{0.1}Sr_{0.9}CoO_{2.85}$ system is *metrically cubic*. In other words, the Co ions form a rigid framework able to accommodate large amounts of oxygen vacancies. The stability of the lattice, even on introducing a large amount of oxygen vacancies, is probably related to the high ionic conduction displayed by $SrCoO_{3-\delta}$ and related systems [2, 4, 34, 92].

The $\delta = 0.15$ NPD data was refined using the cubic space group $Pm3m$ (Figure 3.12 top), because the weakness of the superstructural peaks ruled out the possibility to fit the pattern using the subgroup $P4/mmm$. The refined structural parameters, oxygen content, R_{Bragg} and χ^2 are given in Table 3.2. A schematic side view (bc-plane) of the cubic perovskite structure is shown in Figure 3.13 (top).

The XPD and NPD patterns of the samples with $0.19 \le \delta \le 0.31$ are very similar to the ones in for $\delta = 0.15$, except that the superstructural peaks (especially the lowest angle one) are more pronounced (Figure 3.10). The refinements of the NPD patterns were made in the tetragonal space group $P4/mmm$, with the restriction $a = b = a_p$, $c = 2a_p$. The fits are shown in Figure 3.12 (bottom three graphs). The refined parameters obtained from the neutron data are given in Table 3.2. As shown in Figure 3.13 and in Table 3.1, the z component of the Co sites exactly coincides with that of the cubic perovskite, whereas the apical oxygens O3 and the Sr/Ho atoms are allowed to move away from the cubic positions (arrows in Figure 3.13) along the crystallographic c-axis.

The displacements of the apical oxygens, which, for sake of clarity, have been exaggerated in Figure 3.13, lead two different environments for the Co ions. In order to describe these two positions independently, it is necessary to use a higher symmetry class ($P4/mmm$ is a supergroup to $Pm3m$) in which the Co site (1b) is split into the two sites Co1 (1a) and Co2 (1b). As shown in Table 3.3, the Co1 and Co2 coordination polyhedra have the same in-plane Co-O distances, but the first are squeezed and the second stretched along the c axis. The structure can then be described as a series of elongated and compressed CoO_6 corner-sharing octahedral planes alternating along the c-axis.

Oxygen Vacancy Ordering

We find that the oxygen vacancies prefer one of the two equatorial oxygen positions: oxygen is mainly lost from the basal planes of the elongated octahedra (O2 sites), which display oc-
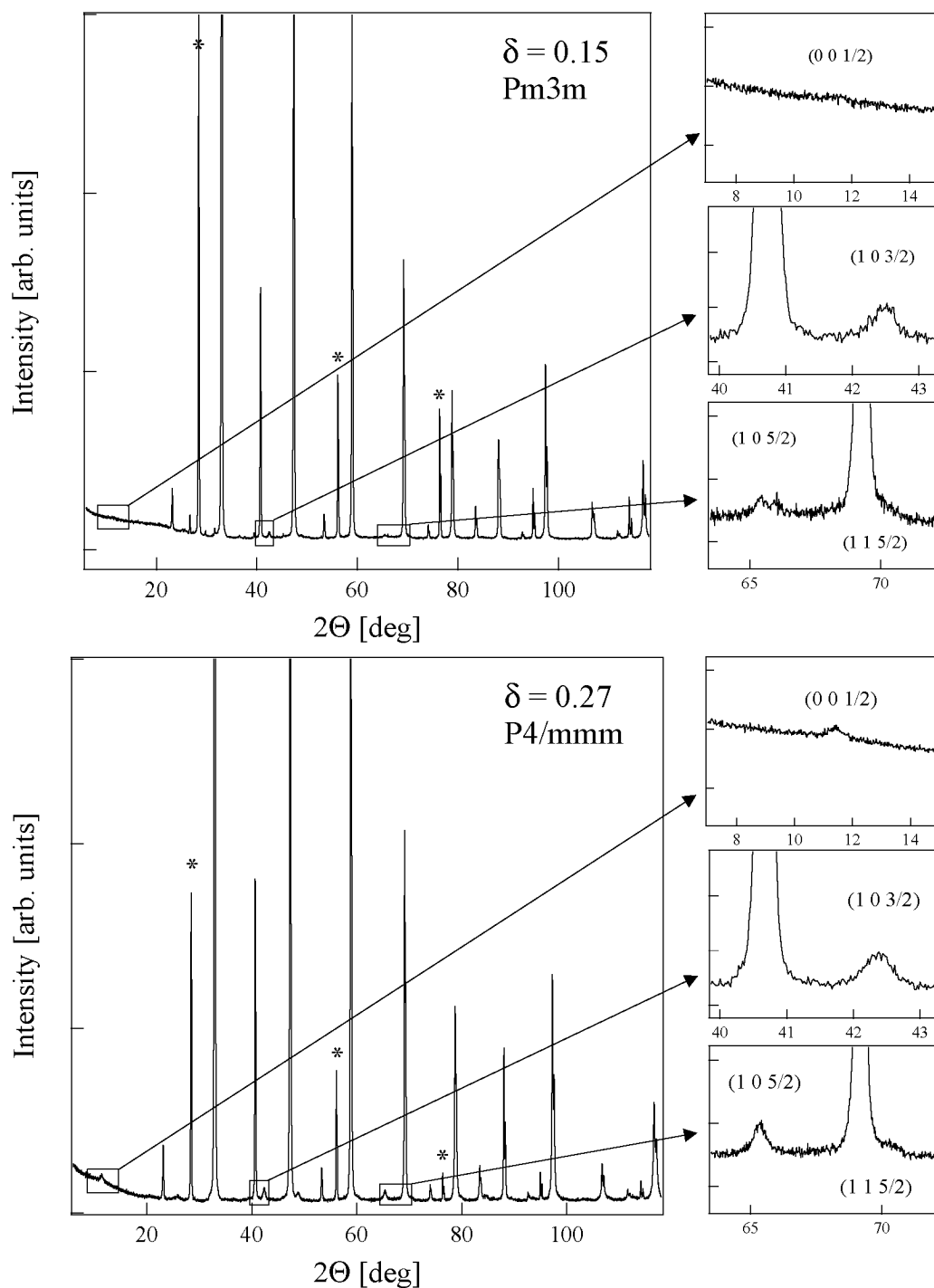
Figure 3.10: Room temperature x-ray diffraction patterns for $Ho_{0.1}Sr_{0.9}CoO_{3-\delta}$ with $\delta = 0.15$ (top) and $\delta = 0.27$ (bottom). The three close ups show weak superstructural peaks, which can be indexed by doubling the unit cell along the c-direction. The indexing corresponds to the $Pm3m$ unit cell. The peaks marked with $*$ are reflections due to the Si internal standard. Note that the same scale used for the $\delta = 0.15$ and 0.27 close ups.

Table 3.2: Crystallographic parameters derived from the $Ho_{0.1}Sr_{0.9}CoO_{3-\delta}$ NPD data. $\delta = 0.15$ is refined im $Pm3m$ space group and $\delta = 0.19, 0.27, 0.31$ are refined in $P4/mmm$. The site descriptions for the two symmetries are given in Table 3.1. χ^2 and R_{Bragg} are also shown.

	δ=0.15	δ=0.19	δ=0.27	δ=0.31
B-Factor				
Sr/Ho	0.98(03)	1.19(03)	1.16(03)	1.32(03)
Co	0.43(04)			
Co(1)		0.61(05)	0.48(04)	0.65(03)
Co(2)		0.61(05)	0.48(04)	0.65(03)
O	1.69(02)			
O(1)		0.76(07)	0.96(06)	1.25(06)
O(2)		2.23(13)	2.63(12)	2.50(11)
O(3)		3.39(15)	2.84(15)	3.55(13)
Occupation Occ.				
Sr/Ho	0.1/0.9	1.8/0.2	1.8/0.2	1.8/0.2
Co	1.0			
Co(1)		1.0	1.0	1.0
Co(2)		1.0	1.0	1.0
O	2.80(1)			
O(1)		1.89(2)	1.94(2)	1.92(2)
O(2)		1.50(2)	1.52(2)	1.49(2)
O(3)		2.04(5)	1.95(5)	1.92(5)
Normalized Occ. P				
O	0.93(1)			
O(1)		0.95(2)	0.97(2)	0.96(2)
O(2)		0.75(2)	0.76(2)	0.75(2)
O(3)		1.02(5)	0.98(5)	0.96(5)
z				
Sr/Ho		0.2582(5)	0.2574(4)	0.2565(5)
O(3)		0.2402(9)	0.2394(6)	0.2417(8)
Oxygen Content	2.80(1)	2.72(3)	2.71(3)	2.67(3)
a_p[Å]	3.8351(4)	3.8367(4)	3.8411(4)	3.8477(5)
χ^2	12.6	6.3	12.2	8.2
R_{Bragg}	4.1	4.8	5.1	5.6

| Atom	Multipl., Wyckoff Lett.	x	y	z
Ho/Sr	1a	0	0	0
Co	1b	0.5	0.5	0.5
O	3c	0	0	0.5
Ho/Sr	2h	0.5	0.5	z
Co1	1a	0	0	0
Co2	1b	0	0	0.5
O1	2f	0.5	0	0
O2	2e	0.5	0	0.5
O3	2g	0	0	z

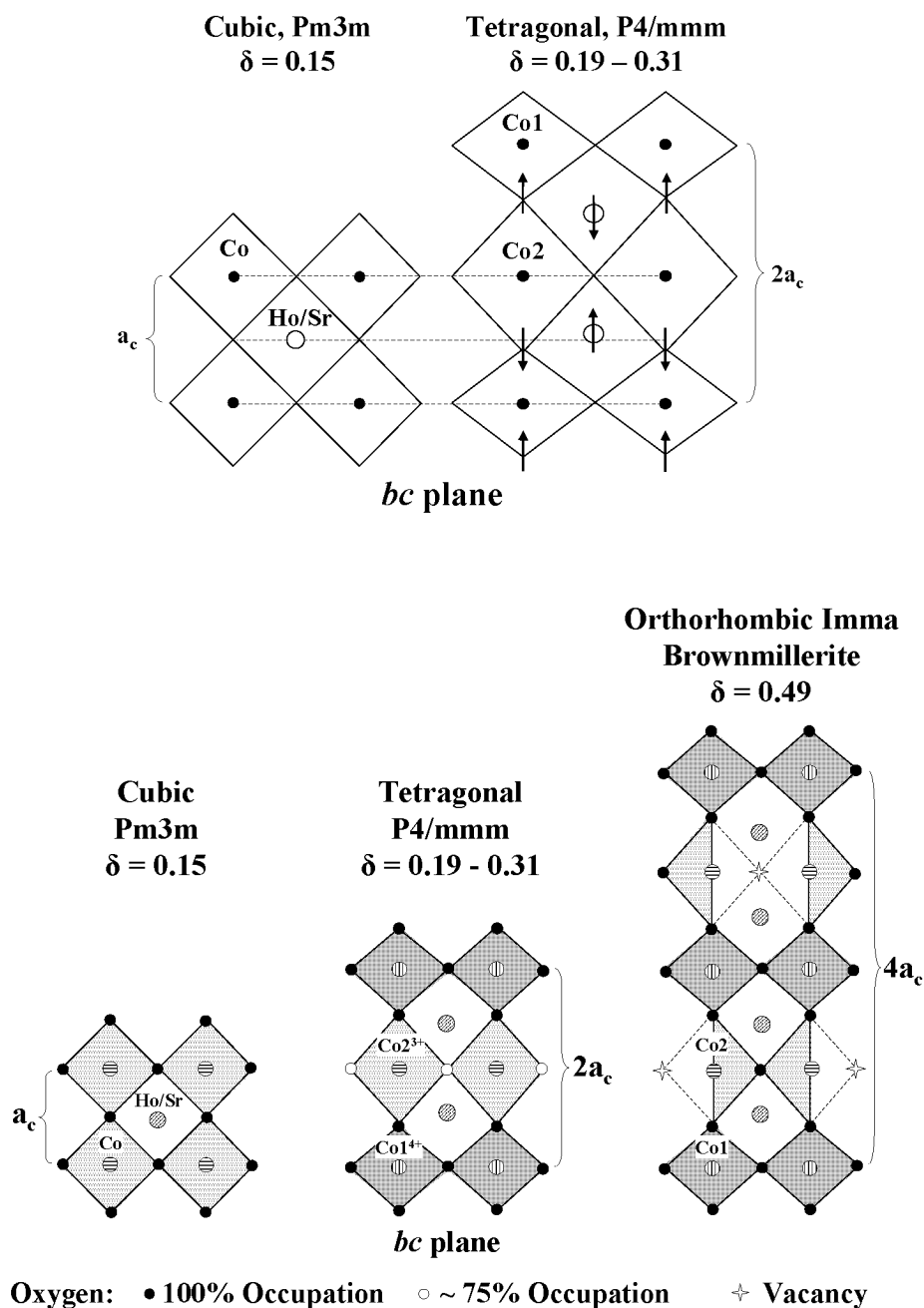**Table 3.1:** Site notation in the $Pm3m$ (top) and $P4/mmm$ (bottom) space group.
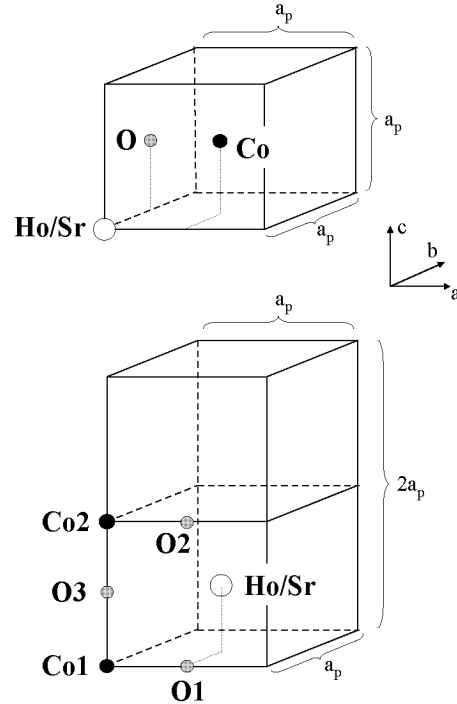
Figure 3.11: Site location in the $Pm3m$ (top) and $P4/mmm$ (bottom) space group.

cupancies of $\sim$ 75% compared with values close to 100 % at the other basal oxygen position O1 and the apical O3 sites (Table 3.2). Since such an oxygen ordering pattern displays $\mathbf{k} =$ (0 0 1/2) periodicity (as does oxygen displacement in the c-direction), it could be argued that oxygen ordering alone is responsible for the observed superstructure peaks. Rietveld refinements including either lattice parameter fluctuations or domain size effects showed, however, that the intensities of the new reflections could only be properly reproduced by allowing the apical oxygens and the Ho/Sr atoms to move away from the $Pm3m$ perovskite positions, see section 3.4.3.

This type of vacancy ordering is consistent with the behaviour observed for the other members of the series with larger oxygen deficiencies. The compounds with $\delta > 0.31$ display a closely related vacancy ordering pattern which, by approaching $\delta = 0.50$, gives rise to the so-called brownmillerite-type structure. In the $P4/mmm$ compounds, the ideally vacancy ordered composition is $\delta = 0.25$. Here 25 % of the oxygen sites of every second basal plane are unoccupied, reducing the effective Co2 coordination from 6 to 5. Due to the absence of x and y components in the observed k-vector ($\mathbf{k} = 0\ 0\ 1/2$), it is concluded that the oxygen vacancies are randomly distributed inside the basal planes. In the brownmillerite-related compounds($\delta \sim 0.50$), each second CoO_6 octahedron along the c direction becomes a tetrahedron due to the loss and the subsequent ordering of 50 % of its basal oxygens (Figure 3.13 (bottom) and Chapter 3.4.4). The Co coordination is in this case reduced from 6 to 4 and the vacancy ordering is described by an enlarged unit cell with $a = \sqrt{2}a_p$, $b = 4a_p$, $c = \sqrt{2}a_p$.
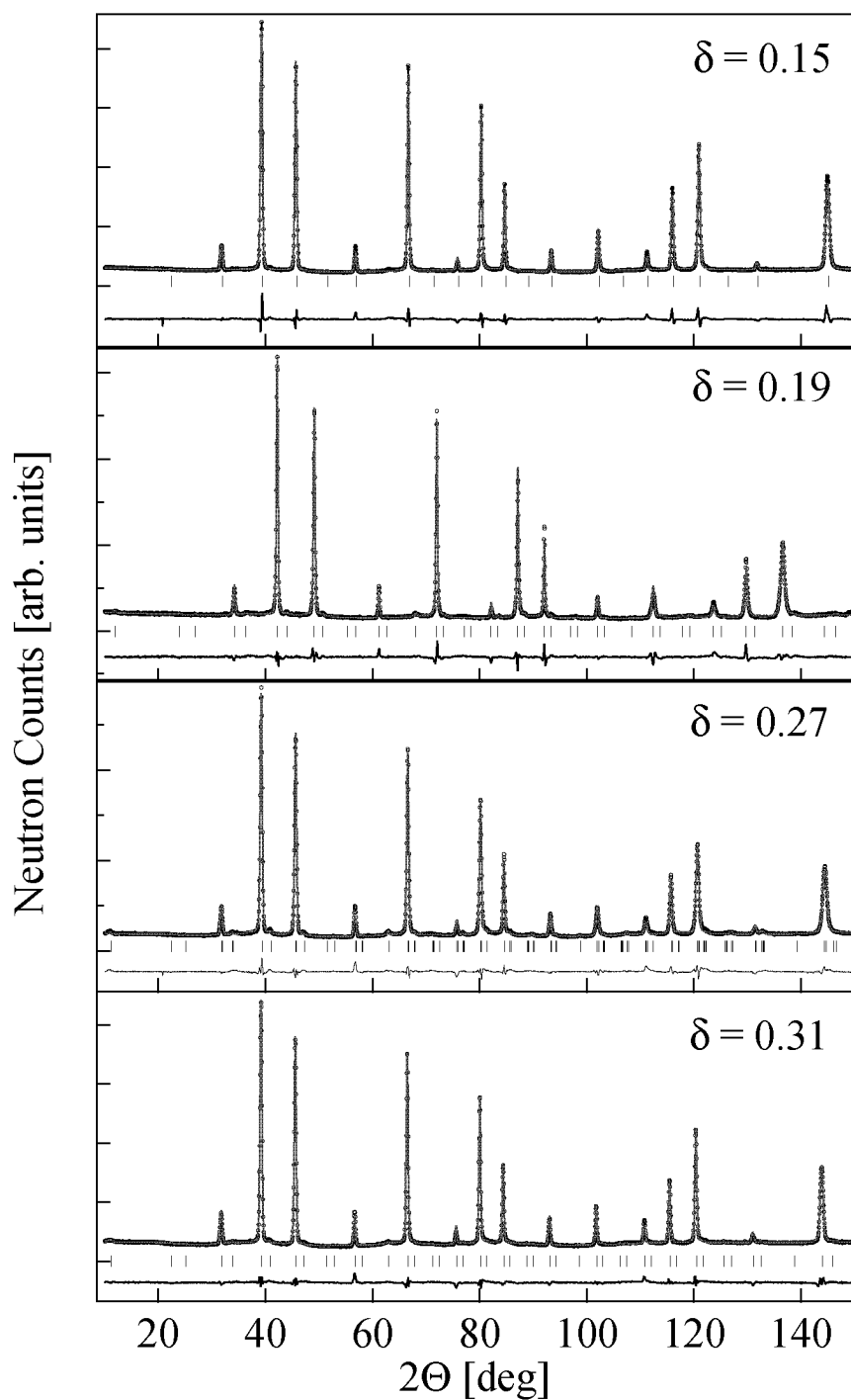
Figure 3.12: Room temperature neutron powder diffraction pattern for $Ho_{0.1}Sr_{0.9}CoO_{3-\delta}$ ($\delta = 0.15, 0.19, 0.27, 0.31$, top to bottom). The data for the $\delta = 0.15$ sample is refined in the cubic $Pm3m$ space group, while for other patterns the tetragonal $P4/mmm$ space group with the restriction $a = b = 2c$ is used. The ticks represent the locations of the nuclear reflections and the last line shows the difference between observed and calculated intensity.

Cubic, Pm3m
δ = 0.15

Tetragonal, P4/mmm
δ = 0.19 – 0.31

bc **plane**

Orthorhombic Imma
Brownmillerite
δ = 0.49

Cubic
Pm3m
δ = 0.15

Tetragonal
P4/mmm
δ = 0.19 - 0.31

bc **plane**

Oxygen: • 100% Occupation   ○ ~ 75% Occupation   ✦ Vacancy

Figure 3.13: Top: Comparison of the schematic cubic (left) and tetragonal (right) structures. Right: elongated/compressed octahedra due to shifts of the oxygen ions from their ideal position in the cubic cell. The Ho ions move in the opposite direction of the oxygen ions. The direction of the shifts is indicated by the arrows.
Bottom: Schematic representation of the three crystallographic structures displayed by $Ho_{0.1}Sr_{0.9}CoO_{3-\delta}$ as a function of the oxygen content. Note that oxygen loss only takes place in the basal planes.
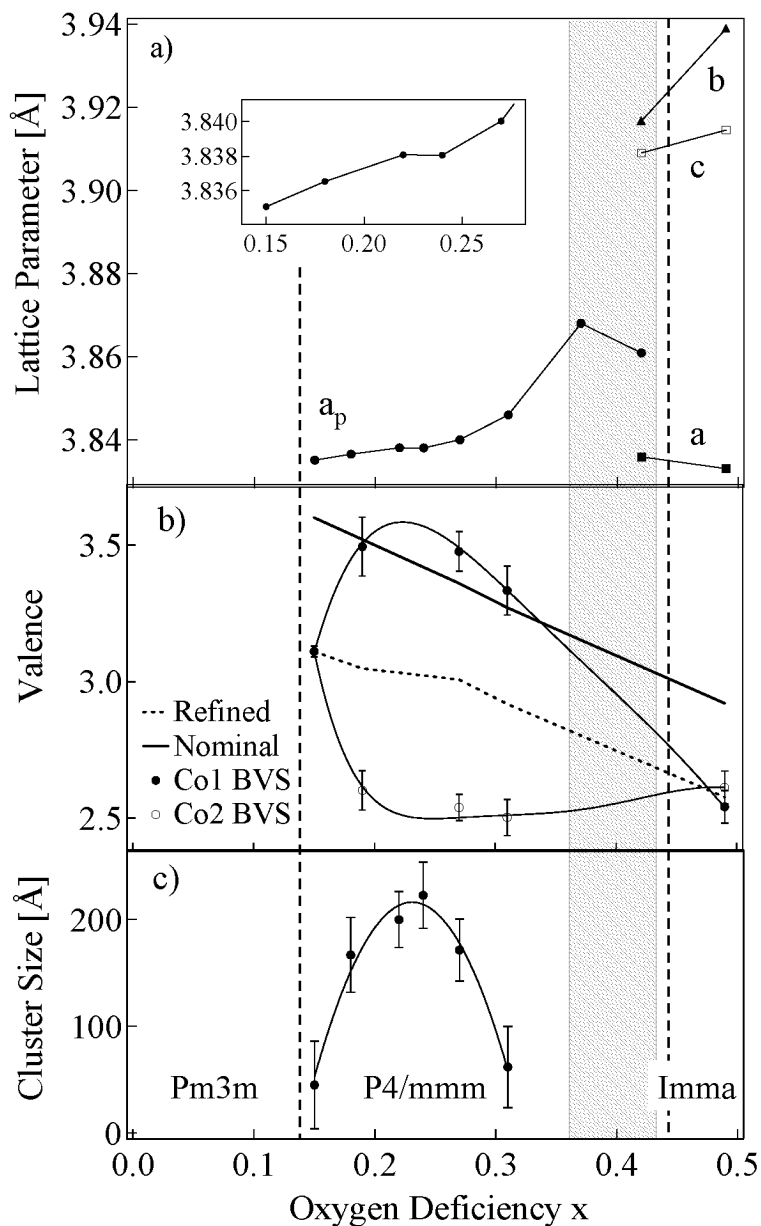
Figure 3.14: Oxygen deficiency dependence of a) the pseudocubic lattice parameters (where $a = a_{brown}/\sqrt{2}$, $b = b_{brown}/4$, $c = c_{brown}/\sqrt{2}$) (from XPD); b) the refined BVS for the Co1 and Co2 sites, the BVS site average (from NPD) and the nominal oxidation state; c) the apparent size D of the charge-ordered clusters (from XPD). Lines are guides to the eye. The vertical lines indicate the structural phase boundaries and the shaded area shows the region of phase co-existence.

3.4.2 $0.19 \leq \delta \leq 0.31$: Charge Order

Structural modulations involving the real-space ordering of ions with different nominal charges have been the subject of intensive investigations during the last two decades. These phenomena, usually denoted by the generic name of charge ordering (CO), appear for some particular compositions, generally corresponding to integer concentration ratios of the involved charge-ordered species. Although the stabilization of a charge-ordered state frequently gives rise to abrupt changes in either the transport or the magnetic properties of the material, the structural modifications associated to the spacial re-arrangement of the ions are in most cases unexpectedly weak. Perhaps the most remarkable example is provided by the half-doped manganites $R_{1/2}A_{1/2}MnO_3$ (R: trivalent ion, A: Ca or Sr), which contain nominally equal amounts of Mn^{3+} and Mn^{4+}. The existence of a Mn^{3+}/Mn^{4+} CO pattern, which was first proposed by Goodenough [93] in order to explain the unusual magnetic structure displayed by these compounds, was one of the major contributions leading to the setting up of the Goodenough-Kanamori-Anderson superexchange rules. Further powder [94, 95] and single crystal [96] neutron diffraction experiments confirmed the presence of superstructure peaks, which were refined using distortion patterns involving two or more Mn sites. However, the very similar average Mn-O distances associated to all of them gave rise to extremely close Bond Valence Sums[6] ($+3.53$ and $+3.50$, far from the expected $+4$ and $+3$ values). Fractional charges were also obtained from the analysis of single-crystal x-ray resonant scattering data [100, 101], suggesting a much weaker charge redistribution than that predicted by Goodenough.

A similar situation has been described for other perovskite-related systems containing nominally equal amounts of Fe^{3+}/Fe^{5+} ($CaFeO_3$) [102], Co^{2+}/Co^{3+} ($YBaCo_2O_5$) [103] and Ni^{2+}/Ni^{4+} ($YNiO_3$) [104]. Even if the stabilization of the CO state is accompanied in all cases by a sudden increase of the electrical resistivity (a metal-insulator transition in the case of $CaFeO_3$ and $YNiO_3$), the expected charge redistribution at T_{CO} has been found to be always partial. Hence, the reported Bond Valence Sums for the aforementioned compounds are $Fe^{4 \pm \delta}$, $Co^{2.5 \pm \delta}$ and $Ni^{3 \pm \delta}$, with $\delta \sim 0.5$, 0.3 and 0.3, respectively, considerably smaller than the ideal values $\delta = 1$, 0.5 and 1 values.

Although estimations of the ionic charges can be obtained from other techniques such as single crystal x-ray diffraction (through electron density maps), Mössbauer or x-ray spectroscopies, the results of the high resolution neutron powder diffraction analysis combined with the bond valence method [97, 98, 99] usually provide a good starting point to approach the problem. This is particulary true in the case of compounds with highly electronegative anions (as oxides and fluorides), as well as for systems exhibiting enough degrees of freedom in their crystallographic structure. Moreover, the relationship between the interatomic distances and bond valence, while extremely simple, has the advantage of providing a fast, straightforward, and (very often) extremely useful picture, which contrasts with extensive computing work necessary in the case of single crystal x-ray diffraction (especially in the case of twinned crystals) and with theoretical difficulties due to the interpretation of x-ray spectroscopies results.

As it was previously mentioned, the 1D structural modulation is observed for oxygen vacancy concentrations ranging from $\delta = 0.15$ to $\delta = 0.31$. The composition close to the center of the interval ($\delta = 0.19$) displays a formal Co oxidation state of $+3.52$. This value almost coincides with $+3.50$, which corresponds to an ideal 1:1 Co^{3+}/Co^{4+} ratio and an oxygen vacancy concentration of $\delta = 0.20$. This fact, together with the anomalies observed in the cell parameters (inset in Figure 3.14a), suggests the existence of Co^{3+}/Co^{4+} charge ordering for vacancy con-

---

[6]The Bond Valence Method relates cation-anion distances in a polyhedron (where the cation is surrounded by the anions) with the charge of the cation [97, 98, 99]. This method is explained in detail in Appendix A

centrations ~ 0.20 and motivated the exploration of the charge distribution on the Co1 and Co2 sites.

To estimate the valence of Co from the observed Co-O bond lengths, the bond valence sums (see Appendix A for details) are calculated according to the expression proposed by Altermatt and Brown [97, 98, 99]:

$$V_j = \sum_i \exp\left(\frac{R_0 - R_{ij}}{B}\right) \quad . \tag{3.1}$$

Here B and R_0 are tabulated parameters [99] ($R_0 = 1.692$ Å, 1.70 Å and 1.75 Å for Co^{2+}, Co^{3+} and Co^{4+} at RT respectively, $B = 0.37$ Å) and R_{ij} are the experimental Co-O bondlengths at RT, determined from the refined atomic positions. In our calculations we had to consider that the O2 site is not fully occupied, which leads to a mixture of 6 and 5 fold coordination for the Co2 site. The oxygen occupancies P (Table 3.2) had to be included in the above expression for the valences:

$$V_j = \sum_i P_i \exp\left(\frac{R_0 - R_{ij}}{B}\right) \quad . \tag{3.2}$$

The results are displayed in Table 3.3, together with the refined Co-O distances d, the average Co-O bondlengths $< d >$, the deviation δ of the refined site BVS from the average BVS and the distortion of the CoO_6 octahedra Δ_d in the charge-ordered phase ($\Delta_d = (d_{apical} - d_{basal}) \times 100$).

The refined lattice parameters from XPD are shown in Figure 3.14a). Their evolution with growing oxygen deficiency will be adressed later in this text. As shown in Figure 3.14b) the average BVS Co valences (<BVS>) are found to be lower than the values calculated from the nominal stoichiometry of the samples. This is a rather common observation in solid solutions and non stoichiometric materials. In the BVS formalism it means that the Co-O distances found experimentally are longer than expected. This is due to an imperfect description of the O and/or Ho/Sr distribution in the Rietveld refinements, which try to include into the Co-O bondlength the fluctuations coming from disorder.

The BVS valences for the individual Co1 and Co2 sites calculated from the results of the neutron diffraction Rietveld refinements are also shown in Figure 3.14b). In the $P4/mmm$ phase the difference between the Co valence at the compressed (Co1) and elongated (Co2) octahedral positions is remarkable. The largest disparity corresponds to $\delta = 0.19$, whose nominal oxidation state (+ 3.52) almost matches the ideal 1:1 Co^{3+}/Co^{4+} ratio value. In the compressed octahedra, the smaller average Co-O distance leads to an effective charge of $+3.48(11)$, 0.88 electrons smaller than in the elongated ones ($+2.60(7)$). By shifting these results in order to match the BVS average valence with the nominal oxidation state, $+3.95(11)$ and $+3.07(7)$ are obtained, which is very close to the ideal $+4.00$ and $+3.00$ values. Hence, these results are interpreted as evidence of a Co^{3+}/Co^{4+} charge-ordered state in this material.

In spite of the large number of studies dealing with $SrCoO_{3-\delta}$ and related systems, this is the first experimental evidence supporting the existence of charge ordering in these compounds. Only James et $al.$ have commented briefly on shorter average Co1-O bonds compared to the Co2-O ones in $Ln_{0.10}Sr_{0.90}CoO_{3-\delta}$ [85] and suggest the possibility of charge order.

An explanation for the nearly complete charge order in $Ho_{0.1}Sr_{0.9}CoO_{3-\delta}$ ($0.19 \le \delta \le 0.31$) may be the extremely simple distortion pattern displayed by these compounds. When comparing it to the much more complex arrangement of charges observed in systems as $R_{1/2}Ca_{1/2}MnO_3$ or $YNiO_3$, it is evident that the elastic energy necessary to accommodate the two Co^{3+} and Co^{4+}

Table 3.3: Individual d and average $< d >$ Co-O distances; refined, average, nominal and normalized BVS; deviations δ of site BVS from average BVS and distortions Δ_d ($\Delta_d = (d_{apical}\text{-}d_{basal})\times 100$) based on NPD measurements. No. indicates the number of bonds of this kind.

		δ=0.15
$d_{Co(1)-O(1)}$	No.=6	1.9175(01)
$< d_{Co(1)-O} >$		1.9175(01)
BVS $Co(1)$		3.11(02)
$< BVS >$		3.11(02)
Nominal value		3.60
shifted BVS $Co(1)$		3.60(02)

		δ=0.19	δ=0.27	δ=0.31		δ=0.49
$d_{Co(1)-O(1)}$	No.=4	1.9183(01)	1.9205(01)	1.9238(1)	No.=4	1.9406(01)
$d_{Co(1)-O(3)}$	2	1.8434(67)	1.8392(46)	1.8602(63)	2	2.2491(14)
$< d_{Co(1)-O} >$		1.8933(16)	1.8934(08)	1.9026(15)		2.0434(02)
$d_{Co(2)-O(2)}$	4	1.9183(01)	1.9205(01)	1.9238(01)	2	1.8045(19)
$d_{Co(2)-O(3)}$	2	1.9933(67)	2.0019(46)	1.9874(63)	1	1.8638(50)
$d_{Co(2)-O(3)}$					1	1.9403(50)
$< d_{Co(1)-O} >$		1.9433(16)	1.9476(08)	1.9450(15)		1.8533(13)
BVS $Co(1)$		3.48(11)	3.48(07)	3.33(09)		2.54(06)
BVS $Co(2)$		2.60(07)	2.54(05)	2.50(07)		2.61(06)
$< BVS >$		3.05(09)	3.00(06)	2.92(08)		2.58(06)
Nominal value		3.52	3.36	3.27		2.92
norm. BVS $Co(1)$		3.95(11)	3.84(07)	3.68(09)		2.87(06)
norm. BVS $Co(2)$		3.07(07)	2.90(05)	2.85(07)		2.95(06)
δ		0.51(2)	0.52(1)	0.47(1)		0.04(1)
$\Delta_d(Co(1))$ [%]		-7.49(7)	-8.13(5)	-6.36(7)		
$\Delta_d(Co(2))$ [%]		7.50(7)	8.14(5)	6.36(7)		

octahedra in an one-dimensional $\mathbf{k} = (0\ 0\ 1/2)$ distortion pattern should be smaller than those needed to arrange the Ni^{2+} and Ni^{4+} octahedra of $YNiO_3$ in the observed three-dimensional $\mathbf{k}$ = $(1/2\ 1/2\ 1/2)$ array. An even less favourable situation is found in manganese perovskites, where the difference between the distortions of the nearly perfect Mn^{4+} and the Jahn-Teller distorted Mn^{3+} octahedra are so large that a 3D arrangement of these objects is topologically impossible without "relaxing" the degree of charge ordering or, in other words, its associated distortions.

3.4.3   Size Effect versus Strain Effect

As mentioned in the previous sections, the $P4/mmm$ superstructure reflections display a pronounced broadening which is absent in the fundamental reflections of the $Pm3m$ parentage. The difference between the superstructural and the nuclear reflections can be seen in Figure 3.10. Two possible origins can be considered to explain this extra broadening: On one side, the fluctuations of the cell parameter c as a consequence of the partial ordering of the oxygen vacancies along this direction (strain effect). On the other, the stabilization of the $(0\ 0\ 1/2)$ distortions associated to the charge ordering over clusters of finite size (size effect). Since these two mechanisms imply completely different dependencies of the extra broadening on the scattering angle, it is possible to distinguish between them by including the appropriated expressions in the analysis of the Rietveld profiles. In the case of most neutron diffractometers, the Bragg reflection profiles can be described by pseudo-Voigt (pV) functions, that is, linear combinations of Lorentzians (L) and Gaussians (G) of the form

$$pV = \eta L + (1 - \eta)G, \qquad 0 \le \eta \le 1. \tag{3.3}$$

The contribution of the strain effects is given by the following expression, to be added to the full width half maximum (FWHM) of the Gaussian component

$$(H_G^{strain})^2 = D_{strain}^2(hkl)\tan^2\Theta. \tag{3.4}$$

Hence,

$$(H_G^{observed})^2 = (H_G^{instrumental})^2 + (H_G^{strain})^2. \tag{3.5}$$

In the case of size effects, the extra broadening appears in the Lorentzian component and has the form

$$H_L^{size} = \frac{F_{size}(hkl)}{\cos\Theta}. \tag{3.6}$$

In consequence

$$H_L^{observed} = H_L^{instrumental} + H_L^{size}. \tag{3.7}$$

Since $H_G^{instrumental}$ and $H_L^{instrumental}$ are known, the particular (hkl) dependence of the strain and size broadenings come into the $D_{strain}(hkl)$ and $F_{size}(hkl)$.

In the case of microstrain broadening, the formalism developed by Rodríguez-Carvajal $et\ al.$ [105] is used. In the present case (fluctuations of the cell parameter c) $D_{strain}(hkl)$ can be written as

$$D_{strain}(hkl) = \tan\Theta \times \frac{4l^2\epsilon_{strain}\sqrt{2\ln 2}}{h^2(c/a)^2 + k^2(c/b)^2 + l^2} \quad . \tag{3.8}$$
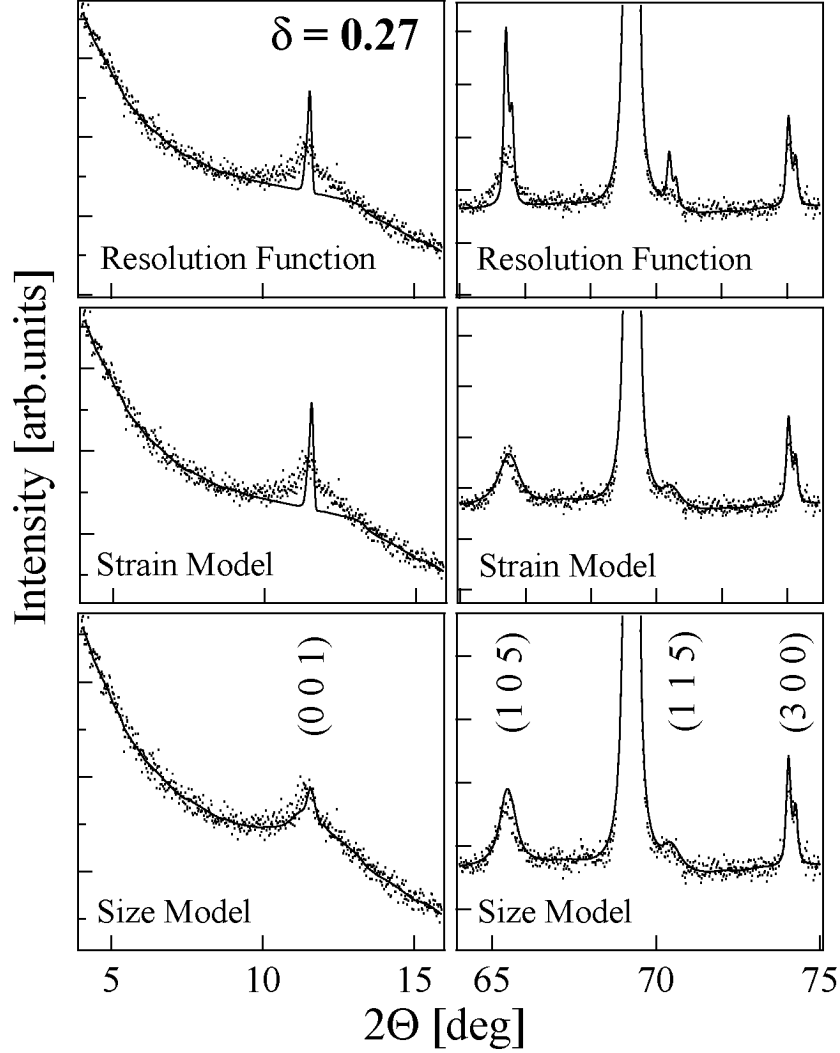
Figure 3.15: Neutron powder diffraction patterns for $Ho_{0.1}Sr_{0.9}CoO_{3-\delta}$ ($\delta = 0.27$) fit with different models. Top: Using just the resolution function. Middle: Fit obtained using the strain model. Bottom: Using the size effect model. Note that the reflections are broadened at low *and* high 2Θ.

where ϵ_{strain} is the weighted average strain. This expression, which is zero for reflections with $l = 0$ (no extra peak broadening), introduces just one additional parameter in the Rietveld refinements ($\epsilon_{strain} = \sigma_{strain}/c$), whose refined value gives information about the standard deviation σ_c of the c parameter distribution.

To describe the size broadening effects, which are assumed to be (hkl)-independent ($\equiv$ spherical diffraction domains), we used $F_{size} = 2\lambda/\pi D_{size}$, which, replaced into Equ. 3.6, gives us the well known Scherrer formula

$$H_L^{size} = \frac{2\lambda}{\pi D_{size} \cos \Theta},$$ (3.9)

where λ is the wavelengh of the neutrons and the apparent size D_{size} is the volume weighted crystallite size perpendicular to the (hkl) plane (in [Å]) [106]. As in the strain case, this

formalism introduces a single additional parameter D_{size} in the Rietveld refinements.

The results obtained using both models are shown in Figure 3.15. The better agreement of the size model is evident, especially at low angles, where the different 2Θ-dependences of the strain and size corrections ($\tan\Theta$ and $1/\cos\Theta$, respectively) are strongest. Hence, we conclude that the origin of the extra broadening is the development of a Co^{3+}/Co^{4+} charge-ordered state over clusters of finite size. The refined values of D_{size}, which range between 50 and 250 Å, are displayed in Figure 3.14c. A clear maximum is observed for $\delta = 0.23$, close to the ideal 1:1 Co^{3+}/Co^{4+} concentration $\delta = 0.20$. It also coincides with the anomaly in the cell parameters and the distortion parameter of the CoO_6, confirming the charge-ordering origin of the broadening.

Since, as we report in the previous sections, the Co^{3+}/Co^{4+} charge ordering in these materials is nearly perfect, the non-observation of a long-range charge-ordered state seems puzzling. A possible explanation may be the competition between the ordering of the oxygen vacancies and that of the Co^{3+}/Co^{4+} species, which, due to the Ho doping, are expected to occur at different oxygen vacancy concentrations ($\delta = 0.25$ and $\delta = 0.20$, respectively). As shown in Figure 3.14b, the maximum size of the charge ordered domains is not found for $\delta = 0.20$ but for $\delta = 0.23$, that is, a composition in between 0.20 and 0.25.

3.4.4 $0.34 \leq \delta \leq 0.49$: Brownmillerite Type Structure

Close inspection of the neutron and x-ray diffraction patterns of $Ho_{0.1}Sr_{0.9}CoO_{3-\delta}$ with $\delta = 0.37$ and 0.42 revealed that these samples were not single-phase. The RT data could only be reasonably refined by assuming the existence of two phases: One (majoritary) with tetragonal $P4/mmm$ symmetry as in the materials discussed in the previous sections, and a second one (minoritary) with orthorhombic, brownmillerite-type $Imma$ symmetry, which, as it will be shown later, is adopted by the most oxygen-defective material studied in this work ($\delta = 0.49$). The weight ratio of the tetragonal to the orthorhombic phase is estimated to be about 5:1 for $\delta = 0.42$. The fit for $\delta = 0.42$ obtained for the NPD data is shown in Figure 3.16 (top).

Due to the strong correlations between the structural parameters of both phases, the values of the atomic coordinates, the occupancies and the Debye-Waller factors of all atoms were fixed to those found in the neighbouring single-phase compounds ($\delta = 0.31$ and $\delta = 0.49$). The lattice parameters could then be reasonably fitted. The refined values of the pseudocubic lattice parameters are displayed in Figure 3.14a).

The $\delta = 0.49$ compound displays much more complex x-ray and neutron powder diffraction patterns than those of the $P4/mmm$ samples (Figure 3.16 bottom). The new reflections could be indexed with a $\sqrt{2}a_p \times 4a_p \times \sqrt{2}a_p$ supercell (Figure 3.13), which corresponds to the brownmillerite-type structure (note the different orientation of the crystallographic axes with respect to the $P4/mmm$ unit cell). Two different orientations of the tetrahedra are possible [78, 107, 108, 109]. Following Greaves et al. [109] we chose the centrosymmetric space group $Imma$ was chosen. As shown in Table 3.4, it describes the two possible orientations using a single Wyckoff position (8i) for Co2 with only half occupation. Using this space group, an excellent fit between the $Ho_{0.1}Sr_{0.9}CoO_{2.51}$ NPD data and the calculated profile was achieved (Figure 3.16 and Table 3.4).

By increasing δ, a continuous decrease of the difference between the BVS valences at the two $P4/mmm$ Co ion sites is observed, indicating a progressive melting of the charge-ordered state. At $\delta = 0.49$, both Co sites display almost identical oxidation states (2.88 and 2.96, see Table 3.3), in spite of their different coordinations (octahedral and tetrahedral), in agreement with previous studies on $Sr_2Co_2O_5$ [110].
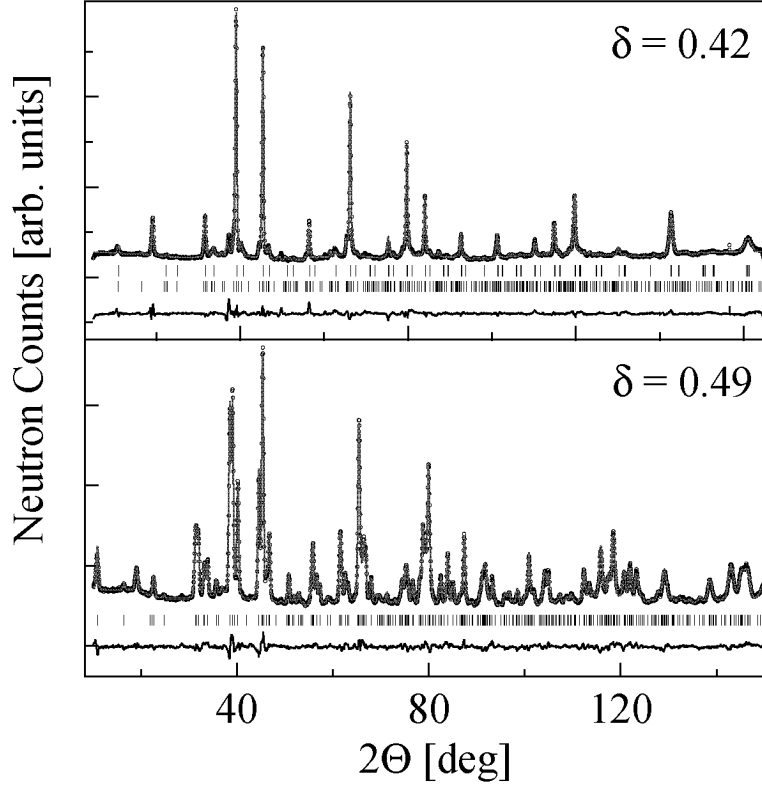
Figure 3.16: Room temperature neutron powder diffraction pattern for the $Ho_{0.1}Sr_{0.9}CoO_{3-\delta}$ compounds with $\delta = 0.42$ (top) and 0.49 (bottom). The $\delta = 0.42$ material is in a two phase state and the data is refined using both tetragonal $P4/mmm$ (top ticks) and orthorhombic $Imma$ (bottom ticks) space groups. The sample with $\delta = 0.49$ is single phase with space group $Imma$. The ticks represent the locations of the nuclear reflections and the last line shows the difference between observed and calculated intensity.

Table 3.4: Crystallographic parameters derived from the $Ho_{0.1}Sr_{0.9}CoO_{3-\delta}$ NPD data: For the orthorhombic $Imma$ ($\delta = 0.49$) the sites are: Sr/Ho 8h (0.5 y z); Co1 4a (0 0 0); Co2 8i (x 0.25 z); O1 8g (0.25 y 0.25); O2 8h (0 y z); O3 8i (x 0.25 z). χ^2 and R_{Bragg} are also shown.

|	B	Occ.	Norm. Occ. P	x	y	z
			$\delta = 0.49$			
Sr/Ho	0.82(2)	7.2/0.8			0.1102(1)	0.0103(3)
Co(1)	1.09(6)	4.0				
Co(2)	1.09(6)	4.0		0.9597(9)		0.9423(7)
O(1)	0.96(2)	8.0	1.0		0.9935(1)	
O(2)	1.36(2)	8.0	1.0		0.1419(1)	0.0423(3)
O(3)	1.25(5)	4.1(2)	0.51(2)	0.6244(5)		0.8688(5)
Oxygen Cont.	2.51(1)					
$a_p[Å]$				3.8331(4)	3.9390(5)	3.9146(4)
χ^2	6.31					
R_{Bragg}	4.89					
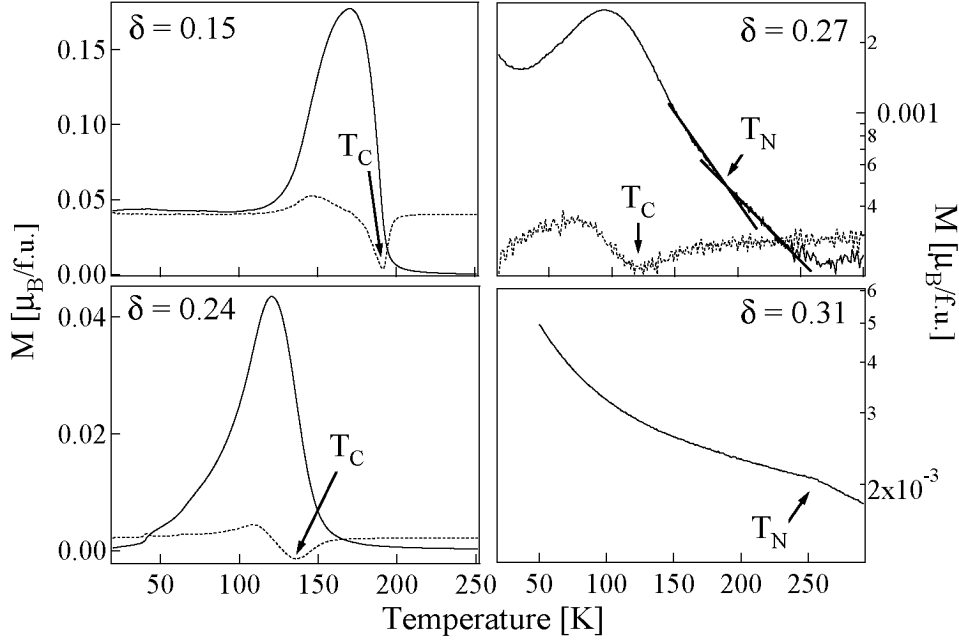
Figure 3.17: ZFC magnetisation data for $Ho_{0.1}Sr_{0.9}CoO_{3-\delta}$ ($\delta = 0.15, 0.27$ with $H = 0.01\,T$ and $\delta = 0.24, 0.31$ with $H = 0.1\,T$). The broken lines represent the first derivation of the magnetization curves (dM/dT), from which T_C was determined. Magnetic transition temperatures T_C and T_N are marked by arrows.

3.5 $Ho_{0.1}Sr_{0.9}CoO_{3-\delta}$: Magnetic Structure

In this Section a systematic investigation of the magnetic properties of the $Ho_{0.1}Sr_{0.9}CoO_{3-\delta}$ series ($0.15 \leq \delta \leq 0.49$) by means of neutron powder diffraction and bulk magnetization measurements is presented. We have determined the evolution of the zero-field magnetic structures and the spin state of the different Co species across the series. We discuss the relevant magnetic coupling mechanism for each composition in the framework of the current exchange theories in oxides. The structural properties can be found in the previous Section 3.4.

The neutron powder diffraction data for the samples with $\delta = 0.15, 0.27, 0.31, 0.42, 0.49$ (prepared as described in Section 3.3) were collected on the high-resolution powder diffractometer HRPT [48] at the neutron spallation source SINQ of the Paul Scherrer Institute, Switzerland. The measurements were performed at $T = 10$ and 300 K in the angular range $5° < 2\Theta < 165°$ with 2Θ steps of $0.05°$, using a wavelength $\lambda = 1.494\,\text{Å}$. Additional NPD measurements were performed at the high intensity diffractometer D20 at ILL, France for the $\delta = 0.19, 0.24$ compounds. Here data were taken between $3\,K < T < 300\,K$ at a constant heating rate of $0.03\,K/sec$, using a wavelength $\lambda = 2.40\,\text{Å}$ ($8° < 2\Theta < 140°$). All NPD data were analyzed using the Rietveld program FullProf [56]. Bulk magnetization measurements were performed on a Quantum Design PPMS device in the temperature range from 2 to 350 K. Temperature dependent NPD across the magnetic transition was performed on DMC, PSI to determine the transition temperatures T_N for the samples with $\delta = 0.27, 0.42, 0.49$. We used $\lambda = 2.56\,\text{Å}$ and measured in the angular range $5° \leq 2\Theta \leq 85.5°$ with temperature ranging between 1.5 and 560 K.

Zero field cooled (ZFC) magnetization measurements for the samples $\delta = 0.15, 0.24, 0.27$ and 0.31 are shown in Figure 3.17. The measurements reveal a strong signal for oxygen deficient
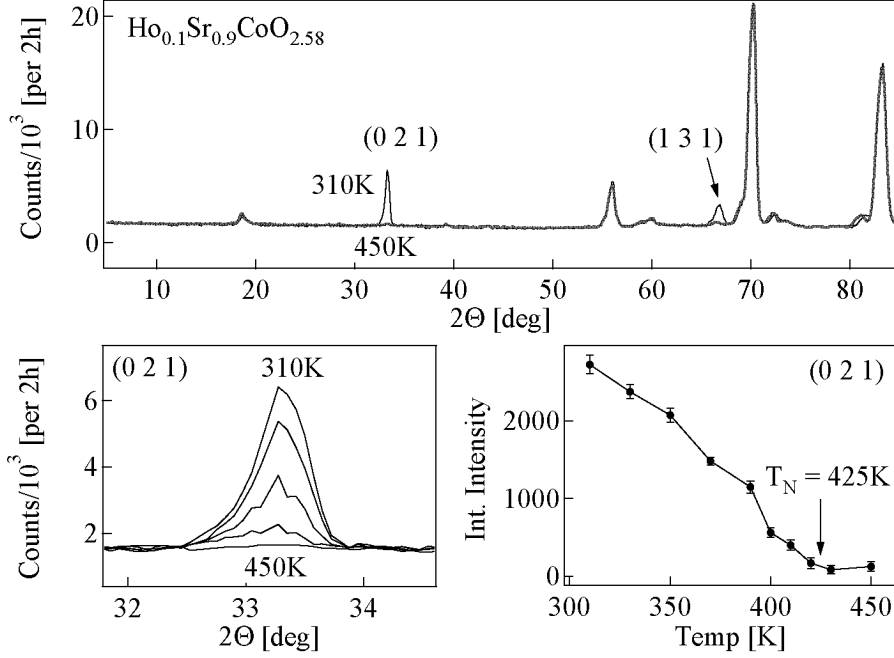
Figure 3.18: Top: NPD measurements for $Ho_{0.1}Sr_{0.9}CoO_{2.58}$ at $T = 310$ and 450 K. Bottom left: temperature evolution of the (0 2 1) peak. Bottom right: temperature dependent integrated intensity of the peak (0 2 1), T_N denotes the onset of the AFM phase.

Table 3.5: Magnetic transition temperatures and magnetic moments (at 10K) for the series $Ho_{0.1}Sr_{0.9}CoO_{3-\delta}$ ($0.15 \leq \delta \leq 0.49$).

	0.15	0.19	0.24	0.27	0.31	0.42	0.49
T_C [K]	185(5)	160(5)	140(5)/170(10)	125(5)			
T_N [K]		180(10)	230(10)	186(10)	256(5)	425(10)	530(10)
μ_{Co1}^{xy} $[\mu_B]$	1.17(2)			0.76(3)	1.95(4)		3.03(2)
μ_{Co2}^{xy} $[\mu_B]$				0.95(3)	1.64(4)		2.40(2)
$< \mu_{Co}^{xy} >$ $[\mu_B]$				0.85(3)	1.80(4)		2.71(2)
μ_{Co}^{z} $[\mu_B]$				0.33(5)	0.28(7)		

samples $\delta \leq 0.27$, which suggest FM ordering. However, since the signal is only present at intermediate temperatures, it is more probable that these compounds are cluster glasses with FM correlations within the clusters (more details in Chapter 3.5.1). For higher deficiencies ($0.31 \leq \delta \leq 0.49$) the response becomes weak. This suggests that the more oxygen deficient samples are AFM ordered. The transition temperatures T_N shifts to above 300 K (out of the range of our PPMS) for $\delta = 0.42, 0.49$, therefore we performed temperature dependent NPD on these two samples (Figure 3.18 for the $\delta = 0.42$ compound). The obtained transition temperatures T_C and T_N are given in Table 3.5.

3.5.1   Ferromagnetic ordering: $\delta = 0.15$

In Figure 3.19 we show the 10 K and RT diffraction pattern for $Ho_{0.1}Sr_{0.9}CoO_{2.85}$. A strong increase of the intensity of the low-angle reflections is seen at 10 K. According to Equ. 2.10 in Chapter 2.1.2 this is clear evidence for FM order. The 10 K magnetic reflections can be indexed with a propagation vector $\mathbf{k}_{FM} = (0\ 0\ 0)$ and we find that the FM coupled Co moments lie in the ab-plane (Figure 3.22, top). The value of the refined magnetic moment (μ_{Co}=1.17(2)μ_B) is lower than reported by Taguchi $et\ al.$ [79] and Takeda $et\ al.$ [111] for $SrCoO_3$ (μ_{Co}=1.55 and 1.60 μ_B, respectively), but agrees with the value (1.04 μ_B) obtained by Watanabe $et\ al.$ [112] for $SrCoO_{2.84}$.

The zero field cooled (ZFC) and field cooled (FC) magnetization measurements (Figure 3.20 left) in $H = 0.01$ T show that the system behaves like a cluster glass[7]: a magnetic field is needed to align the Co ion magnetic moments in different clusters. The transition temperature T_C therefore indicates the temperature where the system enters a state with a spontaneous magnetic moment (as is also found for the layered cobaltites, see Chapter 4.3.1). A cluster glass state has also been proposed for $La_{1-x}Sr_xCoO_3$ by Itoh $et\ al.$ [74]. The field dependent magnetization curves measured at 10 and 150 K are shown in Figure 3.20, right. The curve at 150 K, measured in the state with the spontaneous magnetic moment, is typical for a ferromagnet: the magnetization shows a steep rise below $H < 0.15$ T and reaches a saturation value of 1.25(1) μ_B. However, the hysteris curve measured 10 K in the cluster glass phase, shows an anomaly around 0.15 T (inset in Figure 3.20, right). This is related to the uncorrelated magnetic clusters which become aligned at a magnetic field of $H \sim 0.15$ T. At 10 K the saturation magnetic moment per formula unit is 1.94(1) μ_B. This value is higher than the one obtained by neutrons (1.17(2) μ_B), but this can be due to an ordering of the Ho ions, which possess a large total momentum.

### 3.5.2   Antiferromagnetic ordering: $\delta \geq 0.27$

Several new distinct reflections appear in the low angle region of the NPD pattern for $Ho_{0.1}Sr_{0.9}CoO_{3-\delta}$ ($\delta = 0.27, 0.31$) (Figure 3.21). The new reflections can be indexed with a propagation vector $\mathbf{k}_{AFM} = (1/2\ 1/2\ 0)$, which describes a G-type AFM ordered magnetic phase, where the Co magnetic moments are coupled AFM with their six nearest neighbours (Figure 3.22 bottom). We find that the Co spins lie in the ab-plane (for magnetic moment values see Table 3.5). Close inspection of the NPD pattern reveals a low angle peak (indexed as $(1/2\ 1/2\ 0)$ in $P4/mmm$ notation), which does not exist at RT (Fig. 3.21, right) and which is forbidden by the in-plane G-type magnetic structure. Group theory analysis of the propagation vector group G_k shows that the possible symmetry-allowed magnetic structures require the magnetic moments to be either in the ab-plane or along the c-axis. We find that the actual magnetic structure corresponds to a slightly out-of-plane array, which can be described as a mixture of a G-type AFM structure with moments in the ab-plane and a C-type AFM structure (AFM in the ab-plane and FM along the c-axis) with the magnetic moment along the c-direction. The schematic magnetic structure, which is not collinear, is shown in Figure 3.22 (middle). The value of the magnetic moment out of the plane are given in Table 3.5. The angle between the magnetic moments of two adjacent planes is $\gamma = 137.4(6)°$ and 161.9(9)° for $\delta = 0.27$ and 0.31, respectively (Figure 3.22, middle).

Temperature dependent NPD performed on $\delta = 0.27$ shows that the strongest AFM reflection

---

[7]A cluster glass is so named, because small clusters of magnetic moments achieve their own short-range magnetic order, but frustration between different magnetic interactions (e.g. FM and AFM) prevents long-range magnetic correlation between different clusters.
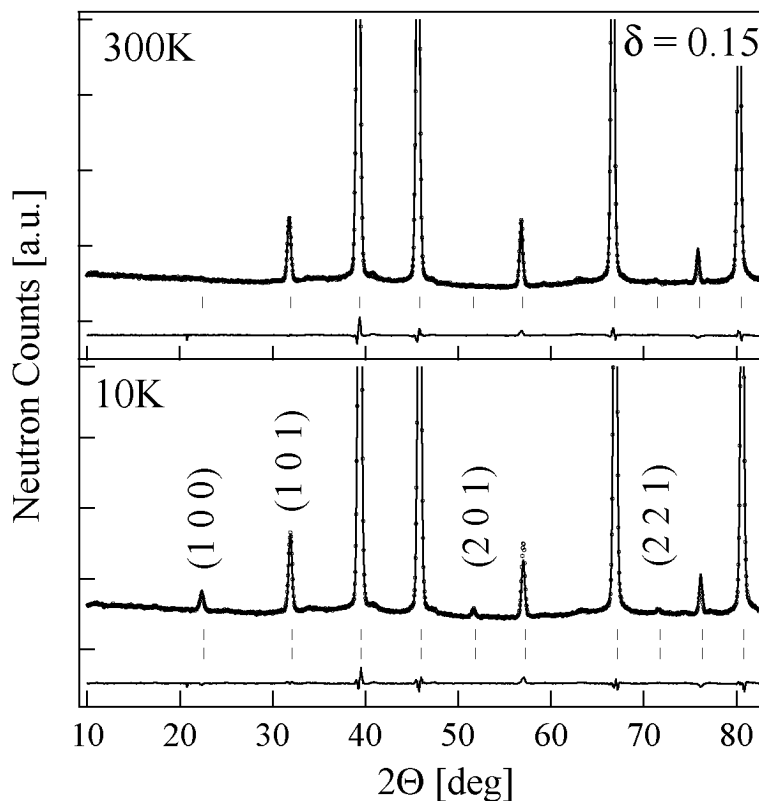
Figure 3.19: Observed, calculated and difference NPD patterns for $Ho_{0.1}Sr_{0.9}CoO_{2.85}$ ($x = 0.15$) at RT (top) and 10 K (bottom). Ticks | indicate peak positions (nuclear $Pm3m$ and magnetic, from top to bottom). The indices of the strongest magnetic reflections are given (in $Pm3m$ symmtery).
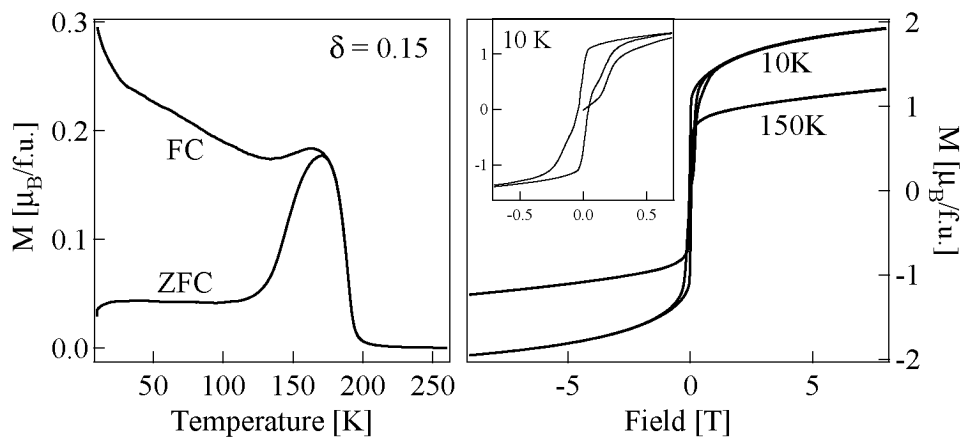
Figure 3.20: Left: ZFC and FC temperature dependent magnetization for $Ho_{0.1}Sr_{0.9}CoO_{2.85}$ ($H = 0.01$ T); Right: field dependent magnetization for $Ho_{0.1}Sr_{0.9}CoO_{2.85}$ at $T = 10$ and 150 K.
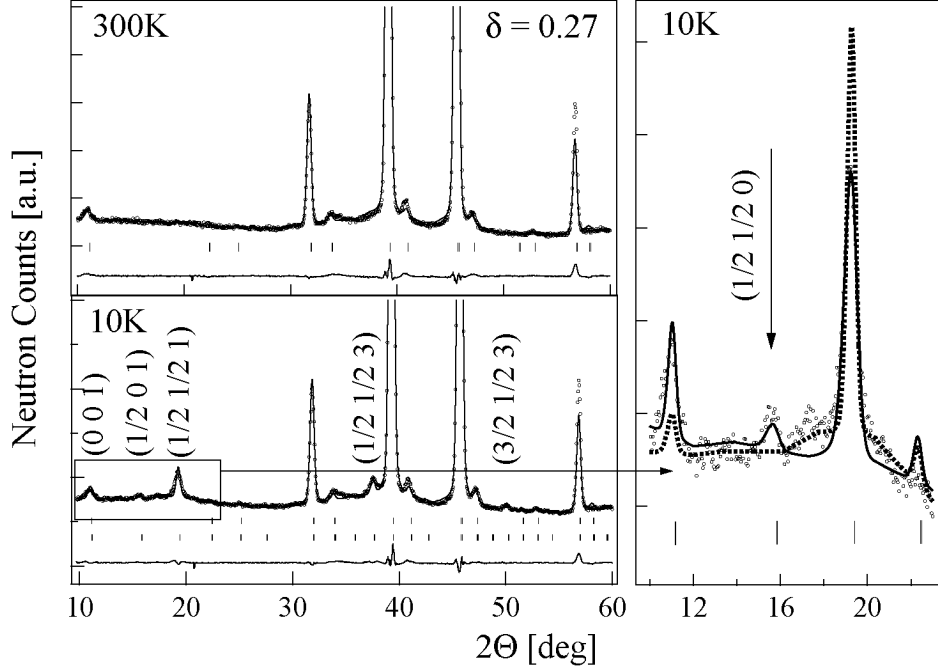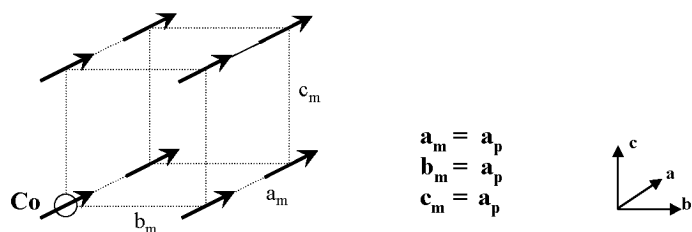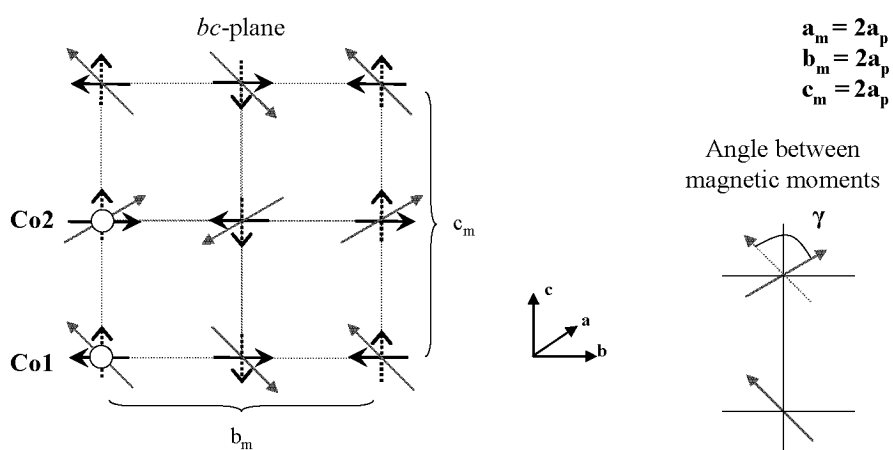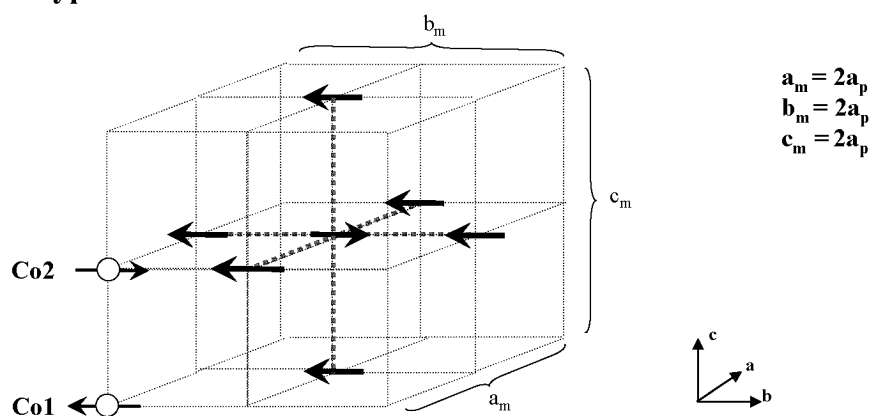
Figure 3.21: Left: Observed, calculated and difference NPD pattern for $Ho_{0.1}Sr_{0.9}CoO_{2.73}$ at RT (top) and 10 K (bottom). Ticks | indicate peak positions (nuclear $P4/mmm$ and magnetic, from top to bottom). The indices of the strongest magnetic reflections are given ($P4/mmm$ symmetry). Right: close up of the peak resulting from the C-type AFM order (arrow). The dotted line is a fit with a simple G-type AFM ordering model, while the solid line is a fit with a model including both G-type and C-type AFM order.

(1/2 1/2 1) disappears at $T_N = 180(10)$ K (Figure 3.23). Bulk magnetisation measurements give values of $T_N = 186(10)$ K for $\delta = 0.27$ and 256(5) K for $\delta = 0.31$ (Figure 3.17), the former in agreement with our NPD data.

Increasing oxygen deficiency to $\delta = 0.42, 0.49$ fully suppresses the c-direction component of the Co-ion spin, but does not affect the G-type AFM ordering. The NPD patterns at 10 and 300 K for $\delta = 0.49$ are shown in Figure 3.24. The transition temperature T_N is raised above RT to $T_N = 425$ (530) K for $\delta = 0.42$ (0.49). This is consistent with T_N between 545 and 570 K found for the parent compound $SrCoO_{2.5}$[78, 83]. As in the tetragonal phase, the magnetic moments lie in the ac plane (corresponding to ab in the $P4/mmm$ setting). Hence, once the cubic symmetry is lost, the easy magnetization direction lies in the basal plane of the CoO_6 and CoO_5 polyhedra. To be noted is the remarkable stability of the easy plane of the Co magnetic moments, which subsists within a large compositional region ($0.19 \leq \delta \leq 0.49$), even after creation of ordered oxygen vacancies in the planes (as in the brownmillerite structure). The refined magnetic moments are given in Table 3.5.

3.5.3   Coexistence of FM and AFM ordering: $0.19 \leq \delta \leq 0.24$

The NPD patterns for the samples with oxygen deficiency $0.19 \leq \delta \leq 0.24$ show no structural changes when lowering the temperature to 10 K. However, the appearance of two distinct magnetic reflections at low angles is clearly observed (Figure 3.25). For one, a gaussian reflection

FM order: δ = 0.15

$\mathbf{a_m} = \mathbf{a_p}$
$\mathbf{b_m} = \mathbf{a_p}$
$\mathbf{c_m} = \mathbf{a_p}$

G-type AFM order with C-type AFM component: δ = 0.27, 0.31

bc-plane

$\mathbf{a_m} = 2\mathbf{a_p}$
$\mathbf{b_m} = 2\mathbf{a_p}$
$\mathbf{c_m} = 2\mathbf{a_p}$

Angle between
magnetic moments

γ

G-type AFM order: δ = 0.49

$\mathbf{a_m} = 2\mathbf{a_p}$
$\mathbf{b_m} = 2\mathbf{a_p}$
$\mathbf{c_m} = 2\mathbf{a_p}$

Figure 3.22: Schematic picture of the magnetic structure in $Ho_{0.1}Sr_{0.9}CoO_{3-\delta}$. Top: $\delta = 0.15$, cluster glass with FM order within the clusters; Middle: $\delta = 0.27, 0.31$, G-type AFM order with a C-type AFM component. Only the bc-plane is shown; Bottom: $\delta = 0.49$, pure G-type AFM order. All magnetic moments couple AFM to their neighbours, as shown for the central moment. For better visibility, not all magnetic moments are shown.
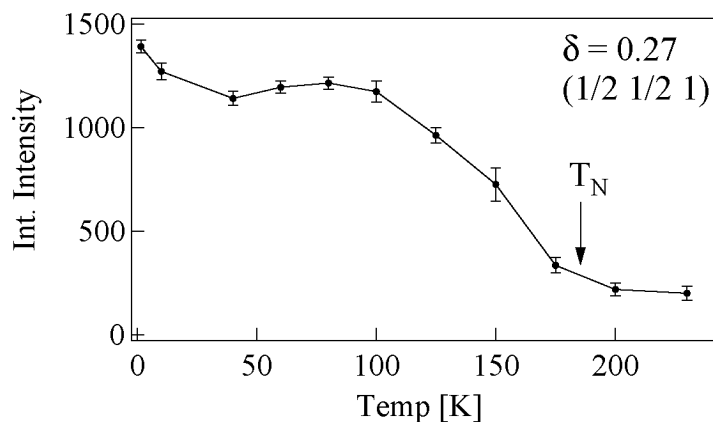
Figure 3.23: Temperature dependent integrated intensity of the AFM reflection (1/2 1/2 1) for $Ho_{0.1}Sr_{0.9}CoO_{2.73}$ with $T_N = 180(10)$ K.
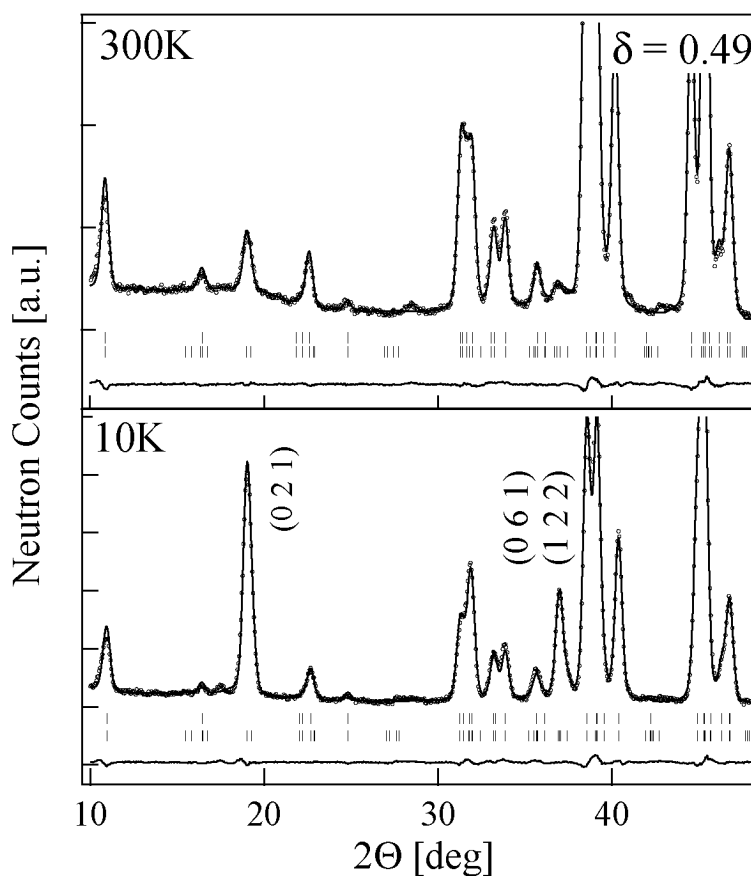
Figure 3.24: Observed, calculated and difference NPD pattern for the $x = 0.49$ $Ho_{0.1}Sr_{0.9}CoO_{3-x}$ compound at RT (top) and 10 K (bottom). Ticks | indicate peak positions (nuclear *Imma* and magnetic, from top to bottom). The indices of the strongest magnetic reflections are given (*Imma* symmetry).
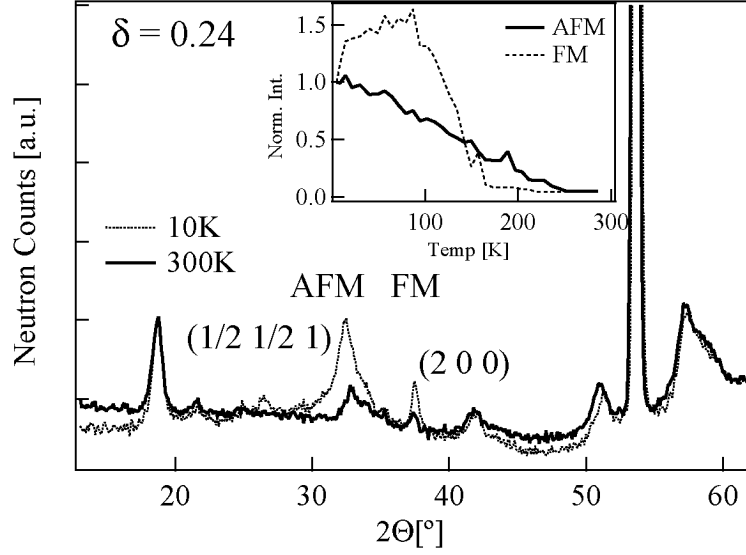
Figure 3.25: Extract of the NPD pattern for the $\delta = 0.24$ $Ho_{0.1}Sr_{0.9}CoO_{3-\delta}$ compound at RT and $10\,K$. The indexing corresponds to $P4/mmm$ symmetry. The inset shows the temperature dependence of the two magnetic peaks marked in the NPD pattern.

(indexed as (2 0 0) in tetragonal $P4/mmm$ symmetry) appears at the position of a nuclear reflection. For the other, a broad peak (1/2 1/2 1) indexed with the same propagation vector as for the $\delta = 0.27$ and 0.31 emerges ($\vec{k}_{AFM} = (1/2\ 1/2\ 0)$). The broadness of the reflection suggests the existence of short-range magnetic correlations in the system. The Gaussian reflection corresponds to the lowest magnetic reflection in the $\delta = 0.15$ NPD pattern and probably belongs to a FM phase similar to the one for $\delta = 0.15$. The broad reflection appears at the position of the lowest angle magnetic reflection in the $\delta = 0.27$ and 0.31 compounds, this peak probably belongs to a similar AFM phase. The temperature dependence of the two magnetic reflections for $\delta = 0.24$ is displayed in the inset of Figure 3.25 Clearly, the two integrated intensities show a different behaviour with temperature and disappear at different temperatures ($T_N \sim 230(10)\,K$ and $T_C \sim 170(10)\,K$). We have interpreted these results as arising from the co-existence of small AFM and larger FM domains.

The so found T_C is similar to the one found by bulk magnetisation measurements ($T_C = 140(5)\,K$). In the magnetization measurement the signal for T_N cannot be detected. For $\delta = 0.19$ we found by NPD: $T_N = 180(10)\,K$ and $T_C = 160(5)\,K$.

In Figure 3.26 we summarize the results in form of a phase diagram, showing the crystallographic and magnetic structures and the region of charge order in dependence of oxygen deficiency. The Curie temperature T_C seems to decrease linearly, while the Neel temperature T_N shows an anomaly around $\delta = 0.24$ and then increases linearly with increasing oxygen deficiency δ starting from $\delta = 0.27$ (Figure 3.26).

3.5.4 Discussion of Exchange Interactions

A possible explanation for our observations is now given. From the refined magnetic moments and the amount of Co^{4+} and Co^{3+} in each sample, it is possible to calculate the spin states of
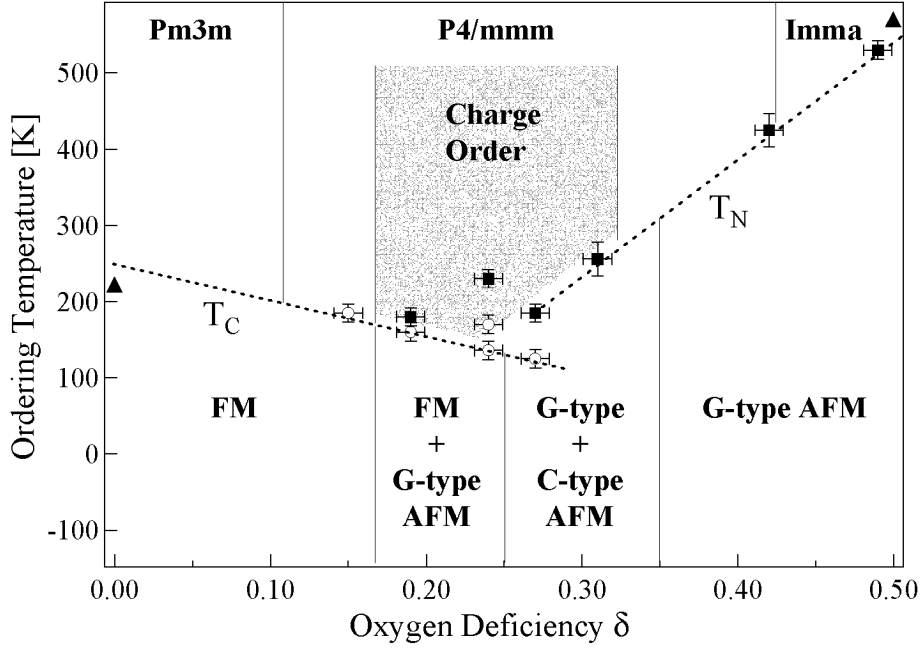
Figure 3.26: Phase diagram for $Ho_{0.1}Sr_{0.9}CoO_{3-\delta}$ ($\delta \leq 0.5$). Open circles ○, black squares ■ and black triangles ▲ denote T_C, T_N and transition temperatures for the parent compounds $SrCoO_3$ and $SrCoO_{2.5}$, respectively. The dotted lines are a guide to the eye and the vertical lines indicate magnetic and crystallographic phase boundaries. The charge ordered region is indicated by the shaded region.

Table 3.6: Calculated spin states (SS, at 10K) for the series $Ho_{0.1}Sr_{0.9}CoO_{3-\delta}$ (for $\delta = 0.15$, 0.27, 0.31 and 0.49.

	0.15	0.27	0.31	0.49
Fraction Co^{4+} [%]	60	36	28	
Fraction Co^{3+} [%]	40	64	72	92
Fraction Co^{2+} [%]				8
SS Co1^{4+}	LS 60%	LS 72%	LS 56%	
SS Co1^{3+}	IS 40%	LS 28%	IS 22%, HS 22%	IS 49%, HS 51%
SS Co2^{4+}				LS 46%
SS Co2^{3+}		LS 52%, IS 48%	LS 18%, IS 82%	
SS Co2^{2+}				HS 54%

the Co ion (Table 3.6). Depending on the Co ion valence and its spin state, different magnetic interactions are possible, if the superexchange interaction (Chapter 1.3) and the Goodenough-Kanamori rules are considered as the relevant coupling between the Co magnetic moments. In Table 3.7 the resulting interactions (FM or AFM) between Co ions of different valence and spin state according to the Goodenough-Kanamori rules are given. The LS Co^{3+} does not contribute to magnetic order, since it does not have unpaired electrons.

In order to have an estimate, which interaction is dominant, it is necessary to know the fraction of such interactions for each sample. Such a calculation has been done by combining statistical and geometrical considerations [113] with the information on spin states and type of interaction in each sample (Tables 3.6 and 3.7).

In three dimensions the probability $P_k(y)$ to have, for a given percentage y of Co^{4+} ions, next to a Co^{4+} ion k (maximal 6) other Co^{4+} ions is

$$P_k(y) = \binom{6}{k} y^k (1-y)^{6-k}, \tag{3.10}$$

$$y = 0.9 - 2\delta. \tag{3.11}$$

The total fractions F_{4-4}, F_{4-3} and F_{3-3} of Co^{4+}-Co^{4+}, Co^{4+}-Co^{3+} and Co^{3+}-Co^{3+} interactions is obtained by adding these probabilities

$$F_{4-4}(y) = P_6(y) + \frac{1}{2} \sum_{k=0}^{5} \frac{k}{6} \times P_k(y), \tag{3.12}$$

$$F_{3-3}(y) = P_0(y) + \frac{1}{2} \sum_{k=1}^{6} \frac{k}{6} \times P_{6-k}(y), \tag{3.13}$$

$$F_{3-4}(y) = 1 - F_{4-4}(y) - F_{3-3}(y). \tag{3.14}$$

However, in the region $0.19 \leq \delta \leq 0.31$ this model does not apply, because the assumption of statistical distribution of Co^{3+} and Co^{4+} ions is not correct due to the existence of charge order. The arrangement of Co^{4+} and Co^{3+} in two separate layers reduces the fraction of Co^{4+}-Co^{3+} interactions and increases the fraction of Co^{4+}-Co^{4+} and Co^{3+}-Co^{3+} interactions. In Figure 3.27 the total fractions F_{4-4}, F_{4-3} and F_{3-3} are shown for the full phase diagram.

$\delta = 0.15$:

For $\delta = 0.15$ (60% Co^{4+} and 40% Co^{3+}), we get a good agreement with the refined magnetic moment ($1.17 \mu_B$) for a combination of LS Co^{4+} ($\mu_{Co^{4+}} = 1 \mu_B$) and IS Co^{3+} ($\mu_{Co^{3+}} = 2 \mu_B$), namely $\mu_{calc} = 1.40 \mu B$ (see Table 3.6). Since our resistivity measurements for this sample give no indication for metallicity, we use the superexchange interaction to explain the magnetic behavior. According to the Goodenough-Kanamori rules the resulting exchange interactions are as described in Table 3.7. In Figure 3.27 it is seen that $\delta = 0.15$ is located in a region where the fraction of FM interactions (only Co^{3+}-Co^{4+}) are comparable to the total fraction of AFM interactions (Co^{4+}-Co^{4+} and Co^{3+}-Co^{3+}). The Co^{4+}-Co^{4+} weak AFM has to be very weak in order to explain the FM order in our sample. We propose the following model: based on the neutron diffraction data, where we see narrow magnetic reflections at $10\,K$ (indication for long-range magnetic order), we assume that large clusters exist within the sample, where the Co magnetic moments are FM coupled. Due to AFM interactions, FM order cannot percolate throughout the sample, giving rise to the observed cluster glass behavior (Section 3.5.1).
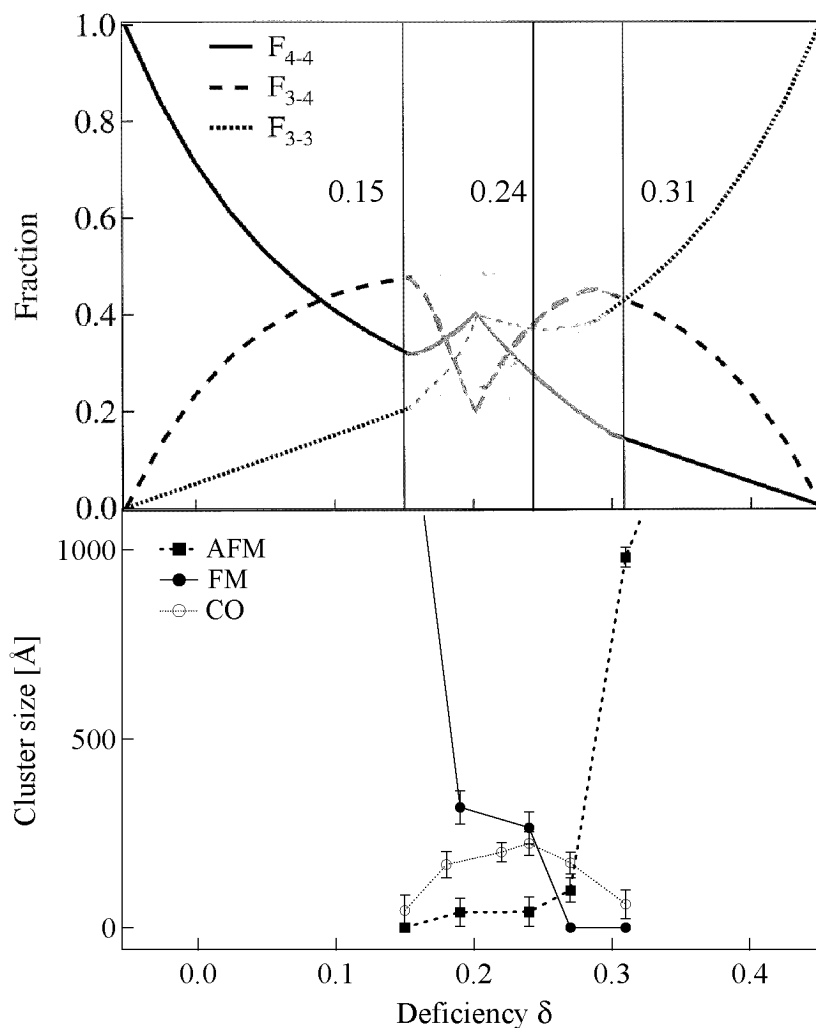
Figure 3.27: Top: Fractions F_{4-4}, F_{4-3} and F_{3-3} of the Co^{4+}-Co^{4+}, Co^{4+}-Co^{3+} and Co^{3+}-Co^{3+} interactions dependent on oxygen deficiency, as calculated based on statistical and geometrical considerations ($\delta \leq 0.15$ and $\delta > 0.31$) and charge ordering considerations ($0.15 < \delta \leq 0.31$). Bottom: Oxygen deficiency dependent cluster sizes of ferromagnetic, antiferromagnetic and charge ordered clusters in $Ho_{0.1}Sr_{0.9}CoO_{3-\delta}$.

Table 3.7: Superexchange couplings between Co ions of different spin and/or different valence states following the Goodenough-Kanamori rules. The top part of the table applies to the tetragonal structure. The bottom two parts apply to the brownmillerite structure, where the Co^{2+} and Co^{4+} ions are situated in tetrahedral t and Co^{3+} in octahedral o environment.
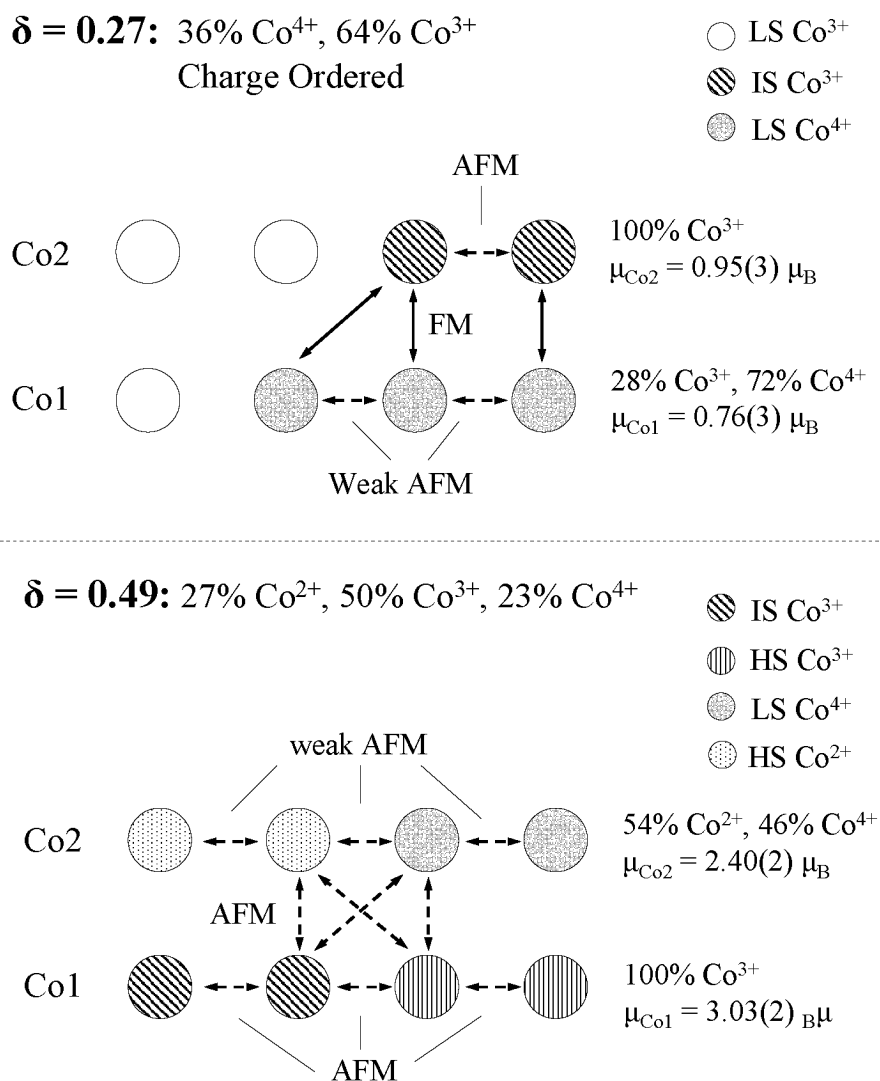
Co^{3+}	Co^{3+}	Exch.	Co^{3+}	Co^{4+}	Exch.	Co^{4+}	Co^{4+}	Exch.
LS	LS	-	LS	LS	-	LS	LS	wAFM
LS	IS	-	LS	IS	-	**LS**	**IS**	**FM**
LS	HS	-	LS	HS	-	**LS**	**HS**	**FM**
IS	IS	AFM	**IS**	**LS**	**FM**	IS	IS	AFM
IS	HS	AFM	IS	IS	AFM	IS	HS	AFM
HS	HS	AFM	IS	HS	AFM	HS	HS	AFM
			HS	**LS**	**FM**			
			HS	IS	AFM			
			HS	HS	AFM			

$Co^{4+}t$	$Co^{3+}o$	Exch.						
LS	LS	-						
LS	IS	AFM						
LS	LS	AFM						

$Co^{2+}t$	$Co^{3+}o$	Exch.	$Co^{2+}t$	$Co^{4+}t$	Exch.	$Co^{2+}t$	$Co^{2+}t$	Exch.
HS	LS	-	HS	LS	wAFM	HS	HS	wAFM
HS	IS	AFM	HS	HS	wAFM			
HS	HS	AFM						

$\delta = 0.19, 0.24$:

In the samples with $\delta = 0.19, 0.24$ we find coexistence of FM and AFM order. From the broadness (full width half maximum, FWHM) of the magnetic reflections we can calculate the correlation length of the FM and AFM interactions, which is equivalent to the cluster size within which the magnetic interactions are correlated. The Scherrer formula introduced in Chapter 3.4.3 was used to calculate the FM and AFM cluster sizes (Figure 3.27 bottom and Table 3.8). The FM clusters are by a factor of ~ 7 larger than the AFM ones (Table 3.8), but still quite small. Since we do not have any information for the magnetic moments in these samples, we cannot say, whether the model in Figure 3.27 can support our observations. From the data point of view, the FM interactions should prevail.

$\delta = 0.27, 0.31$:

Due to the existence of charge order, Co^{3+} and Co^{4+} ions are arranged in layers which alternate along the c-direction. From the values of the refined magnetic moment, we obtain a combination of LS/HS and LS/IS for both sites, as displayed in Table 3.6 and Figure 3.28. As a consequence, the coupling inside both kinds of layers should be AFM, strong for those containing only Co^{3+} and weaker for those with mostly Co^{4+}. Moreover, the interlayer coupling is expected to be FM (Figure 3.28). These predictions are in excellent agreement with our observations, which show the existence of long-range AFM within the layers and weaker FM coupling along the c-direction.

δ = 0.27: 36% Co⁴⁺, 64% Co³⁺
                              Charge Ordered

○ LS Co³⁺
⊗ IS Co³⁺
⊙ LS Co⁴⁺

Co2

AFM

100% Co³⁺
$\mu_{Co2} = 0.95(3)\ \mu_B$

FM

Co1

28% Co³⁺, 72% Co⁴⁺
$\mu_{Co1} = 0.76(3)\ \mu_B$

Weak AFM

δ = 0.49: 27% Co²⁺, 50% Co³⁺, 23% Co⁴⁺

⊗ IS Co³⁺
◍ HS Co³⁺
⊙ LS Co⁴⁺
⊙ HS Co²⁺

weak AFM

Co2

54% Co²⁺, 46% Co⁴⁺
$\mu_{Co2} = 2.40(2)\ \mu_B$

AFM

Co1

100% Co³⁺
$\mu_{Co1} = 3.03(2)\ _B\mu$

AFM

Figure 3.28: Schematic views of a double layer of Co1 and Co2 ions for $\delta = 0.27$ (top) and $\delta = 0.49$ (bottom). The magnetic interactions between the Co ions of different valence and/or spin are indicated.

Table 3.8: Charge ordered (CO), ferromagnetic (FM) and antiferromagnetic (AFM) cluster sizes (in [Å]) in $Ho_{0.1}Sr_{0.9}CoO_{3-\delta}$, as determined from full width half maximum values of according diffraction peaks in XPD (CO) and NPD (FM, AFM) patterns.

	Cluster Size [Å]		
δ	CO	FM	AFM
0.15	45(41)		
0.18	167(35)		
0.19		318(44)	41(37)
0.22	200(26)		
0.24	223(31)	265(42)	42(39)
0.27	171(29)		99(32)
0.31	62(38)		981(27)

$\delta = 0.49$:

In the most oxygen deficient sample $\delta = 0.49$ the Co^{3+} ion located at the Co2 position is now in a tetrahedral environment and the order of the e_g and t_{2g} energy levels are reversed. In oxides with Co in tetrahedral coordination, the Co is found to be either Co^{2+} or Co^{4+}, seldomnly Co^{3+} [110]. The average refined Co-O distance found for the tetrahedra is 1.85 Å, exactly in between what has been found for Co^{2+}-O and Co^{4+}-O (1.79 and 1.95 Å, respectively). In our sample charge disproportionation could occur in the following way: $2Co^{3+} \rightarrow Co^{2+} + Co^{4+}$. Considering this, we obtain for the octahedral position a mixture of IS/HS and for the tetrahedral position LS/HS (Table 3.5). Looking at Figure 3.28 and applying the Goodenough-Kanamori rules (Table 3.7) we obtain the AFM order within and between the ab-planes, as well as the smaller magnetic moment at the Co2 site with respect to the Co1 site value.

In literature a HS state is assumed for the Co^{3+} ions in the $SrCoO_{2.5}$ compound. The above proposed charge disproportination is not in contradiction to this, since the theoretical value for the magnetic moment for HS Co^{3+} as compared to 50% HS Co^{2+} + 50% HS Co^{4+} are almost identical, namely 4.895 and 4.899 μ_B. Our observed average refined value for the magnetic moment (2.71 μ_B) is much lower than the theoretical one for the HS prediction and a little lower than the value reported by Takeda *et al.* [78] for $SrCoO_{2.5}$ (3.3 μ_B). This can be due to the fact that we do not have an ideal 100% Co^{3+} composition.

3.6   Summary and Conclusion

The oxygen defective $Ho_{0.1}Sr_{0.9}CoO_{3-\delta}$ cobaltite series was studied within a broad compositional range ($0.15 \leq \delta \leq 0.49$) by NPD, XPD and bulk magnetic measurements within the temperature range 10 and 550 K. The varying oxygen content allows for the study of the influence of both oxygen vacancies and ratio of Co^{3+} and Co^{4+} ions on crystallographic and magnetic properties. A systematic study has not been published to the date of this work.

The cubic $Pm3m$ and orthorhombic $Imma$ structures of the parent materials $SrCoO_3$ and $Sr_2Co_2O_5$ are observed for $\delta = 0.15$ ($Pm3m$) and for $\delta \geq 0.42$ ($Imma$), respectively. Additionally, our high resolution neutron diffraction data clearly show the existence of a short-range Co^{3+}/Co^{4+} charge order for oxygen vacancy concentrations close to $\delta = 0.20$. The associated structural modulation can be described by the propagation vector $\mathbf{q}_{CO} = (0\ 0\ 1/2)$. It involves a deformation pattern consisting of an array of elongated and compressed CoO_6 corner-sharing

octahedra planes alternating along the c-axis. This leads to a doubling of the cubic perovskite unit cell along the c-direction and the intermediate oxygen content compounds have a tetragonal crystallographic structure with $P4/mmm$ symmetry. The obtained normalized bond valence sum values for the Co^{3+}/Co^{4+} sites are very close to their nominal values ($+3.07$ and $+3.95$, for $\delta = 0.19$). We attribute this astonishing observation to the one-dimensional character of the associated distortion pattern, whose elastic stabilization energy is eased with respect to the 3D arrays reported for other charge ordered perovskite oxides.

The magnetic properties of $Ho_{0.1}Sr_{0.9}CoO_{3-\delta}$ have been established. Increasing oxygen deficiency causes a change in magnetic order from a FM cluster glass ($\delta = 0.15$) to a state where short-range antiferromagnetic clusters coexist with larger ferromagnetic clusters ($\delta = 0.19, 0.24$). A further transition to G-type AFM order with a weak C-type AFM component ($\delta = 0.27, 0.31$) is found, before finally long range G-type antiferromagnetism is established ($\delta = 0.42, 0.49$). The magnetic properties (both ferromagnetic and antiferromagnetic) can be explained on the basis of superexchange interactions and the Goodenough-Kanamori rules.

We have shown, for a series of samples with varying oxygen content, that the oxygen vacancies are located in the basal planes of the polyhedra surrounding the Co2 ion. This is in contrast to other studies [5, 84, 86]. However, the location in the basal plane seems to be more realistic, considering that the oxygen vacancies in the most oxygen deficient compound $\delta = 0.49$ also lie in the basal planes, as has been found in our samples and other studies [78, 83]. The advantage of our study is the availability of a series of samples. Our experiments clearly show that oxygen is lost only from one particular ion site and that the occupation decreases smoothly when decreasing oxygen content.

Due to a simple deformation pattern, consisting of alternating elongated and compressed octahedra, we find almost complete charge ordering of the Co^{3+} and Co^{4+} ions. Other reported charge redistributions have always been found to be partial, as for $CaFeO_3$, $YBaCo_2O_5$ and $YNiO_3$ [102, 103, 104].

Another significant finding concerns the development of magnetic order on reducing oxygen content. We could show that there is a smooth transition from a FM cluster glass to a state with long-range antiferromagnetic order. From our neutron powder diffraction data we see that antiferromagnetic clusters develop gradually, while the ferromagnetic cluster size decreases. This segregation into two different magnetic states which evolve gradually is very similar to that described by M. A. Señarís-Rodríguez and J. B. Goodenough [67] in $La_{1-x}Sr_xCoO_3$. Before the present work the oxygen content dependence of magnetism in these compounds has not been investigated.

Chapter 4

Layered Cobaltites: $LnBaCo_2O_{5+\delta}$ (Ln = Lanthanide)

The importance of being able to control the oxygen content and the oxygen vacancy order in the cobaltites is shown for the compound $PrBaCo_2O_{5.48}$. We found that it is possible to directly determine both the oxygen content and the extent of oxygen order from the characteristics of the temperature dependent zero field and field cooled magnetization measurements. The same compound was investigated at high temperatures ($300\,K \leq T \leq 820\,K$) and a structural transition was found, which can be attributed to the rearrangement of oxygen vacancies, leading to a disordered state. The transport properties of this compound were investigated in the same high temperature region. The material behaves like a semiconductor with thermally activated polaronic hole conductivity, in contrast to the metallicity reported in the literature.

4.1 Motivation

Increasing demand for storage capacity at an affordable price has lead to the development of new technologies in the field of magnetic data storage. One of the major advancements has been the introduction of magnetoresistive (MR)[1] and later of giant magnetoresistive (GMR) reading heads. The primary advantage of GMR over MR heads is greater sensitivity to magnetic fields mediated by the data disk. This increased sensitivity makes it possible to detect smaller recorded areas of information (bits) and to read these bits at higher data rates. However, the GMR effect is a quantum effect and the GMR sensors utilize the quantum nature of electrons, which have two spin states. GMR reading heads are built from thin layers, where one magnetic layer has a fixed magnetic orientation, while the second (sensor) film has a variable magnetic orientation, which is changed according to the external magnetic field provided by the data disk (for more information see [114]).

There are materials, among which are the manganites and the layered cobaltites, which display a colossal magnetoresistance (CMR), which could eventually be used as read heads in magnetic data storage. The values reported for layered cobaltites $LnBaCo_2O_{5.4}$ (Ln = Eu, Gd) are $\Delta\rho$ =66 % for $T = 10\,K$, $H = 7\,T$ and Ln = Gd [1]. In order to improve magnetoresistance values, it is important to know the crystallographic structure of the layered cobaltites, its dependence on oxygen content and oxygen vacancy order, and how the degree of oxygen vacancy ordering

---

[1] A magnetoresistive material shows higher electrical resistivity ρ when the electrical current flow is parallel to the orientation of the magnetic moments. The magnetic moments are aligned in a certain direction by applying an external magnetic field H. The magneto resistance value is defined as $\Delta\rho = \frac{\rho(H)-\rho(H=0)}{\rho(H=0)}$.

order (quality of the sample) can be improved. The arrangement of the Co magnetic moments in these materials is crucial, since the magnetoresistance effect is based on a re-orientation of magnetic moments in an external magnetic field. Therefore it is necessary to know in which direction the magnetic moments can be turned with the least effort. It is also important to know the dependence of the magnetization on oxygen content and if it depends on the quality of oxygen vacancy order. Since the magnetoresistance effect also relies on electrical resistivity, the dependence of resistivity on the crystallographic and magnetic structures should be known. In this chapter special emphasis has, as in Chapter 3, been paid on the oxygen content and oxygen vacancy order influence on the crystallographic structure and on magnetic/electronic properties. Experiments were performed mostly on samples of type $PrBaCo_2O_{5+\delta}$ ($0.28 \leq \delta \leq 0.79$).

Up to date ionic conduction, which is well established for the 3 dimensional cobaltites [59, 2], has not been observed in the layered $LnBaCo_2O_{5+\delta}$ compounds. But since ionic conduction is strongly connected to oxygen vacancies it can be expected that the layered cobaltites are also ionic conductors. Therefore, the high temperature ($T \geq 820\,K$) structure of $PrBaCo_2O_{5.48}$ was investigated, to see if the layered Co-compounds are also candidates as ionic conductors.

4.2 Introduction

Since the discovery of colossal magnetoresistance (CMR) in the manganite perovskites $Ln_{1-x}A_xMnO_3$ (Ln = lanthanide and A = alkaline earth) [60, 115, 116, 117, 118, 119, 120], there has been search for other $3d$ transition metal oxides with CMR properties. Magnetoresistance, however with very small ratios (~ 2) between resistivity values measured with and without applying a magnetic field, was found in the cobalt perovskite $La_{1-x}Sr_xCoO_3$ [121, 122, 123]. It was known that the mixed, oxygen deficient perovskite materials $LnBa(Co_{2-x}M_x)O_{5+\delta}$ ($M =$ Cu, Fe) [124, 125] display complicated magnetic properties, including an AFM to paramagentic transition and a second transition due to a reorientation of the magnetic moments. They adopt an anisotropic structure similar to that of $YBaFeCuO_5$ [126], called the "112" phase (characterized by an ordering of Ln and Ba cations and of oxygen vacancies along the c-direction, leading to a doubling of the unit cell in c-direction. "112" refers to the ratio of the lattice parameters along the three crystallographic directions.). In search of a material with a pure Co "112" phase, in 1997 Martin *et al.* [1] synthesised $LnBaCo_2O_{5.4}$ (Ln = Eu, Gd) and found that these compounds exhibit colossal magnetoresistive behavior, with resistance ratios higher than 10, the highest value known in cobaltites at that time. Around the same time, Troyanchuk *et al.* [127] presented their results on a "new family of magnetic semiconductors exhibiting both antiferromagnetic-ferromagnetic and metal-insulator first-order transitions", together with the observation of magnetoresistance values $\Delta\rho$ of 40% in the compounds $Ln_{0.5}Ba_{0.5}CoO_{3-\delta}$.

4.2.1 Structural Aspects

Symmetry

As mentioned in the Introduction 1.1, the wide allowed oxygen range in $LnBaCo_2O_{5+\delta}$ ($0 \leq \delta \leq 1$) can lead to several crystallographic structures at room temperature, with either pyramidal or octahedral (or both) environments for the Co ions [128, 103, 129, 130, 131]. In the following, the room temperature structures for different values of δ will be presented.

The crystal structure of the stoichiometric $LnBaCo_2O_5$ compound has $P4/mmm$ symmetry and

PrBaCo$_2$O$_5$ **PrBaCo$_2$O$_{5.5}$** **PrBaCo$_2$O$_6$**

Col — Ba — O
Co2 — Pr
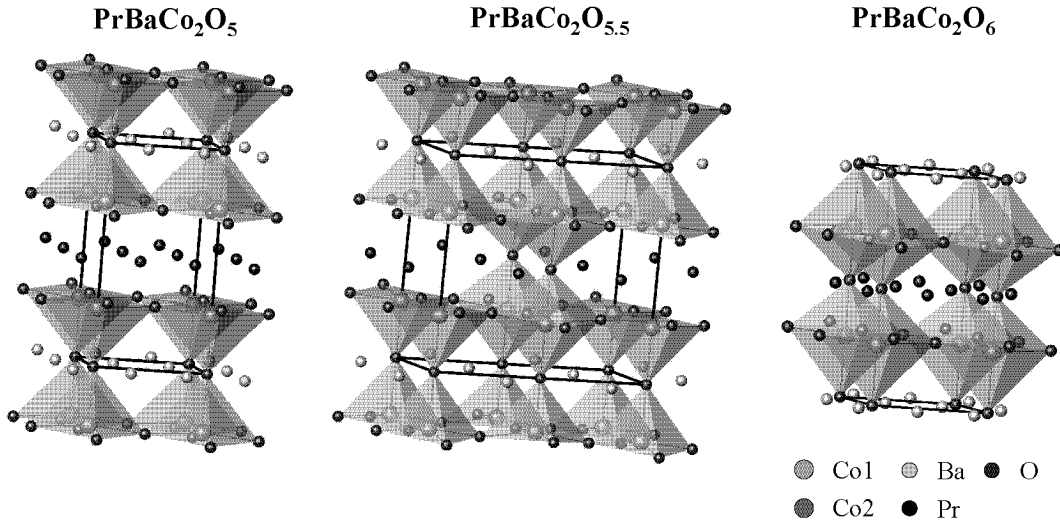
Figure 4.1: Schematic crystal structure of LnBaCo$_2$O$_{5+\delta}$ with a) $a_p \times a_p \times 2a_p$ ($\delta = 0$); b) $a_p \times 2a_p \times 2a_p$ ($\delta = 0.5$); and c) $a_p \times a_p \times 2a_p$ ($\delta = 1$) type unit cell.

is tetragonal with unit cell $a_p \times a_p \times 2a_p$ (where a_p will always refer to the cubic perovskite lattice parameter). This corresponds to a doubling of the original perovskite unit cell along the c-direction due to alternating BaO and LnO$_\delta$ layers (Figure 4.1). The layered structure is best observed in the most oxygen deficient case LnBaCo$_2$O$_5$, because it is assumed that the oxygen ions are absent only in the Ln layer [103, 132, 133, 134, 135, 136]. For $\delta = 0$ the Co^{2+} and Co^{3+} ions (ratio 1:1) are all within square base pyramids formed by their five oxygen neighbours.

In the other stoichiometric case LnBaCo$_2$O$_6$ all the Co^{3+} and Co^{4+} (ration 1:1) ions are in octahedral environment (six neighbouring oxygen ions), where the octahedra again have a square base. Here, the layered structure is not so evident, as the layered character is only visible in the ordering of the Ln and Ba ions along the c-direction. In LaBaCo$_2$O$_6$, the only such compound which was studied by neutron diffraction [137, 138] before the present work, the crystal structure at room temperature is the pure cubic perovskite one, meaning that La and Ba are distributed statistically on the same site. However, this can be due to the similar size of the La and Ba ions. A layered structure is likely to exist in LnBaCo$_2$O$_6$ with a smaller lanthanide, again with a tetragonal unit cell $a_p \times a_p \times 2a_p$ with $P4/mmm$ symmetry (Figure 4.1).

The nonstoichiometric case LnBaCo$_2$O$_{5+\delta}$ is more complex: due to oxygen vacancy order super-structures can arise, which vary with oxygen content. The oxygen content after the synthetization process (solid state reaction method) is strongly dependent on the size of the lanthanides. In Table 4.1 the obtained values for δ are given for the samples without post-reaction treatment, synthesized by different groups [128, 139, 140] by the above described process. The values obtained for the as prepared samples given in these References are qualitatively similar. Clearly, a strong correlation exists between the Ln radius and the amount of oxygen the compound can accommodate.

The first structural study of an ordered oxygen deficient perovskite of type LnBaCo$_2$O$_{5+\delta}$ (Ln = Pr - Ho, for Ln dependent oxygen content see Table 4.1) was presented by Maignan *et al.* [128] in 1999 and up to date has stayed with little competition. All of their x-ray diffraction patterns could be indexed using a tetragonal $P4/mmm$ $a_p \times a_p \times 2a_p$ unit cell, corresponding

Table 4.1: Lanthanide ionic radius (9 fold coordination) [141] and the obtained δ for equilibrium oxygen content.

	Pr	Nd	Sm	Eu	Gd	Tb	Dy	Ho
R_{ionic} [Å]	1.179	1.163	1.132	1.120	1.107	1.095	1.083	1.072
δ [128]	0.7(0.7)	0.7	0.4	0.4	0.4(0.5)	0.4	0.3	0.3(0.4)
δ [139]	0.53(1)	0.57(8)	0.39(4)	0.34(2)	0.43(3)	0.41(0)	0.20(8)	0.20(9)
δ [140]	0.68(3)	0.62(4)	0.54(6)	0.52(5)	0.42(4)	0.41(3)	0.36(4)	0.25(4)
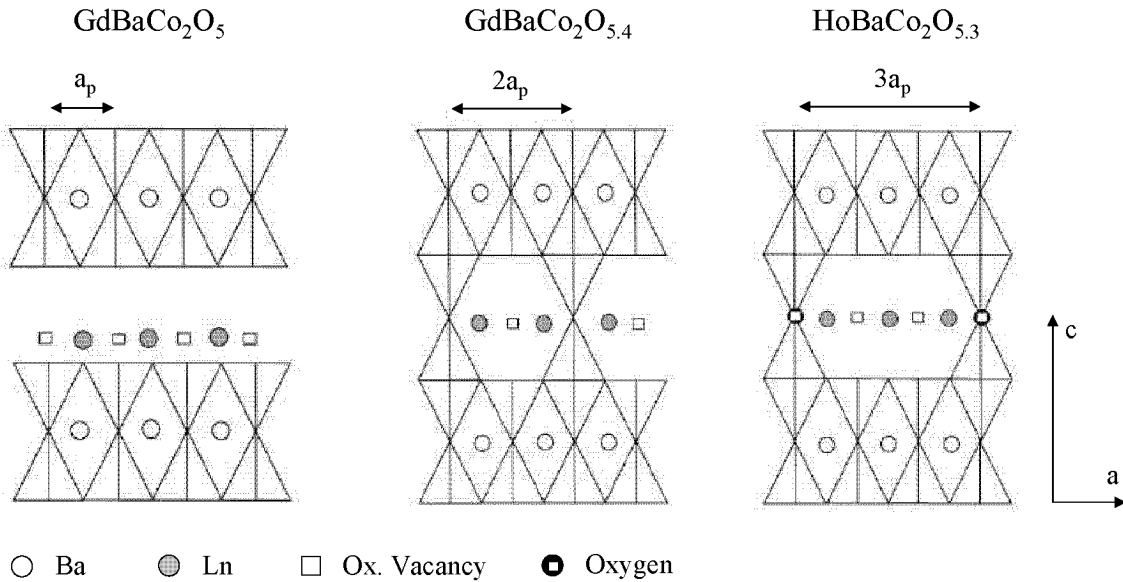
Figure 4.2: Structural models for $GdBaCo_2O_5$, $GdBaCo_2O_{5.4}$ and $HoBaCo_2O_{5.3}$ according to Maignan *et al.* [128]. In these schematic drawings the *bc*-plane is shown.

to the "112" structure. But their electron diffraction measurements additionally revealed two kinds of superstructures, depending on the radius of the lanthanide (or, more likely, the oxygen content). For larger lanthanides (Pr, Nd, Sm, Eu, Gd and Tb) a doubling of one lattice parameter is observed, corresponding to an orthorhombic $Pmmm$ $a_p \times 2a_p \times 2a_p$ supercell, whereas for smaller lanthanides (Ho and Dy) a tripling of two lattice parameters is seen, as in a $3a_p \times 3a_p \times 2a_p$ supercell (Figure 4.2 for schematic views). Maignan *et al.* suggest that ordering of oxygen vacancies is at the origin of the observed superstructures. Importantly, they find that the oxygen vacancies are located uniquely in the LnO_δ layers (apical positions). By changing the oxygen content the superstructures either vanish or change from one to the other: Reducing oxygen content in $GdBaCo_2O_{5+\delta}$ from $\delta = 0.4$ to 0 destroys the superstructure. On the other hand in $HoBaCo_2O_{5.3}$ an increase of δ from 0.3 to 0.4 leads to a change in superstructure from $3a_p \times 3a_p \times 2a_p$ to $a_p \times 2a_p \times 2a_p$. High resolution electron microscopy supported the assumption that the ordering of the oxygen vacancies is responsible for the superstructures.

Burley *et al.* [142] discuss $NdBaCo_2O_{5+\delta}$ ($\delta = 0$, 0.38, 0.5, 0.69). The $\delta = 0$ compound has a tetragonal unit cell $a_p \times a_p \times 2a_p$ where the Nd layer incorporates all the oxygen vancancies. For the slightly higher oxygen content $\delta = 0.38$ the structure is derived from the $\delta = 0$ one, but with oxygen ions inserted randomly into the NdO_δ layers. Oxygen vacancy ordering in *b*-direction resulting in an orthorhombic $a_p \times 2a_p \times 2a_p$ unit cell with $Pmmm$ symmetry was
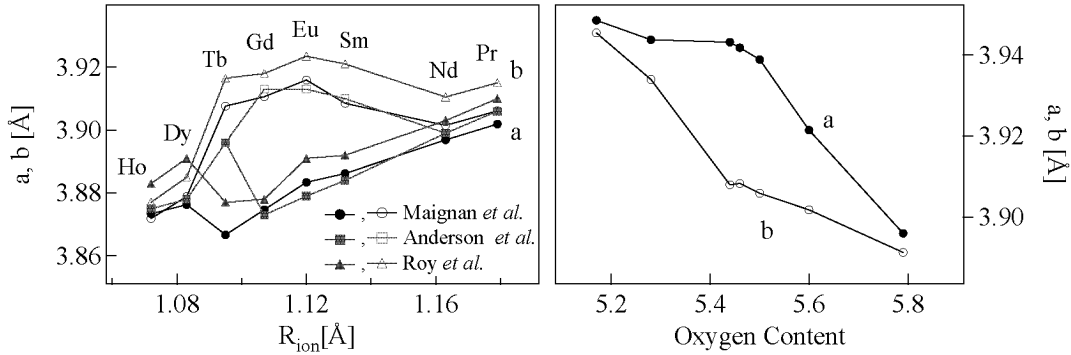
Figure 4.3: Orthorhombic distortions. Left: dependence on Ln ionic radius for $LnBaCo_2O_{5+\delta}$ (after [128, 139, 140]. Right: dependent on oxygen content $PrBaCo_2O_{5+\delta}$ (after [143]).

found for $\delta = 0.5$, in agreement with [128, 139]. The most oxidized material with $\delta = 0.69$ was again described by a tetragonal $a_p \times a_p \times 2a_p$ unit cell, but a very weak peak originating from a doubling of the unit cell along the b-direction was detected.

Chernenkov *et al.* found weak superstructure reflections for $GdBaCo_2O_{5.5}$ which follow the extinction rules of the $Pmma$ space group, the highest subgroup of $Pmmm$. In the $Pmma$ space group the unit cell is additionally doubled along the a-direction $(2a_p \times 2a_p \times 2a_p)$.This phase exists up to temperatures $340\,K$, where again $Pmmm$ symmetry is adopted.

To conclude, a summary of the most commonly used models for compounds with oxygen content $\delta = 0, 0.5, 6$ at room temperature is given (Figure 4.1):

1. $LnBaCo_2O_5$ has the tetragonal unit cell $a_p \times a_p \times 2a_p$ (symmetry $P4/mmm$). Ln alternate with BaO layers along the c-axis (all oxygen vacancies in the Ln layer).

2. $LnBaCo_2O_{5.5}$ has an orthorhombic unit cell $a_p \times 2a_p \times 2a_p$ (symmetry $Pmmm$). $LnO_{0.5}$ alternate with BaO layers along the c-direction. Along the b-direction the oxygen vacancies are ordered. This leads to an alternation of CoO_5 pyramids and CoO_6 octahedra along the b-direction (alternating planes of pyramids or octahedra parallel to the ac-plane).

3. $LnBaCo_2O_6$ is again tetragonal with unit cell $a_p \times a_p \times 2a_p$ (symmetry $P4/mmm$). LnO alternate with BaO layers along the c-direction (no oxygen vacancies).

Lattice Parameters

In the previous Section 4.2.1 the influence of both the lanthanide ion and the oxygen content on the symmetry of the $LnBaCo_2O_{5+\delta}$ compounds was discussed. This Section concentrates on the dependence of the lattice constants on oxygen content and it will be shown how structural changes can be seen in the lattice parameters.

Depending on the lanthanide, the lattice parameters and the unit cell volume vary significantly. For some lanthanides ((Tb), Gd, Eu, Sm) an orthorhombic distortion $a \neq b/2$ is reported [128, 139, 140]. However, it is important to point out the conditions in which these measurements were made: the samples were as prepared, meaning that only few compounds had an oxygen content close to 5.5. It is not the lanthanide which is responsible for the orthorhombic distortion but the an oxygen content close to 5.5. The left graph in Figure 4.3 shows the ionic

radius (lanthanide) dependent lattice parameters a and b, according to [128, 139, 140], where it has been neglected, that the materials have different oxygen contents. The right graph shows our oxygen dependent lattice constants a and b for $PrBaCo_2O_{5+\delta}$, for which an orthorhombic distortion is present in the oxygen content range $5.28 \leq \delta \leq 5.60$.

To show that the orthorhombic distortion is oxygen content dependent, Anderson et al. [140] increased the oxygen content of their samples and then measured the lattice parameters again. After this high oxygen pressure treatment the orthorhombic distortion was shifted to the compounds with $Ln =$ Ho, Dy, Tb, the compounds which before displayed low oxygen contents. Reduction of oxygen content lead to a shift of the distortion to the $Ln =$ Sm, Nd, Pr compounds with initial high oxygen content [140].

From this it follows that finding an orthorhombic distortion for the lattice parameters of a sample of unknown oxygen content is indication that the oxygen content of the sample is close to 5.5. But, as is shown in Section 4.3.1, the orthorhombic distortion of the lattice parameters alone does not guarantee that the oxygen vacancies are ordered on a long-ranged scale.

4.2.2   Magnetic Properties

$LnBaCo_2O_5$

Since the materials investigated for this work were mostly of type $LnBaCo_2O_{5.5}$, the discussion of the magnetic properties for $LnBaCo_2O_5$ will be short. This is also justified, since the magnetism in these compounds is less complicated and controversial than in the compounds $LnBaCo_2O_{5+\delta}$ with $\delta \sim 0.5$. $LnBaCo_2O_5$ compounds undisputedly undergo two transition: the first from a paramagnetic to an antiferromagnetic state at T_N ($P4/mmm$ to $Pmmm$ symmetry) and the second one to a charge ordered state at T_{CO} ($Pmmm$ to $Pmmb$ symmetry) [103, 132, 133, 134]. Almost independent of the lanthanide, the transition temperatures are $T_N \sim 340$ K and $T_{CO} \sim 210$ K. The magnetic ordering of the Co ions are indexed by a propagation vector $\vec{k} = (1/2\ 1/2\ 0)$ in the $a_p \times a_p \times 2a_p$ unit cell. This so-called G-type AFM structure is characterized by the Co ions being antiferromagnetically coupled to their six nearest neighbours along the three crystallographic axes. Below the charge order temperature T_{CO}, where the Co^{2+} and Co^{3+} ions alternate along the b-direction, it is possible to distinguish the a and b directions and Fauth et al. [134] find that the Co magnetic moments lie along the a-direction.

Even though the magnetic structure is simple, the electronic configuration of the Co ion is still under debate. According to Fauth et al. [133, 134], who for $HoBaCo_2O_5$ obtain magnetic moments of $\sim 3.7\ \mu_B$ and $\sim 2.7\ \mu_B$ for the Co^{3+} and Co^{2+} ions respectively, two spin state models are able to explain their data equally well. One assigns an intermediate spin state (IS, $t_{2g}^5 e_g^1$) to the Co^{3+} ion, the other model a high spin state (HS, $t_{2g}^4 e_g^2$) to the Co^{3+} ion, while Co^{2+} is in the HS state for both models. The first model is favored by local spin-density approximation (LSDA) $+U$ (Coulomb potential) methods performed by Kwon et al. [136] for $YBaCo_2O_5$. The second model is supported by Soda et al. [132] for $NdBaCo_2O_5$.

$LnBaCo_2O_{5.5}$

Few studies exist describing possible magnetic structures at temperatures $T < T_N$. One way to derive magnetic structures is to analyze neutron powder diffraction data, which does not lead to unambiguous results. Single crystal diffraction studies would be desired, but to our knowledge only one single crystal magnetic neutron study exists. Magnetization measurements performed
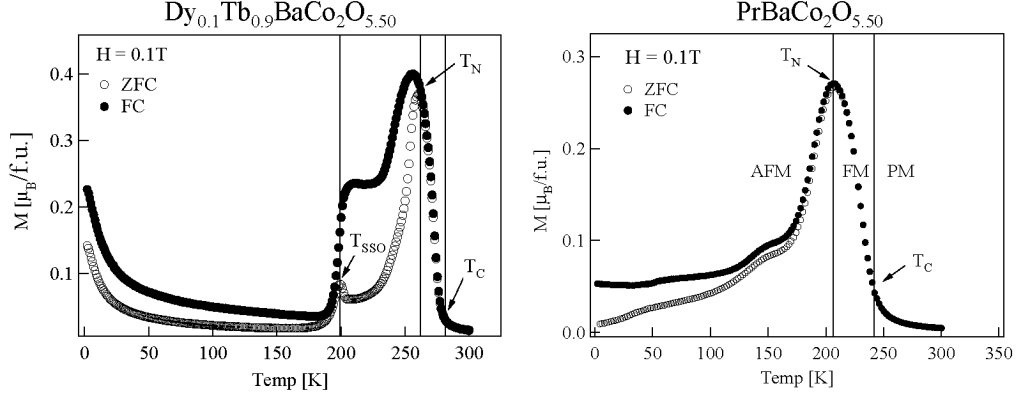
Figure 4.4: Temperature dependent magnetization measurements for $Dy_{0.1}Tb_{0.9}BaCo_2O_{5.50}$ and $PrBaCo_2O_{5.50}$.

on detwinned single crystals give information on the direction/magnitude of magnetic moments and together with structural studies can lead to models for the magnetic structure. Synchrotron x-ray diffraction help to determine the structure of the samples more accurately. Superstructures can be identified, which is of help in deciding on the correctness of existing magnetic models.

Independently of the lanthanide, the $LnBaCo_2O_{5.5}$ compounds undergo several magnetic transitions. First, at T_C, there is a transition from a paramagnetic to a state with a net magnetic moment, which is followed by a transition to an antiferromagnetic state at T_N. For several lanthanides a third transition is seen at T_{SSO}, most probably to a second AFM state with spin state order (SSO). In Figure 4.4 typical field cooled and zero field cooled magnetization measurements are shown for $Ln = Dy_{0.1}Tb_{0.9}$ and Pr. The three transition temperatures are indicated by the arrows.

The increase of the magnetization at T_C is indication that a phase with a spontaneous magnetic moment is developed. This state can be described in different ways, e.g.: 1) ferrimagnetic ordering of the Co spins[2]. This leads to a net magnetic moment (described by Plakthy et al. [144], Figure 4.5 left); 2) substituting all magnetic Co ion in the octahedral plane which point in a certain direction by a non-magnetic Co ion. This will also lead to a net magnetic moment (described by Khalyavin et al. [145], Figure 4.6 left).

The decrease of the magnetization below T_N (Figure 4.4) is indication that a transition to an AFM state occurs. The arrangement of the Co ion magnetic moments in this AFM state is still controversial, though many models exist. Two are shown in Figures 4.5 (middle) and 4.6 (right). The last transition at T_{SSO} (Figure 4.4 left) is often attributed to a spin state ordering, where Co ions of different spin state order along a certain direction. In Figure 4.5 (right) it is shown that the octahedral Co ions adopt alternating, antiparallel HS and IS states. In support of such a spin arrangement, Khomskii and Löw [146] have calculated that such spin superstructures can be energetically favorable.

Early neutron diffraction experiments performed on powder samples [147, 148] and a single

---

[2]In the case of a G-type AFM the arrangement of the magnetic moments can be considered as two interpenetrating sublattices, made up from magnetic moments of equal value. On one of the sublattices the magnetic moments point in one direction and on the other one in the opposite direction. The overall net magnetization is zero. If the magnitudes of the magnetic moments on the two sublattices are different, then the net magnetization is not zero. This phenomena is known as ferrimagnetism

TbBaCo$_2$O$_{5.5}$

| 255K < T < 290K | 170K < T < 255K | T < 170K |
| Ferrimagnetic | AFM 1 | AFM 2 |
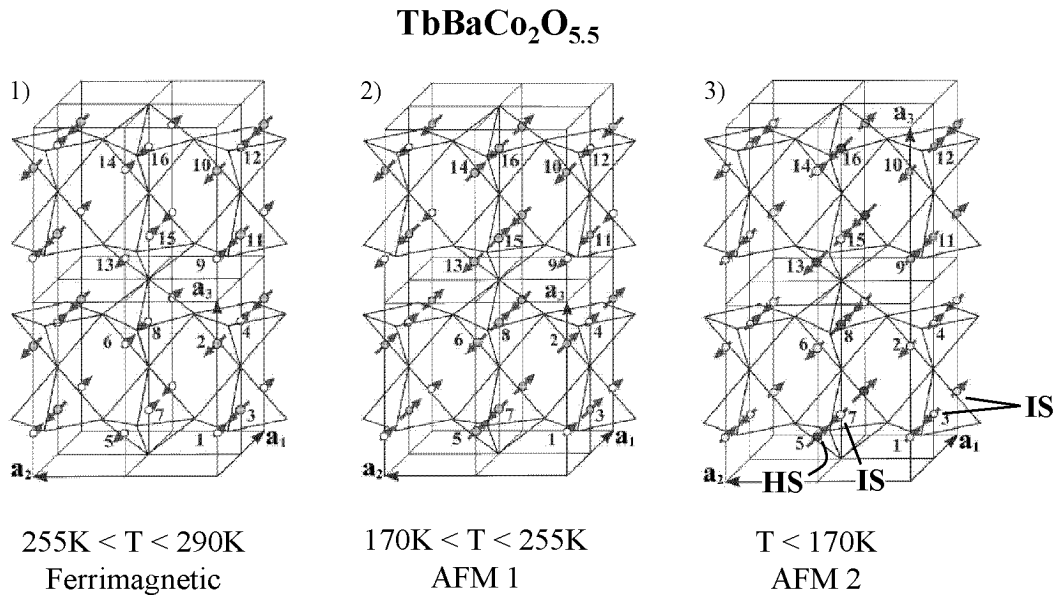
Figure 4.5: Structural magnetic models obtained by Plakthy *et al.* [144] for TbBaCo$_2$O$_{5.5}$ in three different temperature regions.

LnBaCo$_2$O$_{5.5}$

| T$_N$ < T < T$_C$ | T < T$_N$ |
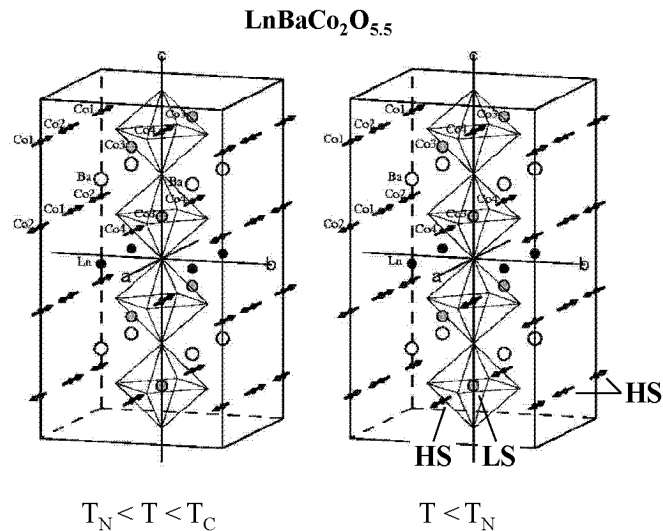
Figure 4.6: Magnetic structures presented by Khalyavin *et al.* [145] for LnBaCo$_2$O$_{5.5}$ in the state with spontanoues magnetic moment (left) and in the AFM state (right).

crystal [149] all encountered the same problem when trying to determine the magnetic structure for $T_N < T < T_C$, namely to explain the small reported magnetic moment at the Co site (magnetization measurements performed on powder samples). Magnetization measurements performed by Taskin *et al.* [150] on single crystals reveiled a strong magnetic anisotropy, and it was found that the Co ion spins lie along the a-direction.

Ferrimagnetic ordering implies that the unit cell accomodates four non-equivalent Ci ion sites, equivalent to an additional doubling of the unit cell along the a-direction. The doubling of the unit cell and with it the existence of four non-equivalent Co ion sites was confirmed by Cher-

nenkov *et al.* [151]. This group performed x-ray diffraction on $GdBaCo_2O_{5.5}$ and $DyBaCo_2O_{5.5}$
single crystals and found very weak superstructure reflections which follow the *Pmma* extinc-
tion rules. This directly confirms the doubling of the unit cell in a-direction.

The doubling of the unit cell along the a-direction was also seen in a NPD experiments per-
formed by Plakthy *et al.* [144] on $TbBaCo_2O_{5.5}$. They observe three magnetic phases, as
described above, all of which have the magnetic moments aligned parallel to the a-axis: 1)
$255 < T < 290\,K$: ferrimagnetic; 2) $170 < T < 255\,K$: AFM 1; and 3) $T < 170\,K$: AFM 2
(Figure 4.5). This group uses magnetic ordering arguments to show that the crystal structure
of phases 1 and 2 belong to the space group *Pmma* with unit cell $2a_p \times 2a_p \times 2a_p$. The magnetic
ordering of the third phase can only be explained by introducing a structural transition with
a change of unit cell to $2a_p \times 2a_p \times 4a_p$ and of symmetry to *Pcca*. The spontaneous magnetic
moment of phase 1 can be explained by ferrimagnetic (antiparallel) ordering of the Co spins in
two nonequivalent pyramidal sites. The model for ferrimagnetism, as well as the AFM ordering
for phases 2 and 3 are shown in Figure 4.5. Plakhty and coworkers suggest that the superstruc-
tures (*Pmma* and *Pcca*) are due to spin/orbital state ordering of the Co^{3+} ions as reported by
Khomskii and Löw [146]. In phase 3, the two nonequivalent Co ions in pyramidal environment
adopt the IS state, while the nonequivalent Co ions in octahedral coordination have IS and HS,
which are arranged in the before mentioned chessboard like manner.

A last study to be presented here is by Khalyavin *et al.* [145], who use the *Pmma* space group
to reconstruct the magnetic structure of $LnBaCo_2O_{5.5}$. On the basis of neutron diffraction
data for $LnBaCo_2O_{5+\delta}$ [129, 134, 152] this group concludes, that the pyramidal cobalt ions
are in HS state over the whole temperature range, while the superstructure develops in the
plane containing the LS/HS Co ions in octahedral environment (Figure 4.6). Above T_N the
spontaneous magnetic comes from the spins in the octahedral plane, which are all coupled FM,
opposed to the AFM coupling in the pyramidal planes. The AFM magnetic state below T_N
follows from this state by doubling the unit cell in c-direction, where the spins in the one half
of the cell point in the opposite direction compared to the other half of the cell. Both magnetic
structures found by this group are shown in Figure 4.6.

It can be said that a general agreement exists insofar as the pyramidal Co ion is reported to
be present in only one spin state, while for the octahedral Co ions two different spin states are
proposed, which order along the a-direction. However, the actual spin states are still under
debate.

4.2.3 Transport Properties

$LnBaCo_2O_5$

The $LnBaCo_2O_5$ compounds remain insulating for the measured temperature ranges $T < 700\,K$.
Below T_{CO} the resistivity is best approximated by the variable range hopping model. The cal-
culated density of the localized states at the Fermi level ($\sim 2.8 \times 10^{18}$ eV^{-1} cm^{-3}) is typical for
a disordered semiconductor. Above T_N a simple activation model and a small polaron model
reproduce equally well the resistance curve [134]. The different models for transport are ex-
plained in Chapter 1.4.

It should be noted that $LnBaCo_2O_5$ compounds are hole conductors already at room tempera-
ture (at temperatures $T > 230\,K$ for $GdBaCo_2O_5$, as reported in Ref. [153]), which can be seen in
the positive Seebeck coefficient [153, 154]. Since, according to charge neutrality considerations,
in $LnBaCo_2O_5$ Co^{2+} and Co^{3+} ions are present in the same amount, this implies that charge
disproportionality of the form $2Co^{3+} \rightarrow Co^{2+} + Co^{4+}$ is needed to obtain hole conduction. This

allows hole conduction to take place via the Co^{4+} ion. The charge disproportionality leads to a configuration which is usually not favored by bond valence sum considerations, namely that Co^{4+} ions are located in a fivefold pyramidal environment (details on bond valence sums can be found in Appendix A).

LnBaCo$_2$O$_{5.5}$

It is described in literature that the layered LnBaCo$_2$O$_{5+\delta}$ compounds with $\delta \sim 0.5$ undergo a metal insulator (MI) transition at $T_{MI} \sim 340$ K (depending on the lanthanide) [130, 153, 155, 156, 157]. This transition is found to be connected to a spin state transition of the Co ion. Frontera et $al.$ [155] give a plausible explanation of the metal-insulator transition (GdBaCo$_2$O$_{5.53}$ powder sample): they find that the pyramids and octahedra are distorted both above and below the transition temperature and because of that the stabilization of $d_{3x^2-r^2}/d_{3y^2-r^2}$ type orbital ordering below T_{MI} cannot be the mechanism for the MI transition. Instead, they report that on raising temperature above T_{MI} the volume of the octahedra (pyramids) increases (decreased). This increase of octahedral volume is attributed to a spin state transition from LS to HS (larger ionic radius compared to ion in IS state) , while the Co ion in pyramidal environment retains its IS state. The HS state is therefore responsible for the metallicity in these materials.

Another fact worth mentioning is the anisotropy in and out of the ab-plane of resistivity (Figure 4.7). For a GdBaCo$_2$O$_{5.46}$ single crystal Khalyavin et $al.$ [156] find that the in plane resistivity ρ_{ab} is larger than the out of plane resistivity ρ_c (Figure 4.7, left). Unfortunately a different result is presented by the group of Taskin et $al.$ [153] for another GdBaCo$_2$O$_{5.50}$ single crystal (Figure 4.7, right). They find just the opposite, namely $\rho_{ab} < \rho_c$ for $T < T_N$ and $\rho_{ab} = \rho_c$ for $T > T_N$. The coupling of the resistivity anisotropy to the magnetic transition temperature implies that the charge motion is sensitive to the Co ion magnetic moments arrangement and that the anisotropic spin arrangement is responsible for the anisotropy in resistivity.

Even though the transition seen in resistivity measurements is always referred to as an insulator to a metal transition, it is not clear, if a truly metallic state exists. As Taskin et $al.$ [153] write "although GdBaCo$_2$O$_{5+\delta}$ never behaves as a normal metal, the temperature dependence of its resistivity does not follow that of a simple insulator or semiconductor either".

4.2.4 Magneto-Transport Properties

Martin et $al.$ [1] were the first to report on a giant negative magnetoresistance (ratio $R_{H=0T}/R_{H=7T} \sim 10$) in the compounds LnBaCo$_2$O$_{5+\delta}$ (Ln = Eu, Gd). The negative magnetoresistance is seen for values $T < 250$ K $= T_N$, implying that the magnetoresistance is coupled to the antiferromagnetic order in these systems.

A simple picture for magnetoresistive phenomena is given by Taskin et $al.$ [153, 157] for single crystals GdBaCo$_2$O$_{5.5}$. It is based on a model where the magnetic structure is composed of weakly coupled ferromagnetic ladders with Ising-like magnetic moments. Since most probably GdBaCo$_2$O$_{5.5}$ is a narrow gapped semiconductor, where the carrier generation goes through formation of Co^{2+}-Co^{4+} pairs, the activation energy for these states may depend on the magnetic order. Applied magnetic fields align the FM ladders and reduce the insulating gap, which increases the carrier concentration and therefore decreases the resistivity. A typical resistivity plot for ρ_c (along c-direction) measured without and with field is shown in Figure 4.8a, while the resulting field dependent magnetoresistance is shown in Figure 4.8b. There is a large difference in magnetoresistance depending on the direction of the applied field: a field along the c-direction
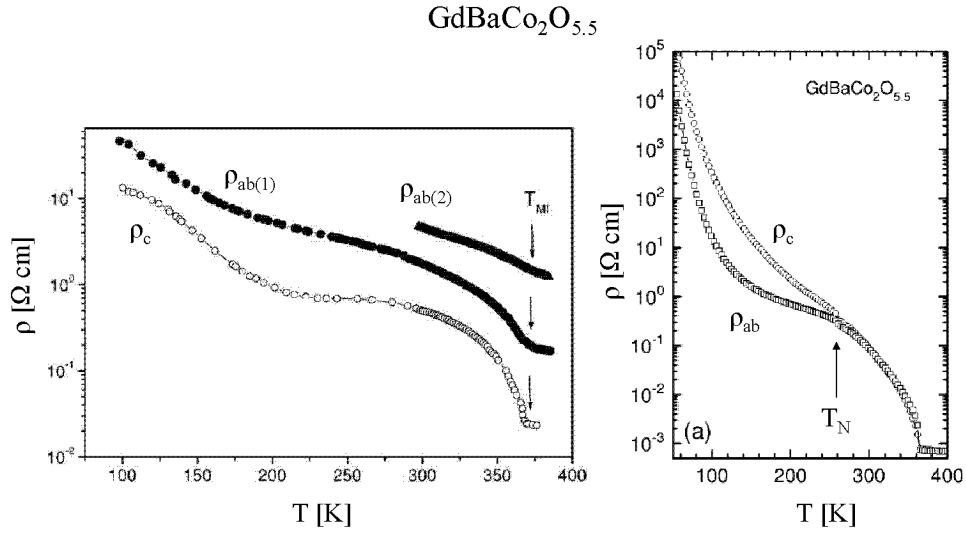
GdBaCo$_2$O$_{5.5}$

Figure 4.7: Resistivity measured along the c-axis and in the ab-plane for GdBaCo$_2$O$_{5.5}$. Left: after Khalyavin *et al.* [156]; Right: after Taskin *et al.* [150, 153].
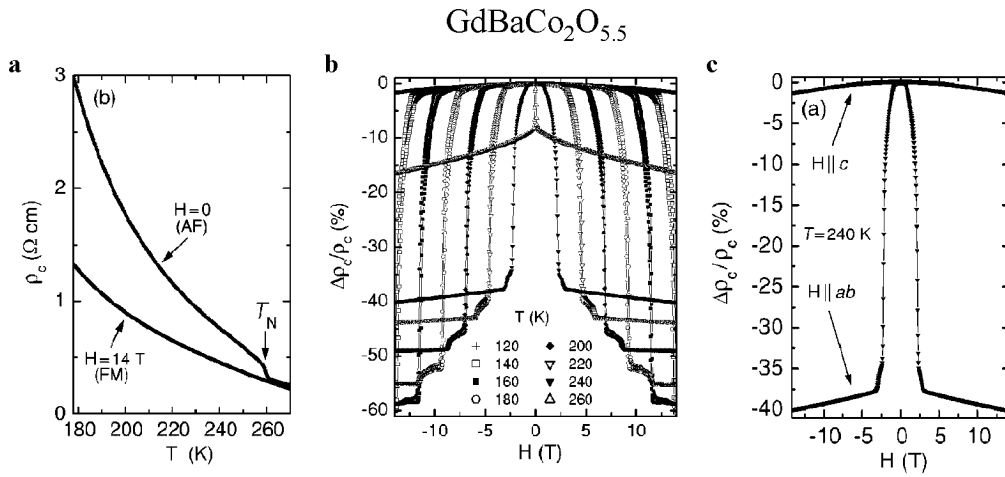
GdBaCo$_2$O$_{5.5}$

Figure 4.8: a) Temperature dependence of ρ_c measured at $H = 0$ and 14 T; b) Field dependence of $\Delta\rho_c/\rho_c$ magnetoresistance of GdBaCo$_2$O$_{5.5}$ crystals measured at several temperatures; c) Dependence of magnetoresistance $\Delta\rho_c/\rho_c$ on the field direction measured at $T = 240$ K for fields along or perpendicular to the ab-plane after Taskin *et al.* [150, 153].

hardly has an effect (Figure 4.8c), which again illustrates that the magnetic moments lie within the *ab*-plane.

4.3   Polycrystalline PrBaCo$_2$O$_{5+\delta}$

4.3.1   Effect of Oxygen Ordering on the Structural and Magnetic Properties

As explained in Section 4.2.1, for a layered cobaltite LnBaCo$_2$O$_{5.5}$ it is crucial that the oxygen vacancies are ordered to be sure that it has $P4/mmm$ symmetry. For this reason we synthesized PrBaCo$_2$O$_{5+\delta}$ powder samples with both varying oxygen contents and different synthesis histories. For all samples the structures were refined and bulk magnetization measurements performed. Depending on the synthesis history (for equal or similar oxygen contents) different crystallographic structures and also magnetization curves are found. The main achievement from this systematic study is the possibility to conclude from magnetization measurements on whether oxygen vacancies are ordered [143].

Synthesis

An initial ceramic material was synthesized by conventional solid state reaction, starting with the high-purity oxides Pr$_6$O$_{11}$, Co$_3$O$_4$ and barium carbonate BaCO$_3$. The powders were mixed, pressed into pellets and heated in air several times, the temperature being increased in steps from 1073 to 1413 K. The samples were then oxidized at 2 bar of pure oxygen by heating up to 1073 K for 24 h. The as-synthesized compound had an oxygen stoichiometry of $\delta = 0.79(1)$ as determined from iodometric titration analysis (Chapter 2.2). The powder was then separated into two badges, which were processed in two different ways:

1. Slowly Cooled (SC): the oxygen content of each compound of the first series was individually reduced by annealing (1123 K, 10 h) in an evacuated quartz ampoule filled with the appropriated amount of metallic copper getter and then cooled very slowly at a rate of 6 K/h.

2. Rapidly Quenched (RQ): different oxygen contents for the samples of the second series were obtained by annealing in helium flow at different temperatures (see Table 4.3) in a vertical tube furnace for 10 h. The samples were then dropped into liquid metal gallium, to achieve rapid quenching.

Since for these experiments it was very important to know the oxygen content δ of the different samples as precisely as possible, we used both iodometric titration and gas volumetric analysis to determine the oxygen content in the samples. These techniques, as described in Chapter 2.2 and Ref. [52], each have an accuracy of ±0.005. The agreement between the iodometric titration and volumetric analysis is within ±0.02. The oxygen contents for both sets of samples are given in Table 4.2 and 4.3.

Structure

We used room temperature x-ray powder diffraction with Cu Kα radiation (see Chapter 2.2 for details) to obtain the diffraction patterns (Figure 4.9). Analysis of this data was done with the program Fullprof [56]. For both sets of samples with low oxygen content ($\delta < 0.3$) the Rietveld

Table 4.2: Annealing temperature for the RQ samples (top), type of magnetic order and transition temperatures of both the RQ (top) and SC (bottom) PrBaCo$_2$O$_{5+\delta}$ compounds.

	δ	T_{an} [K]	Type of order	Transition temp. (K)
RQ	0.23(1)	1188	AFM	290(5)
	0.28(1)	1093	AFM	290(5)
	0.35(1)	993	Cluster Glass (CG)	305(5)
	0.48(1)	723	CG	224(5)
	0.54(1)	623	CG	222(5)
	0.56(1)	573	CG	198(5)
	0.59(1)	523	CG	169(5)
	0.71(1)	293	FM	140(3)
SC	0.17(1)		AFM	286(5)
	0.28(1)		CG	306(5)
	0.44(1)		CG	300(5)
	0.46(1)		CG	300(5)
	0.50(1)		AFM/FM	190(3)/229(3)
	0.60(1)		CG	186(10)
	0.79(1)		FM	167(3)

Table 4.3: Unit cell, lattice parameters, pseudocubic cell volume V and orthorhombic distortions $O_S = (a - b)/(a + b)$ of the RQ (top) and SC (bottom) PrBaCo$_2$O$_{5+\delta}$ compounds.

|	δ	Supercell	a(Å)	b(Å)	$c/2$(Å)	V(Å^3)	$O_S \times 10^3$
RQ	0.23(1)	$a_p \times a_p \times 2a_p$	3.9401(2)	3.9331(2)	3.7999(3)	58.886	0.88
	0.28(1)	$a_p \times a_p \times 2a_p$	3.9374(2)	3.9296(2)	3.8035(3)	58.849	0.99
	0.35(1)	$a_p \times a_p \times 2a_p$	3.9414(2)	3.9163(2)	3.8082(3)	58.782	3.19
	0.48(1)	$a_p \times a_p \times 2a_p$	3.9288(2)	3.9044(2)	3.8079(3)	58.412	3.11
	0.54(1)	$a_p \times a_p \times 2a_p$	3.9266(2)	3.9024(2)	3.8103(3)	58.386	3.08
	0.56(1)	$a_p \times a_p \times 2a_p$	3.9166(2)	3.9025(2)	3.8146(3)	58.304	1.81
	0.59(1)	$a_p \times a_p \times 2a_p$	3.9090(2)	3.9037(2)	3.8147(3)	58.210	0.68
	0.71(1)	$a_p \times a_p \times 2a_p$	3.9009(2)	3.8994(2)	3.8172(3)	58.064	0.20
SC	0.17(1)	$a_p \times a_p \times 2a_p$	3.9486(2)	3.9455(2)	3.7953(3)	59.137	0.38
	0.28(1)	$a_p \times a_p \times 2a_p$	3.9438(2)	3.9340(2)	3.8032(3)	59.007	1.25
	0.44(1)	$a_p \times 2a_p \times 2a_p$	3.9432(2)	3.9080(2)	3.8039(3)	58.617	4.48
	0.46(1)	$a_p \times 2a_p \times 2a_p$	3.9418(2)	3.9083(2)	3.8027(3)	58.584	4.26
	0.50(1)	$a_p \times 2a_p \times 2a_p$	3.9389(2)	3.9059(2)	3.8041(3)	58.526	4.21
	0.60(1)	$a_p \times a_p \times 2a_p$	3.9215(2)	3.9018(2)	3.8145(3)	58.365	2.52
	0.79(1)	$a_p \times a_p \times 2a_p$	3.8960(2)	3.8913(2)	3.8238(3)	57.970	0.60
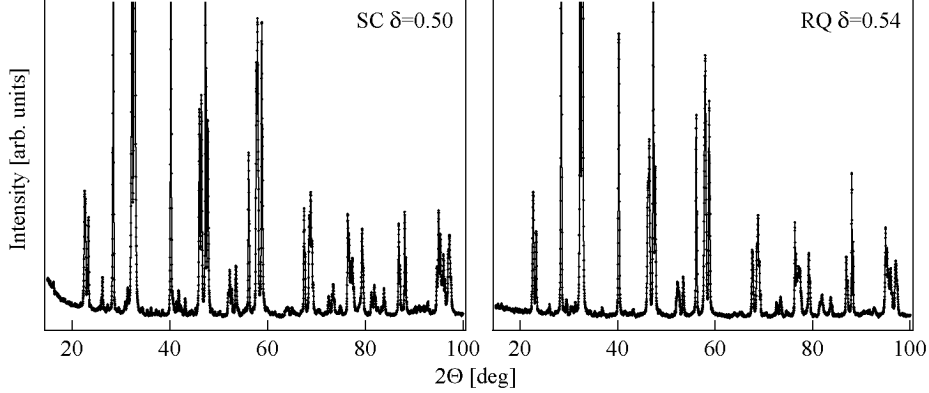
Figure 4.9: X-ray powder diffraction patterns for a SC ($\delta = 0.50$, left) and a RQ ($\delta = 0.54$, right) $PrBaCo_2O_{5+\delta}$ sample.

analysis reveals an orthorhombic *Pmmm* space group, with lattice parameters $a \sim b \sim a_p$ and $c \sim 2a_p$. Here a_p refers to the cell parameter of the ideal cubic perovskite. The orthorhombic distortion in the *ab*-plane is rather small (Figure 4.10 and table 4.3), which is in agreement with structural studies performed on $LnBaCo_2O_5$ ($\delta = 0$ and $Ln = $ Eu, Gd) [128], (Tb, Dy, Ho) [134], Y [103, 135], and Nd [152]. The lattice parameter c grows with δ, while a and b decrease. Increasing the oxygen content $\delta \in [0.35 - 0.7]$ results in a fast growing orthorhombic distortion (Figure 4.10a), which reaches its maximum value near $\delta \sim 0.5$ and almost vanishes again for $\delta > 0.7$. The strength of the orthorhombic distortion is found to depend on the synthesis history in the following way: the values of the lattice parameters b and c nearly coincide for both sets of samples, while the parameter a of the SC materials is systematically larger than the one of the RQ series, as shown in Figure 4.10b. In addition, the dependence of the c parameter upon oxygen content reveals a kink anomaly around $\delta \sim 0.5$ for both series. As seen in the inset of Figure 4.10b, the volume of the pseudocubic unit cell contracts almost linearly with increasing oxygen content in the whole measured δ range at an average rate of 0.3% per $\delta = 0.1$.

In order to explain the values of the a/b anisotropy close to $\delta = 0.5$ it was proposed that the oxygen/vacancy order within the PrO_δ layers results in an alternation of oxygen-rich and -deficient *ac*-planes, and consequently in a doubling of the unit cell along the b direction [128]. After close examination of our x-ray data (Figure 4.11), we find that the diffraction patterns of the SC samples in the $\delta \in [0.44 - 0.50]$ range exhibit a weak, yet sharp resolution-limited Bragg peak ((0 1 1) in $a_p \times 2a_p \times 2a_p$ supercell), in contrast to the diffraction patterns of the RQ samples, where only traces of broad diffuse scattering were detected. The pronounced Bragg scattering confirms the proposed long-range oxygen ordering in the slowly cooled samples with $\delta \in [0.44 - 0.50]$, while the existence of a broad (0 1 1) reflection indicates a disordered oxygen distribution in the PrO_δ layers of the rapidly quenched samples. **Therefore, the present x-ray results show that orthorhombic distortions alone are not sufficient to infer long-range oxygen ordering in the PrO_δ layers.**
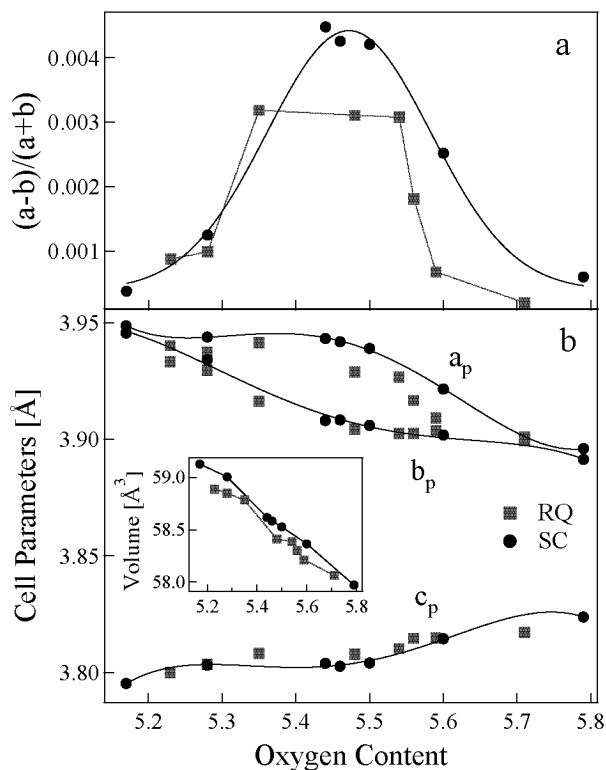
Figure 4.10: a) Orthorhombic distortion and b) lattice parameters of $PrBaCo_2O_{5+\delta}$ as a function of oxygen content for both SC (•) and RQ (■) compounds. The lines are guides to the eye. The inset in b) shows the volume of the pseudocubic unit cell.
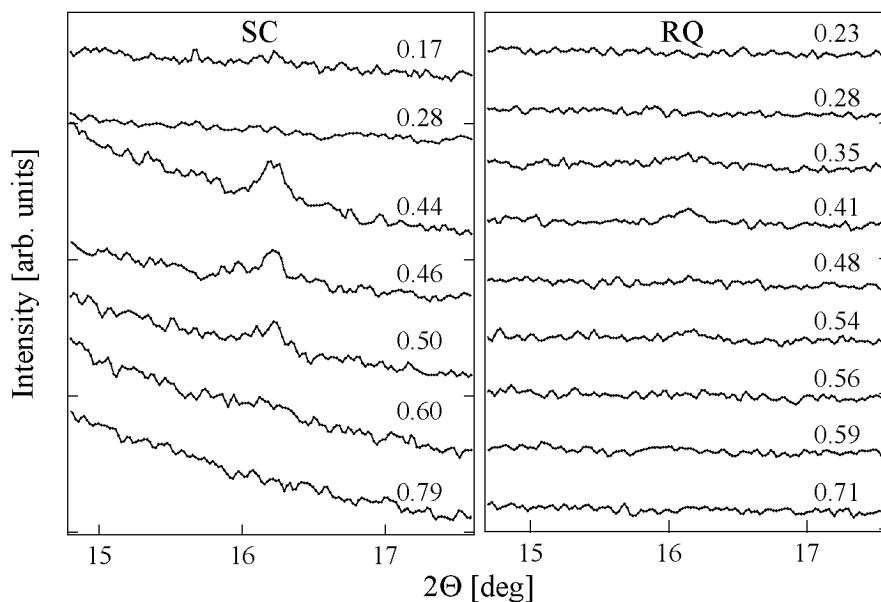
Figure 4.11: X-ray diffraction patterns around the 2Θ range corresponding to the (0 1 1) Bragg peak (emerging for oxygen vacancy ordering) for SC (left) and RQ (right) samples of type $PrBaCo_2O_{5+\delta}$.
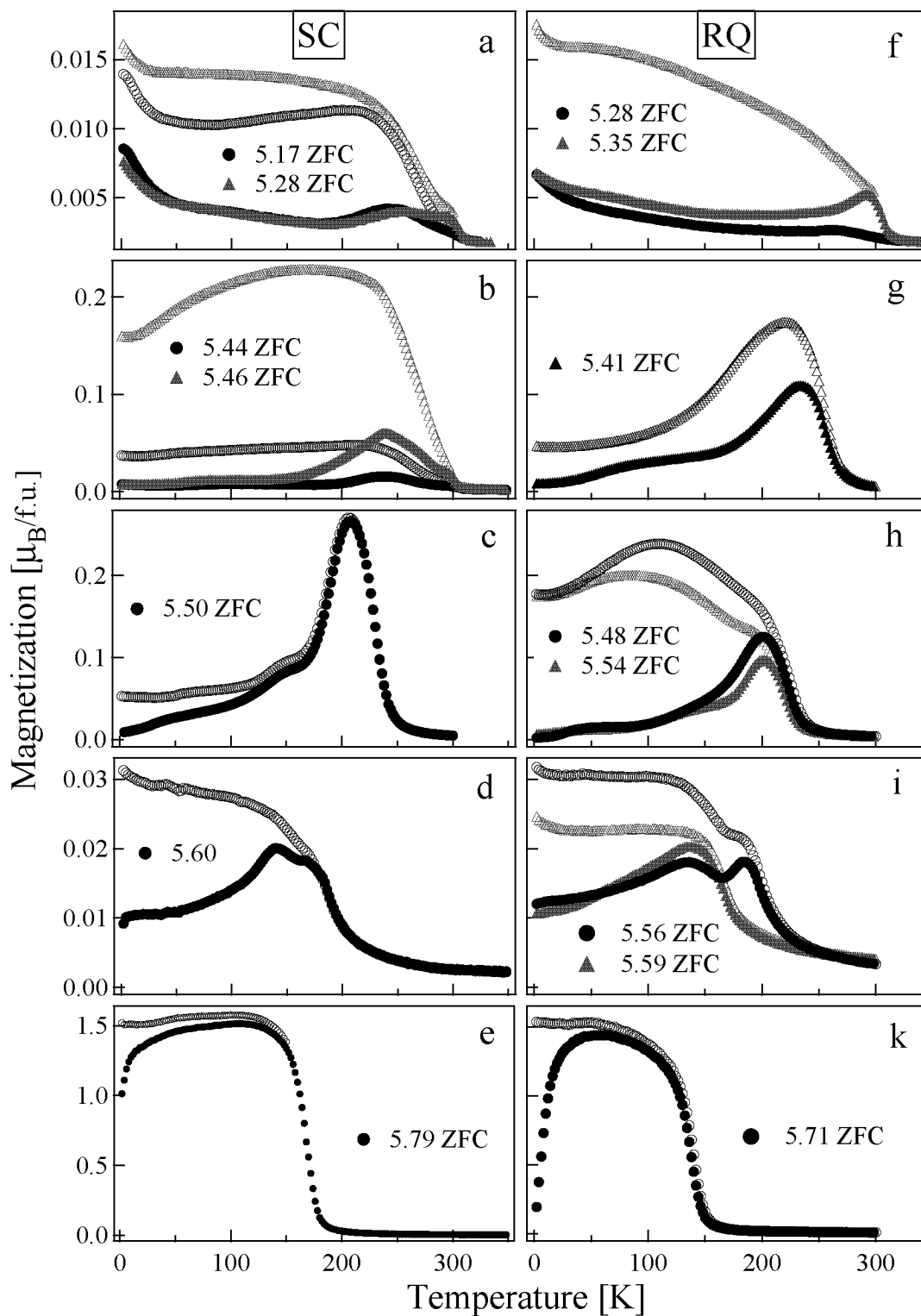
Figure 4.12: Magnetization of the slowly cooled (a-e) and rapidly quenched (f-k) series of $PrBaCo_2O_{5+\delta}$. Filled and open marks denote ZFC and FC magnetization measurements in $H = 0.1$ T, respectively. Note the different orders of magnitude of the magnetization for the different graphs.

Magnetic properties

We now turn to the analysis of the magnetic properties of these materials. According to our magnetic measurements, which are shown in Figure 4.12, all compounds with $\delta < 0.3$ exhibit a PM↔AFM transition around room temperature. The relevant transition temperatures are given in Table 4.2. Similarly to the structural aspect discussed above, the synthesis history of the compounds with low δ seems to have little influence on their magnetic properties.

On contrary, the magnetic properties of the compounds with $0.35 < \delta < 0.7$ depend strongly on oxygen nonstoichiometry as well as on synthesis history (Figure 4.12 b,c,d,g,h,i). The FC magnetization curves show broad maxima which strongly depend upon the external field, while ZFC magnetization data demonstrate a more complicated behavior, typically with broad, weak peaks. As illustrated in Figure 4.12, even a slight deviation of the oxygen content from the ideal composition of $\delta = 0.5$ considerably reduces the magnitude of the signal.

Only for the SC sample $PrBaCo_2O_{5.50}$ ($\delta = 0.50$, Figure 4.12 c), we find nearly coinciding ZFC and FC magnetization curves together with the well known successive PM↔FM↔AFM transitions [135, 130]. The magnitude of spontaneous magnetization for this sample is far above that of any other sample.

Despite the fact that the ZFC spontaneous magnetization of both the RQ and SC compounds with $\delta \in [0.35 - 0.7]$ shows a marked increase at T_C, followed by a drop below T_N, we do not believe that our samples, except for the slowly cooled $\delta = 0.5$ sample, display simple long-range magnetic ordering. The large difference between ZFC and FC magnetization curves indicates rather the existence of a cluster-glass state as earlier reported in $R_{1-x}Sr_xCoO_3$ (R = La, Nd) [74, 158, 159]. The strong variation of the magnetization with δ shows that only a fraction of the sample volume is in a FM ordered state. Since in addition our field-dependent magnetization measurements $M(H)$ at different temperatures below T_{cg} show a lack of saturation in external fields up to 9 T (not shown), we conclude that upon oxygen doping the system separates into oxygen-rich clusters (with predominant FM Co^{3+}/Co^{4+} states) and an oxygen-poor matrix (with predominant AFM Co^{2+}/Co^{3+} states). In Figure 4.13 we show a schematic view of the cluster glass state as compared to the long range ordered one. Since in the oxygen ordered SC $\delta = 0.5$ compound only Co^{3+} ions are present, we suggest that the spontaneous magnetic moment comes from ferrimagnetic ordering of the Co^{3+} spins, as also proposed by Plakthy *et al.* [144] in a recent paper.

$PrBaCo_2O_{5+\delta}$ samples in the range $\delta > 0.7$ exhibit a qualitatively similar behavior for both series, namely the observation of a PM↔FM transition (Figure 4.12 e,k). The existence of a ferromagnetic state can be explained within the framework of a percolating network of FM clusters, when the concentration of oxygen-rich domains exceeds a critical value[3]. The discrepancy observed by García-Muñoz *et al.* [160] between DC magnetization measurements at $H = 1$ T, where FM behavior was observed, and zero-field neutron powder diffraction measurements, where AFM order was found, can be explained within such a percolation model, since the concentration of FM clusters is expected to grow as a function of increasing magnetic field.

---

[3]Note: in an independent study, the critical value for the appearance of FM ordering was found to be $\delta > 0.85$ [160], a value larger than the one found in the current work. Clearly, more detailed structural (preferably neutron diffraction as well as synchrotron X-ray) and magnetic relaxation studies are necessary to understand these discrepancies.
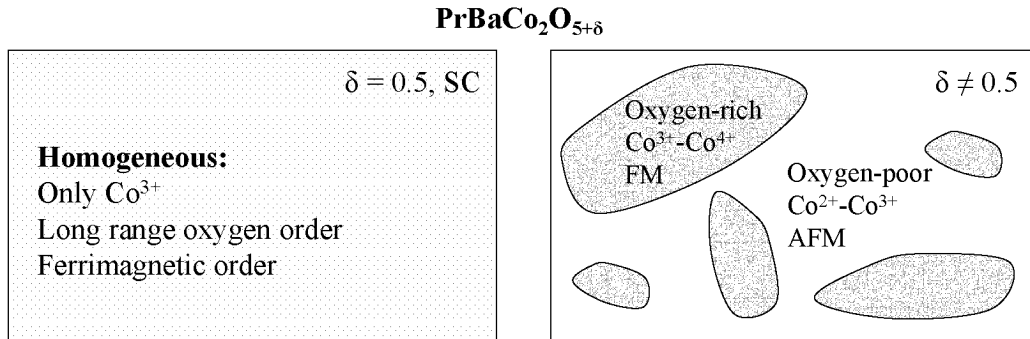
PrBaCo₂O₅₊δ

Figure 4.13: Schematic view of the magnetism and oxygen order/disorder in PrBaCo₂O₅₊δ for a) slowly cooled $\delta = 0.5$, oxygen ordered and long range magnetic order; and b) $\delta \neq 0.5$, cluster spin glass with separation into oxygen-rich FM domains and oxygen poor AFM matrix.
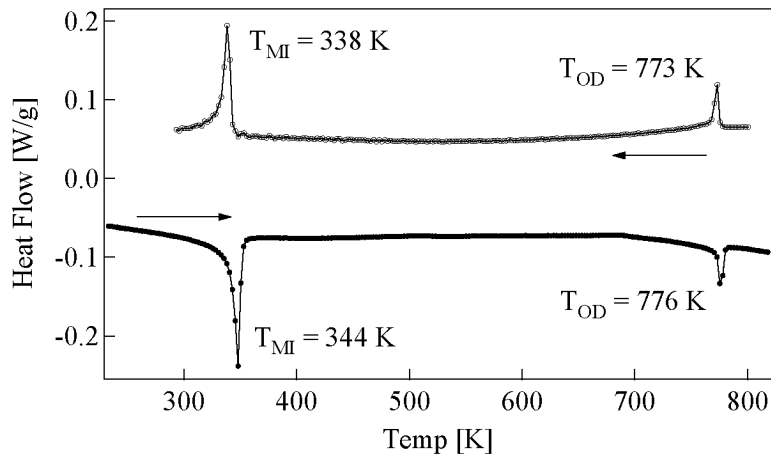
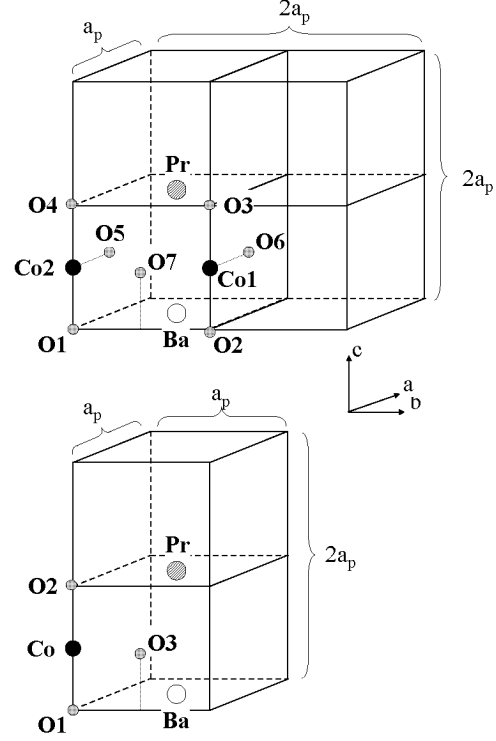**Figure 4.14:** Differential Scanning Calorimetry for PrBaCo₂O₅.₄₈ on heating and on cooling.

4.3.2   Oxygen Order-Disorder Phase Transition at High Temperature

The motivation behind the high temperature study is the differential scanning calorimetry measurement, which revealed two transitions (Figure 4.14). One can be attributed to the so called metal-insulator transition [128, 134, 155], taking place at $T_{MI} = 344$ K. The other one, **which has not been reported before**, is located at a higher temperature $T_{OD} = 776$ K. Since nothing was known about this second transition we decided to perform high temperature neutron powder diffraction in order to find out if the transition is a structural one and if so, what the high temperature structure is [161]?

The PrBaCo₂O₅₊ₓ sample used for these high temperature measurements has an oxygen content of 5.48±0.01 as determined by iodometric titration, see Chapter 2.2 and [52] (synthesis was according to the SC process described in Section 4.3.1). We checked by thermogravimetry in inert atmosphere, that there is no mass change (oxygen loss) of the sample up to 825 K. This ensures constant oxygen content within the whole temperature range of our NPD measurements. Phase purity was checked with a conventional x-ray powder diffractometer (Cu$K\alpha$

Atom	Multipl., Wyckoff Lett.	x	y	z
Ba	2o	0.5	y	0
Pr	2p	0.5	y	0.5
Co1	2r	0	0.5	z
Co2	2q	0	0	z
O1	1a	0	0	0
O2	1e	0	0.5	0
O3	1g	0	0.5	0.5
O4	1c	0	0	0.5
O5	2s	0.5	0	z
O6	2t	0.5	0.5	z
O7	4u	0	y	z
Ba	1c	0.5	0.5	0
Pr	1d	0.5	0.5	0.5
Co	2g	0	0	z
O1	1a	0	0	0
O2	1b	0	0	0.5
O3	4i	0	0.5	z

Table 4.4: Site notation in the $Pmmm$ (top) and $P4/mmm$ (bottom) space group.


Figure 4.15: Site location in the $Pmmm$ (top) and $P4/mmm$ (bottom) space group.

radiation). Differential scanning calorimetry (DSC) was performed on a NETZSCH DSC 204 N1 in the temperature range from 250 to 828 K.

The neutron powder diffraction measurements were carried out on the high resolution diffractometer HRPT [48] at SINQ (PSI, Switzerland) in the angular range $7° < 2\Theta < 165°$ and temperature range $300\,\mathrm{K} \leq T \leq 820\,\mathrm{K}$, using a wavelength $\lambda = 1.494\,\text{Å}$. The sample holder was made out of steel and and tightly sealed under helium atmosphere in order to guarantee a constant oxygen content even at high temperatures. The NPD data were refined using the program Fullprof [56].

The NPD for temperatures $T \leq 780\,\mathrm{K}$ could be refined using the $Pmmm$ space group with orthorhombic unit cell $a_p \times 2a_p \times 2a_p$. According to the international tables for crystallography, the positions of the atoms for this symmetry are as given in Table 4.4 and the locations within the unit cell are shown in Figure 4.15. A schematic view of the structure in the bc-plane is shown in Figure 4.16. We find that the O4 site is almost empty, while the O3 position is nearly fully occupied. This results in the well known planes of Co_2O_5 pyramids and Co_2O_6 octahedra parallel to the ac-plane, which alternate along the b-direction.

For structural refinement several restrictions were needed in order not to reduce the number of free parameters. The symmetry of the positions justifies the chosen constraints. The parameters which were refined without restrictions are the lattice parameters and the crystallographic positions according to Table 4.4. Restrictions were applied for the occupancies of the oxygen positions in so far as it was assumed that oxygen was lost only from the positions O3 and O4 located in the Pr ion plane. Trial runs without fixed oxygen occupancies showed that indeed the only position with oxygen loss at room temperature is the O4 one. The other constraint concerns the anisotropic temperature factors (B factors): The B factors for the ions Co1/Co2,

Orthorhombic, Pmmm
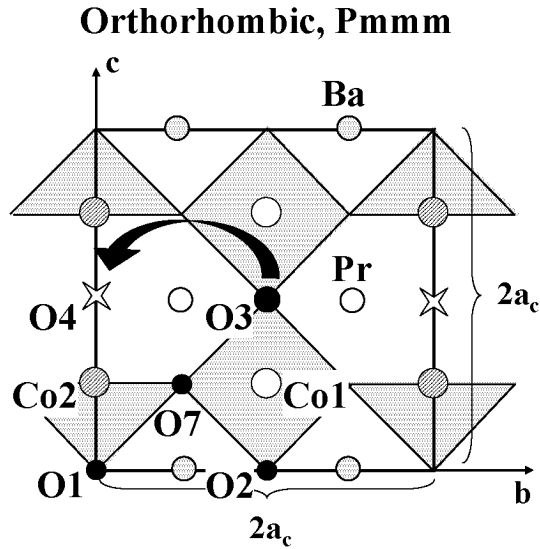
Figure 4.16: Schematic view of the $PrBaCo_2O_{5.48}$ *Pmmm* structure in the *bc*-plane. For clarity only O1, O2, O3, O4 and O7 are shown. The arrow indicates the high temperature rearrangement of oxygen.

as well as for O1/O2, O3/O4 and O5/O6/O7 were fixed to the same value.

A typical Rietveld plot at 300 K is shown in Figure 4.17. The difference plot only shows large variations around the positions of the strongest peaks, which come from the steel container. Refined structural parameters, occupancies, χ^2 and R_{Bragg} values for representative temperatures are shown in Table 4.5. The temperature dependent refined lattice parameters, oxygen occupancies and oxygen contents are shown in Figure 4.18. The obtained oxygen contents (inset in Figure 4.18b) agree within 1.6% with the value of 5.48 obtained by iodometric titration. The temperature dependence of the lattice parameters and site occupancies of O3 and O4 will be discussed later in this Section.

As mentioned, the DSC measurement reveals a first transition at $T_{MI} = 344$ K (Figure 4.14). At this temperature, our neutron diffraction measurements display a jump of the lattice parameters (Figure 4.18a). We also see a marked increase of the Co1-O7 distance and a simultaneous shrinking of the Co2-O7 distance (Figure 4.19). The temperature dependence of these distances leads to an increased (decreased) volume of the octahedra (pyramids). This behavior has been reported before by Frontera *et al.* [155] for a $GdBaCo_2O_{5.5}$ powder sample investigated by ultrahigh resolution synchrotron radiation. Frontera *et al.* associate the metal-insulator transition to a spin-state transition (LS to higher spin) of the Co1 ions located in the octahedral environment: since Co^{3+} ions in a higher spin state have a larger ionic radius due to the less localized electrons, the volume of the octahedra has to increase. Due to the planes of octahedra along the *a*-direction, the only direction of expansion is the *b*-direction, thus moving the O7 ions towards the Co2 ion situated in the pyramidal environment.

The DSC measurement shows a second transition at $T_{OD} = 776$ K (Fig. 4.14). A typical NPD for $T = 820$ K is shown in Fig. 4.20. In the NPD patterns one sees a merging of peaks across T_{OD} for which $k_2 = 2h_1$ (in orthorhombic notation), i.e. merging of (4 0 0) with (0 8 0), see inset in Fig. 4.20. As can be seen in Fig. 4.18a, the values of the lattice parameters a and $b/2$ converge with increasing temperature, indicating that the symmetry evolves from orthorhombic
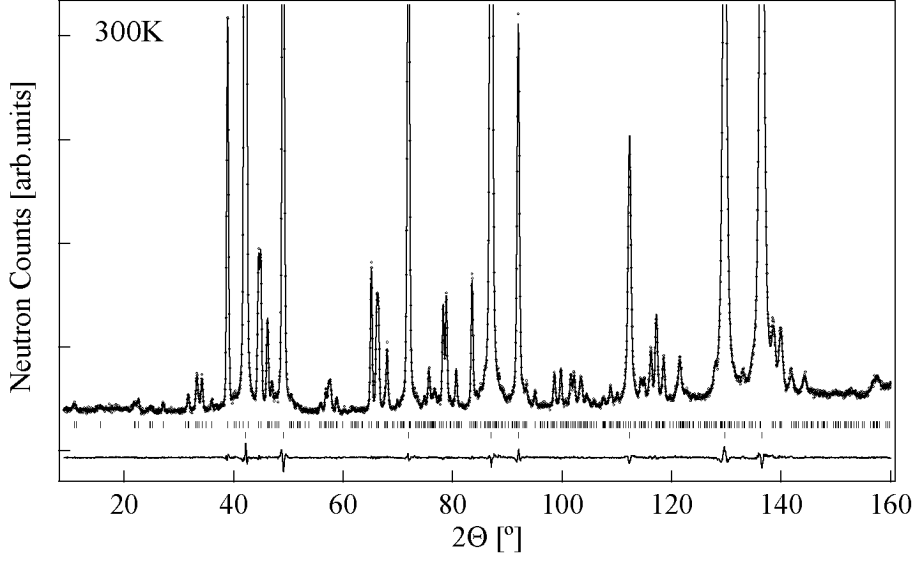
Figure 4.17: Observed, calculated and difference NPD pattern for PrBaCo$_2$O$_{5.48}$ at 300 K. The peak positions are shown by ticks ı: the upper set comes from the sample, the lower one from the steel container. The scale of the y-axis is such that the steel reflections are cut.

Table 4.5: Structural Parameters for PrBaCo$_2$O$_{5.48}$ for $T \leq 780$ K, refined in $Pmmm$ space group.

$Pmmm$	300 K	375 K	600 K	750 K	775 K	780 K
a [Å]	3.9068(1)	3.8978(1)	3.9104(1)	3.9284(1)	3.9353(1)	3.9381(1)
b [Å]	7.8807(1)	7.8981(1)	7.9316(1)	7.9408(1)	7.9354(2)	7.9318(2)
c [Å]	7.6145(2)	7.6438(2)	7.6782(2)	7.7004(2)	7.7031(2)	7.7039(2)
Ba(y)	0.2508(15)	0.2515(15)	0.2545(13)	0.2512(16)	0.2476(19)	0.2456(21)
Pr(y)	0.2670(15)	0.2675(20)	0.2624(16)	0.2657(21)	0.2675(23)	0.2682(23)
Co1(z)	0.2524(18)	0.2509(24)	0.2523(20)	0.2537(26)	0.2510(30)	0.2502(32)
Co2(z)	0.2481(18)	0.2498(25)	0.2444(20)	0.2438(26)	0.2454(30)	0.2480(32)
O5(z)	0.3055(11)	0.3048(13)	0.3043(11)	0.3034(14)	0.2991(19)	0.2973(23)
O6(z)	0.2669(14))	0.2653(17)	0.2645(13)	0.2766(13)	0.2791(18)	0.2816(21)
O7(y)	0.2405(08)	0.2370(11)	0.2376(08)	0.2366(11)	0.2375(13)	0.2370(15)
O7(z)	0.2836(09)	0.2864(10)	0.2870(08)	0.2824(10)	0.2826(12)	0.2838(13)
Occ. O3	0.92(2)	0.86(3)	0.84(2)	0.73(4)	0.70(4)	0.52(5)
Occ. O4	0.06(1)	0.14(2)	0.14(2)	0.33(3)	0.37(4)	0.50(5)
Ox. Cont.	5.49(1)	5.50(2)	5.49(2)	5.53(2)	5.54(3)	5.52(3)
χ^2	3.14	1.55	2.79	2.20	2.57	2.63
R$_{Bragg}$	4.77	4.60	4.89	4.90	5.32	5.05
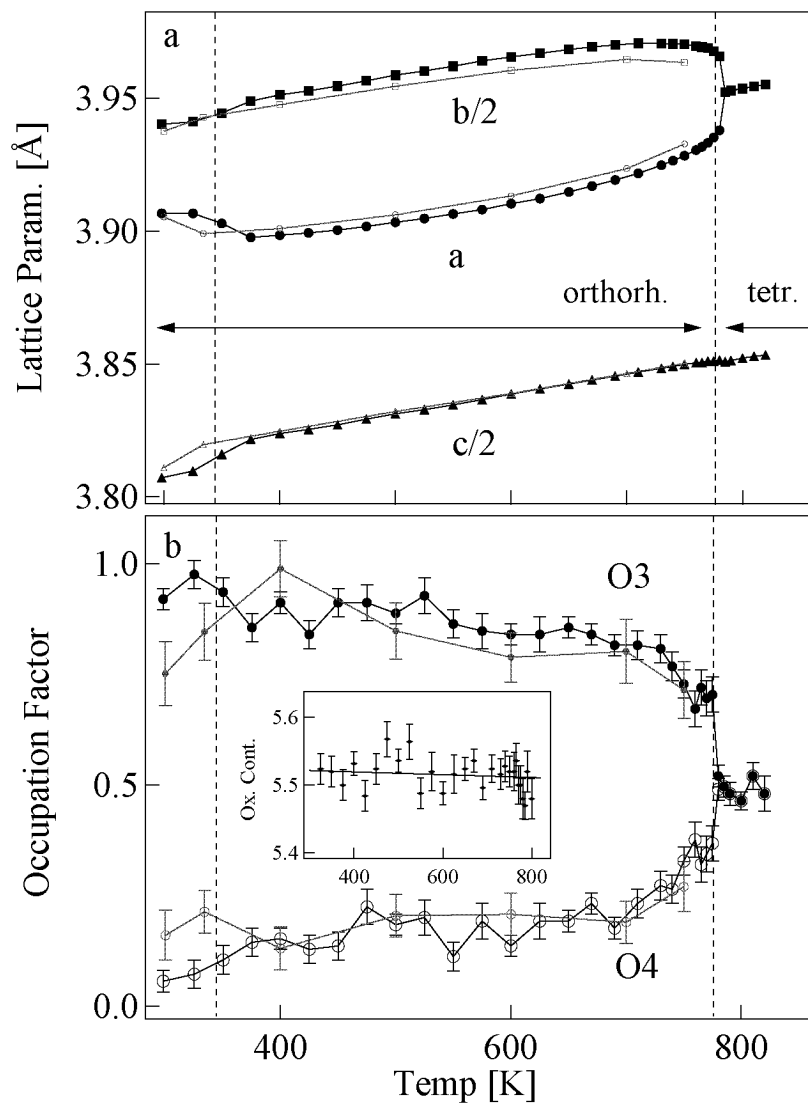
Figure 4.18: Temperature evolution on heating (big symbols) and cooling (small symbols) of a) the lattice parameters; b) the occupancy of the oxygen ion sites O3 and O4, inset: Oxygen Content. The vertical lines mark the positions of T_{MI} and T_{OD} as determined by DSC (Figure 4.14).
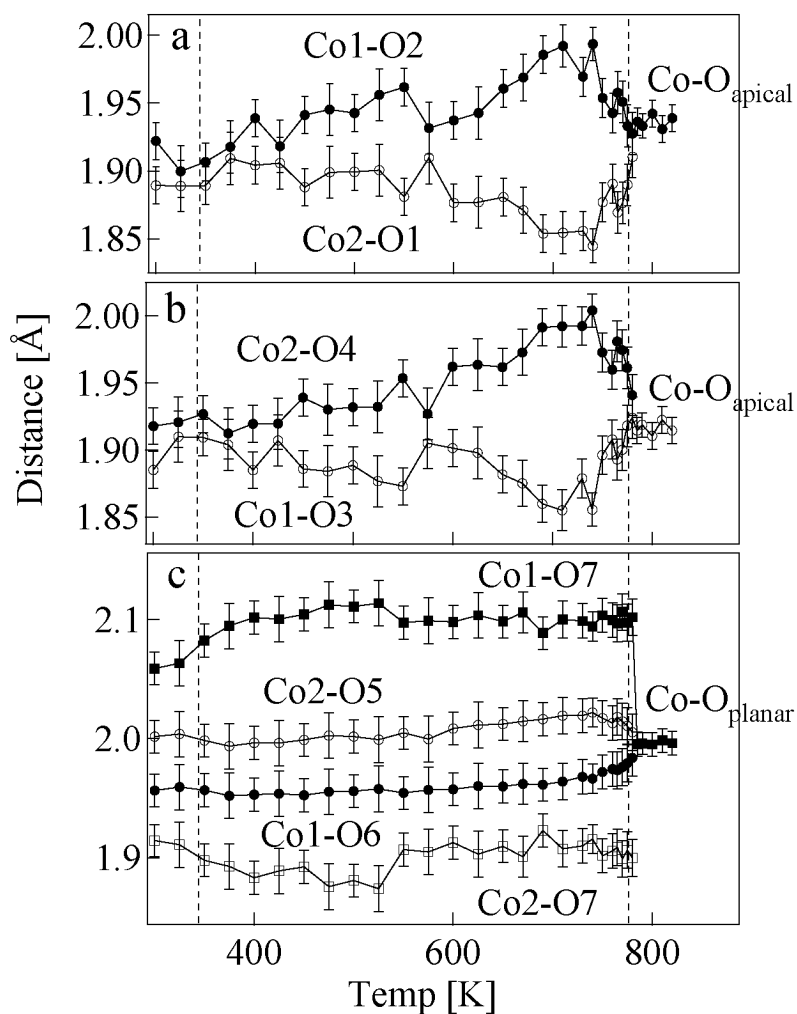
Figure 4.19: Temperature evolution of the Co-O distances for a) Co1-O2, Co2-O1; b) Co1-O3, Co2-O4; and c) Co1-O7, Co2-O5, Co1-O6 and Co2-O7 (Orthorhombic notation). The vertical lines mark the positions of T_{MI} and T_{OD} as determined by DSC (see inset in Fig. 4.14).

Table 4.6: Structural Parameters for $PrBaCo_2O_{5.48}$ for $T \geq 785\,K$, refined in $P4/mmm$ space group.

$P4/mmm$	785 K	790 K	820 K
a [Å]	3.9524(1)	3.9530(1)	3.9553(1)
c [Å]	7.7018(1)	7.7028(1)	7.7068(2)
Co(z)	0.2514(10)	0.2504(09)	0.2514(13)
O3(z)	0.2872(03)	0.2867(02)	0.2867(04)
Occ. O2	0.51(2)	0.50(2)	0.49(2)
Ox. Cont.	5.51(2)	5.50(2)	5.49(2)
χ^2	2.8	2.9	1.5
R_{Bragg}	4.7	4.6	6.0

to tetragonal. Indeed, above 780 K we obtain good refinements (Table 4.5) using the tetragonal space group $P4/mmm$ (unit cell $a_p \times a_p \times 2a_p$). Additionally, we observe a redistribution of oxygen ions: the oxygen O4 occupancy increases at the expense of the O3 one, until the two sites display equivalent occupancies (see Fig. 4.17 left and Fig. 4.18b). No change of the occupancy of both planar and the other apical oxygen ions occurs across T_{OD}. This redistribution of oxygen leads to a disordered state in view of oxygen vancancies, since the planes of CoO_5 pyramids and CoO_6 octahedra no longer alternate along the b-direction.

The transition is reversible, as can be seen in Figures 4.14 and 4.18. A slight hysteresis effect is observed in the DSC measurement, where the transition temperature T_{OD} on cooling is by 3 K lower than on heating and T_{MI} lies 6 K below the initial value. The NPD data taken on cooling is from a first NPD experiment performed on HRPT (with $\lambda = 1.886$ Å and the sample can also closed in Helium atmosphere), where we first saw the high temperature structural transition. The oxygen contents of the two samples after the NPD experiments were 5.46(2) and 5.58(3) for the first and second experiment, respectively. The value 5.46 is extracted from the Rietveld refinement of the 300 K data (Figure 4.18). After the second experiment, where we had not taken NPD data on cooling, we made an XPD measurement on the sample and by comparing the so obtained lattice constants to the ones in Chapter 4.3.1 (Figure 4.10) we could conclude on the oxygen content. Oxygen content determination by the iodometric titration method gave an oxygen content of 5.56(1), which is in good agreement with the one extracted from the XPD data. This additionally proves that the oxygen content determination via the lattice parameters given in Chapter 4.3.1 is reliable.

To conclude, the redistribution of oxygen leads to disorder in the system, since the planes of CoO_5 pyramids and CoO_6 octahedra are no longer ordered along the b-direction: the layered structure along the b-direction is lost.

4.3.3 Polaronic Conductivity in $PrBaCo_2O_{5.48}$

We were also interested in the transport properties of $PrBaCo_2O_{5.48}$ in the same temperature region. DC Resistivity and thermoelectric power were measured[4] in He atmosphere (300 K to 830 K) by the four-probe method on a bar-shaped 2x2x15 mm³ ceramic $PrBaCo_2O_{5.48}$ sample [162]. Additionally, coulometric titration[4] (see chapter 2.2 and [163]) was used to determine the equilibrium oxygen content in $PrBaCo_2O_{5+\delta}$ $0.16 \leq \delta \leq 0.76$ cobaltites at different values of

---

[4]Measurements were done by M. V. Patrakeev, I. A. Leonidov and V. L. Kozhvnikov from the Insitute of Solid State Chemistry RAS in Ekaterinburg, Russia on an instrument designed in their institute.
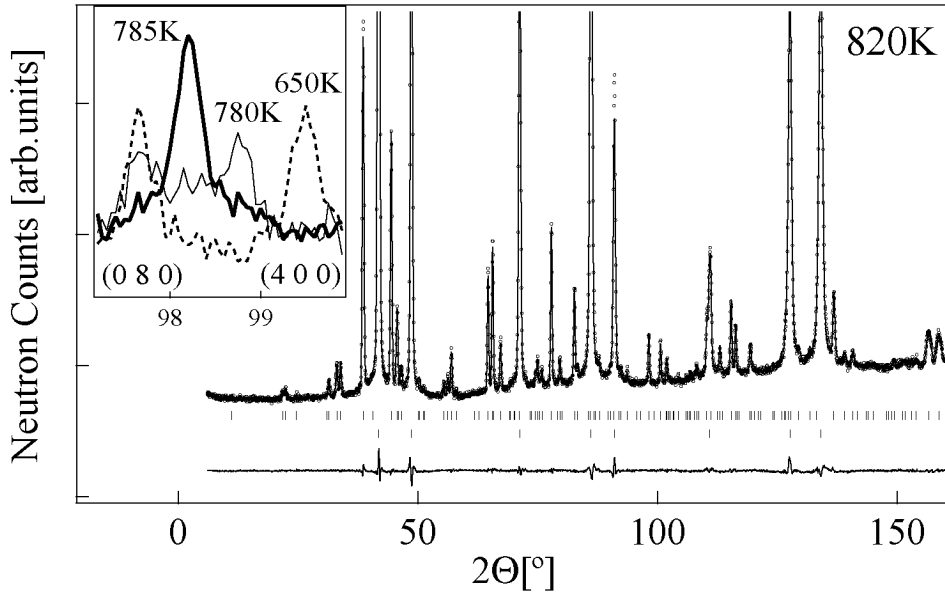
Figure 4.20: Observed, calculated and difference NPD pattern for $PrBaCo_2O_{5.48}$ at 820 K. The peak positions are shown by ticks ı: the upper set comes from the sample, the lower one from the steel container. The scale of the y-axis is such that the steel reflections are cut. The inset shows the merging of the (0 8 0) and (4 0 0) peaks (indexed in the orthorhombic notation) on crossing T_{OD}.

temperature and partial oygen pressure. A four probe arrangement was used to simultaneously measure high temperature conductivity and thermopower.

We now discuss in some details our transport data. The drop in resistivity ρ at $T_{MI} = 344$ K and subsequent weak temperature increase (Figure 4.21 a) seems to indicate metallic conductivity in $PrBaCo_2O_{5.48}$. However, the experimental value $\rho \sim 1200$ $\mu\Omega$ cm above T_{MI} ($\rho_{ab} \sim 600$ $\mu\Omega$ cm according to single crystal measurements by Taskin et $al.$ [157]) is still higher than the resistivity of many 3d-metal oxides [164]. Furthermore, the temperature dependence of the resistivity in $PrBaCo_2O_{5.48}$ does not show a simple metallic behavior. For a metal it would be expected that resistivity increases according to Bloch's T^5 law for temperatures below the Debye temperature Θ_D[5] and for $T > \Theta_D$ the increase would be linear in T. No such behavior can be seen in our data, which show a very weak temperature dependence of $\rho(T)$.

Instead, above T_{MI} the weak temperature dependence of the conductivity ρ is consistent with a temperature-activated mobility, similar to that proposed for $La_{1-x}Sr_xCoO_3$ [164] and $Ca_2Co_{0.8}Ga_{0.2}O_{4.8}$ [166]. The positive sign of our thermopower measurements for $T > 570$ K (Figure 4.21 b) indicates that holes form the majority charge carriers. Hole conductivity is usually related to the presence of Co^{4+} ions in cobaltites [164, 166, 33] and thermally-activated mobility is an important characteristic of small polaron conduction. We suggest that the high temperature transport properties in $PrBaCo_2O_{5.5}$ can be explained by thermally activated polaronic hole conduction [161].

This model incorporates charge disproportionation [164, 166, 33], which is the origin of the

---

[5]The Debye temperature is defined by $k_B\Theta_D = \hbar\Omega_D$, where Ω_D is the Debye frequency which is such that the total number of excited states is $3rN$ (r = number of atoms in the unit cell, N = number of unit cells). For $T > \Theta_D$ all states are excited with the same probability. [165].
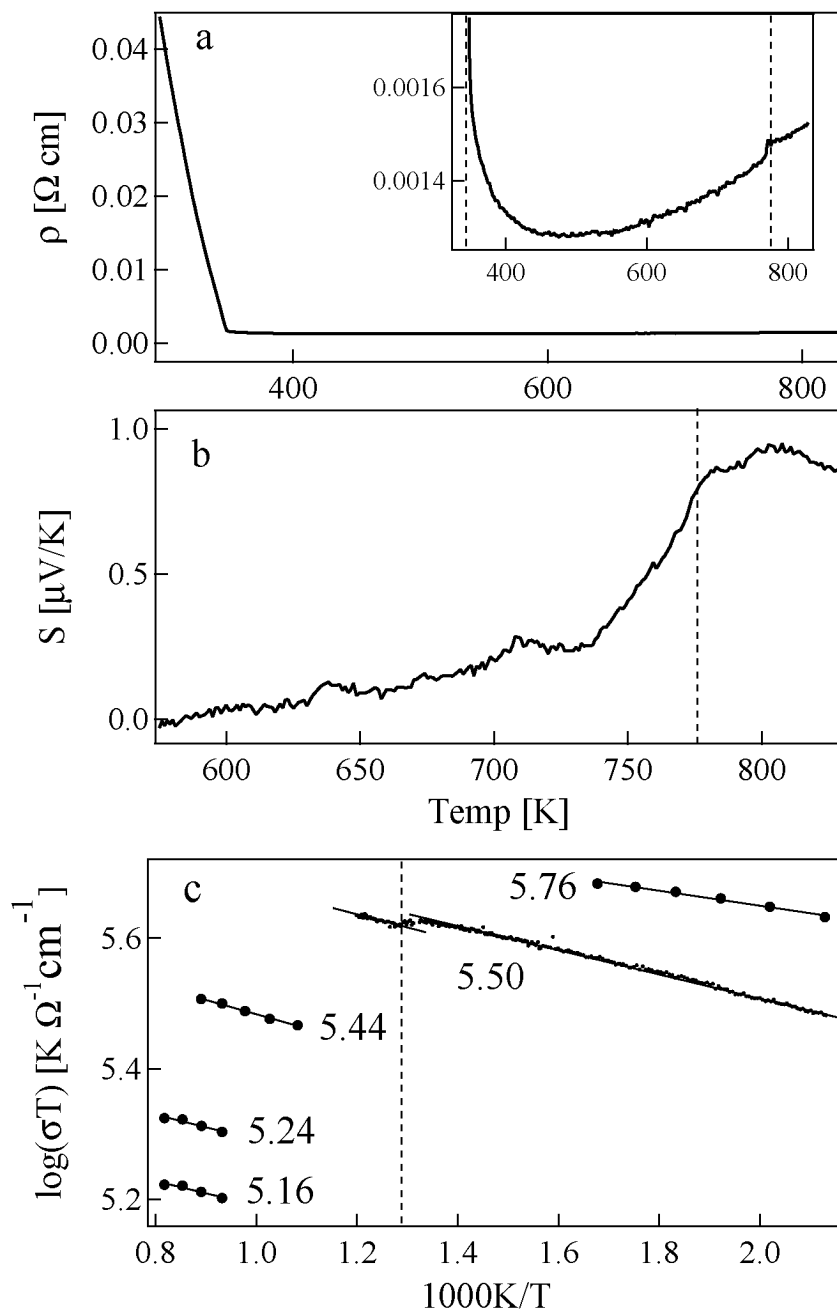
Figure 4.21: Temperature dependence of the a) DC resistivity ρ and b) thermoelectric power for S of PrBaCo$_2$O$_{5.5}$; c) Arrhenius plot for PrBaCo$_2$O$_{5+\delta}$ (δ = 0.16, 0.24, 0.44, 0.50 and 0.76).

mobile holes. Charge disproportination involves the transfer of electrons between adjacent Co^{3+} ions in the form 2Co^{3+} → Co^{2+} + Co^{4+}. Sites consisting of a Co^{2+} or Co^{4+} ion and the associated lattice distortions are occupied by an n- or p-type small (localized) polaron, respectively. In our case the electrons are localized at the Co^{2+} ion site, while the holes hop over the array of Co^{3+} and Co^{4+} ions. Isotomin et $al.$ [166] suggest that the jump of a polaron from a Co^{4+} to a Co^{3+} ion is facilitated by an intermediate oxygen ion. This suggests that the conduction takes place in the octahdral CoO$_6$ planes, which in turn would be an indication that the Co^{4+} ions are preferably located at the octahdral position. From bond valence sum considerations this is likely, but since the charge disproportination is a dynamic process and the hopping frequency large, this leads to the observation of an average valence [33], meaning that experimentally the charge disproportionation can not be resolved. What we can say is that in a time average the Co^{2+} are probably located at the pyramidal sites, whereas the Co^{3+} and Co^{4+} are at the octahedral sites.

The polaronic hopping conductivity is given by

$$\sigma = |e|\mu p = |e|p\frac{\mu_0}{T}exp\{-\frac{E_a}{k_B T}\} \quad , \tag{4.1}$$

where E_a is the mobility activation energy, μ and p represent mobility and a volume concentration of holes (Co^{4+}), respectively [167]. With temperature the exponential term increases, while the pre-exponential factor decreases. Usually, the exp$\{-E_a/k_B T\}$ dominates and conductivity $\sigma(T)$ increases with temperature. However, an opposite temperature dependence of $\sigma(T)$ can be observed for low activation energies E_a.

As follows from Equation (4.1) log σT versus $1/T$ enables estimation of the activation energy E_a (Arrhenius plot, shown in Fig. 4.21 c). A nearly constant activation energy $E_a \sim 0.04$ eV (slope of the curves) was obtained from these plots $independently$ of the oxygen content over the wide range of $0.16 \leq \delta \leq 0.50$ involved in the analysis.

In literature the compounds with $\delta \leq 0.4$ LnBaCo$_2$O$_{5+\delta}$ are reported to be semiconductors and do not exhibit a MI transition [153]. Consequently, since our compounds with $0.16 \leq \delta \leq 0.50$ display the same activation behaviour, we conclude that the low resistivity at high temperatures as well as the weak temperature dependence of $\rho(T)$ for $\delta = 0.5$ is more consistent with a temperature-activated hole mobility (small polaron conduction), than with metallic conductivity.

The obtained low value of $E_a \sim 0.04$ eV is not exceptional for $3d$ perovskites. An activation energy of $E_a \sim 0.15$ eV was found in the Ruddlesden-Popper ferrites Sr$_3$Fe$_2$O$_{6-\delta}$ [92], which exhibit a quasi-2D conductivity in the FeO$_2$ planes. And a very low value of $E_a \sim 0.08$ eV was recently reported for La$_{0.4}$Sr$_{0.6}$CoO$_{3-\delta}$ [164].

The anomalies in the temperature behaviors of both conductivity $\sigma(T) = 1/\rho(T)$ and thermoelectric power $S(T)$ (Fig. 4.21a and b) across the phase transition at $T_{OD} = 776$ K can be explained by a decrease of the charge carrier concentration p. Oxygen disorder above T_{OD} breaks an ideal alternation of octahedra and pyramids and hampers hole creation. It follows from equation (4.1) that a reduction of p results in a decrease of conductivity $\sigma(T)$. On the other hand, according to the equation for thermopower

$$S = \frac{k_B}{|e|} \ln \frac{1-p}{p} \quad , \tag{4.2}$$

a decrease of hole concentration p results in an increase of S. Both effects are observed in our measurements.

The oxygen disorder above T_{OD} can favor ionic conductivity due to the random distribution of

Table 4.7: Specifications of our four single crystals $Ln\mathrm{BaCo_2O_{5.5}}$, $Ln = \mathrm{Gd}$, Dy, $\mathrm{Dy_{0.1}Tb_{0.9}}$.

Ln	m [mg]	length [mm]	width [mm]	depth [mm]	volume [mm^3]
Gd 1	211.1	7	3	2	42
Gd 2	146.5	4	3	2	24
Dy	56.4	3	3	1	9
$\mathrm{Dy_{0.1}Tb_{0.9}}$	890.3	15	5	2	150

the structural oxygen vacancies over the O3 and O4 positions. It has been shown that both oxygen vancancy disorder and a large number of oxygen vacancies favor ionic conductivity. This makes the high temperature phase of $\mathrm{PrBaCo_2O_{5.48}}$ an ideal environment for ionic conduction. Oxygen diffusion measurements have to be conducted in order to prove this assumption.

To conclude, the transport measurements suggest a semiconducting rather than metallic behaviour above T_{MI}. The activation energy is comparable to that of semiconducting $\mathrm{PrBaCo_2O_{5+\delta}}$ ($\delta \leq 0.44$) and suggests a thermally activated hole (polaronic) conductivity. Oxygen vacancy disorder above T_{OD} reduces hole conductivity, due to the destruction of the ideally ordered network of pyramidal and octahedral planes.
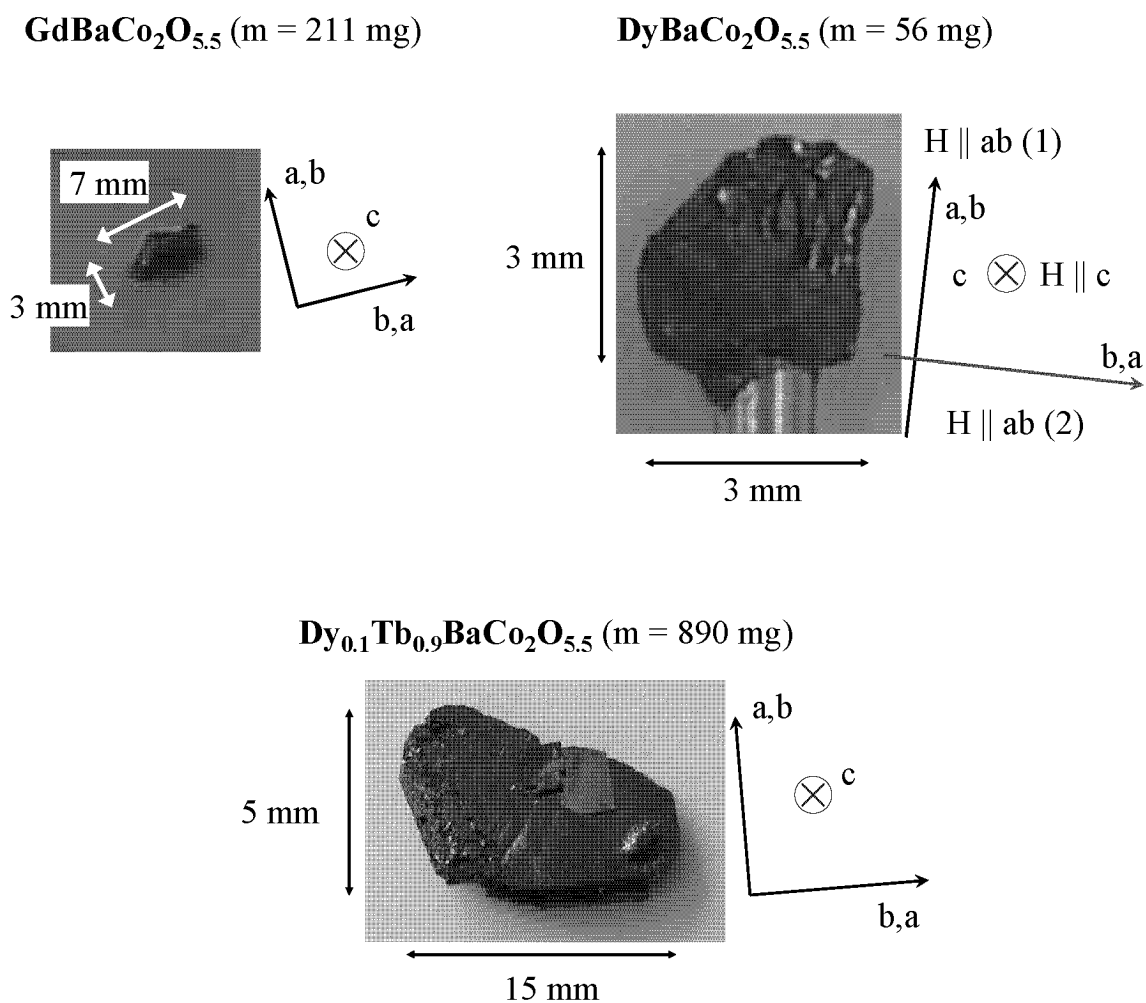
4.4   Single Crystals

All our single crystals were synthesized by the group of S. N. Barilo in Minsk (Belarussia)[6]. We received four $Ln\mathrm{BaCo_2O_{5.5}}$ crystals with $Ln = \mathrm{Gd}$, Dy and $\mathrm{Dy_{0.1}Tb_{0.9}}$. Unfortunately, Gadolinium and in a lesser extent Dysprosium, strongly absorb neutrons (see Appendix B), and these two crystals could not used for neutron scattering experiments.

The single crystals were grown by the flux technique from overstoichiometric flux melts. A positive vertical temperature gradient was applied to the flux melt and at the bottom of the crucible powder of the corresponding rare earth oxide was put as a feeder to keep the overstoichiometric flux melt saturated. An aluminium rod was dipped into the flux melt by a few millimeters and rotated constantly. The crystals (up to 120 mmm^3) were found on the surface of the rod. The details of this process are decribed by Barilo *et al.* [168]. The reason for inclusion of 10% of Dy at the place of Tb lies in the much more stable growth conditions when adding a little amount of Dy oxide to the oxide feeder [168].

The specifications of the single crystals are given in Table 4.7 and three of them are shown Figure 4.22. The orientations shown in Figure 4.22 indicate the direction of applied magnetic field for the magnetization measurements. Laue diffraction measurements showed that the samples are of good quality. From Laue diffraction we learned two things: First, the c direction is perpendicular to the surface of the crystals (in the plane the reflections are not distinguishable, which is the case for $a = a_p$, $2a_p = b$); and 2) the directions of a or b relative to the crystal. Since the lattice parameters in a and b direction are so similar, the crystals are most likely to be twinned in these two directions (Figure 4.22 for the orientations).

---

[6]Institute of Solid State and Semiconductor Physics, National Academy of Sciences, Minsk 220072, Belarus

GdBaCo$_2$O$_{5.5}$ (m = 211 mg)   **DyBaCo$_2$O$_{5.5}$** (m = 56 mg)

Dy$_{0.1}$Tb$_{0.9}$BaCo$_2$O$_{5.5}$ (m = 890 mg)

Figure 4.22: Picture of the GdBaCo$_2$O$_{5.5}$, DyBaCo$_2$O$_{5.5}$ and Dy$_{0.1}$Tb$_{0.9}$BaCo$_2$O$_{5.5}$ single crystals.

Table 4.8: Transition temperature in [K] found for our single crystals $LnBaCo_2O_{5.5}$ with $Ln=$ Gd, Dy and $Dy_{0.1}Tb_{0.9}$.

	T_C	T_N	T_{SSO}
Gd	262	246	-
Dy	292	282	-
$Dy_{0.1}Tb_{0.9}$	280	260	200

4.5 Bulk Magnetization Measurements

4.5.1 $GdBaCo_2O_{5.5}$

Temperature dependent magnetization measurements were performed with a small magnetic field of $H = 0.01$ T applied once in the ab-plane and once perpendicular to it (along the c-direction). The measurements were performed for both zero field cooling (ZFC) and field cooling (FC) (Figure 4.23). We find two transitions, at $T_C = 262$ K and at $T_N = 246$ K. In Table 4.8 the transition temperatures obtained from our magnetization measurements are given for the three single crystal samples.

The difference between the curves with the magnetic field applied along different crystallographic axis is remarkable: The ratio of the magnetization at T_N for the two geometries is $Mag_\parallel : Mag_\perp = 14$. This clearly shows that the only possible orientation of the Co magnetic moments is in the ab-plane.
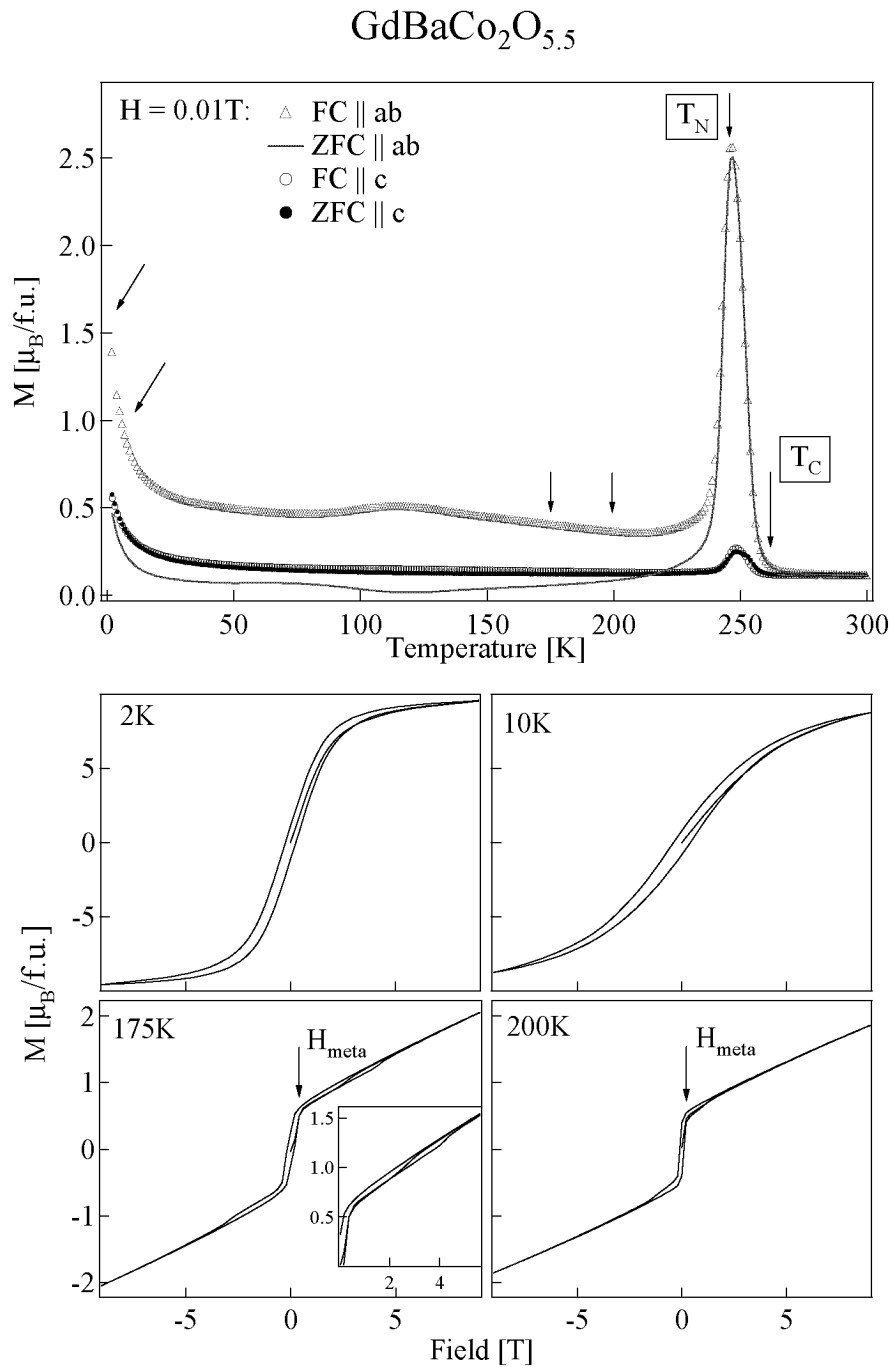
Magnetic field dependent measurements (Figure 4.23), with the field applied in the ab plane, were performed for temperatures T=2, 10, 175 and 200 K (in the magnetization measurements shown in Figure 4.23 these temperatures are indicated by arrows). At 2 K, the magnetization almost saturates at $H = 9$ T with a magnetic moment per unit cell of 9.55 μ_B. In the high temperature (175 and 220 K) field dependent magnetic measurements a change of slope is seen at $H_{meta} = 0.6$ and 0.4 T for 175 and 220 K, respectively. This is a sign for a transition into a metamagnetic phase[7], in this case the metamagnetic phase probably corresponds to the state with a net magnetic moment as found in the temperature range from 246 to 262 K. It will be shown for $Ln =$ Dy that on applying a magnetic field in the temperature dependent measurements the state with net magnetic moment can be extended to lower temperatures. With increasing temperature less energy is needed to realign the spins, therefore the transition field decreases.

The temperature dependent resistivity in the ab-plane is shown in Figure 4.24. In agreement with the literature the compound on warming shows the so-called insulator to metal transition with $T_{MI} = 347$ K [169].

4.5.2 $DyBaCo_2O_{5.5}$

Temperature dependent magnetization measurements were again performed with a magnetic field applied both perpendicular and parallel (Figure 4.22) to the ab-plane. Very similar results as for $GdBaCo_2O_{5.5}$ (Section 4.5.1) were found (Figure 4.25). This time three different magnetic fields ($H = 0.01$, 1, and 5 T) were applied. Again we find a transition to a state with a net magnetic moment at $T_C = 292$ K and to the AFM state at T_N=282 K for $H = 0.01$ T. As for

---

[7]Metamagnets are antiferromagnets which undergo a transition to a state with relatively high magnetization on applying a magnetic field.

Figure 4.23: Top: temperature dependent ZFC and FC magnetization measurement on GdBaCo$_2$O$_{5.5}$. A magnetic field of $H = 0.01$ T was applied once perpendicular to the ab-plane and once parallel to it. The arrows denote the temperatures at which field dependent magnetization measurements were done (see bottom graph). Bottom: field dependent magnetization measurements at $T = 2$, 10, 175 and 200 K for GdBaCo$_2$O$_{5.5}$ for a field applied parallel to the ab-plane.
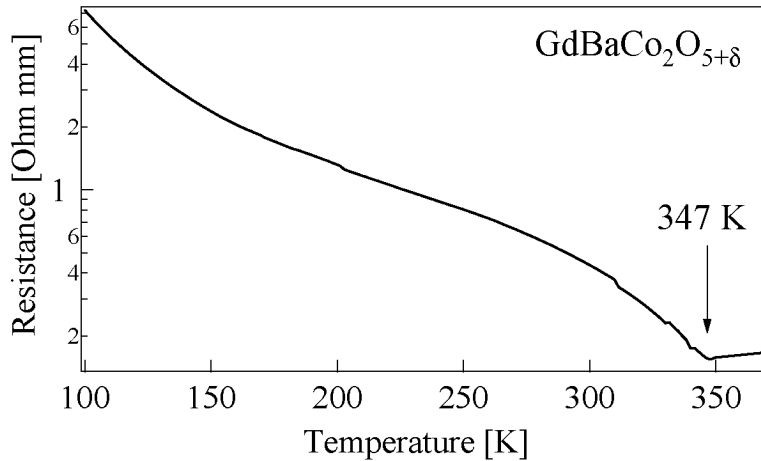
Figure 4.24: Resistivity measured in the ab-plane for GdBaCo$_2$O$_{5.5}$.

GdBaCo$_2$O$_{5.5}$, a remarkable difference is seen between the magnetization obtained by applying the field perpendicular or parallel to the ab-plane. There is also a large difference between the magnetizations taken for the two parallel orientations of the magnetic field. The ratios at T_N are the following: Mag$_a$: Mag$_b$: Mag$_c$ = 23 : 14: 1. The preferred axis along which the spins align themselves is the a-axis [150, 144]. The application of an external magnetic field stabilizes the phase with the net magnetic moment and the transition is broadened extensively.

Magnetic field dependent measurements were performed for this crystal as well. These measurements were performed in two geometries: Once with the field applied parallel to a (with the strongest signal in magnetization measurements (Figure 4.22) and once with the field perpendicular to the ab-plane. The results are shown in Figure 4.26 for temperatures 2, 175, 211, and 275 K. Saturation of the magnetization is not reached in the 2 K data (contrary the GdBaCo$_2$O$_{5.5}$ data).

An interesting feature in the low temperature hysteresis with H parallel to the ab-plane is the transition at field values H = 4.2 - 4.7 T, which is absent in the other geometry. This transition can probably be attributed to a detwinning of the system, since this transition only occurs for the first magnetization process: at the transition field, enough energy is available to flip the spins of domains with different orientations along the field direction.

A sharp metamagnetic transition is again seen in the hysteresis curve taken at $T = 276$ K, where $H_{meta} = 0.2$ T is needed to create a state with larger magnetization. The data taken at 211 K is at a temperature which is just on the lower limit of the range influenced by the magnetic field in the temperature dependent magnetization measurements (Figure 4.25), while the 175 K data is outside this region. This explains why these two curves only barely or not at all show a metamagnetic transition. The reason for the strange behaviour of the $T = 176$ K curve is unknown. The magnetization curve at 300 K shows that the system is in the paramagnetic state at this temperature.

4.5.3   Dy$_{0.1}$Tb$_{0.9}$BaCo$_2$O$_{5.5}$ and Low Temperature Lanthanide behavior

The FC and ZFC DC magnetization measurements for H= 0.1 T are shown in Figure 4.27. Again the response is stronger for the field applied in parallel to the ab-plane, but not as
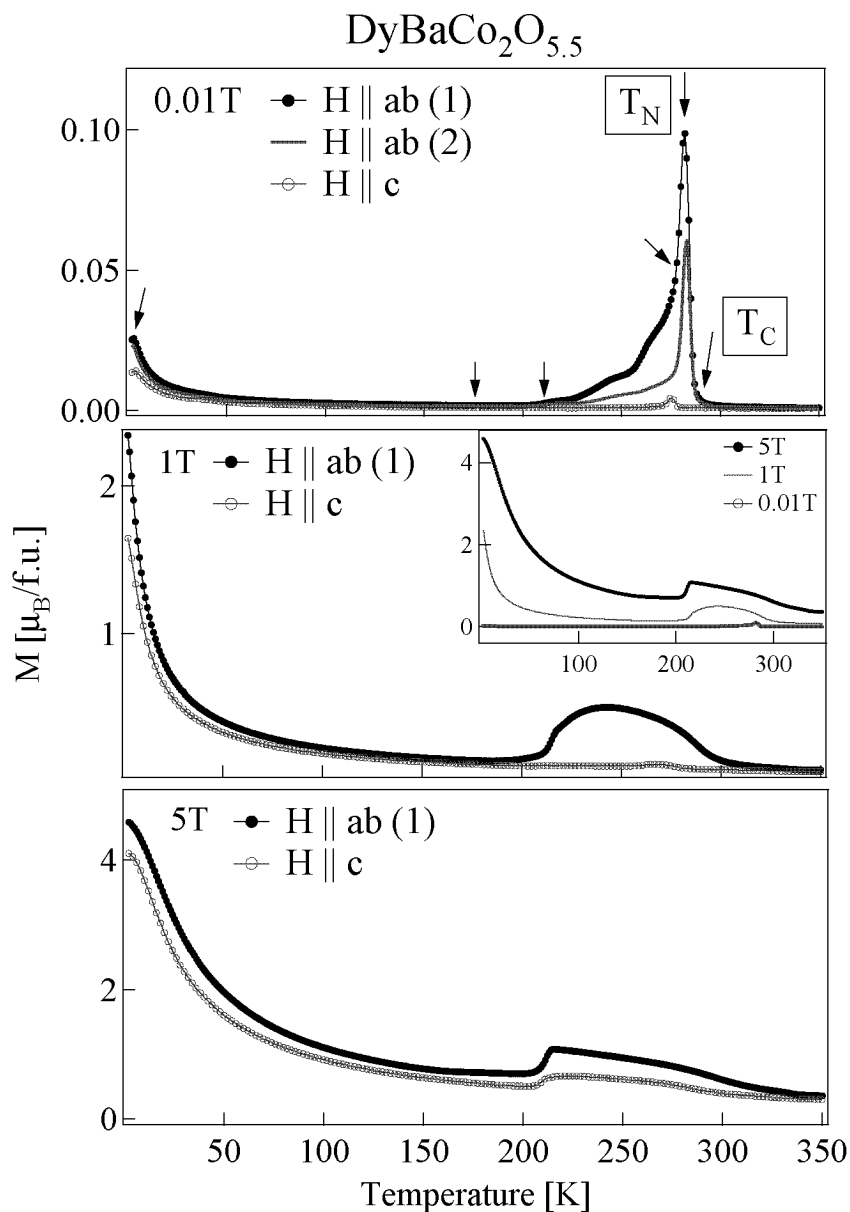
Figure 4.25: Temperature dependent ZFC and FC magnetization measurement on DyBaCo$_2$O$_{5.5}$. Top: H = 0.01T applied in three different directions. The arrows denote the temperatures at which field dependent magnetization measurements were done (see Figure 4.26). Middle and Bottom: H = 1 and 5 T applied along two different directions (geomtries for H shown in Figure 4.22).
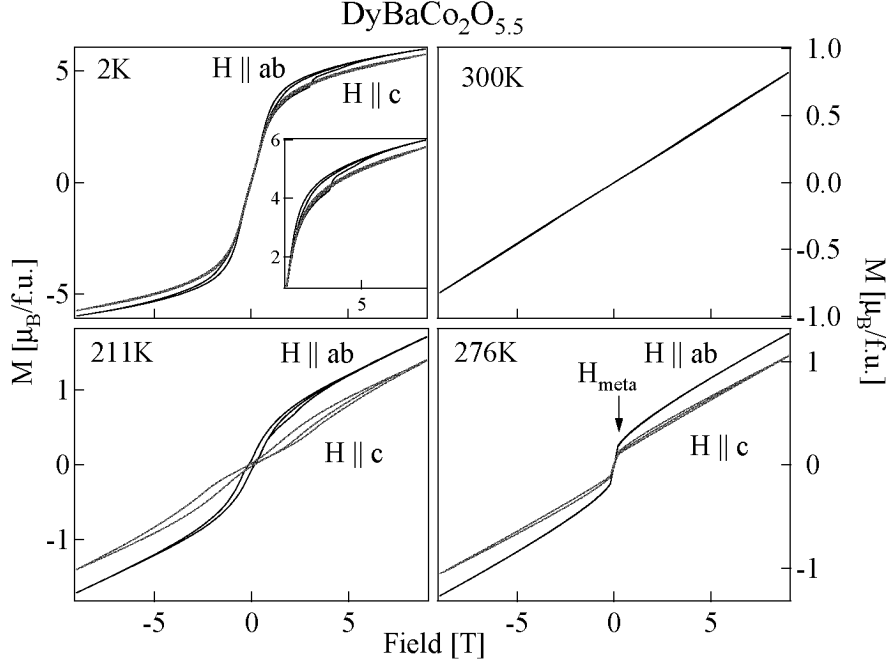
Figure 4.26: Field dependent magnetization measurements at $T = 2, 211, 276$ and 300 K for $DyBaCo_2O_{5.5}$ for fields applied parallel and perpendicular to the ab-plane.

pronounced as in the previou two cases ($Mag_{\parallel}$: $Mag_{\perp} = 4$ at T_N). We obtain $T_C = 280$ K and $T_N = 260$ K and $T_i = 200$ K. The FC curve was once measured decreasing temperature with field and then increasing temperature with the magnetic field still applied (indicated by the arrows in Figure 4.27). A clear difference can be seen: Applying the magnetic field at high temperatures can more easily orient the cobalt magnetic moments, and the transition to the AFM state is shifted to lower temperatures ~ 200 K. It should be noted that all other FC curves were measured while decreasing temperature with an applied field.

The Curie-like paramagnetic behaviour of the temperature dependent magnetization curves (Figure 4.28) for T $<$ 100 K can be attributed to the rare earth moments. The Curie-Weiss expression for the magnetization can be written as:

$$M(T) \quad = \quad \frac{C \cdot H}{T - \Theta_{CW}} = \chi(T) \cdot H \quad , \tag{4.3}$$

$$C \quad = \quad \frac{N_A g_J^2 J(J+1)\mu_B^2}{3k_B} = \frac{N_A \mu_{eff}^2}{3k_B} \quad , \tag{4.4}$$

where Θ_{CW} is the Curie-Weiss temperature, $\chi(T)$ is the temperature dependent susceptibility and C is the Curie constant with the g_J-factor and total angular momentum J dependent on the rare earth, see Table 4.9. The calculated effective moment for a Ln-system is given Table 4.9. It is found that purely non-interacting Ln magnetic moments ($\Theta_{CW} = 0$) cannot explain the low temperature magnetization data (Figure 4.28 top). Including a simple antiferromagnetic correlation (Curie-Weiss temperature T_{CW}) leads to fairly good results (Figure 4.28 middle and bottom). However, the values obtained for the effective magnetic moments show two discrepancies: First, the two values T_{CW} and μ_B(calc) obtained for the two different geometries ($H\|c$ and $H\|ab$) are different, (see Table 4.9). Second, the obtained values for the effective
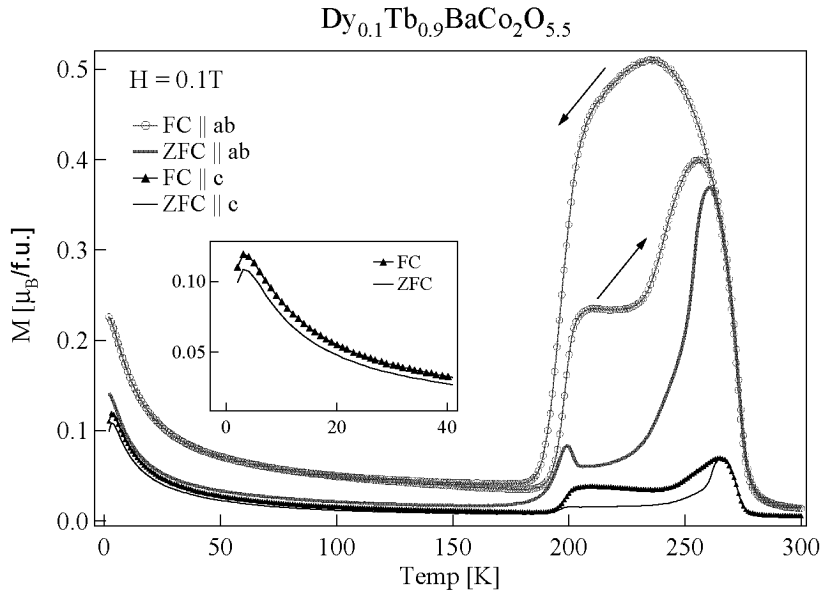
Figure 4.27: Temperature dependent ZFC and FC DC magnetization measurement for $Dy_{0.1}Tb_{0.9}BaCo_2O_{5.5}$. The magnetic field is applied once perpendicular and once parallel to the ab-plane. The FC curve was once measured decreasing temperature with field and then increasing temperature with the magnetic field still applied (indicated by the arrows). The inset show a close up of the low temperature ZFC and FC data with $H||c$.

magnetic moments are by 10 - 25% smaller than those predicted by theory. In Figure 4.28 (top) we show the fit to the low temperature data obtained by assuming a full Tb moment $J = 6$, which does not fit the data as well as the fit with the reduced moment $J = 5.5$. Therefore we conclude, that an interaction must exist between the Ln ions and Co spins and that the crystal field splitting leads to a lifting of the degeneracy of the total moment J on the lanthanide Ln. The second conclusion is in strong contrast to previous publications on LnBaCo$_2$O$_{5.5}$ single crystals with $Ln = $ Gd [170] and $Dy_{0.1}Tb_{0.9}$ [171]. Both groups find a completely saturated magnetic moment based on temperature dependent magnetization measurements.

The close up of the low temperature magnetization data for $Dy_{0.1}Tb_{0.9}Co_2O_{5.5}$ for a magnetic field applied parallel to the c-direction shows that the Tb moment orders below $T \sim 4\,K$ in contrast to the geomtery where $H \parallel ab$-plane. This suggests that the lanthanide moments lie along the c-axis.

The finding that the rare earth magnetic moments interact with the Co ion spins is consistent with our single crystal neutron diffraction measurements, where we find strong diffuse scattering at low temperatures and fields [172, 173].

4.6 Summary and Conclusion

This chapter was mainly concerned with the polycrystalline layered compound $PrBaCo_2O_{5+\delta}$. Special attention was paid to $PrBaCo_2O_{5.48}$, since the intermediate oxygen content ($\delta = 0.5$) compounds show oxygen vacancy ordering, which is thought to be the origin for the observed magnetoresistance

In a first study the influence of sample preparation on the oxygen vacancy ordering and the
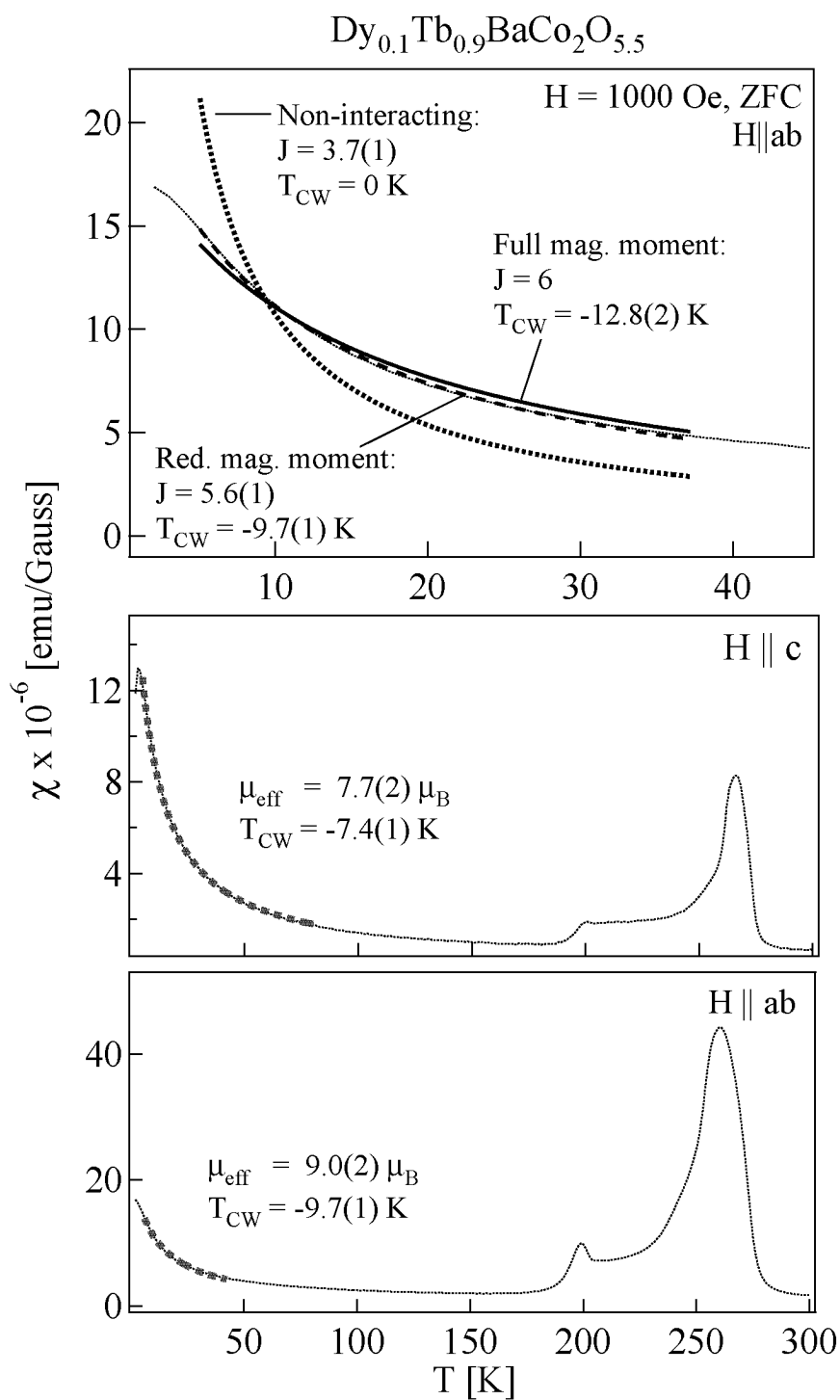
Figure 4.28: Top: comparison between Curie-Weiss fits with different fiiting parameters. Middle and bottom: Curie-Weiss fit to the magnetization data for weakly coupled Tb ions for H perpendicular to the ab-plane and (middle) H parallel to the ab-plane (bottom).

Table 4.9: Tabulated g_J, J, μ_{eff} values for $Ln =$ Dy, Tb along with fitted values for effective magnetic moment μ_{eff}(fit) and Curie-Weiss temperature Θ_{CW} as determined from the Curie-weiss law.

| | g_J | J | μ_{eff} | $H \parallel ab$ | | $H \parallel c$ | |
				μ_{eff}(fit)	Θ_{CW} [K]	μ_{eff}(fit)	Θ_{CW} [K]
Gd	2	7/2	7.94	-	-	-	-
Dy	4/3	15/2	10.64	9.51(6)	-7.3(1)	8.06(7)	-10.2(4)
Tb	3/2	12/2	9.72	9.04(2)	-9.7(1)	7.65(1)	-7.4(1)

magnetic properties in $PrBaCo_2O_{5+\delta}$ ($0.17 \leq \delta \leq 0.79$) was investigated by means of x-ray diffraction and bulk magnetic measurements. It was found that oxygen vacancy ordering on a long range scale is only guaranteed when the cooling part of the synthesis process is done slowly (6 K/h). The oxygen vacancy ordering is reflected in the magnetic properties, where a clear difference is seen between the magnetization curves for samples with the same oxygen content, but different synthesis history.

High temperature ($T < 820$ K) neutron powder diffraction experiments performed on $PrBaCo_2O_{5.48}$ revealed a change in the crystallographic structure upon heating above $T_{OD} = 776$ K. Structure refinements show that above T_{OD} the oxygen vacancy order is lost.

$PrBaCo_2O_{5.48}$ has also been investigated by resistivity and thermoelectric power measurements. In contrast to the metallic properties usually attributed to the layered cobaltites above the insulator to metal transition T_{MI}, we propose that thermally activated polaronic hole conduction is more appropriate to describe the conduction mechanism. We base this assumption on thermo-electric power measurements performed on a series of $PrBaCo_2O_{5+\delta}$ samples ($0.16 \leq \delta \leq 0.50$), which all show the same activation behavior and activation energy. Since the compounds with $\delta \leq 0.40$ are known to be semiconductors, we conclude that also $PrBaCo_2O_{5.50}$ falls into this category.

A last section concentrates on single crystals of type $LnBaCo_2O_{5.5}$ ($Ln =$ Gd, Dy, $Dy_{0.1}Tb_{0.9}$) for which bulk magnetic measurements have been carried out. The experiments were performed in different geometries (with external magnetic fields applied perpendicular and parallel to the ab-planes of the crystals). By fitting the low temperature data with the Curie-Weiss law, an interaction between the lanthanide ions was found.

We have shown that not every $LnBaCo_2O_{5+\delta}$ compound with $\delta = 0.5$ has ordered oxygen vacancies. Instead, the degree of oxygen vacancy ordering strongly depends on the synthesis process. A simple method to decide whether oxygen vacancies are ordered are bulk magnetization measurements, the curves of which show different behaviors for oxygen vacancy ordered and disordered compounds with the same oxygen content.

The high temperature structural transition at $T_{OD} = 776$ K, where oxygen vacancy ordering is lost, can open new prospects, since it is well known that oxygen vacancy disorder eases ionic conductions [5, 34]. Therefore, the high-temperature order-disorder transition could be connected to the onset of ionic conductivity in the $LnBaCo_2O_{5.5}$ compounds. Ionic conduction has not been observed in these compounds up to the date of the present work.

Study of the transport properties in $PrBaCo_2O_{5+\delta}$ ($0.16 \leq \delta \leq 0.50$) leads to the conclusion that the conduction in all these material can be described by thermally activated hole mobility (polaronic conduction).

Chapter 5

Outlook

Many new questions arose in the course of this work. The answers to which will either support/discard our findings or provide insight into further physical properties of cobaltites. A non-exhaustive list of future research projects is listed in the following.

3D, $Ho_{0.1}Sr_{0.9}CoO_{3-\delta}$:

1) No information is available concerning the electronic transport in our samples. Knowledge of the electronic properties could help to decide whether or not the proposed magnetic exchange interactions and Co ion spin states are plausible. However, it is hard to measure the resistivity in these compounds, since they are polycrystalline. Sintered materials could be used to measure resistivity, but the temperature needed to sinter the materials is so high that oxygen will be lost. Improvement of the single crystal growth technique could solve this problem.

2) The series we investigated was doped with the rare earth Ho; in this series the 1:1 mixture of Co^{3+} and Co^{4+} does not occur at the same oxygen content value as in the undoped $SrCoO_{3-\delta}$. It is unknown if the undoped series shows a similar evolution of crystallographic and magnetic properties. Investigation of $SrCoO_{3-\delta}$ could give further insight on the correlations between crystallographic and magnetic properties.

2D, $LnBaCo_2O_{5+\delta}$:

3) The high temperature structural transition should be investigated more thoroughly: especially the question of whether the transition is connected to the onset of ionic conductivity should be answered. Measuring ionic conductivity needs sintered polycrystalline samples, where, as in point 1) the sintering temperature is higher than the one at which oxygen diffuses out of the sample. Also here, as in point 1), single crystal samples are desired.

4) Macroscopic magnetization measurements performed on single crystals show that large anisotropies are present, but it is impossible to conclude on the magnetic orderings or spin states of the Co ions. Neutron powder diffraction experiments also lead to unambiguous results. With the availability of larger and higher quality (detwinned) single crystals, neutron scattering experiments will become easier, which will hopefully allow to refine the magnetic structures unambiguously.

5) The interaction of the Ln magnetic moment with the Co magnetic moment should be investigated in detail. The possible magnetic order of the lanthanide sublattice and the influences this order has on the magnetic ordering of the Co sublattice should also be clarified.

Appendix A

Bond Valence Sums

An important tool in crystal structure investigations is the bond valence method [97, 98, 99], with which the ideal chemical structure can be predicted (a cation is surrounded by a certain number of anions in a regular way). However, when mapping the ideal structure into three-dimensional space, constraints are imposed on the geometry and the ideal bond lengths can be strained. Particularly in compositions with bonds of intermediate strength (i.e. oxides), the relaxation of this strain can lead to non-stoichiometry, stabilization of unusual oxidation states, distortion of the bonding environment and lowering of symmetry.

The coordination environment of most cations in inorganic solids is isotropic, but there are cations with distorted environments, i.e. Cu^{2+} is situated in a tetragonally distorted environment, where two bonds are long and four short. The distortion is due to steric effects, arising from geometric constraints that force certain bondlengths to be shortened and others elongated. Most cations have regular coordination spheres, and therefore it is interesting to investigate the interplay between the steric and chemical requirements and see what can lead to the distortions. The bond valence model is based on the assumption that both the cation and the anion should have as regular coordination spheres as possible, this leads to the prediction that the bond lengths should take on an ideal value for a certain compound. Deviations from these ideal lengths are caused by electronic or steric effects. The strength of a bond is defined as [174]:

"In a stable coordination structure the electric charge of each anion tends to compensate the strength of the electrostatic valence bonds reaching it from the cations at the centers of the polyhedra of which it forms a corner; that is for each anion

$$V_j = \sum_i \frac{V_i}{N_i} = \sum_i s_i \quad , \tag{A.1}$$

where V_j is the anion valence, V_i the cation valence, N_i the coordination number and s_i is the bond valence or 'Pauling bond strength' of the cation. It is important that bonds occur only between neighbouring atoms whose valence have opposite signs. Bonds are characterized by their bond valence s and their bond lengths R. The equations

$$\sum_j s_{ij} = V_i \quad , \tag{A.2}$$

$$\sum_{loop} s_{ij} = 0 \tag{A.3}$$

are valid. Equation A.2 is called the valence-sum rule, while equation A.3 guarantees the most symmetric distribution of atomic valence among the bonds. The usefulness of this description
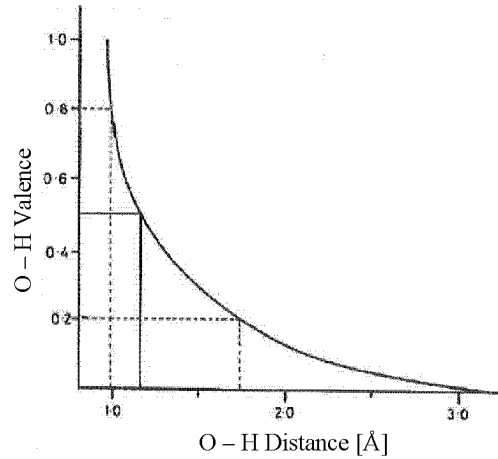
Figure A.1: Bond valence as a function of bondlength for bonds between H and O (after Brown [175]).

lies in the relationship that exists between the bond valences and physical properties. The relationship of the bond valence and bond length R is very well determined, since very accurate measurements of bond lengths are possible. It is given by

$$s_{ij} = \exp\left(\frac{R_0 - R_{ij}}{B}\right) \quad . \tag{A.4}$$

$$\tag{A.5}$$

R_0 and B are tabulated parameters. R_0 is the length of the bond of unit valence, which has been determined for many ideal structures and it was found that for most bonds B can be set to 0.37 Å [99]. R_{ij} is the measured bond length. This leads to the formula for the bond valence sum:

$$V_j = \sum_i \exp\left(\frac{R_0 - R_{ij}}{0.37}\right) \quad . \tag{A.6}$$

The distortion theorem states that:
Any deviation of the valences of the bonds formed by an atom from their average valence will increase the average value, providing that the average bond length stays constant.
which is equivalent to
Any deviation of the bond lengths of the bonds formed by an atom from their average length will increase the average length, providing the average bond valence remains constant.
From Figure A.1 it the relationship between the bond length and the bond valence is clearly seen. The elongated/compressed bonds between Co1-O/Co2-O we found in Chapter 3.4.1 for the compound $Ho_{0.1}Sr_{0.9}CoO_{3-\delta}$ lead us to think that the charge distribution on the Co1/Co2 site must be different. Calculations using the bond valence sum formula A.6 confirmed this assumption and the values found for the two valences turned out to be extremely different (Chapter 3.4.2).

Appendix B

Neutron Scattering Lengths and Cross Sections

It was written in Chapter 4.4 that the $GdBaCo_2O_{5.5}$ single crystals could not be used in neutron experiments because of they strongly absorb neutrons. This is directly related to their large scattering length and therefore a short explanation on the term scattering length will be given here.

The scattering length of the neutron-nucleus system is the basic quantity which describes the strength and the character of the interaction of low-energy neutrons with the individual nuclei. In a mono-atomic sample different scattering lengths occur: for one, isotopes of the same element have different scattering lengths; for the other, the scattering length depends on the relative coupling between the neutron spin and the nuclear spin of the isotope (parallel or antiparallel). The scattering cross section σ (probability that a neutron is scattered into a certain energy and angular range) of an atom is derived from the scattering length of the same atom. There are two kinds of scattering: coherent and incoherent. Coherent scattering involves correlations between the positions of an atom j at the time zero and the position of a second atom at a time t > 0. The coherent scattering therefore describes interference between the waves produced by the scattering of a single neutron from all the nuclei in the sample (average scattering length $\bar{b}$). Incoherent scattering involves correlations between the positions of an atom j at time zero and the position of the *same* atom at a time t > 0. Thus, in incoherent scattering, the scattered waves from different nuclei do not interfere with each other. The different scattering cross sections can be written as:

$$\sigma_{coh} = 4\pi(\bar{b})^2 \quad , \tag{B.1}$$

$$\sigma_{inc} = 4\pi\left(\bar{b^2} - (\bar{b})^2\right) \quad , \tag{B.2}$$

$$\sigma_{scat} = 4\pi\bar{b^2} \tag{B.3}$$

The physical interpretation is as follows: The actual scattering system has different scattering lengths associated with different nuclei. The coherent scattering is the scattering which would result, if all nuclei had a scattering length equal to $\bar{b}$. The incoherent takes account of the actual system and gives the extra term which has to be added to σ_{coh} in order to obtain the total scattering σ_{scat}. The incoherent scattering can be seen as coming from the random distribution of the deviations of the scattering lengths from their mean value.

The scattering length mostly is complex. One can distinguish between nuclei with small and large imaginary parts. For the first type the scattering length does not depend on the energy of the incoming neutron. For the second type of nuclei the scattering length varies strongly with

Table B.1: Coherent, incoherent, scattering and absorption cross sections σ_{abs} in [barn] for elements appearing in the materials used for this work. 1 barn $= 10^{-24}$ cm^{-2}.

Isotope	σ_{coh}	σ_{incoh}	σ_{scatt}	σ_{abs} [barn]
O	4.232(6)	0.000(8)	4.232(6)	0.00019(2)
^{16}O	4.323(6)	0	4.232(6)	0.00010(2)
^{17}O	4.20(22)	0.004(3)	4.20(22)	0.236(1)
Co	0.779(13)	4.8(3)	5.6(3)	37.18(6)
Sr	6.19(4)	0.06(11)	6.25(10)	1.28(6)
Ba	3.23(4)	0.15(11)	3.38(10)	1.1(1)
Pr	2.64(6)	0.015(3)	2.66(6)	11.5(3)
Gd	29.3(8)	151.0(2.0)	180.0(2.0)	49'700(125)
Tb	6.84(6)	0.004(3)	6.84(6)	23.4(4)
Dy	35.9(8)	54.4(1.2)	90.3(9)	994(13)
Ho	8.06(8)	0.36(3)	8.42(16)	64.7(1)

the energy of the neutron. This is because at certain energies a compound nucleus (original nucleus plus neutron) is formed, which is called a resonance phenomenon. Since the imaginary part of the scattering length corresponds to absorption, such nuclei strongly absorb neutrons (at resonant energies). The absorption cross section is given by

$$\sigma_{abs} = \frac{4\pi}{k} b''_{coh} \quad , \tag{B.4}$$

where k is the neutron wave vector and b''_{coh} is the imaginary part of the scattering length. The absorption cross section is tabulated for a specific wave vector (generally $k = 3.494$ Å^{-1}, which corresponds to $\lambda = 1.798$ Å). The scattering lengths are mostly independent of incoming neutron energy, excpetions are ^{113}Cd, ^{149}Sm, ^{151}Eu, ^{157}Gd, ^{176}Lu, and ^{180}Ta, each of which has a neutron absorption resonance at the energy of thermal neutron.

In Table B.1 the cross sections for the elements used in the cobaltites for this work are shown. The large absorption cross section of Gd made it impossible to measure the single crystal GdBaCo$_2$O$_{5.5}$ we had otained from the group of S. Barilo[1]. Also the DyBaCo$_2$O$_{5.5}$ crystal was hard to measure and the measurement not continued to the extent planned.

A complete list of scattering cross sections can be obtained from H. Rauch and W. Waschkowski [176] or in the internet:

http://www.ati.ac.at/%7Eneutropt/scattering/Scattering_lengths_table_20010419.pdf

---

[1]Institute of Solid State and Semiconductor Physics, National Academy of Sciences, Minsk 220072, Belarus

Bibliography

[1] C. Martin, A. Maignan, D. Pelloquin, N. Nguyen, and B. Raveau. *Appl. Phys. Lett.*, 71:1421, 1997.

[2] Y. Teraoka, T. Nobunaga, K. Okamoto, N. Miura, and N. Yamazoe. *Solid State Ionics*, 48:207, 1991.

[3] H. Kruidhof, H. J. M. Bouwmeester, R. H. E. van Doorn, and A. J. Burggraaf. *Solid State Ionics*, 63-65:816, 1993.

[4] M. V. Patrakeev, I. A. Leonidov, E. B. Mitberg, A. A. Lakhtin, V. G. Vasiliev, V. L. Kozhevnikov, and K. R. Poeppelmeier. *Ionics*, 5:444, 1999.

[5] R. H. E. van Doorn and A. J. Burggraaf. *Solid State Ionics*, 128:65, 2000.

[6] K. Takada, H. Sakurai, E. Takayama-Muromachi, F. Izumi, R. Dilanian, and T. Sasaki. *Nature*, 422:53, 2003.

[7] V. M. Goldschmidt. *Geochemische Verteilungsgesetze der Elemente 8: Untersuchungen über Bau und Eigenschaften von Krystallen.* Norsk. Vid. Akad., Math.-Naturvid. Kl. 1926(8), 1927.

[8] A. S. Bhalla, R. Guo, and R. Roy. *Mat. Res. Innovat.*, 4:3, 2000. And references therein.

[9] M. Johnsson and P. Lemmens. *condmat/0506606*, 2005.

[10] A. F. Wells. *Structural Inorganic Chemistry.* Oxford Science Publications, 1995.

[11] U. Müller. *Inorganic Structural Chemistry.* Wiley & Sons Ltd, 1993.

[12] P. Lemmens and P. Millet. Spin-orbit-topology, a triptych. In U. Schollwöck, J. Richter, and D. J. Farnell, editors, *Quantum Magnetism.* Springer Verlag, Berlin, 2004.

[13] O. Madelung. *Introduction to Solid-State Theory.* Editors: M. Cardona, P. Fulde and H.-J. Queisser; Springer-Verlag Berlin Heidelberg, 1978.

[14] G. M. Bodner:
http://chemed.chem.purdue.edu/genchem/topicreview/bp/ch12/crystal.php.

[15] C. Zener. *Phys. Rev.*, 81:440, 1951.

[16] C. Zener. *Phys. Rev.*, 82:403, 1951.

[17] P. W. Anderson and H. Hasegawa. *Phys. Rev.*, 100:675, 1955.

[18] P. G. deGennes. *Phys. Rev.*, 118:141, 1960.

[19] S. Blundell. *Magnetism in Condesed Matter.* Oxford University Press, New York, 2001.

[20] P. Schiffer, A. P. Ramirez, W. Bao, and S.-W. Cheong. *Phys. Rev. Lett.*, 75:3336, 1995.

[21] P. G. Radaelli, D. E. Cox, M Marezio, and S.-W. Cheong. *Phys. Rev. B*, 55:3015, 1997.

[22] A. P. Ramirez. *J. Phys.: Condens. Mat.*, 9:8171, 1997.

[23] C. N. R. Rao, A. Arulraj, P. N. Santosh, and A. K. Cheetham. *Chem. Mater.*, 10:2714, 1998.

[24] J. M. González-Calbet, E. Herrero, N. Rangavittal, J. M. Alonso, J. L. Martínez, and M. Vallet-Regí. *J. Solid State Chem.*, 148:158, 1999.

[25] H. A. Kramers. *Physica*, 1:182, 1934.

[26] P. W. Anderson. *Phys. Rev.*, 79:350, 1950.

[27] P. W. Anderson. *Phys. Rev.*, 80:922, 1950.

[28] J. Kanamori. *J. Phys. Chem. Solids*, 10:87, 1959.

[29] J. B. Goodenough. *Phys. Rev. B*, 100:564, 1995.

[30] M. Imada, A. Fujimori, and Y. Tokura. *Rev. of Mod. Phys.*, 70:1039, 1998.

[31] P. A Cox. *Transition Metal Oxides.* Oxford, Clarendon, 1992.

[32] D. Emin and T. Holstein. *Am. Phys. (N.Y.)*, 53:439, 1969.

[33] S. R. Sehlin, H. U. Anderson, and D. M. Sparlin. *Phys. Rev. B*, 52:11681, 1995.

[34] M. Cherry, M. S. Islam, and C. R. A. Catlow. *J. Sol. State Chem.*, 118:125, 1995.

[35] S. B. Adler, S. Russek, J. Reimer, M. Fendorf, A. Stacy, Q. Huang, A. Santoro, J. Lynn, J. Baltisberger, and U. Werner. *Solid State Ionics*, 68:193, 1994.

[36] J. Chadwick. *Nature*, 129:312, 1930.

[37] J. Chadwick. *Z. Elektrochem. Angew. Phys. Chem.*, 38:546, 1932.

[38] J. Chadwick. *Proc. Roy. Soc. A*, 136:692, 1932.

[39] W. M. Elsasser. *Comptes Rendus*, 202:1029, 1936.

[40] P. Preiswerk and H. von Halban. *Comptes Rendus*, 203:73, 1938.

[41] E. Fermi. *Ricerca Scientifica*, 7:13, 1936.

[42] E. Fermi. *Collected Papers.* Univ. Chicago Press, Vol. I, 1952.

[43] G. L. Squires. *Introduction to the Theory of Thermal Neutron Scattering.* Cambridge University Press, 1978.

[44] S. W. Lovesay. *Theory of Neutron Scattering from Condensed Matter.* Clarendon Press, Oxford, 1984.

[45] G. Shirane, S. M. Shapiro, and J. M. Tranquada. *Neutron Scattering wit a Triple Axis Spectrometer: Basic Techniques.* Cambridge University Press, 2002.

[46] http://capsicum.me.utexas.edu/ChE386K/html/powder_diffraction_4.htm.

[47] A. W. Hull. *J. Am. Chem. Soc.*, 41:1168, 1919.

[48] P. Fischer, G. Frey, M. Koch, M. Konnecke, V. Pomjakushin, J. Schefer, R. Thut, N. Schlumpf, R. Burge, U. Greuter, S. Bondt, and E. Berruyer. *Physica B*, 276:146, 2000.

[49] J. A. Dean. *The Analytical Chemistry Handbook.* New York [etc.]: McGraw-Hill, 1995.

[50] E. Pungor. *A Practical Guide to Instrumental Analysis.* Boca Raton [etc.]: CRC Press, 1995.

[51] D. A. Skoog, F. J. Holler, and T. Nieman. *Principles of Instrumental Analysis.* Philadelphia [etc.]: Saunders College Publishing, 1998.

[52] K. Conder, E. Pomjakushina, A. Soldatov, and E. Mitberg. *Mater. Res. Bull.*, 40:257, 2005.

[53] H. M. Rietveld. *J. Appl. Cryst.*, 2:65, 1969.

[54] G. Malmros and J. O. Thomas. *J. Appl. Cryst.*, 10:7, 1977.

[55] R. A. Young, editor. *Rietveld Refinement.* International Union of Crystallography, Oxford University Press, 1993.

[56] J. Rodríguez-Carvajal. *Physica B*, 192:55, 1993.

[57] H. Y. Tu, N. Imanishi, and O. Yamamoto. *Solid State Ionics*, 100:283, 1997.

[58] S. B. Adler. *Solid State Ionics*, 111:125, 1998.

[59] Y. Teraoka, S. Furukawa, H. M. Zhang, and N. Yamazoe. *J. Chem. Soc. Jpn*, 7:1084, 1988.

[60] G. H. Jonker and J. H. Van Santen. *Physica*, 19:120, 1953.

[61] H. Watanabe. *J. Phys. Soc. Jpn.*, 12:515, 1957.

[62] G. Thornton, B. C. Tofield, and A. W. Hewat. *J. Solid State Chem.*, 61:301, 1986.

[63] P. G. Radaelli and S. W. Cheong. *Phys. Rev. B*, 66:094408, 2002.

[64] M. A. Señarís-Rodríguez and J. B. Goodenough. *J. Solid State Chem.*, 116:224, 1995.

[65] V. G. Bhide, D. S. Rajoria, G. R. Rao, and C. N. R. Rao. *Phys. Rev. B*, 6:1021, 1972.

[66] P. M. Raccah and J. B. Goodenough. *Phys. Rev.*, 155:932, 1967.

[67] M. A. Señarís-Rodríguez and J. B. Goodenough. *J. Solid State Chem.*, 118:323, 1995.

[68] P. M. Raccah and J. B. Goodenough. *J. Appl. Phys.*, 39(2):1209, 1968.

[69] V. G. Bhide, D. S. Rajorie, C. N. R. Rao, G. Rama Rao, and V. G. Jadhao. *Phys. Rev. B*, 12:2832, 1975.

[70] C. N. R. Rao, O. M. Parkash, D. Bahadur, P. Ganguly, and S. Nagabhushana. *J. Solid State Chem.*, 22:353, 1975.

[71] J. B. Goodenough. *Mater. Res. Bull.*, 6:967, 1971.

[72] G. Thornton, B. C. Tofield, and D. E. Williams. *Solid State Commun.*, 44:1213, 1982.

[73] G. Thornton, F. C. Morris, S. Partington, B. C. Tofield, and D. E. Williams. *J. Phys. C Solid State Phys.*, 21:2871, 1988.

[74] M. Itoh, I. Natori, S. Kubota, and K. Motoya. *J. Phys. Soc. Jpn.*, 63:1486, 1994.

[75] K. Asai, O. Yokokura, N. Nishimori, H. Chou, J. M. Tranquada, G. Shirane, S. Higuchi, Y. Okajima, and K. Kohn. *Phys. Rev. B*, 50:3025, 1994.

[76] H. Watanabe and T. Takeda. *Proc. of the Int. Conf. on Ferrites, Japan*, page p. 588, 1970.

[77] P. Bezdicka, A. Wattiaux, J. C. Grenier, M. Pouchard, and P. Hagenmuller. *Z. Anorg. Allg. Chem.*, 619:7, 1993.

[78] T. Takeda, Y. Yamaguchi, and W. Watanabe. *J. Phys. Soc. Jpn*, 33:970, 1972.

[79] H. Taguchi, M. Shimada, and M. Koizumi. *J. Solid State Chem.*, 29:221, 1979.

[80] T. Takeda and W. Watanabe. *J. Phys. Soc. Jpn*, 33:973, 1972.

[81] H. Taguchi, M. Shimada, and M. Koizumi. *Mater. Res. Bull.*, 15:1225, 1978.

[82] R. H. Potze, G. A. Sawatzky, and M. Abbate. *Phys. Rev. B*, 51:11501, 1995.

[83] J. Grenier, S. Ghodbane, G. Demazeau, M. Pouchard, and P. Hagenmüller. *Mat. Res. Bull.*, 14:831, 1979.

[84] M. James, D. Cassidy, K. F. Wilson, J. Horvat, and R. L. Withers. *Solid State Sciences*, 6:655, 2004.

[85] M. James, D. Cassidy, D. J. Goossens, and R. L. Withers. *J. Solid State Chem.*, 177:1886, 2004.

[86] M. James, T. Tedesco, D. J. Cassidy, and R. L. Withers. *Mat. Res. Bull.*, 40:990, 2005.

[87] D. J. Goossens, K. F. Wilson, and M. James. *J. Phys. Chem. Solids*, 66:169, 2005.

[88] R. L. Withers, M. James, and D. J. Goossens. *J. Solid State Chem.*, 174:198, 2003.

[89] X. G. Luo, H. Li, X. H. Chen, Y. M. Xiong, G. Y. Wang, C. H. Wang, W. J. Miao, and X. Li. *cond-mat/*, 0501562, 2005.

[90] S. Hebert, A. Maignan, V. Caignaert, V. Pralong, D. Pelloquin, and B. Raveau. *Solid State Commun.*, 134:815, 2005.

[91] S. Streule, M. Medarde, A. Podlesnyak, E. Pomjakushina, K. Conder, S. Kazakov, J. Karpinski, and J. Mesot. *Phys. Rev. B*, 73:024423, 2006.

[92] Y. A. Shilova, M. V. Patrakeev, E. B. Mitberg, I. A. Leonidov, V. L Kozhevnikov, and K. R. Poeppelmeier. *J. Sol. State Chem.*, 168:275, 2002.

[93] J. B. Goodenough. *J. Phys. Chem. Solids*, 6:287, 1958.

[94] P. G. Radaelli, D. E. Cox, M Marezio, , and S.-W. Cheong. *Phys. Rev. B*, 55:3015, 1997.

[95] R. J. Goff and J. P. Attfield. *Phys. Rev. B*, 70:140404(R), 2004.

[96] A. Daoud-Aladine, J. Rodríguez-Carvajal, L. Pinsard-Gaudart, M. T. Fernández-Díaz, and A. Revcolevschi. *Phys. Rev. Lett.*, 89:097205, 2002.

[97] I. D. Brown. *Chem. Soc. Rev.*, 7:359, 1978.

[98] D. Altermatt and I. D. Brown. *Acta Cryst.*, B41:240, 1985.

[99] I. D. Brown and D. Altermatt. *Acta Cryst.*, B41:244, 1985.

[100] S. Grenier, J. P. Hill, D. Gibbs, K. J. Thomas, M. v. Zimmermann, C. S. Nelson, V. Kiryukhin, Y. Tokura, Y. Tomioka, D. Casa, T. Gog, and C. Venkataraman. *Phys. Rev. B*, 69:134419, 2004.

[101] J. Herrero-Martín, J. García, G. Subías, J. Blasco, , and M. Concepción Sánchez. *Phys. Rev. B*, 70:024408, 2004.

[102] P.M. Woodward, D.E. Cox, E. Moshopoulou, A.W. Sleight, and S. Morimoto. *Phys. Rev. B*, 62:844, 2000.

[103] T. Vogt, P. M. Woodward, P. Karen, B. A. Hunter, P. Henning, and A. R. Moodenbaugh. *Phys. Rev. Lett.*, 84:2969, 2000.

[104] J. A. Alonso, J. L. García-Muñoz, M. T. Fernández-Díaz, M. A. G. Aranda, M. J. Martínez-Lope, and M. T. Casais. *Phys. Rev. Lett.*, 82:3871, 1999.

[105] J. Rodríguez-Carvajal, M.T. Fernández-Diaz, and J.L. Martínez. *J. Phys: Condens. Matt.*, 3:3215, 1991.

[106] B. E. Warren. *X-ray diffraction*. Reading Massachusetts [etc.]: Addison-Wesley, 1969.

[107] P. D. Battle, T. C. Gibb, and P. Lightfoot. *J. Solid State Chem.*, 76:334, 1988.

[108] M. Von-Harder and Müller-Buchshbaum. *Z. Anorg. Allg. Chem.*, 464:169, 1980.

[109] C. Greaves, A.J.C. Jacobson, B.C. Tofield, and B.E.F. Fender. *Acta Cryst.*, B31:641, 1975.

[110] J. Rodríguez-Carvajal. *Ph. D. Thesis, University of Barcelona, Spain*, 1984.

[111] T. Takeda, W. Watanabe, S. Komura, and H. Fujii. *J. Phys. Soc. Jpn*, 56:731, 1987.

[112] H. Watanabe, Y. Yamaguchi, H. Oda, and H. Takei. *J. Magn. Magn. Mater.*, 15-18:521, 1980.

[113] J. Mesot, P. Allenspach, U. Staub, and A. Furrer. *Phys. Rev. Lett.*, 70:865, 1993.

[114] S. X. Wang and A. M. Taratorin. *Magnetic Information Storage Technology.* San Diego: Academic Press, 1999.

[115] G. H. Jonker and J. H. Van Santen. *Physica,* 16:599, 1953.

[116] G. H. Jonker and J. H. Van Santen. *Physica,* 16:337, 1953.

[117] E. O. Wollan and W. C. Koehler. *Phys. Rev.,* 100:545, 1955.

[118] S. Jin, T. H. Tiefel, M. McCormack, R. A. Fasnacht, R. Ramesh, and L. H. Chen. *Science,* 264:413, 1994.

[119] A. J. Millis, P. B. Littlewood, and B. I. Shraiman. *Phys. Rev. Lett.,* 74:5144, 1995.

[120] R. von Helmholt, J. Wecker, B. Holzapfel, L. Schultz, and K. Samwer. *Phys. Rev. Lett.,* 71:2331, 1993.

[121] G. Briceno, H. Chang, X. Sun, P. G. Schultz, and X. D. Xiang. *Science,* 270:273, 1995.

[122] S. Yamaguchi, H. Taniguchi, H. Takagi, T. Arima, and Y. Tokura. *J. Phys. Soc. Jpn,* 54:1885, 1995.

[123] R. Mahendiran and A. K. Raychaudhuri. *Phys. Rev. B,* 54:16044, 1996.

[124] L. Barbey, N. Nguyen, V. Caignaert, M. Hervieu, and B. Raveau. *Mater. Res. Bull.,* 27:295, 1992.

[125] L. Barbey, N. Nguyen, V. Caignaert, F. Studer, and B. Raveau. *J. Solid State Chem.,* 112:148, 1994.

[126] L. Er-Rakho, C. Michel, Ph. Lacorre, and B. Raveau. *J. Solid State Chem.,* 73:531, 1988.

[127] I. O. Troyanchuk, N. V. Kasper, D. D. Khalyavin, H. Szymczak, R. Szymczak, and M. Baran. *Phys. Rev. Lett.,* 80:3380, 1998.

[128] A. Maignan, C. Martin, D. Pelloquin, N. Nguyen, and B. Raveau. *J. Solid State Chem.,* 142:247, 1999.

[129] E. Suard, F. Fauth, V. Caignaert, I. Mirebeau, and G. Baldinozzi. *Phys. Rev. B,* 61:11871(R), 2000.

[130] Y. Moritomo, T. Akimoto, M. Takeo, A. Machida, E. Nishibori, M. Takata, M. Sakata, K. Ohoyama, and A. Nakamura. *Phys. Rev. B,* 61:13325(R), 2000.

[131] Y. Moritomo, M. Takeo, X. J. Liu, T. Akimoto, and A. Nakamura. *Phys. Rev. B,* 58:13334(R), 1998.

[132] M. Soda, Y. Yasui, M. Ito, S. Iikubo, and M. Sato. *J. Phys Soc. Japan,* 73:2857, 2004.

[133] E. Suard, F. Fauth, V. Caignaert, I. Mirebeau, and G. Baldinozzi. *Phys. Rev. B,* 61:11871(R), 2000.

[134] F. Fauth, E. Suard, V. Caignaert, B. Domengès, I. Mirabeau, and Lukas Keller. *Eur. J. Phys. B,* 21:163, 2001.

[135] D. Akahoshi and Y. Ueda. *J. Solid State Chem.*, 156:355, 2001.

[136] S. K. Kwon, J. H. Park, and B. I. Min. *Phys. Rev. B*, 62:14637(R), 2000.

[137] E. Suard, F. Fauth, and V. Caignaert. *Physica B*, 276-278:254, 2000.

[138] T. Nakajima, M. Ichihara, and Y. Ueda. *J. Phys. Soc. Japan*, 74:1672, 2005.

[139] S. Roy, I. S. Dubenko, M. Khan, E. M. Condon, J. Craig, N. Ali, W. Liu, and B. S. Mitchell. *Phys. Rev B*, 71:024419, 2005.

[140] P. S. Anderson, C. A. Kirk, J. Knudsen, I. M. Reaney, and A. R. West. *Solid State Sciences*, 7:1149, 2005.

[141] R. D. Shannon. *Acta Cryst.*, A32:751, 1976.

[142] J. C. Burley, J. F. Mitchell, S. Short, D. Miller, and Y. Tang. *J. Solid State Chem.*, 170:339, 2005.

[143] S. Streule, A. Podlesnyak, D. Sheptyakov, E. Pomjakushina, M. Stingaciu, K. Conder, M. Medarde, J. Mesot, M. V. Patrakeev, I. A. Leonidov, and V. L. Kozhevnikov. *J. Phys.: Condens. Matter*, 17:3317, 2005.

[144] V. P. Plakhty, Y. P. Chernenkov, S. N. Barilo, A. Podlesnyak, E. Pomjakushina, D. D. Khalyavin, E. V. Moskvin, and S. V. Gavrilov. *Phys. Rev. B*, 71:214407, 2005.

[145] D. D. Khalyavin. *Phys. Rev. B*, 72:134408, 2005.

[146] D. I. Khomskii and U. Löw. *Phys. Rev. B*, 69:184401, 2004.

[147] D. D. Khalyavin, I. O. Troyanchuk, and N. V. Kasper. *J. Mater. Res.*, 17:838, 2002.

[148] F. Fauth, E. Suard, V. Caignaert, and I. Mirebeau. *Phys. Rev. B*, 66:184421, 2002.

[149] M. Soda, Y. Yasui, T. Fujita, T. Miyashita, M. Sato, and K. Kakurai. *J. Phys. Soc. Japan*, 72:1729, 2003.

[150] A. A. Taskin, A. N. Lavrov, and Y. Ando. *Phys. Rev. Lett.*, 90:227201, 2003.

[151] Y. P. Chernenkov, V. P. Plakhty, V. I. Fedorov, S. N. Barilo, S. V. Shiryaev, and G. L. Bychkov. *Phys. Rev. B*, 71:184105, 2005.

[152] J. F. Mitchell, J. Burley, and S. Short. *J. Appl. Phys.*, 93:7364, 2003.

[153] A. A. Taskin, A. N. Lavrov, and Y. Ando. *Phys. Rev. B*, 71:134414, 2005.

[154] H. D. Zhou and J. B. Goodenough. *J. Solid State Chem.*, 177:3339, 2004.

[155] C. Frontera, J. L. García-Muñoz, A. Llobet, and M. A. G. Aranda. *Phys. Rev. B*, 65:180405(R), 2002.

[156] D. D. Khalyavin, S. N. Barilo, S. V. Shiryaev, G. L. Bychkov, I. O. Troyanchuk, A. Furrer, P. Allenspach, H. Szymczak, and R. Szymczak. *Phys. Rev. B*, 67:214421, 2003.

[157] A. A. Taskin and Y. Ando. *Phys. Rev. Lett.*, 95:176603, 2005.

[158] P. L. Kuhns, M. J. R. Hoch, W. G. Moulton, A. P. Reyes, J. Wu, and C. Leighton. *Phys. Rev. Lett.*, 91:127202, 2003.

[159] A. Ghoshray, B. Bandyopadhyay, K. Ghoshray, V. Morchshakov, K. Bärner, I. O. Troyanchuk, H. Nakamura, T. Kohara, G. Y. Liu, and G. H. Rao. *Phys. Rev. B*, 69:064424, 2004.

[160] J. L. García-Muñoz, C. Frontera, A. Llobet, A. E. Carrillo, A. Caneiro, M. A. G. Aranda, M. Respaud, C. Ritter, and E. Dooryee. *J. Magn. Magn. Mater.*, 272-276:1762, 2004.

[161] S. Streule, A. Podlesnyak, J. Mesot, M. Medarde, K. Conder, E. Pomjakushina, E. Mitberg, and V. Kozhevnikov. *Phys. Rev. B*, 73:094203, 2006.

[162] M. V. Patrakeev, I. A. Leonidov, V. L. Kozhevnikov, and K. R. Poeppelmeier. *J. Solid State Chem.*, 178:921, 2005.

[163] M. V. Patrakeev, E. B. Mitberg, A. A. Lakhtin, I. A. Leonidov, V. L. Kozhevnikov, and K. R. Poeppelmeier. *Ionics*, 4:191, 1998.

[164] E. B. Mitberg, M. V. Patrakeev, I. A. Leonidov, V. L. Kozhevnikov, and K. R. Poeppelmeier. *Solid State Ionics*, 130:325, 2000.

[165] N. W. Ashcroft and N. D. Mermin. *Solid State Physics*. Saunders College Publishing, 1976.

[166] S. Ya. Istomin, E. V. Antipov, G. Svensson, J. P. Attfield, V. L. Kozhevnikov, I. A. Leonidov, M. V. Patrakeev, and E. B. Mitberg. *J. Sol. State Chem.*, 167:196, 2002.

[167] H. L. Tuller. *Ceramic Materials for Electronics*. Editor R. C. Buchanan; Dekker, N.Y., 1986.

[168] S. N. Barilo, S. V. Shiryaev, G. L. Bychkov, V. P. Plakhty, A. S. Shestak, A. G. Soldatov, A. Podlesnyak, K. Conder, M. Baran, W. R. Flavell, and A. Furrer. *J. Cryst. Growth*, 275:120, 2005.

[169] M. Respaud, C. Frontera, J. L. García-Muñoz, M. A. G. Aranda, B. Raquet, J. M. Broto, H. Rakoto, M. Goiran, A. Llobet, and J. Rodríguez-Carvajal. *Phys. Rev. B*, 64:214401, 2001.

[170] Z. X. Zhou, S. McCall, C. S. Alexander, J. E. Crow, P. Schlottmann, A. Bianchi, C. Capan, R. Movshovich, K. H. Kim, M. Jaime, N. Harrison, M. K. Haas, R. J. Cava, and G. Cao. *Phys. Rev. B*, 69:024425, 2004.

[171] M. Baran, V. I. Gatalskaya, R. Szymczak, S. V. Shiryaev, S. N. Barilo, G. L. Bychkov, and H. Szymczak. *J. Phys.: Condens. Matter*, 17:5613, 2005.

[172] S. Streule, A. Podlesnyak, Ch. Niedermayer, S. Barilo, and J. Mesot. *http://num.web.psi.ch/reports/2004/LNS/lns-sc-02.pdf*, 2004.

[173] S. Streule, A. Podlesnyak, S. Gvasaliya, S. Barilo, and J. Mesot. *http://num.web.psi.ch/reports/2003/LNS/s-05.pdf*, 2003.

[174] L. Pauling. *J. Am. Chem. Soc.*, 51:1010, 1929.

[175] I. D. Brown. *J. Chem. Inf. Comput. Sci.*, 29:266, 1989.

[176] H. Rauch and W. Waschkowski. *Editor: H. Schopper. Landolt-Börnstein - Group I Elementary Particles, Nuclei and Atoms: Volume 16 A1, Chapter 6.* Springer-Verlag GmbH, 2000.

Acknowledgement

Curriculum Vitae

Full Name: Sabine Streule

Date of Birth: July 13, 1975

Place of Birth: Basel, Switzerland

From: Ennetbaden (AG), Switzerland

Nationality: Switzerland

2002-2006   Ph.D Thesis, Laboratory for Neutron Scattering,
ETH Zürich & Paul Scherrer Institute
Supervisors: Dr. J. Mesot and Dr. A. Podlesnyak

2002   Awarded Dipl. Phys. ETH

2002   Diploma Thesis, Laboratory for Neutron Scattering,
ETH Zürich & Paul Scherrer Institute
Supervisors: Dr. R. Gilardi and Dr. J. Mesot

1996-2002   Study of Physics at ETH Zürich

1996   5 months practical training at the UBS in Zürich, Switzerland

1996   Swiss Federal Matura, Type D (new languages)

1991-1996   Gymnasium at the Kantonsschule Stadelhofen, Zürich, Switzerland

1987-1991   Gymnasium at the German School New York in White Plains NY, USA

1982-1987   Elementary School in Reinach BL, Switzerland

Publications

2006

S. Streule, A. Podlesnyak, D. Sheptyakov, E. Pomjakushina, M. Stingaciu, K. Conder, M. Medarde, J. Mesot, M. V. Patrakeev, I. A. Leonidov, V. L. Kozhevnikov
High-temperature Order-Disorder Transition and Polaronic Conductivity in $PrBaCo_2O_{5.48}$
Phys. Rev. B **73** (2006) 094203

A. Podlesnyak, **S. Streule**, J. Mesot, M. Medarde, E. Pomjakushina, K. Conder, A. Tanaka, M. W. Haverkort, D. I. Khomskii
Spin-state transition in $LaCoO_3$: direct neutron spectroscopic evidence of excited magnetic states
Phys. Rev. Lett., in press

S. Streule, A. Podlesnyak, E. Pomjakushina, K. Conder, D. Sheptyakov, M. Medarde, J. Mesot
Oxygen order-disorder phase transition in $PrBaCo_2O_{5.48}$ at high temperature
Physica B, **380** (2006) 539

A. Podlesnyak, **S. Streule**, K. Conder, E. Pomjakushina, J. Mesot, A. Mirmelstein, P. Schützendorf, R. Lengsdorf, M. M. Abd-Elmeguid
Pressure effects on crystal structure, magnetic and transport properties of layered perovskite $TbBaCo_2O_{5.5}$
Physica B, **380** (2006) 537

S. Streule, M. Medarde, A. Podlesnyak, E. Pomjakushina, K. Conder, S. Kazakov, J. Karpinksi, J. Mesot
Short Range Charge Ordering in $Ho_{0.1}Sr_{0.9}CoO_{3-\delta}$
Phys. Rev. B **73** (2006) 024423

C.R.H. Bahl, K. Lefmann, A.B. Abrahamsen, H.M. Rønnow, F. Saxild, T.B.S. Jensen, L. Udby, N.H. Andersen, N.B. Christensen, H.S. Jakobsen, T. Larsen, P.S. Häfliger, **S. Streule** and Ch. Niedermayer
Inelastic neutron scattering experiments with the monochromatic imaging mode of the RITA-II spectrometer
Nuclear Instruments and Methods B, **246** (2006) 452

2005

O. Zaharko, H. M. Ronnow, A. Daoud-Aladine, **S. Streule**, F. Juranyi, J. Mesot, H. Berger, P.-J. Brown
Incommensurate magnetism in the coupled spin tetrahedra system $Cu_2Te_2O_5Cl_2$
Low Temperature Physics **31** (2005) 814

K. Conder, E. Pomjakushina, V. Pomjakushin, M. Stingaciu, **S. Streule**, A. Podlesnyak
Oxygen isotope effect on metal-insulator transition in layered cobaltites $RBaCo_2O_{5.5}$
J. Phys.: Condens. Matter **17** (2005) 5813

S. Streule, A. Podlesnyak, J. Mesot, M. Medarde, K. Conder, E. Pomjakushina, E. Mitberg,
V. Kozhevnikov
Effect of oxygen ordering on the structural and magnetic properties of the layered perovskites $PrBaCo_2O_{5+\delta}$
J. Phys.: Condens. Matter **17** (2005) 3317

A. Podlesnyak, **S. Streule**, M. Medarde, K. Conder, E. Pomjakushina, J. Mesot
Effect of oxygen non-stoichiometry on structural and magnetic properties of $PrBaCo_2O_{5+\delta}$
Physica B **359-361** (2005) 1348

2004

O. Zaharko, A. Daoud-Aladine, **S. Streule**, J. Mesot, P.-J. Brown, H. Berger
Incommensurate Magnetic Order in $Cu_2Te_2O_5X_2$ (X = Cl, Br) Studied by Neutron Diffraction
Phys. Rev. Lett. **93** (2004) 217206

S. Streule, A. Podlesnyak, J. Mesot, K. Conder, N. Golosova, E. Mitberg, S. Kazakov
Effect of oxygen nonstoichiometry on structural and magnetic properties of $Ho_{0.1}Sr_{0.9}CoO_{3-x}$ perovskites ($0.15 \leq x \leq 0.49$)
Physica B **350** (2004) E281

S. Streule, A. Podlesnyak, K. Conder, N. Golosova, E. Mitberg
Magnetic Properties of $Ho_{0.1}Sr_{0.9}CoO_{3-x}$ ($0.15 \leq x \leq 0.49$)
J. Magn. Magn. Mat. **272-276** (2004) E457